UNIVERSITY OF CYPRUS

DEPARTMENT OF MATHEMATICS AND STATISTICS

NUMERICAL SIMULATIONS OF COMPRESSIBLE GENERALIZED NEWTONIAN FLOWS

Ph.D. Dissertation

ELENI G. TALIADOROU

November 2008

UNIVERSITY OF CYPRUS

DEPARTMENT OF MATHEMATICS AND STATISTICS

NUMERICAL SIMULATIONS OF COMPRESSIBLE GENERALIZED NEWTONIAN FLOWS

By

Eleni G. Taliadorou

SUBMITTED IN PARTIAL FULFILLMENT OF THE

REQUIREMENTS FOR THE DEGREE OF

DOCTOR OF PHILOSOPHY

AT

UNIVERSITY OF CYPRUS

NICOSIA, CYPRUS

NOVEMBER 2008

To my family

Contents

Acknowledgments

I would like to express my deep gratitude to my supervisor, Professor Georgios Georgiou for all his help, encouragement and guidance through my PHD studies. I also wish to thank our collaborators Professors Andreas Alexandrou, Evangelos Mitsoulis, Christos Xenophontos and Marina Neophytou for their help and my colleague and friend Maria Chatzimina for her support and friendship.

To my family a special acknowledgement for their continuous help, support and solidarity.

Eleni G. Taliadorou

Nicosia, November 2008.

Abstract

In this thesis we have studied weakly compressible Newtonian and generalized Newtonian flows using numerical and perturbation solutions, which have become very important in the field of computational rheology. In the past two decades laminar Poiseuille flows of weakly compressible materials have gained interest due to the importance of compressibility in many processes involving liquid flows in relatively long tubes, such as waxy crude oil transport, injection molding and polymer extrusion. Several numerical solutions of weakly compressible Poiseuille flows have already been reported for Newtonian fluids, generalized Newtonian fluids, such as the Carreau fluid and the Bingham plastic, as well as for viscoelastic fluids.

First we have numerically studied the time-dependent compressible extrusion of a Carreau fluid in the full reservoir-capillary-extrudate geometry using finite elements. The objective was to investigate the validity of the compressibility/slip mechanism proposed for the stick-slip polymer extrusion instability. We assumed that slip occurs along the die wall following a nonmonotonic slip law that is based on experimental measurements on polyethylene melts. Our results demonstrate that the combination of compressibility and nonlinear slip leads to self-sustained oscillations of the pressure drop and of the mass flow rate in the unstable regime of the flow curve. The effects of the reservoir volume, the imposed flow rate, and the capillary length on the amplitude and the frequency of the pressure and free surface oscil-

lations have been studied and our findings were consistent with experimental observations. The period of the pressure and flow rate oscillations was found to increase linearly with the reservoir length, while their amplitudes and waveforms are fairly constant. The period of the pressure oscillations, when plotted versus the reservoir volume, appears to pass through the origin which is not the case with extrapolated experimental data. In agreement with certain experiments, the period of the pressure oscillations passes through a minimum, when this is plotted versus the imposed volumetric flow rate.

We have also solved numerically the axisymmetric and plane extrudate swell flows of a strongly compressible Newtonian fluid and studied the effects of the compressibility and the equation of state, slip, geometry, and inertia on the expansion of the jet. Compressibility effects were investigated using both a linear and an exponential equation of state. The numerical results confirm previous reports that the swelling of the extrudate decreases initially as the compressibility of the fluid is increased and then increases considerably together with the angle of separation of the jet. Our simulations revealed for the first time that in the case of non-zero inertia, high compressibility was found to lead to a contraction of the extrudate after the initial expansion and then to decaying free surface oscillations. The time-dependent calculations showed that these oscillatory steady-state solutions are stable and insensitive to the length of the extrudate region and the boundary condition along the capillary wall.

The perturbation solutions for the planar and axisymmetric Poiseuille flows of weakly compressible Newtonian fluids with constant shear and bulk viscosities have also been solved up to the second-order. A linear equation of state has been employed and a perturbation analysis of the primary variables is performed using compressibility as the perturbation parameter. The effects of compressibility, the bulk viscosity, the aspect ratio, and the Reynolds number on the velocity and pressure fields were studied and comparisons were made with available

analytical results.

Finally we have derived approximate semi-analytical solutions of the steady, creeping, weakly compressible two-dimensional plane and axisymmetric Poiseuille flows of a Herschel-Bulkley fluid. The effects of compressibility have been taken into account by means of a linear and an exponential equation of state. Both equations of state gave similar predictions for sufficiently low compressibility numbers and/or for short tube. Under the assumption of zero transverse velocity, the pressure distribution along the flow direction was first calculated by means of numerical integration and the two-dimensional axial velocity was then be constructed. The effects of compressibility, equation of state, the Bingham number and the power-law exponent on the solutions were investigated. In particular it has been demonstrated that the pressure required to drive the flow for a given tube length is reduced with compressibility and the two-dimensional axial velocity is characterized by plug-like regions the size of which increases upstream, in agreement with more sophisticated two-dimensional numerical simulations .

ΠΕΡΙΛΗΨΗ

Στη παρούσα διατριβή μελετήσαμε με αριθμητικές μεθόδους και μεθόδους διαταραχών ασθενώς συμπιεστές Νευτώνειες και γενικευμένες Νευτώνειες ροές, οι οποίες έχουν καταστεί σημαντικές στην περιοχή της υπολογιστικής ρεολογίας. Τις τελευταίες δύο δεκαετίες, οι στρωτές ροές Poiseuille ασθενώς συμπιεστών υλικών βρέθηκαν στο επίκεντρο του ενδιαφέροντος πολλών ερευνητών, λόγω της σημασίας της συμπιεστότητας σε πολλές διεργασίες, οι οποίες περιλαμβάνουν ροές σε σχετικά μεγάλου μήκους αγωγούς, όπως η μεταφορά αργού πετρελαίου, η τυποποίηση πολυμερών μέσω έγχυσης, και η εκβολή πολυμερών. Αρκετές αριθμητικές λύσεις για ασθενώς συμπιεστές ροές Poiseuille έχουν ήδη αναφερθεί στη βιβλιογραφία για Νευτώνεια, γενικευμένα Νευτώνεια, για παράδειγμα τα ρευστά Carreau και τα πλαστικά Bingham, καθώς και για ιξωδοελαστικά ρευστά.

Αρχικά, μελετήσαμε αριθμητικά την χρονομεταβαλλόμενη συμπιεστή εκβολή ρευστού Carreau σε όλο το πεδίο ροής που περιλαμβάνει τη δεξαμενή τροφοδοσίας, τον τριχοειδή αγωγό και το έκβολο, χρησιμοποιώντας την μέθοδο των πεπερασμένων στοιχείων. Ο στόχος ήταν η διερεύνηση της ισχύος του μηχανισμού συμπιεστότητας/ολίσθησης στη λεγόμενη αστάθεια μη-ολίσθησης/ολίσθησης (stick-slip instability) που παρατηρείται κατά την εκβολή πολυμερών. Υποθέσαμε ότι υπάρχει ολίσθηση του ρευστού στα τοιχώματα του τριχοειδούς η οποία υπακούει μια μη μονότονη εξίσωση ολίσθησης, που είναι βασισμένη σε πειραματικές μετρήσεις με τήγματα πολυαιθυλενίου. Τα αποτελέσματά μας δείχνουν ότι ο συνδυασμός συμπιεστότητας και μη γραμμικής ολίσθησης οδηγεί σε αυτοσυντηρούμενες ταλαντώσεις της βαθμίδας πίεσης και της ογκομετρικής παροχής στην ασταθή περιοχή της καμπύλης ροής. Μελετήσαμε συστηματικά τις επιδράσεις του όγκου της δεξαμενής, της επιβαλλόμενης ογκομετρικής παροχής, και του μήκους του αγωγού στο πλάτος και τη συχνότητα των ταλαντώσεων της πίεσης και της ελεύθερης επιφάνειας και τα ευρήματά μας συμφωνούν γενικά με τις πειραματικές παρατηρήσεις. Με βάση τις αριθμητικές μας προσομοιώσεις. η περίοδος των ταλαντώσεων της πίεσης και της ογκομετρικής παροχής αυξάνεται γραμμικά με το μήκος της δεξαμενής, ενώ τα πλάτη και οι κυματομορφές παραμένουν σχεδόν αμετάβλητες. Η περίοδος των ταλαντώσεων της πίεσης συναρτήσει του όγκου της δεξαμενής διέρχεται από την αρχή των αξόνων σε αντίθεση με πειραματικές μετρήσεις. Σε συμφωνία με ορισμένες πειραματικές εργασίες, η περίοδος των ταλαντώσεων της πίεσης συναρτήσει της επιβαλλόμενης ογκομετρικής παροχής, διέρχεται από ελάχιστο.

Επιλύσαμε επίσης αριθμητικά την αξονοσυμμετρική και την επίπεδη ροή διαστολής εκβόλου (extrudate swell) ισχυρά συμπιεστών Νευτώνειων ρευστών και μελετήσαμε το ρόλο που παίζουν στη

διαστολή του εκβαλλόμενου πίδακα η συμπιεστότητα, η καταστατική εξίσωση, η ολίσθηση, η γεωμετρία, και η αδράνεια. Οι επιδράσεις της συμπιεστότητας διερευνήθηκαν χρησιμοποιώντας μια γραμμική και μια εκθετική καταστατική εξίσωση. Τα αριθμητικά αποτελέσματα επιβεβαιώνουν προηγούμενες αναφορές για την αρχική μείωση της διαστολής του εκβόλου με τη συμπιεστότητα και την εν συνεχεία αύξησή της μαζί με τη γωνία διαχωρισμού του πίδακα. Οι προσομοιώσεις έδειξαν για πρώτη φορά ότι στην περίπτωση μη-μηδενικών αδρανειακών όρων, η υψηλή συμπιεστότητα οδηγεί σε σημαντική συστολή του εκβόλου και σε φθίνουσες ταλαντώσεις της επιφάνειας του εκβόλου, μετά από την αρχική διαστολή του. Οι χρονομεταβαλλόμενοι υπολογισμοί έδειξαν ότι αυτές οι ταλαντούμενες βασικές λύσεις είναι ευσταθείς και δεν επηρεάζονται ούτε από το μήκος της περιοχής του εκβόλου ούτε από τις συνοριακές συνθήκες στο τοίχωμα του τριχοειδούς αγωγού.

Έχουμε, επίσης επιλύσει με την μέθοδο διαταραχών μέχρι και τους όρους δεύτερης τάξης την επίπεδη και την αξονοσυμμετρική ροή Poiseuille ασθενώς συμπιεστών Νευτώνειων ρευστών. Χρησιμοποιήσαμε μια γραμμική καταστατική εξίσωση και εφαρμόσαμε τη μέθοδο διαταραχών στις πρωταρχικές μεταβλητές με παράμετρο διαταραχής τη συμπιεστότητα. Μελετήσαμε την επίδραση της συμπιεστότητας, του ιξώδους, του λόγου μορφής, και του αριθμού Reynolds στην ταχύτητα και την πίεση, και κάναμε συγκρίσεις με άλλες διαθέσιμες αναλυτικές λύσεις.

Τέλος, βρήκαμε προσεγγιστικές ημι-αναλυτικές λύσεις για την στάσιμη, έρπουσα, ασθενώς συμπιεστή διδιάστατη επίπεδη και αξονοσυμμετρικη ροή Poiseuille ρευστού που υπακούει στην καταστατική εξίσωση των Herschel-Bulkley. Η επίδραση της συμπιεστότητας λήφθηκε υπόψη με τη χρήση μιας γραμμικής και μιας εκθετικής καταστατικής εξίσωσης. Οι δύο αυτές εξισώσεις δίνουν παρόμοια, αποτελέσματα σε χαμηλού αριθμούς συμπιεστότητας ή/και για μικρό μήκος αγωγού. Με την παραδοχή μηδενικής εγκάρσιας ταχύτητας, η κατανομή της πίεσης κατά μήκος της ροής μπορεί να υπολογιστεί σ' ένα πρώτο στάδιο με αριθμητική ολοκλήρωση επιτρέποντας στη συνέχεια την κατασκευή της κατανομής της διδιάστατης αξονικής ταχύτητας. Μελετήσαμε τις επιπτώσεις της συμπιεστότητας, του αριθμού Bingham και του εκθέτη στις λύσεις. Τα αποτελέσματά μας έδειξαν ότι η απαιτούμενη πίεση για την δημιουργία και συντήρηση της ροής σε αγωγό δοσμένου μήκους μειώνεται με τη συμπιεστότητα και η διδιάστατη αξονική ταχύτητα χαρακτηρίζεται από εμβολικές περιοχές, το μέγεθος των οποίων αυξάνεται στα ανάντη, σε συμφωνία με πιο εξεζητημένες διδιάστατες αριθμητικές προσομοιώσεις.

List of Figures

List of Tables

Chapter 1

Introduction

Laminar Poiseuille flows of weakly compressible materials have gained interest in the past two decades due to their applications in many processes involving liquid flows in relatively long tubes, such as waxy crude oil transport [15, 90], injection molding [50] and polymer extrusion [29, 32, 86]. Numerical solutions of weakly compressible Poiseuille flows have been reported for Newtonian fluids [32], generalized Newtonian fluids [14, 35, 47, 55, 76, 86], such as the Carreau fluid [29] and the Bingham plastic [90], as well as for viscoelastic fluids [6]. The compressibility-slip mechanism has been the most popular explanation for the stick-slip polymer extrusion instability and is the only one consistent with experimental observations. Georgiou and Crochet [32, 33] have tested the compressibility-slip mechanism in the Newtonian case for the Poiseuille and extrudate-swell flows with slip at the wall. By using compressibility and a non-monotonic slip equation, they were able to model the self-sustained pressure and flow rate oscillations observed in the experiments. The same mechanism has been employed in various one-dimensional phenomenological models describing the pressure and flow rate oscillations [30]. More recently, Georgiou [29] solved the time-dependent, compressible, axisymmetric Poiseuille and extrudate-swell flows of a Carreau fluid with slip at the

wall, using finite elements in space and finite differences in time. Vinay et al. [90] examined the numerical simulation of isothermal transient flows for a weakly compressible viscoplastic fluid in an axisymmetric pipe geometry using the Bingham model.

As noted by Kwon [50] the effect of material compressibility plays a significant role quite often in polymer processing. In modeling modern processing operations, such as injection molding and high speed extrusion where pressure and flow rate are extremely high, the compressibility of a viscoelastic liquid may have to be taken into account in order to accommodate various flow phenomena. In formulating the Hadamard stability criteria for incompressible viscoelastic liquids, he employed two classes of quasilinear differential and time-strain separable single integral constitutive equations and demonstrated that the difference between stability problems of incompressible and compressible systems lies in the possibility of longitudinal wave propagation.

Keshtiban et al. [47] also pointed out that low Mach number flows play an important role both in nature and in industrial processing. In many technical applications, liquid flows may exhibit significant compressibility effects. These authors introduced a hybrid element/finite volume algorithm for Newtonian and viscoelastic weakly-compressible liquid flows at low Mach number and Reynolds number under isothermal conditions. They pointed out that the compressibility of viscoelastic liquids should be taken into account, in order to accommodate flow phenomena, such as cavitation or flow instabilities. Also, in capillary rheometry, compressibility effects may have a major impact upon the time-dependent pressure changes in the system.

More recently, Tang and Kalyon [86] demonstrated the important role played by the compressibility and wall slip in the simple shear flow by developing a mathematical model for the time-dependent circular tube flow of compressible liquids subject to pressure-dependent slip

at the wall and applied to polydimethylsiloxane (PDMS) for which experimental data were available.

Mitsoulis et al. [55] studied the transient capillary rheometry of compressible LLDPE melt, experimentally and theoretically. They used different die designs to demonstrate the effect of compressibility on the transient pressure distributions for wide range of shear rates. They also reported that compressibility effects are important in understanding the pressure builds-up in start-up capillary experiments of polymer melts.

Other contributions in the literature concerning weakly compressible flows of non-Newtonian fluids are those of Cawkwell and Charles [14] for 1D compressible thixotropic viscoplastic flows, Golay and Helluy [35] for viscous compressible flows and Silva and Coupez [76], and Keshtiban et al. [47] for compressible viscoelastic flows. Finally, Davidson et al. [15] have proposed a semi-analytical 1D approach to restart a pipeline filled with a compressible gelled waxy crude oil.

To study the effects of compressibility, two alternative equations of state, a linear and an exponential one, are most frequently used. At constant temperature and low pressures, the density can be represented by the linear approximation

$$\rho \,=\, \rho_0 \,[1 \,+\, \beta\,(p \,-\, p_0)\,]\ ,$$

where $\beta \equiv -(\partial V/\partial p)_{p_0,T}/V_0$ is the isothermal compressibility assumed to be constant, V is the specific volume, ρ_0 and V_0 are, respectively, the density and the specific volume at a reference pressure p_0, and T is the temperature. The following exponential equation is also used:

$$\rho \,=\, \rho_0\, e^{\beta\,(p\,-\,p_0)}\ .$$

This is equivalent to the linear equation of state for sufficiently small values of β and low pressures. A disadvantage of this equation is the fast growth of the density (for high values of

β). On the other hand, the linear model may lead to negative values of the density. Obviously more sophisticated equations of state should be used for highly compressible flows.

A linear equation of state has been employed in previous numerical studies of the compressible extrudate swell flow [10, 28], by Hatzikiriakos and Dealy [39] for a HDPE, and in previous studies concerning the simulation of the stickslip extrusion instability [29, 32]. Exponential equations of state have been employed, for example, by Ranganathan et al. [70] for a HDPE and, more recently, by Vinay et al. [90], in simulations of weakly compressible Bingham flows. Our objective in Chapter 2, is to simulate numerically the stick-slip extrusion instability. We study the time-dependent, compressible extrusion of a Carreau fluid over the reservoir-die-extrudate region, assuming that slip occurs along the die wall following a nonmonotonic slip law that is based on the experimental measurements of Hatzikiriakos and Dealy [39, 40]. to solve the governing equations, the finite element method is used in space and an implicit Euler scheme is used in time. The effects of the reservoir volume and the imposed flow rate on the pressure and flow rate oscillations are investigated and the numerical simulations are compared with experimental observations.

In Chapter 3, the time-dependent extrusion of strongly compressible Newtonian liquids (such as foams) is simulated using finite elements. To study the effects of compressibility, two alternative equations of state, a linear and exponential one, are used. It is demonstrated that compressibility affects significantly the swelling of the jet and leads to oscillatory steady-state free surfaces.

In Chapter 4, the perturbation solutions of both the planar and axisymmetric Poiseuille flows of weakly compressible Newtonian liquids are derived. Explicit analytical solutions for the pressure, the density and the velocity are obtained up to the second order. A linear equation of state is assumed and a perturbation analysis of the primary flow is performed with

the compressibility number serving as the perturbation parameter. Results concerning the effects of compressibility, the Reynolds number, the aspect ratio, and the bulk viscosity on the velocity and pressure fields are presented and compared with available solutions in the literature.

In Chapter 5, we approximately solve the plane and axisymmetric weakly compressible Poiseuille flows of a Herschel-Bulkley fluid and investigate the effects of compressibility by means of two different equations of state, i.e. a linear and exponential one. Analytical and semi-analytical results are presented for both the incompressible and compressible flows of a Herschel-Bulkley fluid, and the effects of yield stress on the yield point and the velocity are discussed.

Finally in Chapter 6, the conclusions of this thesis are summarized and suggestions for future work are provided.

Chapter 2

A two-dimensional numerical study of the stick-slip extrusion instability

2.1 Introduction

Among the various types of polymer extrusion instabilities, the stick-slip instability is the only one that is associated with pressure oscillations at constant throughput, i.e. at constant piston speed in the reservoir region[1][30]. The instantaneous flow rate at the capillary exit is also oscillatory and the extrudate emerges from the capillary in bursts, and is characterized by alternating rough and relatively smooth zones. It is well known that the pressure and flow rate oscillations follow the stable branches of the apparent flow curve, i.e. the plot of the wall shear stress, σ_w, versus the apparent shear rate, γ_A, as shown in Fig. 2.1.

The apparent wall shear rate is calculated from the volumetric flow rate Q as follows:

$$\dot{\gamma}_A \equiv \frac{32\,Q}{\pi\,D^3}\,, \tag{2.1}$$

[1]Some of the results presented in this chapter appear also in References [78, 79, 80, 82].

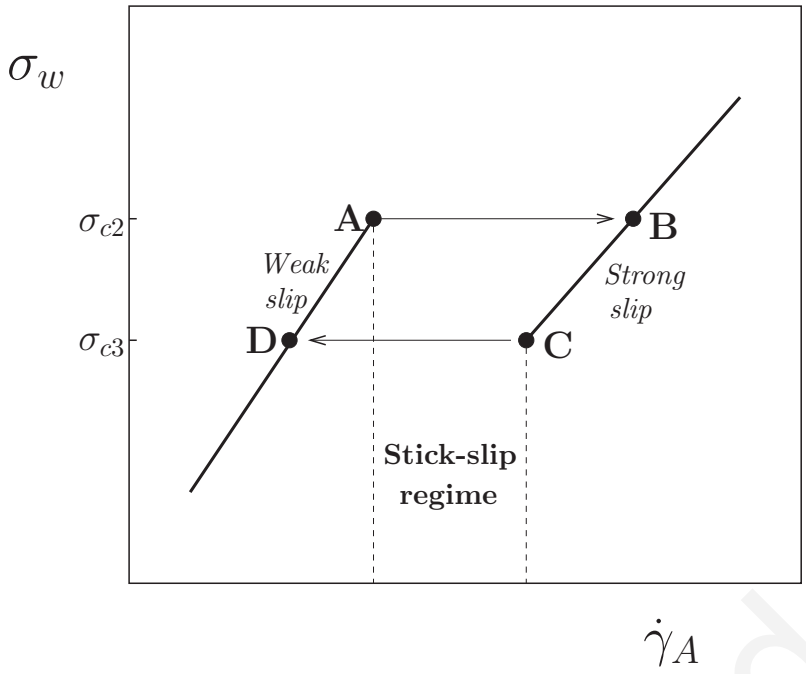

Figure 2.1: *Schematic of an apparent flow curve and the stick-slip regime.*

where D is the diameter of the capillary. The wall shear stress is calculated by

$$\sigma_w = \frac{(P_d - P_{end})}{4L/D} \tag{2.2}$$

where P_d is the driving pressure determined for the force on the piston, P_{end} is the Bagley end correction for the pressure drop, and L is the length of the capillary.

Due to the oscillations of the wall shear stress, the flow curve is discontinuous and consists of two stable positive-slope branches separated by the unstable stick-slip instability regime [20, 40, 65, 74], as illustrated in Fig. 2.1. Experiments with fluids exhibiting the stick-slip instability revealed that the flow curve depends on the capillary diameter. This dependence, which becomes stronger as the apparent shear rate increases, is due to the occurrence of slip at the capillary wall. The lower part of the low-flow-rate branch is insensitive to the capillary diameter, which implies the absence of wall slip. The upper part may be weakly dependent on D, which indicates that weak slip is possible [39, 46, 69]. The high-flow-rate branch is strongly dependent on D, which is an indication of strong slip [1, 39, 46, 22, 21, 69]. Based on slip

velocity estimates, Hatzikiriakos and Dealy [40] proposed a power-law slip equation for the right branch of their flow curve. El Kissi and Piau [21] also derived a single nonmonotonic slip equation for both the branches of the flow curve. These indirect observations for the occurrence of stick and slip phenomena during the extrusion of certain polymer melts have also been confirmed by recent direct slip velocity measurements with optical methods [57, 72]. The role of wall slip in extrusion instabilities is discussed in detail in [18, 41].

When the imposed shear rate is in the unstable regime, the wall shear stress and the apparent shear rate oscillate (with the same period and phase) following closely, in the clockwise sense, the hysteresis cycle ABCD [20, 40, 74]. The critical wall shear stresses for the nearly instantaneous jumps from point A to point B and from C to D are denoted here by σ_{c2} and σ_{c3}, respectively. These two critical stresses correspond to the transition from weak to strong slip and vice versa, and define the limiting values between which the wall shear stress oscillates. Hence, the amplitude of the wall shear stress oscillation is equal to $(\sigma_{c2} - \sigma_{c3})$. Similarly, the amplitudes of the sudden apparent shear rate increase and decrease are determined by the shear rate differences between points A and B and points C and D, respectively [20, 40]. Hence, for a given capillary (i.e. given D and L/D), the onset of the stick-slip instability (i.e. the critical shear stress σ_{c2}) and the amplitudes of the oscillations are determined solely by the steady-state flow curve [20, 40, 53, 96].

The oscillations of the pressure and the extrudate flow rate are obviously analogous to those of the wall shear stress and apparent flow rate, respectively. The variation of the extrudate flow rate, in spite of the constant piston speed, arises from the compressibility of the melt in the reservoir, and causes the characteristic appearance of the extrudate which consists of alternating rough and relatively smooth regions [20, 40, 65].

The generation of self-sustained pressure and flow rate oscillations when compressibility is combined with nonlinear slip has been confirmed by the two-dimensional simulations of Georgiou and Crochet [33, 32]. These authors employed an arbitrary nonmonotonic slip equation relating the wall shear stress to the slip velocity and numerically solved the time-dependent compressible Newtonian Poiseuille and extrudate-swell flows. Their simulations showed that steady-state solutions in the negative-slope regime of the flow curve are unstable, and that oscillatory solutions are obtained at constant volumetric flow rate. In a recent work, Georgiou [29] carried out numerical simulations for a shear-thinning Carreau fluid using an empirical slip equation that is based on the experimental measurements of Hatzikiriakos and Dealy with a HDPE melt [39, 40]. His time-dependent calculations at fixed volumetric flow rates in the unstable negative-slope regime of the flow curve showed that the pressure and flow rate oscillations do not follow the stable branches of the flow curve, in contrast to the experiments. As stated in Ref. [29], including the reservoir region in the simulations is necessary in order not only to account for the compression and decompression of most part of the fluid but also for obtaining limit cycles following the steady-state branches of the flow curve, i.e. for getting pressure and extrudate flow rate oscillations characterized by abrupt changes, as is the experiments.

The objective of the present work is to extend the simulations in [29] to the full reservoir-capillary-extrudate geometry, in order (a) to study the effects of the reservoir length, the imposed flow rate, and the capillary length on the pressure and free surface oscillations and (b) to make comparisons with experimental observations on extrusion under constant piston speed. As discussed below, experimental results from different studies are not always in agreement. The present simulations may be helpful in understanding some of the experimental observations.

Experiments with different materials showed that as the reservoir is emptying, the period of the pressure and flow rate oscillations is reduced while the hysteresis loop of the flow curve remains unchanged, which implies that the amplitudes of the pressure and flow-rate oscillations remain the same [20, 40, 46, 53, 58, 96]. The period of the oscillations has been found to vary linearly with the volume of the melt in the reservoir, and that the extrapolations of the experimental period data do not pass through the origin [13, 20, 40, 73, 74]. On the other hand, the waveform of the pressure oscillations appears to be insensitive to the reservoir length, meaning that the relative durations of the compression and relaxation phases do not change as the extrusion experiment proceeds [20, 40, 96].

According to experimental observations, as the imposed flow rate is increased in the unstable regime, the waveform of the pressure oscillations changes so that the relative duration of the compression part is reduced, while their amplitude is not affected [20, 40, 58, 92, 96]. The reports concerning the effect on the period of the pressure and flow rate oscillations are somehow conflicting. In experiments with HDPEs, Hatzikiriakos and Dealy [40], Durand et al. [20] and Den Doelder et al. [16] observed that the period is decreased as the flow rate is increased. A period reduction has also been reported in experiments on a LLDPE [46] and a PB [52]. On the other hand, the earlier experiments of Myerholtz [58], Weill [96] and Okubo and Hori [61] on HDPEs and those of Vinogradov et al. [92] on PBs showed that the period passes through a minimum in the unstable regime.

Experiments with HDPEs have shown that as the capillary length increases, the stick-slip regime is shifted to lower volumetric flow rates and its size increases, the hysteresis loop of the flow curve becomes larger, and both the amplitude and the period of the pressure oscillations increase [20, 40, 74]. The experiments of Durand et al. [20] and Vergnes et al. [89] showed that reducing the capillary length eventually leads to a continuous (monotonic) flow curve.

According to Den Doelder et al. [16], HDPEs do not exhibit pressure oscillations for short dies ($L/D < 5$), since these are overruled by the entry and exit pressure losses.

The critical wall shear stress, σ_{c2}, at which the stick-slip instability is observed may increase or decrease or remain constant as the capillary length to the capillary diameter ratio, L/D, increases. Experiments with HDPE melts [20, 40, 58, 74] and EPDM compounds [89] showed that σ_{c2} and the stress difference $(\sigma_{c2} - \sigma_{c3})$ increase with the capillary length. Hatzikiriakos and Dealy [40] attribute this effect to the pressure dependence of wall slip. Experiments with other materials, however, show that σ_{c2} is not always an increasing function of the L/D ratio. This was found to slightly decrease with L/D in the experiments of Vinogradov et al. with PBs [92], El Kissi and Piau with PDMS [22], and Kalika and Denn with a LLDPE [46], and to be independent of L/D in the experiments of Ramamurthy with a LLDPE [69] and Wang and Drda with entangled linear PEs [94, 95].

In Section 2.2, the governing equations, the slip equation, and the boundary and initial conditions are presented and their dimensionless forms are provided. In Section 2.3, after a brief description of the numerical method, the numerical results are presented and discussed and comparisons are made with experimental observations. Finally, Section 2.4 summarizes the conclusions.

2.2 Governing Equations

The geometry of the flow corresponds to the actual setup used in the experiments of Hatzikiriakos and Dealy [40]. There is a contraction region at 45 degrees between the barrel and the capillary as shown in Fig.2.2.

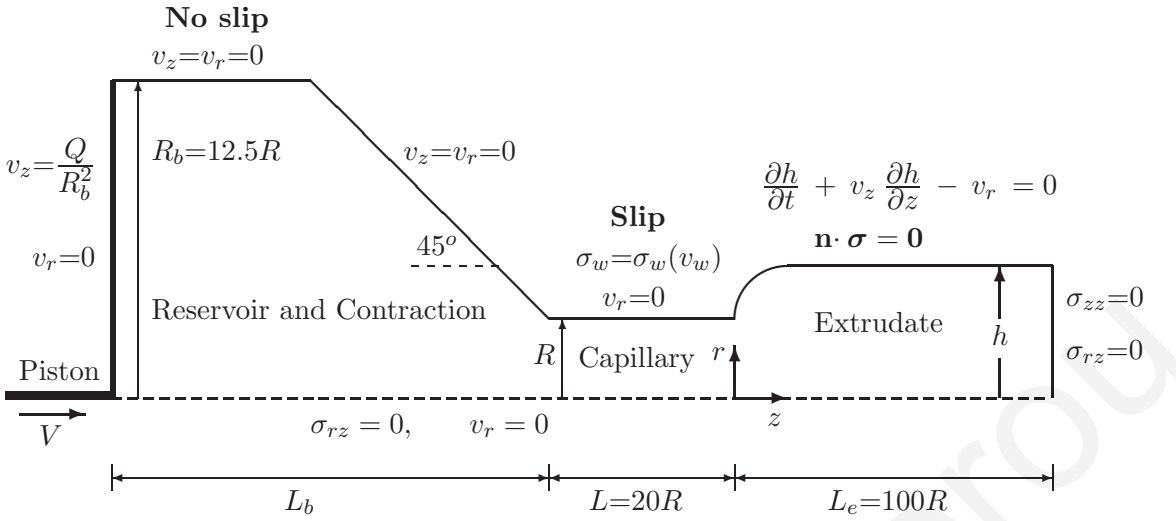

Figure 2.2: *Geometry and boundary conditions for the time-dependent, compressible, axisymmetric extrusion of a Carreau fluid with slip along the capillary wall, including the reservoir region.*

The actual values of the radii of the barrel and the capillary, denoted respectively by R_b and R, and the length of the capillary, L, are tabulated in Table 2.1.

The continuity and the momentum equations for time-dependent, compressible, isothermal viscous flow in the absence of body forces are as follows :

$$\frac{\partial \rho}{\partial t} + \nabla \cdot \rho \, \mathbf{v} = 0 \,, \tag{2.3}$$

$$\rho \left(\frac{\partial \mathbf{v}}{\partial t} + \mathbf{v} \cdot \nabla \mathbf{v} \right) = \nabla \cdot \boldsymbol{\sigma} \,, \tag{2.4}$$

where ρ is the density, $\mathbf{v}$ is the velocity vector, p is the pressure, and $\boldsymbol{\sigma}$ is the stress tensor. For the density, the following linear equation is employed:

$$\rho = \rho_0 \, [1 + \beta \, (p - p_0) \,] \,, \tag{2.5}$$

where β is the isothermal compressibility, and ρ_0 is the density at the reference pressure p_0.

Table 2.1: *Symbols and values of various lengths concerning the flow geometry.*

Symbol	Parameter	Value
R_b	Radius of the barrel	0.9525 cm
L_b	Length of the barrel	
	Contraction angle	45 degrees
R	Capillary radius	3.81 10^{-2} cm
L_c	Capillary length	0.762 cm
L_e	Length of the extrudate	3.81 cm

Table 2.2: *Values of the slip model parameters.*

Parameter	Value
a_1, $(\text{MPa})^{-m_1}$ cm/s	125.09
m_1	3.23
a_2, $(\text{MPa})^{-m_2}$ cm/s	1000
m_2	2.86
a_3, $(\text{MPa})^{-m_3}$ cm/s	5.484 10^{-3}
m_3	-4.434
σ_{c2}, MPa	0.27
σ_{min}, MPa	0.19
v_{c2}, cm/s	1.82
v_{min}, cm/s	8.65

Even though the fluid studied by Hatzikiriakos and Dealy [40] is considered to behave as a power-law one, we employ the Carreau model in order to avoid the well-known numerical difficulties caused by the former model, which predicts infinite zero-shear-rate viscosity. For compressible flow of a Carreau fluid with zero infinite-shear-rate viscosity, the stress tensor is written as

$$\boldsymbol{\sigma} \;=\; -p\,\mathbf{I} \;+\; \eta_0 \,\left[1 \;+\; \lambda^2 \;(2\mathit{II}_{\mathbf{d}})^2\right]^{(n-1)/2} \,\left(2\mathbf{d} \;-\; \frac{2}{3}\,\mathbf{I}\,\nabla\cdot\mathbf{v}\right)\,, \tag{2.6}$$

where $\mathbf{I}$ is the unit tensor, $\mathbf{d}$ is the rate-of-deformation tensor, defined as

$$\mathbf{d} \;=\; \frac{1}{2}\,\left[(\nabla\mathbf{v}) \;+\; (\nabla\mathbf{v})^T\right]\,, \tag{2.7}$$

the superscript T denotes the transpose, $\mathit{II}_{\mathbf{d}}$ is the second invariant of $\mathbf{d}$, η_0 is the zero-shear-rate viscosity, λ is a time constant, and n is the power-law exponent.

2.2.1 The slip equation

We use the same three-branch multi-valued slip model as in [29]:

$$v_w \;=\; \begin{cases} a_1\,\sigma_w^{m_1}\,, & 0 \le v_w \le v_{c2} \\ a_3\,\sigma_w^{m_3}\,, & v_{c2} \le v_w \le v_{min} \\ a_2\,\sigma_w^{m_2}\,, & v_w \ge v_{min} \end{cases} \tag{2.8}$$

where v_w is the relative velocity of the fluid with respect to the wall, σ_w is the shear stress on the wall, v_{c2} is the maximum slip velocity at σ_{c2}, and v_{min} is the minimum slip velocity at σ_{min}. The values of all slip parameters are given in Table 2.2. The plot of the slip equation is given in Fig. 2.3.

This is based on the experimental data of Hatzikiriakos and Dealy [39]. The low-flow-rate (low velocity) branch is a simplification of the corresponding slip equation proposed by the

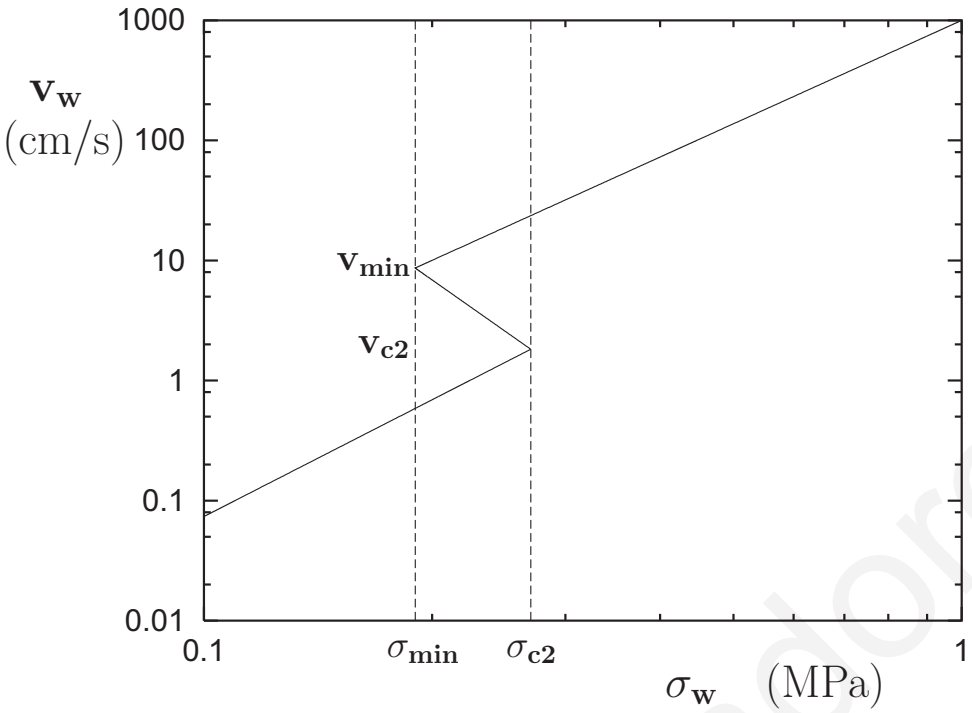

Figure 2.3: *The nonmonotonic slip law based on the experimental data of Hatzikiriakos and Dealy [39, 40].*

latter authors, under the assumption of infinite normal stress. The high-flow-rate branch is exactly the power-law slip equation proposed by the same authors for the right branch of their experimental flow curve. The intermediate branch, which corresponds to the unstable region of the flow curve, is just an arnitrary line connecting the other two branches. It should be noted that for a finite normal stress the first branch of the slip equation moves closer to the third one; for zero normal stress, the two branches almost overlap. It should be noted that in reality, the wall shear stress is expressed as a function of the slip velocity and not vice versa, i.e. σ_w=$\sigma_w(v_w)$. In other words, the inverse of Eq. (2.8) is used.

2.2.2 Dedimensionalization

To dedimensionalize the governing equations, we scale the lengths by the capillary radius R, the velocity by a reference velocity, V, in the capillary, the pressure and the stress components by $\eta_0 \lambda^{n-1} V^n / R^n$, the density by ρ_0, and the time by R/V. With these scalings, one gets:

$$\frac{\partial \rho}{\partial t} + \nabla \cdot \rho \, \mathbf{v} = 0 \,, \tag{2.9}$$

$$Re \, (1 + B \, p) \left(\frac{\partial \mathbf{v}}{\partial t} + \mathbf{v} \cdot \nabla \mathbf{v} \right) = \nabla \cdot \boldsymbol{\sigma} \,, \tag{2.10}$$

and

$$\boldsymbol{\sigma} = -p \, \mathbf{I} + \Lambda^{1-n} \left[1 + \Lambda^2 \, (2 I\!I_{\mathbf{d}})^2 \right]^{(n-1)/2} \left(2\mathbf{d} - \frac{2}{3} \, \mathbf{I} \, \nabla \cdot \mathbf{v} \right) , \tag{2.11}$$

where all variables are now dimensionless. (For simplicity the same symbols are used for the dimensionless variables.) The dedimensionalization results in three dimensionless numbers, the Reynolds number, Re, the compressibility number, B, and Λ in the constitutive equation, which are defined as follows:

$$Re \equiv \frac{\rho_0 \, R^n V^{2-n} \, \lambda^{1-n}}{\eta_0} \,, \quad B \equiv \frac{\beta \, \eta_0 \, V^n}{\lambda^{1-n} R^n} \,, \quad \Lambda \equiv \frac{\lambda V}{R} \,. \tag{2.12}$$

For resin A at 180 ^{o}C, Hatzikiriakos and Dealy [40] provide the following values: β=9.923 10^{-4} (MPa)$^{-1}$, n=0.44 and, for the consistency index, K=0.0178 $MPa\, s^n$. Assuming that η_0=0.03 $MPa\ s$, we calculate λ from $\eta_0 \lambda^{n-1}$=K. For the reference velocity, we get V=$R\dot{\gamma}/4$=5.24 cm/s, assuming that $\dot{\gamma}$=500 s^{-1} and R=3.81 $10^{-2} cm^2$. Under these assumptions, the values of the three dimensionless numbers are: Re=1.43 10^{-5}, B=1.54 10^{-4}, and Λ=349.2.

The dimensionless form of the slip equation is

$$v_w = \begin{cases} A_1 \, \sigma_w^{m_1} \,, & 0 \le v_w \le v_{c2} \\ A_3 \, \sigma_w^{m_3} \,, & v_{c2} \le v_w \le v_{min} \\ A_2 \, \sigma_w^{m_2} \,, & v_w \ge v_{min} \end{cases} \tag{2.13}$$

where

$$A_i \equiv \frac{a_i \, \eta_0^{m_i} \, V^{m_i n-1}}{\lambda^{m_i(1-n)} R^{m_i n}} , \qquad i = 1, 2, 3 , \tag{2.14}$$

and the dimensionless values of v_{c2} and v_{min} correspond to

$$\sigma_{c2}^* \equiv \frac{\sigma_{c2} R^n \lambda^{1-n}}{\eta_0 \, V^n} \qquad \text{and} \qquad \sigma_{min}^* \equiv \frac{\sigma_{min} R^n \lambda^{1-n}}{\eta_0 \, V^n} , \tag{2.15}$$

respectively. The values of the above dimensionless numbers are given in [29].

2.2.3 Boundary and initial conditions

The dimensionless boundary conditions for the full extrusion flow are shown in Fig.2.2. The usual symmetry conditions apply along the axis of symmetry. Along the barrel and the contraction walls both velocity components are zero (no slip). Along the capillary wall, only the radial velocity is zero, whereas the axial velocity satisfies the slip equation (2.13). At the inlet plane, it is assumed that the radial velocity component is zero while the axial velocity is uniform (corresponding to the motion of the piston at constant speed):

$$u_z = \frac{Q}{R_b^2}$$

where Q is the imposed volumetric flow rate (scaled by $\pi R^2 V$). It should be noted that the simulations are carried out on a fixed domain, i.e. the motion of the piston is not taken into account. This is a reasonable assumption provided that the piston speed is low.

When the extrudate region is excluded, we assume that the radial velocity component vanishes at the capillary exit. In the case of the extrudate-swell flow, the weaker condition σ_{rz}=0 is used at the outflow plane. In both cases, the total normal stress is assumed to be zero, σ_{zz}=0. Finally, on the free surface, we assume that surface tension is zero and impose

vanishing normal and tangential stresses. Additionally, the unknown position $h(z,t)$ of the free surface satisfies the kinematic condition:

$$\frac{\partial h}{\partial t} + v_z \frac{\partial h}{\partial z} - v_r = 0 \,. \tag{2.16}$$

When the extrudate region is excluded, we use as initial condition the steady-state solution corresponding to a given volumetric flow rate Q_{old} at the inlet that we perturb to Q at t=0. In the case of the extrudate-swell flow, we start with the steady-state solution of the stick-slip flow (i.e., with flat free surface) for a given volumetric flow rate Q and release the free surface at t=0.

2.3 Numerical results

The finite element formulation is used for solving the free-surface flow problem under study. The unknown position of the free surface is calculated simultaneously with the velocity and pressure fields (full-Newton method). The standard biquadratic-velocity (P^2-C^0) and bilinear-pressure (P^1-C^0) elements with a quadratic representation for the position h of the free surface are employed. For the spatial discretization, the standard Galerkin forms of the continuity, momentum and kinematic equations are used, while for the time discretization, the standard fully-implicit (Euler backward-difference) scheme has been chosen.

As already mentioned, the dimensionless capillary length is L=20. In order to study the effect of the capillary length on the stick-slip instability, additional capillary lengths are considered in the last part of this section. The extrudate length L_e has been taken to be 100, while the reservoir length L_b ranged from 20 to 200. Figure 2.4 shows some of the meshes used in the simulations (excluding the extrudate region) with L=20. The finite element meshes were

refined near the walls, and around the entrance and exit of the capillary. The longest mesh (L_b=200) consisted of 4511 elements in the reservoir-capillary region and of 18386 elements when the extrudate region was included. The corresponding total numbers of unknowns were 42403 and 169504, respectively. With the exception of the Reynolds number, Re, the values of the dimensionless parameters are those given in Section 2, i.e. B=1.54 10^{-4} and Λ=349.2. For comparison purposes, in addition to the Carreau flow ones (n=0.44), results are also presented for the Newtonian flow (n=1).

We first constructed the steady-state flow curves for the reservoir-capillary region (excluding the extrudate region). In Fig. 2.5, we show both the regular (Fig. 2.5a) and log-log (Fig. 2.5b) plots of the pressure drop versus the volumetric flow rate obtained with Re=0.01 and L_b=80 in the case of Newtonian flow. Four different possibilities for the pressure drop are shown: (a) $\Delta P_{\mathrm{tot,w}}$ is the pressure difference along the wall from the piston to the capillary exit; (b) $\Delta P_{\mathrm{tot,c}}$ is the pressure difference along the centerline from the piston to the capillary exit; (c) $\Delta P_{\mathrm{cap,w}}$ is the pressure difference along the wall from the capillary entrance to the capillary exit; and (d) $\Delta P_{\mathrm{cap,c}}$ is the pressure difference along the centerline from the capillary entrance to the capillary exit. The pressures $\Delta P_{\mathrm{tot,w}}$ and $\Delta P_{\mathrm{tot,c}}$ are essentially the same for all volumetric flow rates and correspond to the piston driving pressure, P_d, in Eq. (2.2). $\Delta P_{\mathrm{cap,w}}$ and $\Delta P_{\mathrm{cap,c}}$ are slightly different from $\Delta P_{\mathrm{tot,w}}$ and $\Delta P_{\mathrm{tot,c}}$ along the left positive-slope branch of the flow curve. Much bigger differences are observed in the negative-slope and the right positive-slope branches of the flow curves. In these regimes, $\Delta P_{\mathrm{cap,w}}$ is much lower than $\Delta P_{\mathrm{cap,c}}$ due to the effect of the singularity at the capillary entrance. It should be noted that differences between $\Delta P_{\mathrm{tot,w}}$ and $\Delta P_{\mathrm{tot,c}}$ at high volumetric flow rates are much bigger in the case of the Carreau fluid. A careful examination of the solution near the piston region shows that these differences are solely due to the region near the piston and the barrel

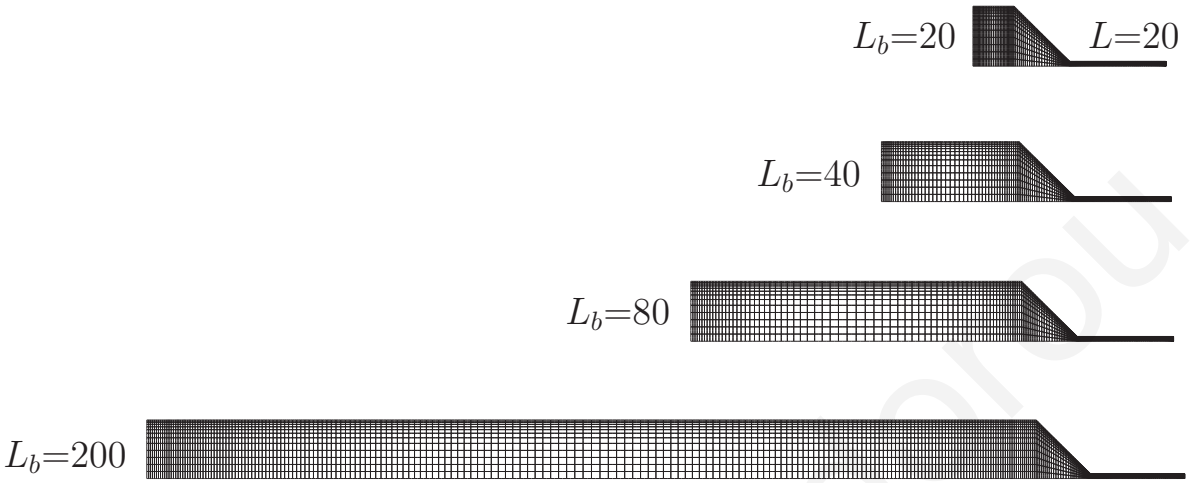

4511 elements, 42403 unknowns

(a)

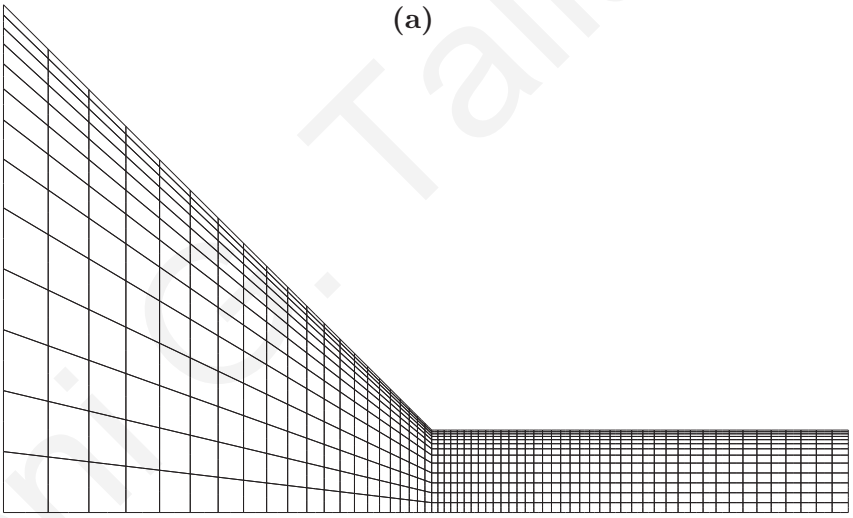

(b)

Figure 2.4: *(a) Various meshes for different barrel lengths and L=20 used in the simulations (the extrudate region is excluded); (b) Detail of the meshes near the die entrance.*

wall. Moreover, unlike their Newtonian counterparts, $\Delta P_{\mathrm{cap,w}}$ and $\Delta P_{\mathrm{cap,c}}$ almost coincide, which implies that the effect of the singularity at the capillary entrance is much weaker than in the Newtonian case. In what follows, the pressure drop ΔP corresponds to the piston pressure $\Delta P_{\mathrm{tot,c}}=P_d$, unless otherwise indicated.

The flow curves obtained in the case of Carreau flow (n=0.44) are quite similar. In Fig. 2.6, the Newtonian and Carreau flow curves ($\Delta P=\Delta P_{\mathrm{tot,c}}$) are compared. We observe that as n is reduced, the negative slope regime is slightly shifted to the right and reduces in size. Moreover, the resulting hysteresis loop, which is also shifted to the right, is much bigger. This implies that one would expect slightly bigger pressure oscillations and much bigger jumps of the volumetric flow rate. From Fig. 2.6, it can be deduced that the biggest volumetric flow rate will be about 8 times its lowest value. This agrees well with the report of Hatzikiriakos and Dealy [40] that with resin A at 160^{o}C the mass flow rate suddenly increases by a factor of about 8.

Figure 2.7 shows the (steady-state) contours of the two velocity components, the pressure and the streamfunction, ψ, obtained for the Carreau flow with Re=0.01, L_b=80, and Q=1.5, i.e. near the middle of the negative-slope regime of the flow curve. We see the rearrangement of the flow near the capillary entrance, and observe that the differences between ΔP_{tot} and ΔP_{cap} are basically due to the entrance region. Far from the capillary entrance, the pressure in the reservoir is practically constant, which verifies that one of the basic assumptions made in one-dimensional phenomenological models proposed in the literature (see, e.g., Ref. [19]) is valid.

When the extrudate region is excluded, the steady-state solutions are perturbed by changing the volumetric flow rate from an old value to the desired one, Q. Given that the flow is

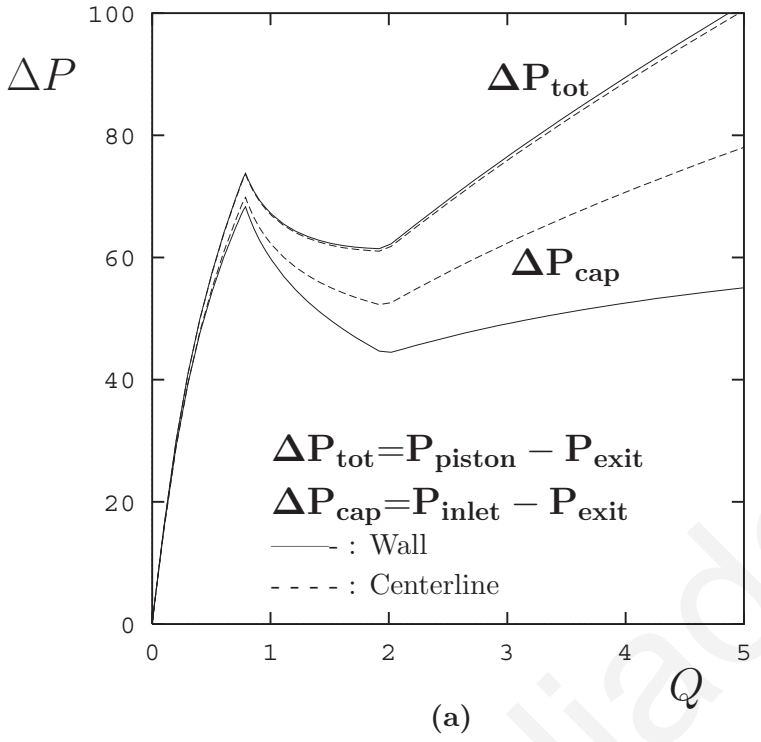

(a)

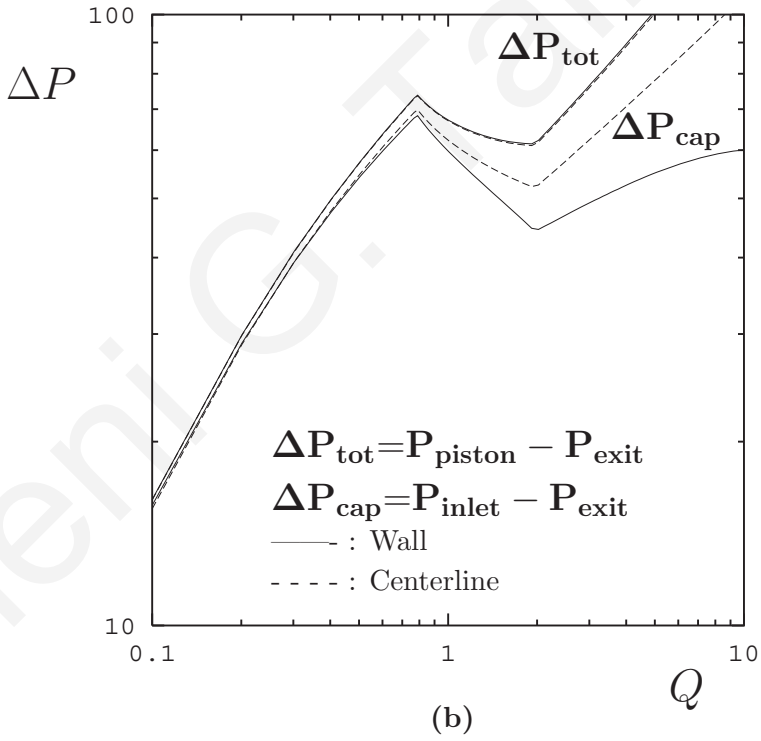

(b)

Figure 2.5: *Newtonian flow curves with Re=0.01 and L_b=80: (a) regular plot; (b) log-log plot.*

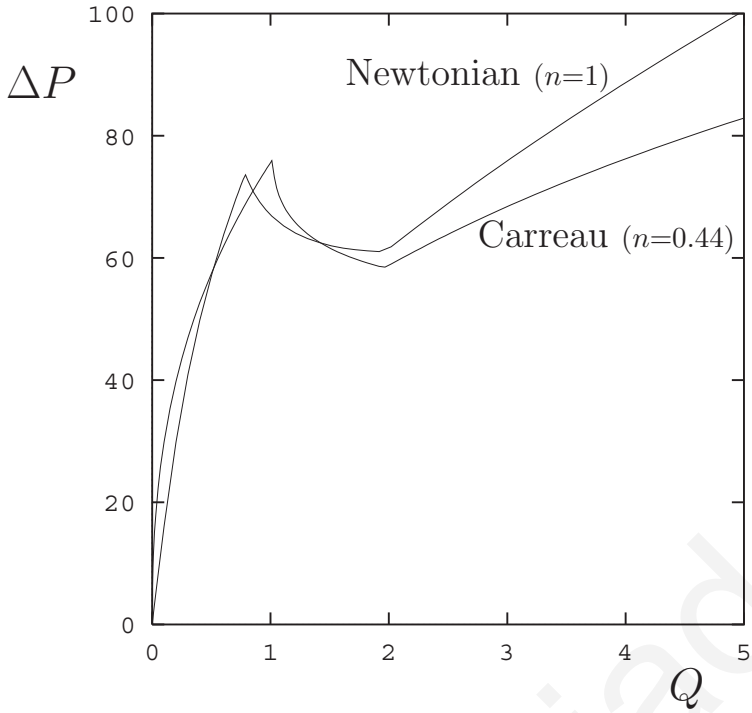

Figure 2.6: *Effect of the power-law exponent on the flow curve; Re=0.01 and L_b=80.*

compressible, the behavior of the time-dependent solution depends on whether the new value of Q corresponds to the stable positive-slope branches or to the unstable negative-slope one. In the former case, the new steady-state is obtained without any oscillations, whereas, in the latter one, the solution is oscillatory and becomes periodic after a transition period. Self-sustained oscillations of the pressure drop and the mass flow rate are obtained which are similar to those observed experimentally in the stick-slip extrusion instability regime. All the results presented below have been obtained in the unstable regime.

In Fig. 2.8, we show the oscillations of the pressure drop and the volumetric flow rate obtained by perturbing the Newtonian steady-state solution for Re=0.01, L_b=80 and Q=1.35. We note in Fig. 2.8a that sudden jumps of the pressure drop are observed when this is measured across the capillary. No jumps are observed when ΔP is measured between the piston and the

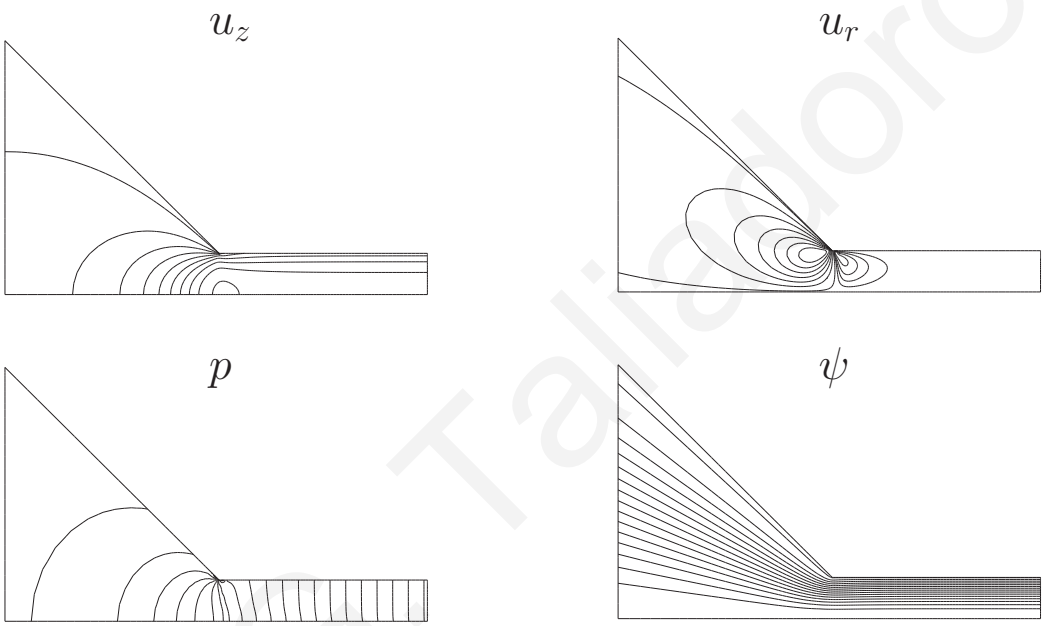

Figure 2.7: *Contours of the steady-state Carreau solution (n=0.44) inside the barrel and the die (the extrudate-region has been excluded) for Re=0.01, L_b=80 and Q=1.5.*

capillary exit. The volumetric flow rate at the capillary exit (Fig. 2.8b) is also characterized by sudden jumps which is consistent with experimental observations [20, 40].

The results in the case of Carreau flow are similar but the amplitude and the period of the oscillations are higher (Fig. 2.9), as expected.

Plotting the trajectory of the solution on the flow curve plane (Fig. 2.10) shows that, after a transition period, a limit cycle is reached which follows exactly the positive-slope branches of the steady-state flow curve. The volumetric flow rate increases together with the pressure following exactly the left positive-slope branch of the flow curve and, when the pressure reaches its maximum value, Q jumps to the right positive slope branch. The volumetric flow rate then starts decreasing together with the pressure following this branch till the pressure reaches its minimum and then jumps to the left positive-slope branch and starts the next oscillation cycle. This behavior agrees well with experimental observations [20, 40]. Note also that in our previous study [29], the limit cycles did not follow the steady-state flow curve due to the omission of the reservoir region. This drawback was also exhibited by the one-dimensional model of Greenberg and Demay [36], which does not include the barrel region. Note that most one-dimensional phenomenological relaxation/oscillation models require as input the experimental (steady-state) flow curve. These models are based on the compressibility/slip mechanism and describe oscillations of the pressure and the volumetric flow rate in the stick-slip instability regime (see [1, 17, 19] and references therein) under the assumption that these follow the experimental flow curve. The present simulations are the first to predict that the limit cycle indeed follows the steady-state flow curve.

In an attempt to approach the experimental value Re=1.43 10^{-5}, we reduced the value of the Reynolds number from 0.01 to 0.001. Figure 2.11 shows a comparison of the pressure and flow rate oscillations during a cycle, obtained with Re=0.01 and 0.001 for both the Newtonian

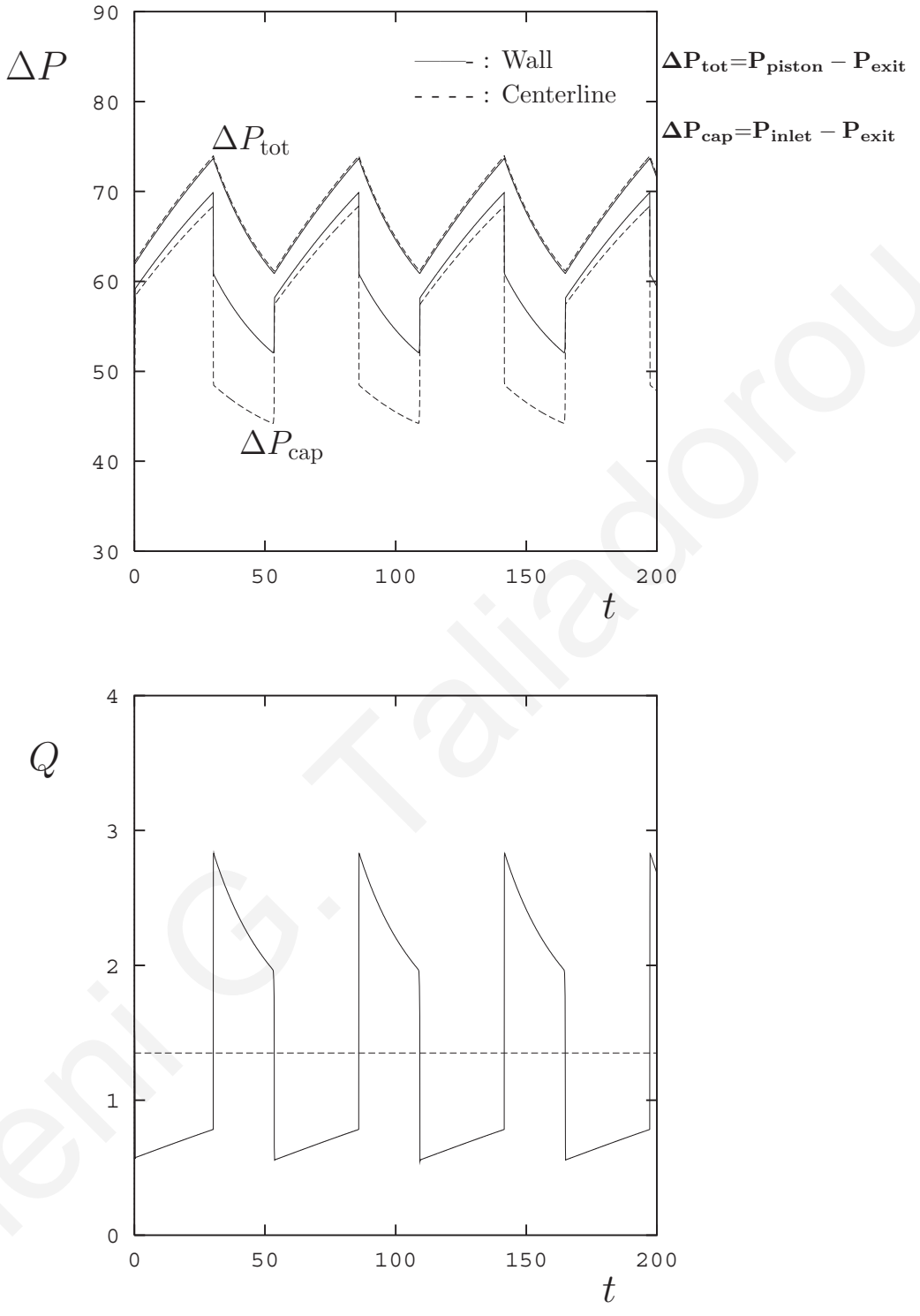

Figure 2.8: *Pressure and flow rate oscillations for Newtonian flow (n=1), Re=0.01, L_b=80 and Q=1.35.*

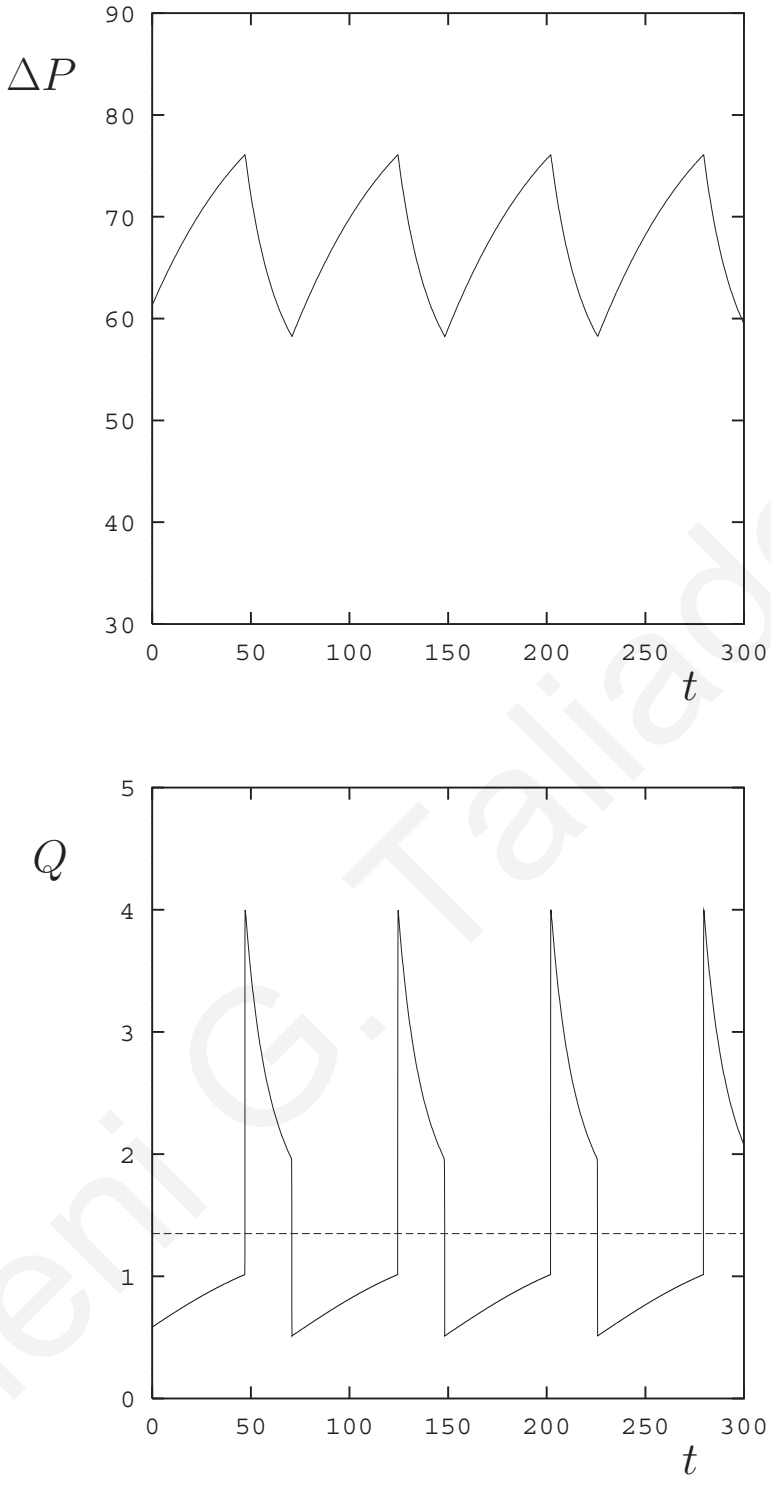

Figure 2.9: *Pressure and flow rate oscillations for Carreau flow (n=0.44), Re=0.01, L_b=80 and Q=1.35.*

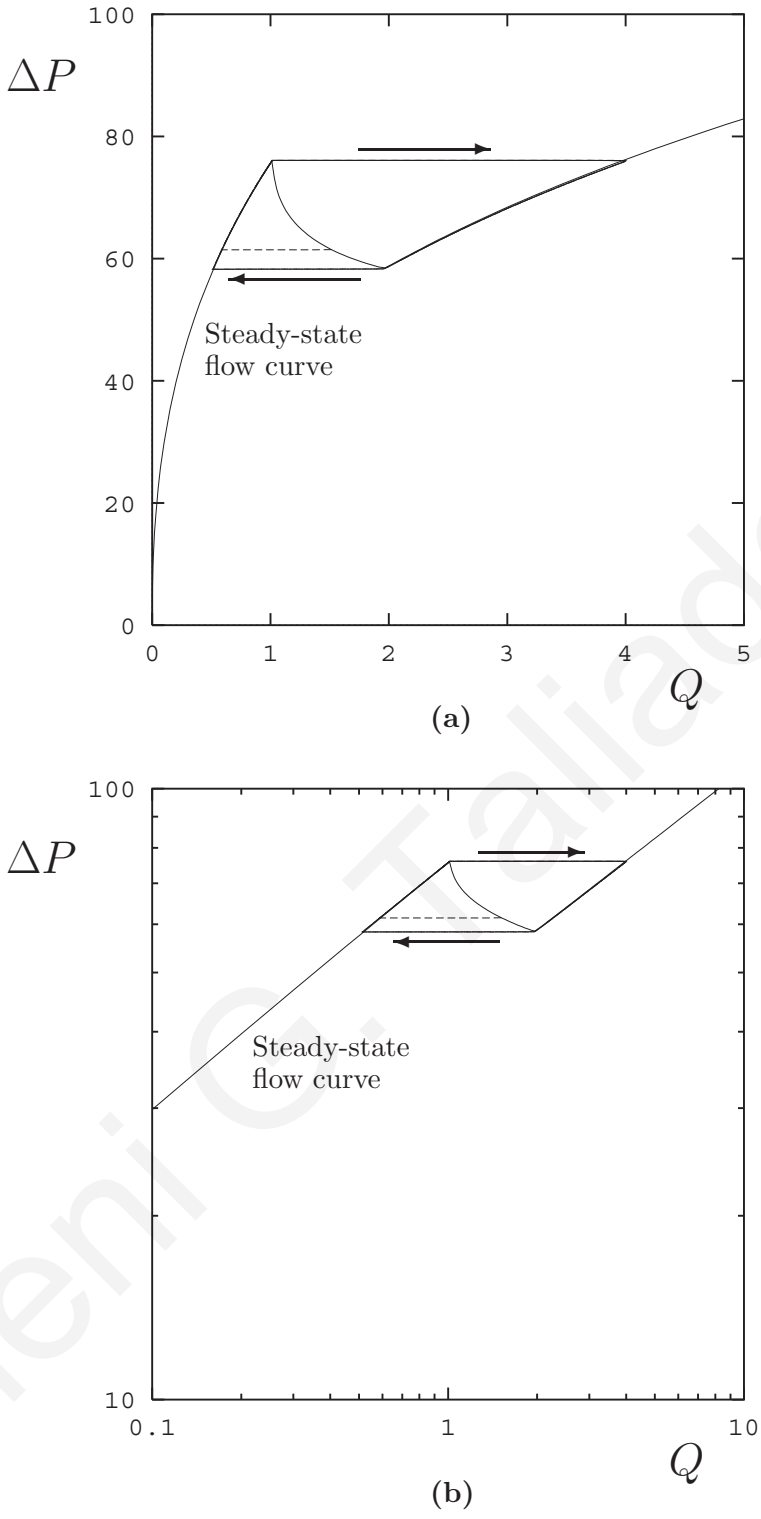

Figure 2.10: *Trajectory of the solution on the flow curve plane for Carreau flow (n=0.44), Re=0.01, L_b=80 and Q=1.35: (a) regular plot; (b) log-log plot.*

and the Carreau flows (with L_b=80 and Q=1.35). It is clear that decreasing the Reynolds number has no practical effect on the oscillations with the exception of the artificial flow rate overshoots obtained with the lower Re. Instead of trying to eliminate the overshoots by reducing the time step (which would have resulted into much longer runs), we decided to continue the runs with Re=0.01. Note that when the reservoir region is excluded, the results are sensitive to the Reynolds number: the amplitude of the pressure-drop oscillations is reduced, the amplitude of the mass-flow-rate oscillations is increased and the frequency of the oscillations is considerably increased, as the Reynolds number is reduced [29]. This shows once again the importance of including the reservoir region.

In order to study the effect of the reservoir length on the pressure oscillations, we obtained results for various values of L_b. The pressure oscillations for different values of L_b, Re=0.01 and Q=1.35 are given in Figs. 2.12 and 2.13 for the Newtonian and the Carreau flow, respectively. In both cases, the period of the pressure oscillations increases with L_b while their amplitude seems to be less sensitive.

This is more clearly shown in Fig. 2.14, where the corresponding periods and the amplitudes of the pressure oscillations are plotted versus the reservoir volume. As already mentioned, the period and the amplitude of the pressure oscillations are higher in the case of the Carreau fluid. In agreement with experiments [20, 40, 73, 74], the period T increases linearly with the reservoir volume, while the amplitude is essentially constant. However, the period appears to pass through the origin, which is not the case with the experiments [20, 40, 74, 73].

To show the effect of the reservoir length on the waveform of the pressure oscillations, we compare in Fig. 2.15 the normalized pressure oscillations during one cycle for both fluids, L_b=20 and 200. The waveform is independent of the reservoir length, i.e. the durations of both the compression and the relaxation increase linearly with the reservoir length, which

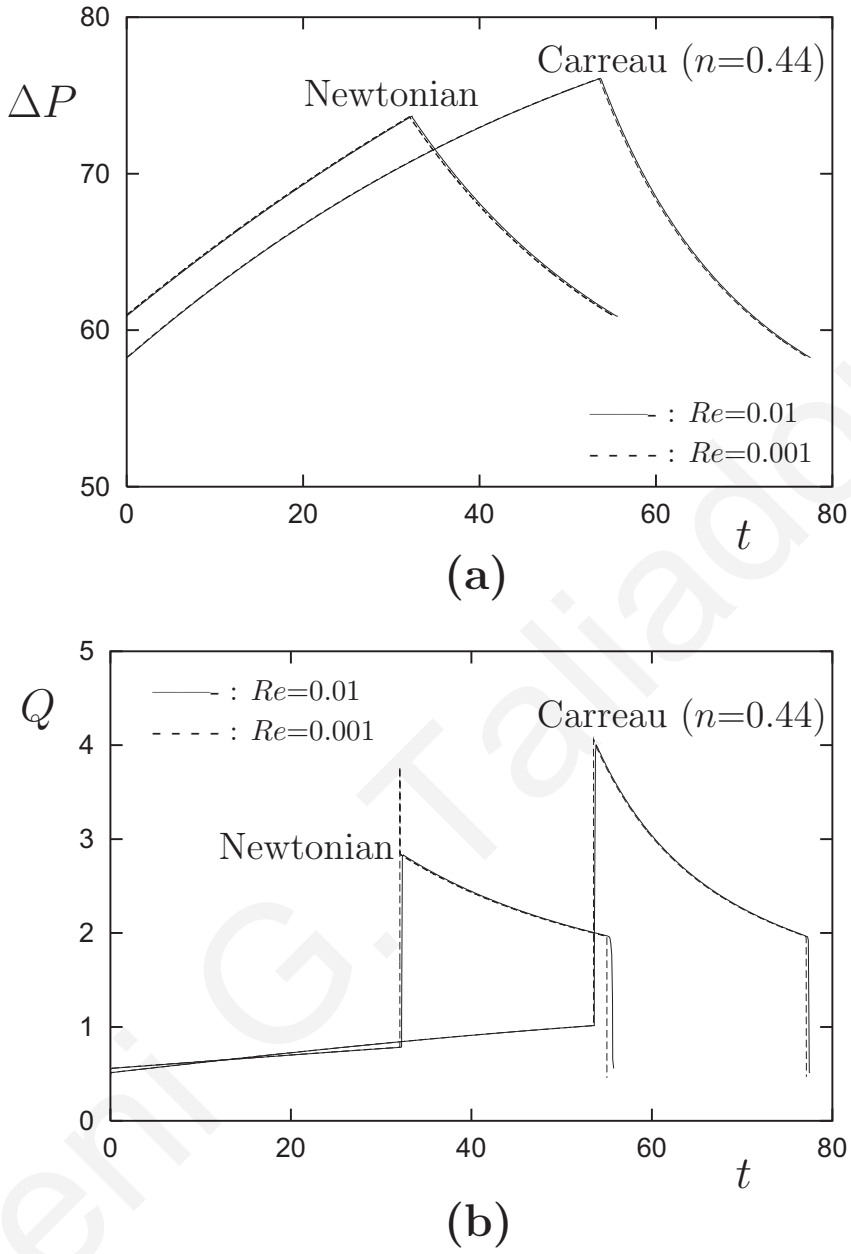

Figure 2.11: *Comparison of the pressure (a) and flow rate (b) oscillations for Re=0.01 and 0.001; L_b=80 and Q=1.35.*

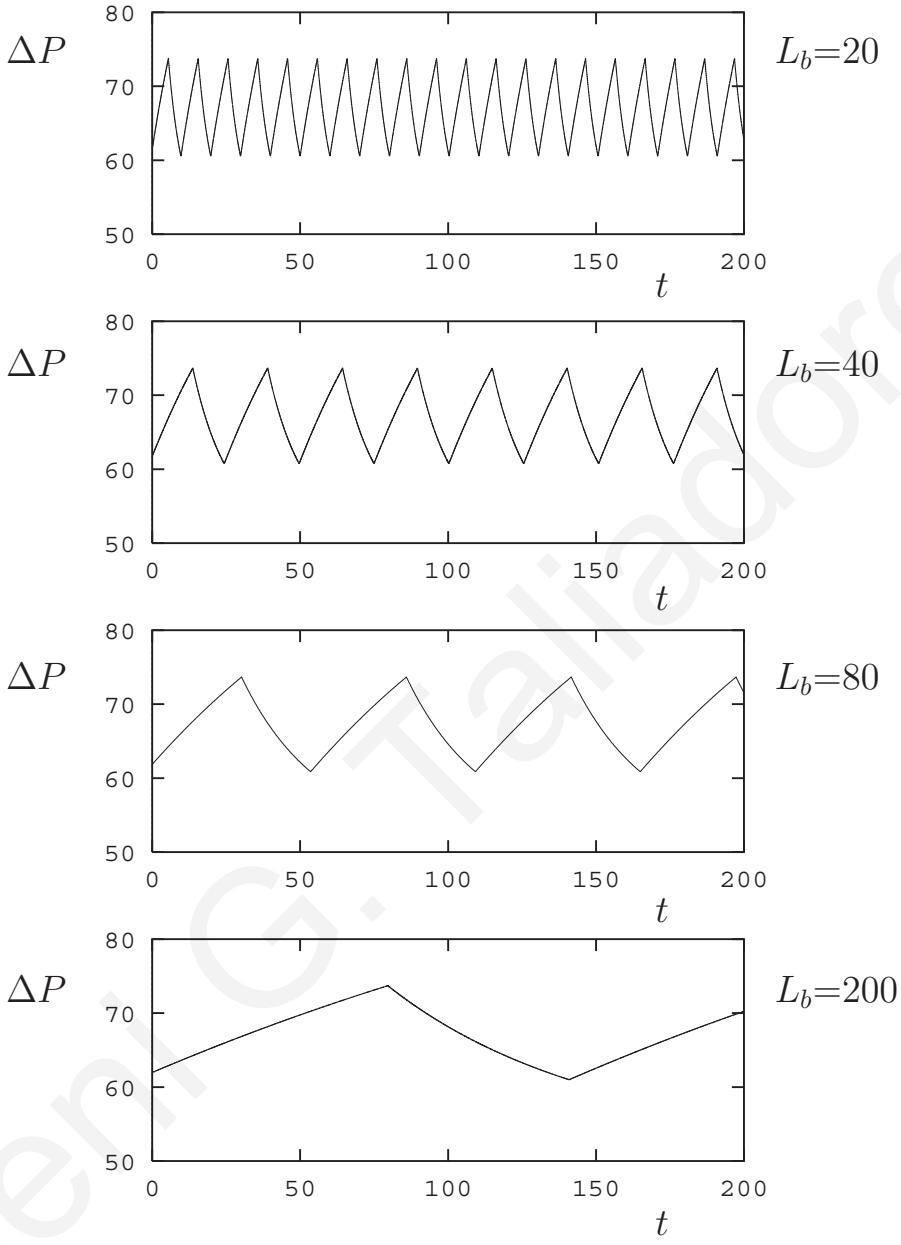

Figure 2.12: *Effect of the reservoir length on the pressure oscillations; Newtonian flow (n=1), Re=0.01 and Q=1.35.*

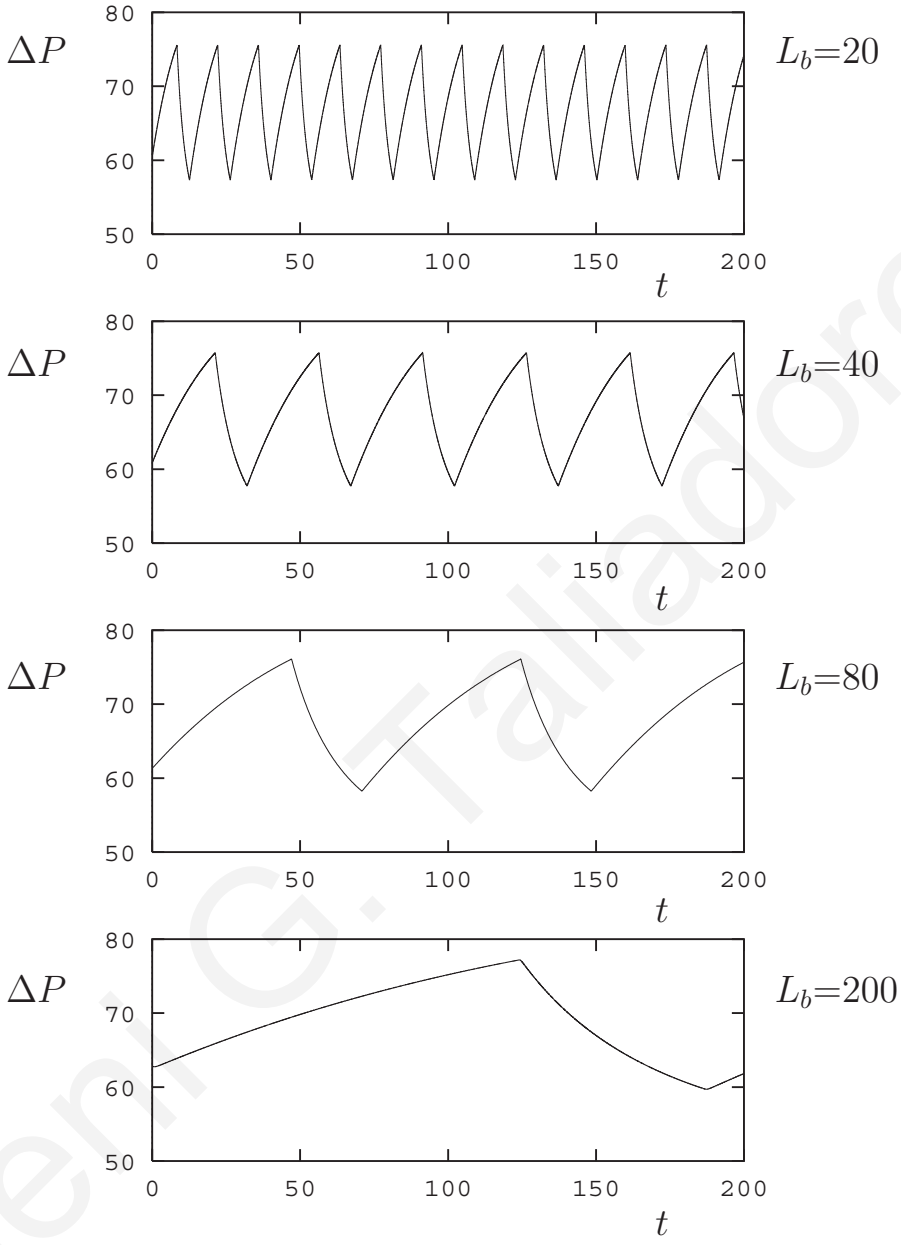

Figure 2.13: *Effect of the reservoir length on the pressure oscillations; Carreau flow (n=0.44), Re=0.01 and Q=1.35.*

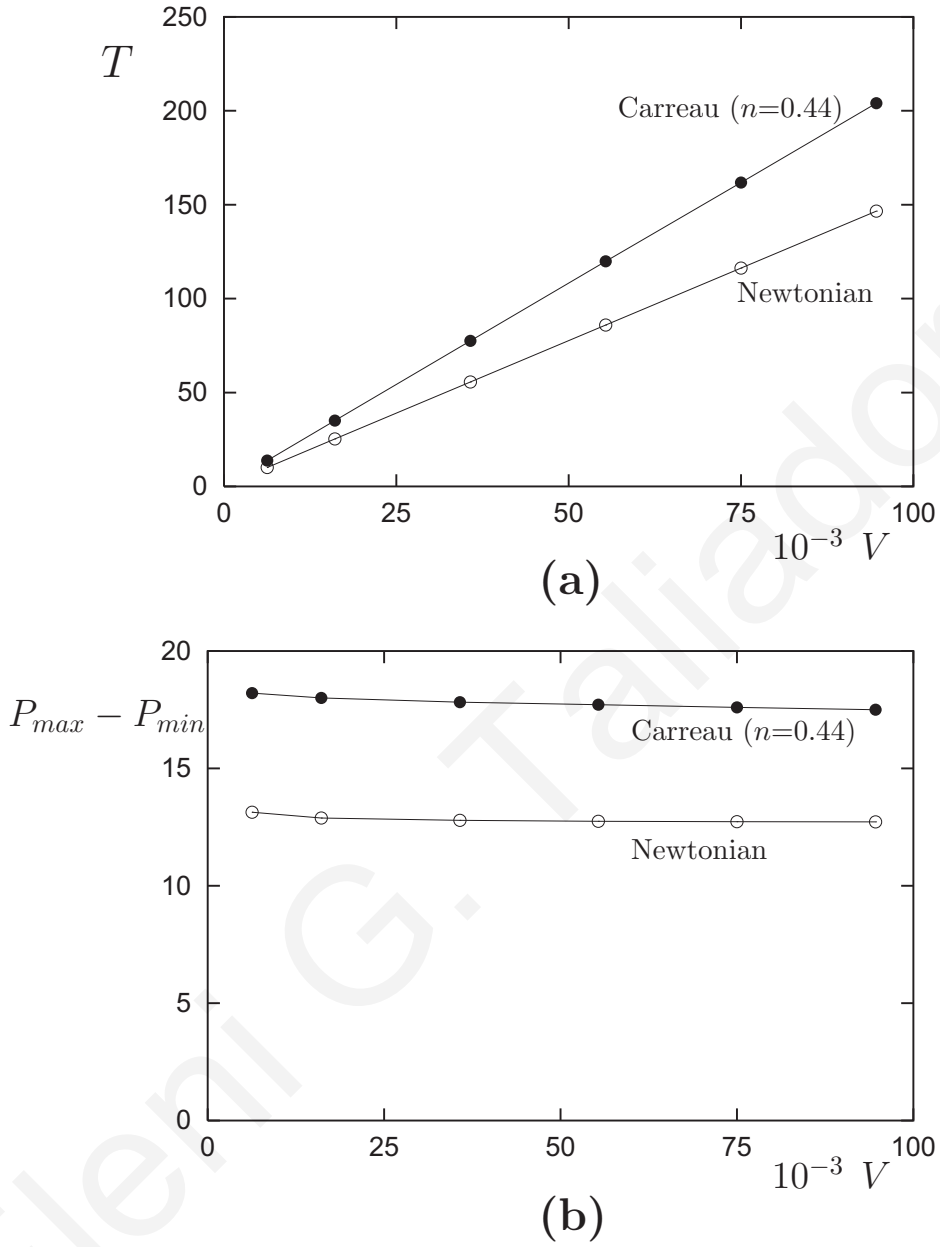

Figure 2.14: *Period (a) and amplitude (b) of the pressure oscillations versus the reservoir volume; Re=0.01 and Q=1.35.*

agrees well with the experiments of Hatzikiriakos and Dealy [40] and Durand et al. [20].

Results for various values of Q in the unstable regime, Re=0.01 and L_b=80, have been obtained in order to investigate the effect of the imposed volumetric flow rate on the pressure oscillations. Figure 2.16 shows the periods of the resulting pressure oscillations versus Q for both the Newtonian and Carreau flows. The period decreases initially reaching a minimum in the middle of the unstable regime and then starts increasing slowly. This was also the case in the experiments of Myerholtz [58], Okubo and Hori [61] and Weill [96] on HDPEs and those of Vinogradov et al. [92] on a polybutadiene. In other experiments, Hatzikiriakos and Dealy [40], Durand et al. [20] and Robert et al. [73] reported that the period decreases with Q. However, the latter authors carried out experiments only for a few values of Q, which were not sufficient for capturing the minimum and the slight increase of the period in the rightmost part of the unstable regime.

The effect of Q on the pressure oscillations is illustrated in Figs. 2.17 and 2.18 for the Newtonian and Carreau flows, respectively, where pressure oscillations obtained with Re=0.01, L_b=80 and various values of Q are shown. It is again clear that the period of the oscillations passes though a minimum. The ascending part (compression) of the oscillations is relatively reduced in agreement with experimental observations [20, 40, 61, 73]. The descending part of the oscillation does not remain constant but increases significantly at high values of Q, in disagreement with the experiments of Hatzikiriakos and Dealy [40], Durand et al. [20] and Robert et al. [73], in which, however, the period was found to be a decreasing value of Q. In the present simulations, the period is decreasing only in the first half of the unstable regime, where the growth of the descending part of the oscillation is not as pronounced.

The time-dependent simulations of the full extrusion flow have been obtained by starting

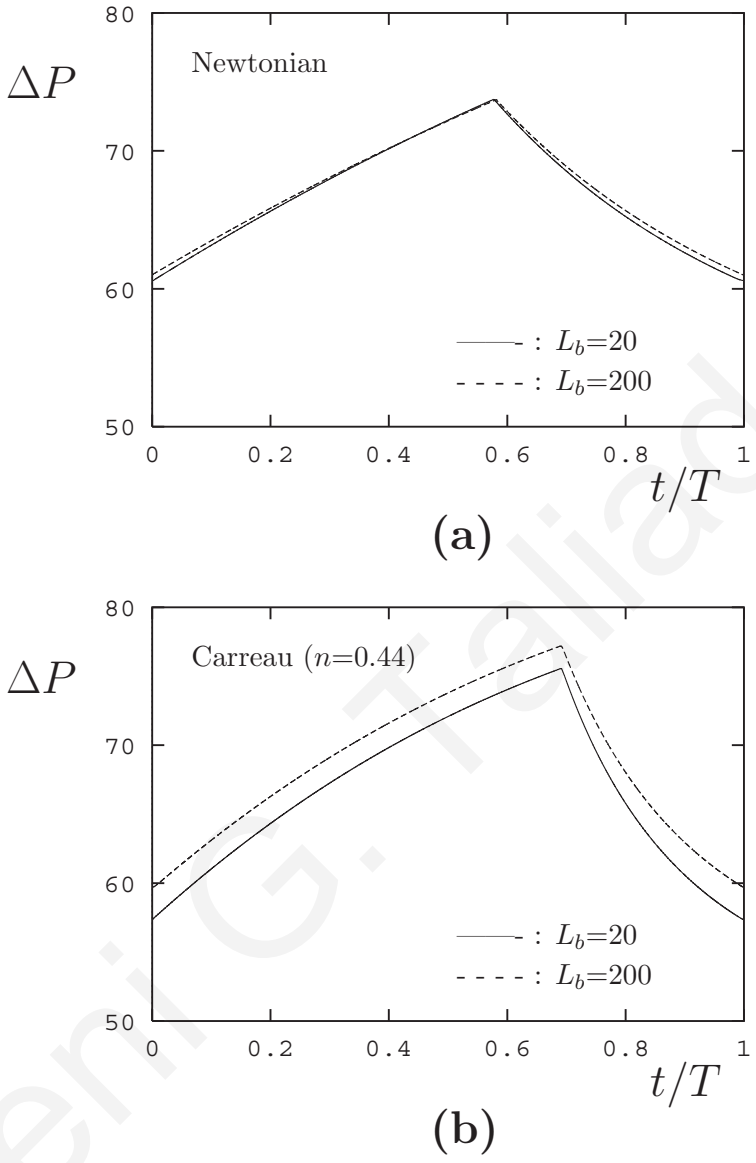

Figure 2.15: *Effect of the reservoir length on the waveform of the pressure oscillations; (a) Newtonian flow (n=1); (b) Carreau flow (n=0.44); Re=0.01 and Q=1.35.*

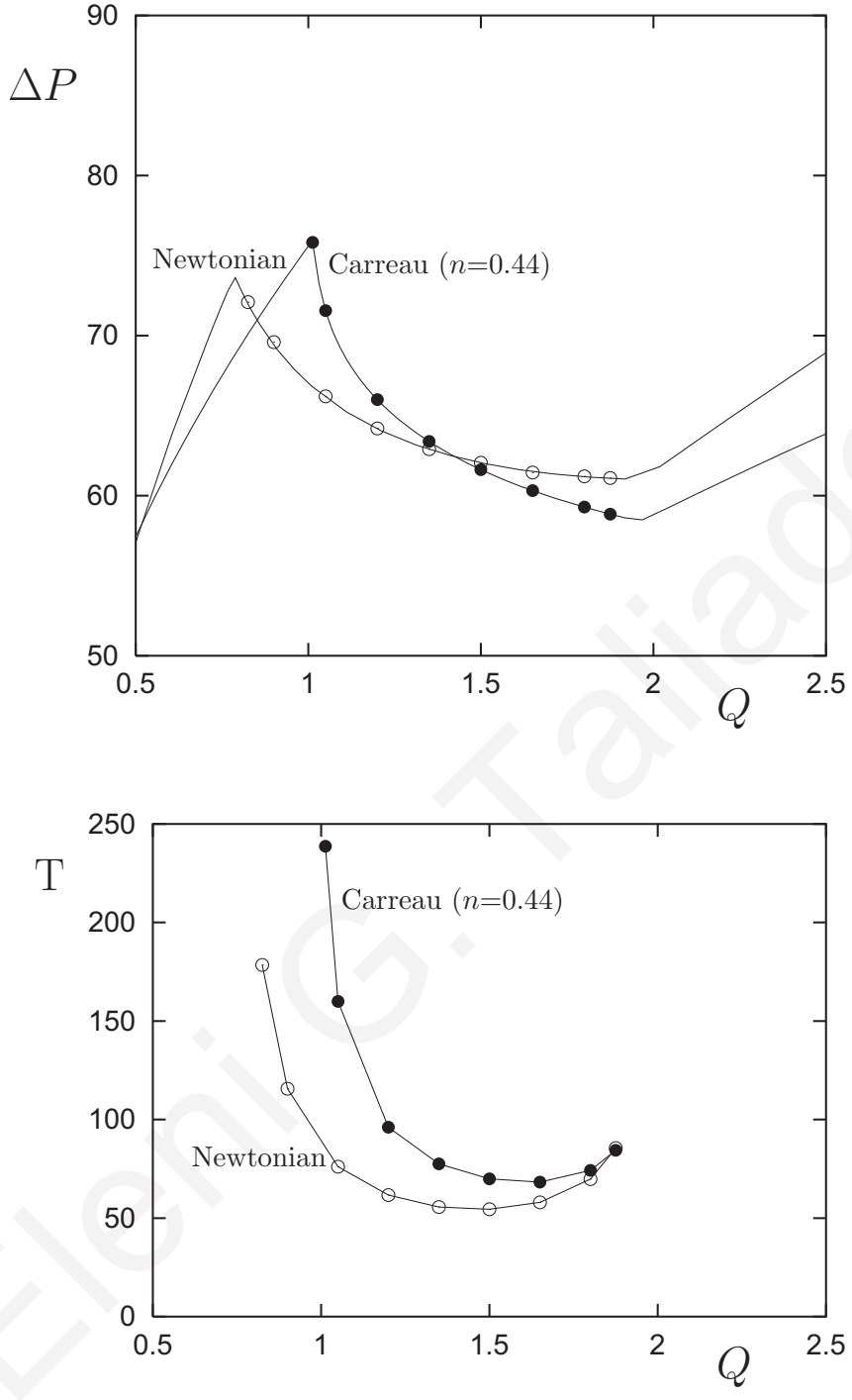

Figure 2.16: *Effect of the imposed volumetric flow rate on the period of the pressure oscillations; Re=0.01 and L_b=80.*

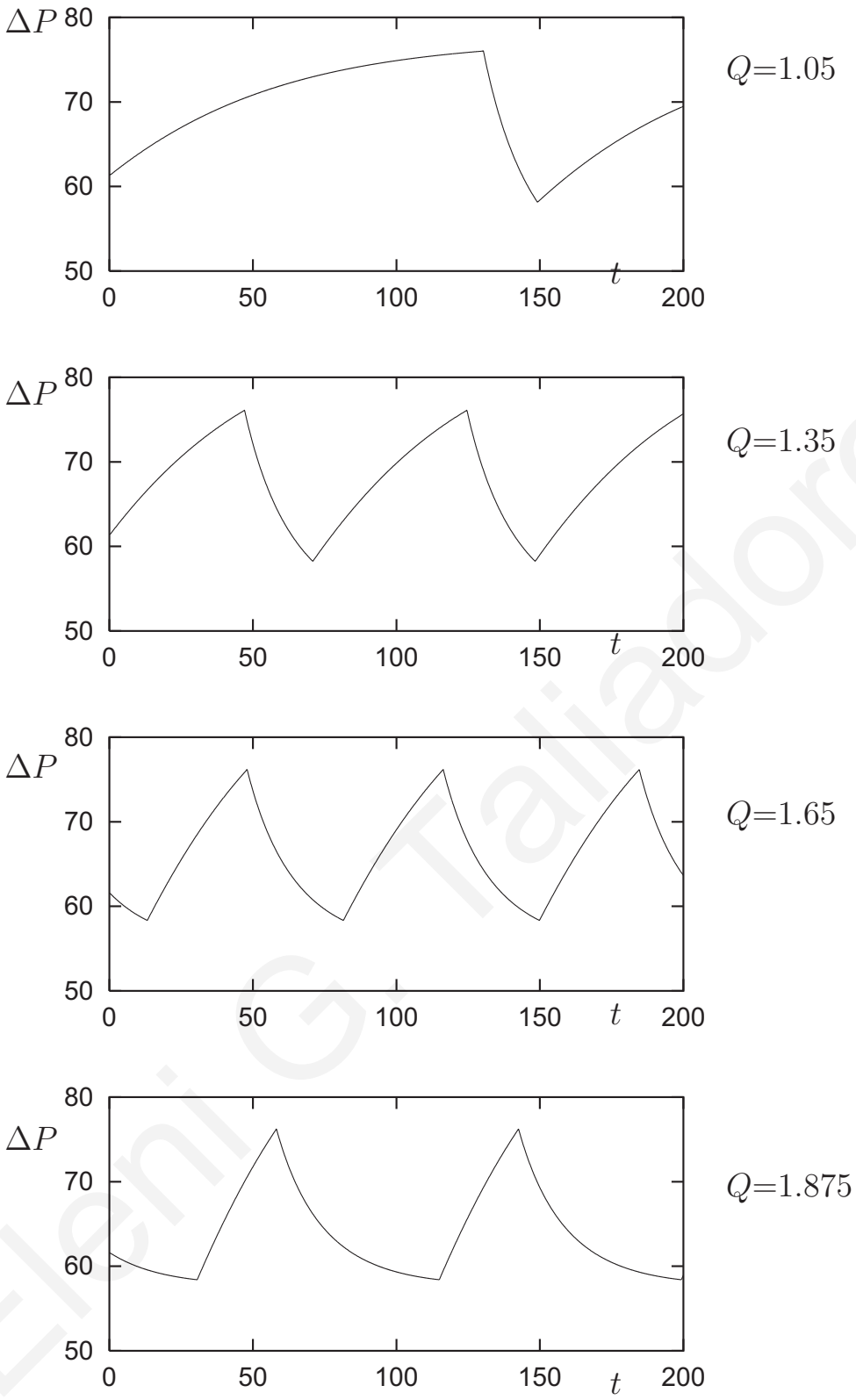

Figure 2.17: *Effect of the imposed volumetric flow rate on the pressure oscillations; Carreau flow (n=0.44), Re=0.01 and* L_b*=80.*

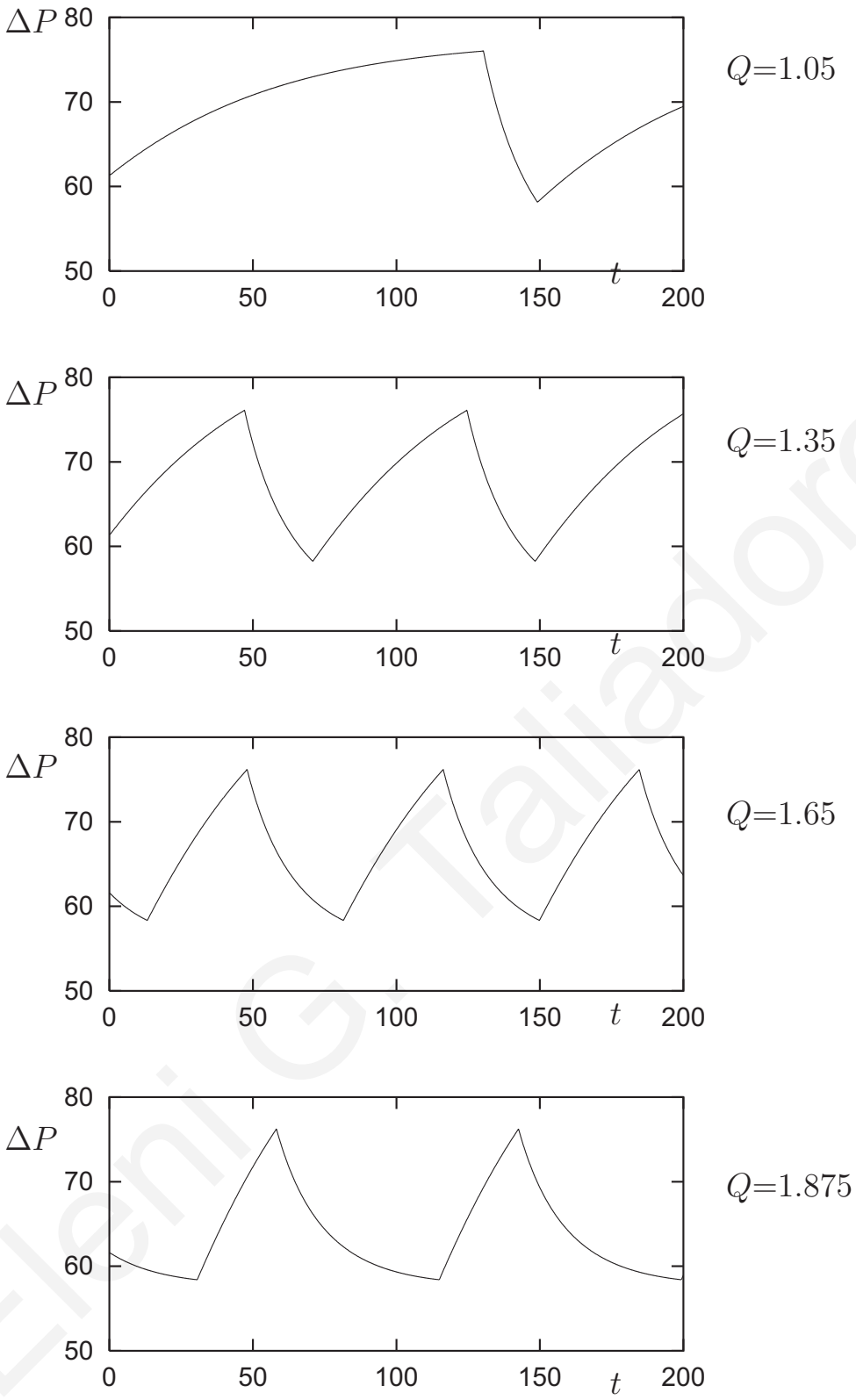

Figure 2.18: *Effect of the imposed volumetric flow rate on the pressure oscillations; Carreau flow (n=0.44), Re=0.01 and* L_b*=80.*

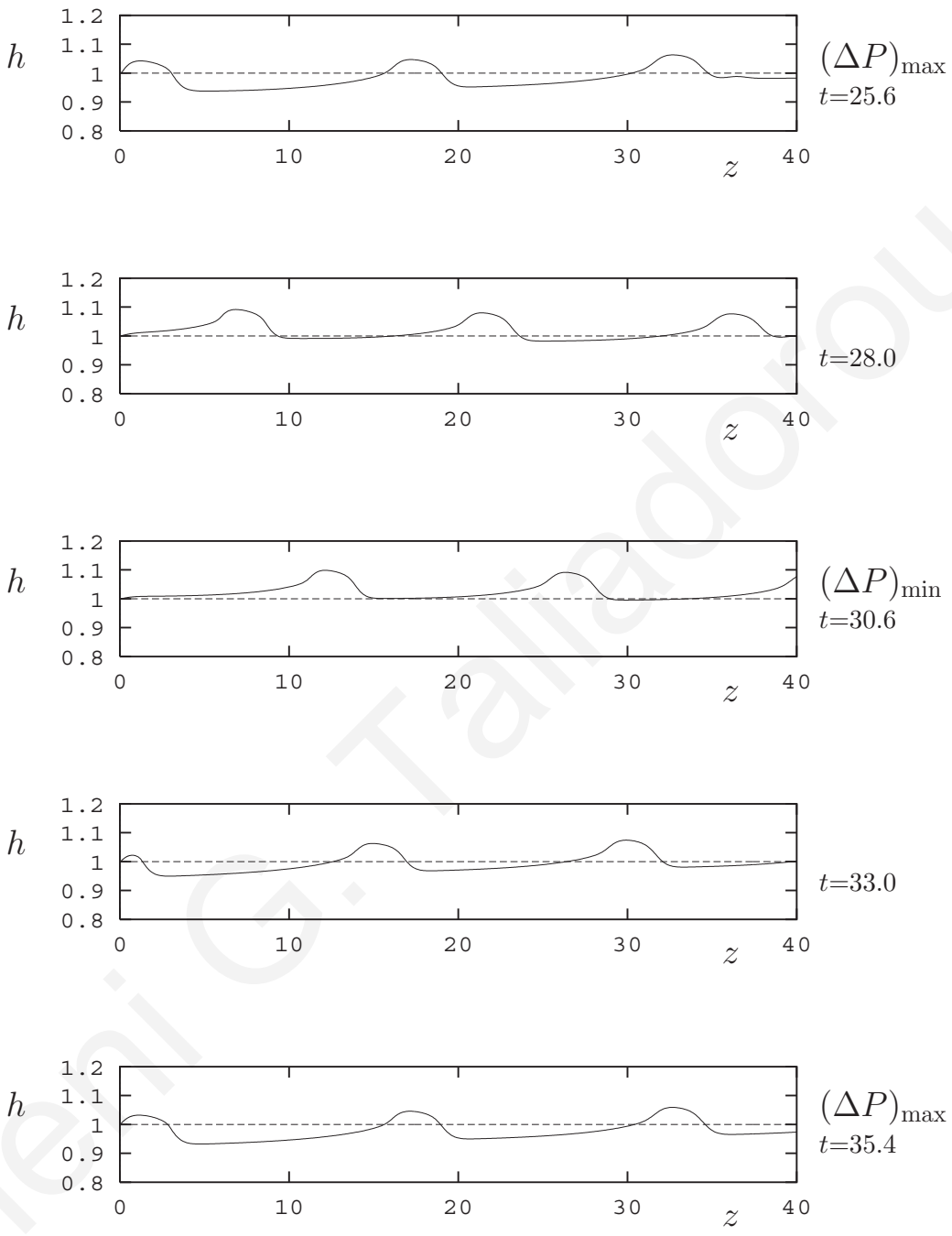

Figure 2.19: *Free surface oscillations during one cycle; Newtonian flow (n=1), Re=0.01, L_b=20 and Q=1.5.*

with the steady-state solution corresponding to a flat free surface (stick-slip flow) and letting the free surface move at t=0. In Fig. 2.19, we present free surface profiles obtained for the Newtonian flow with Re=0.01, Q=1.5 and a small reservoir length, L_b=20, during one cycle of the pressure oscillations (from a pressure-drop maximum to the next one) after the periodic solution is established. The free surface oscillations resemble to the 'bamboo' instability pattern with a long 'smooth' part and a shorter 'distorted' part. As in Ref. [29], in addition to the motion of the free surface waves in the flow direction, the free surface also oscillates in the radial direction; swelling is minimized at pressure-drop maxima. This result agrees with the experiments of Pérez-González et al. [64], who worked with polyethylene melts and observed that severe contractions in the extrudate diameter occur at pressure maxima. From Fig. 2.19, it can easily be deduced that the motion of the extrudate is accelerated just after the pressure drop maximum, which is, of course, due to the sudden jump of the volumetric flow rate from the left to the right stable branch of the flow curve. Similarly, the extrudate motion is decelerated just after the pressure drop minimum, since the flow rate jumps from the right to the left stable branch.

A comparison with Fig. 2.20, where Newtonian free surface profiles obtained with L_b=80 are shown, reveals that with a longer reservoir (i.e. for a bigger period of pressure oscillations), the wavelength of the resulting free surface waves is much bigger. The amplitude and the relative length of the distortions also appear to increase. Similar results have been obtained for the case of Carreau flow, as illustrated in Figs. 2.21 and 2.22, which show free surface profiles obtained with L_b=20 and 80, respectively.

In addition to L=20, we have also considered the values L=0.1, 1, 5, 10 and 40, in order to study the effect of the capillary length. In Fig. 2.3a, we plotted the flow curves of the Carreau fluid obtained for all capillary lengths. As expected, the pressure drop as well as

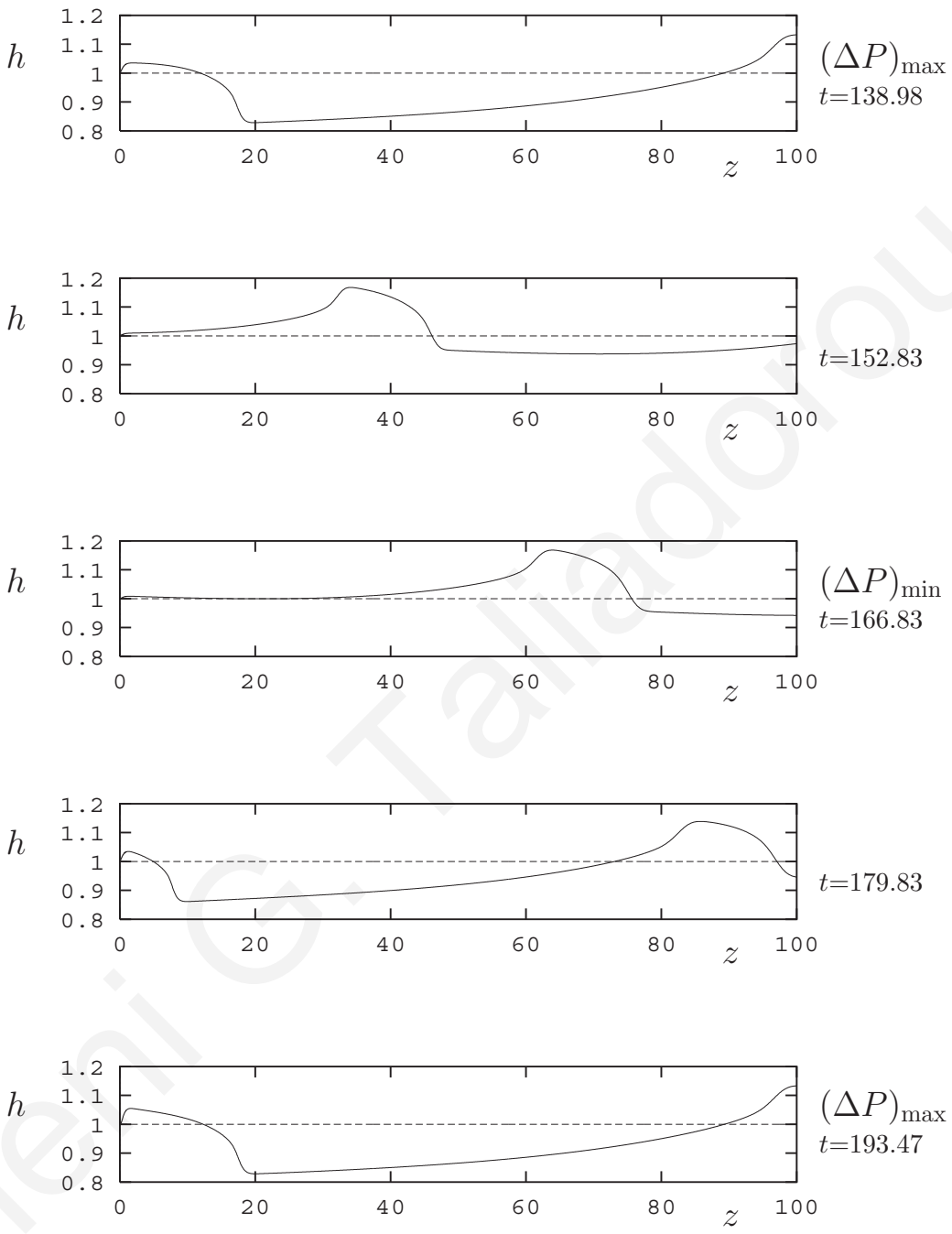

Figure 2.20: *Free surface oscillations during one cycle; Newtonian flow (n=1), Re=0.01, L_b=80 and Q=1.5.*

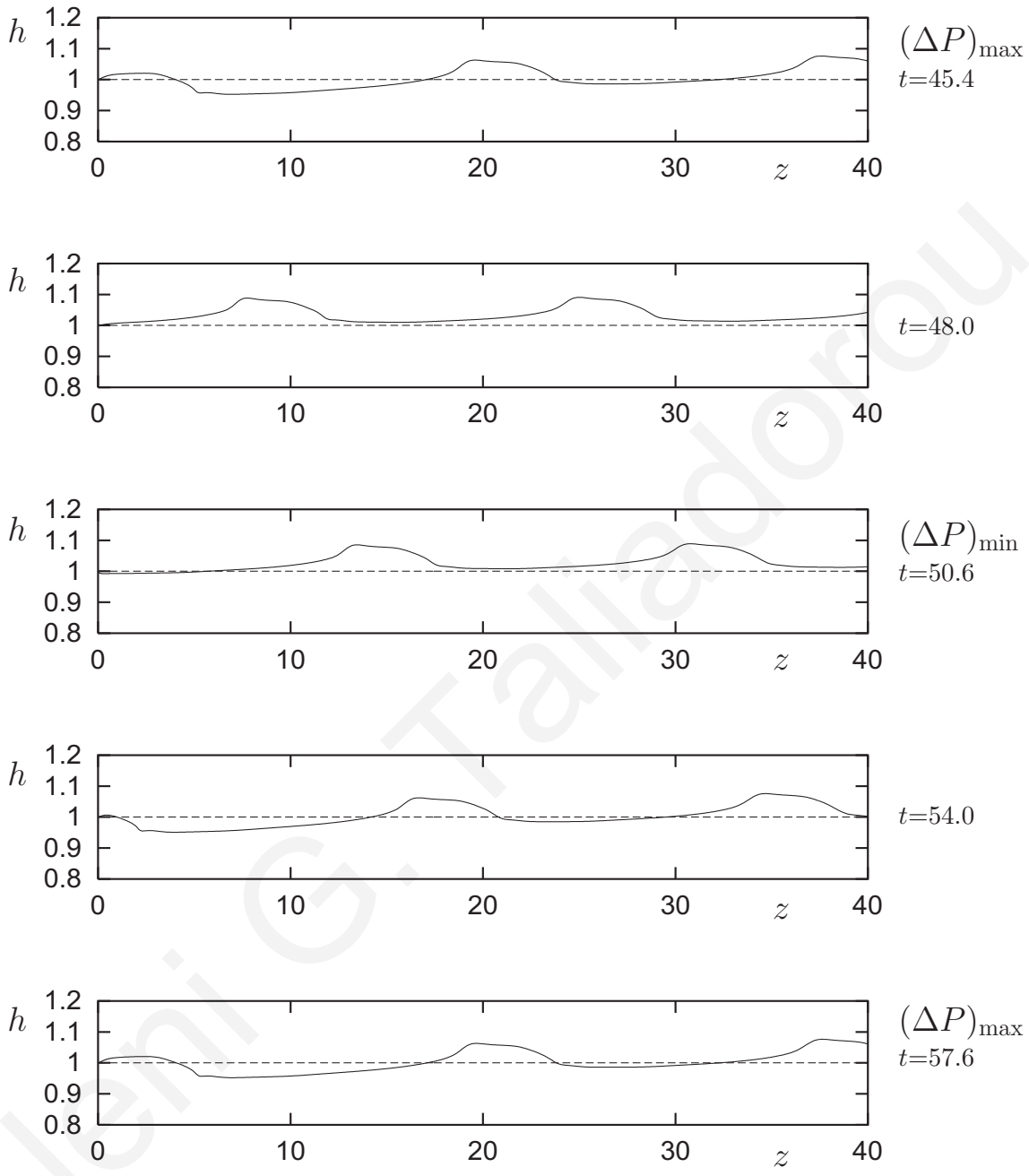

Figure 2.21: *Free surface oscillations during one cycle; Carreau flow (n=0.44), Re=0.01, L_b=20 and Q=1.5.*

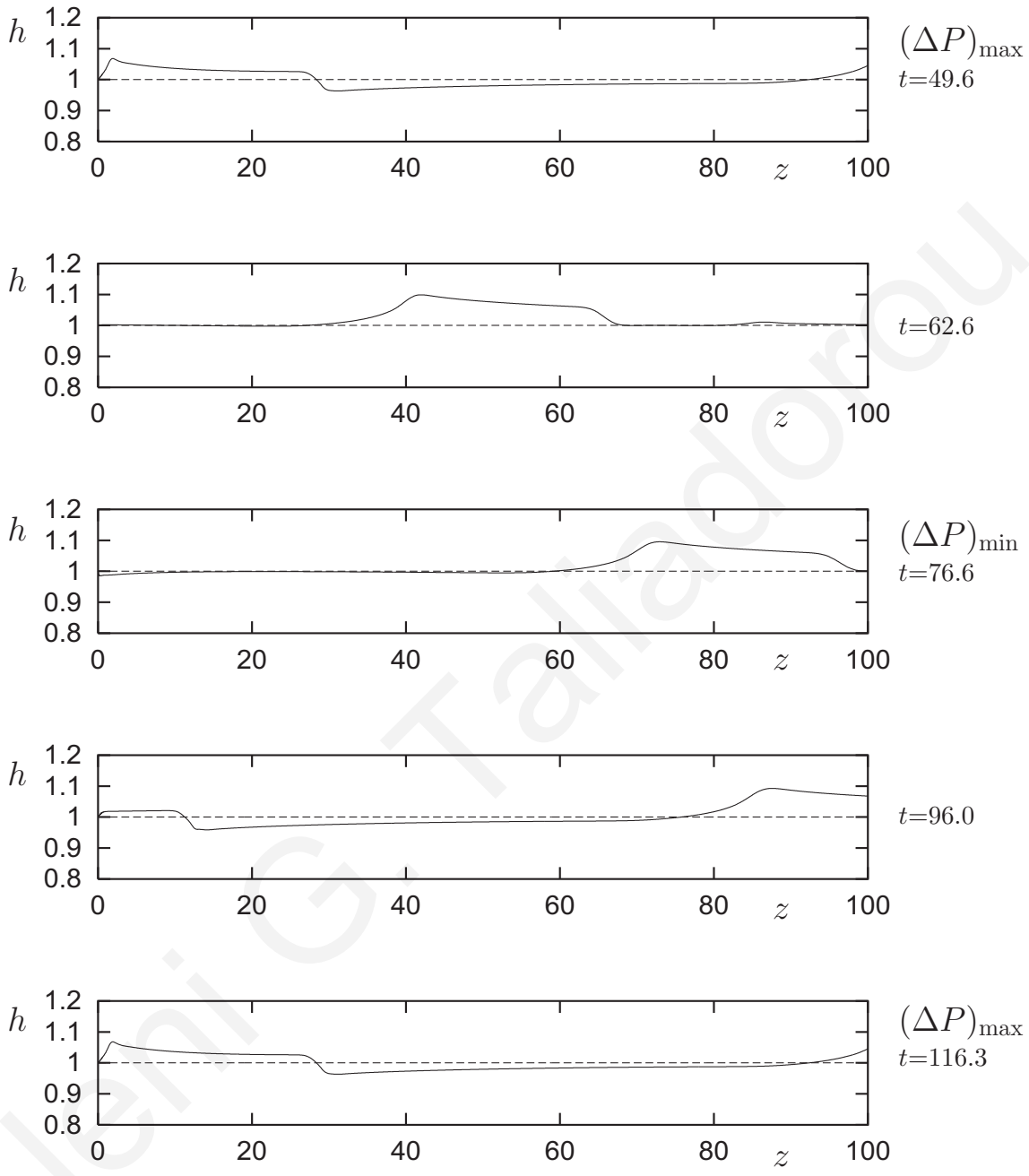

Figure 2.22: *Free surface oscillations during one cycle; Carreau flow (n=0.44), Re=0.01, L_b=80 and Q=1.5.*

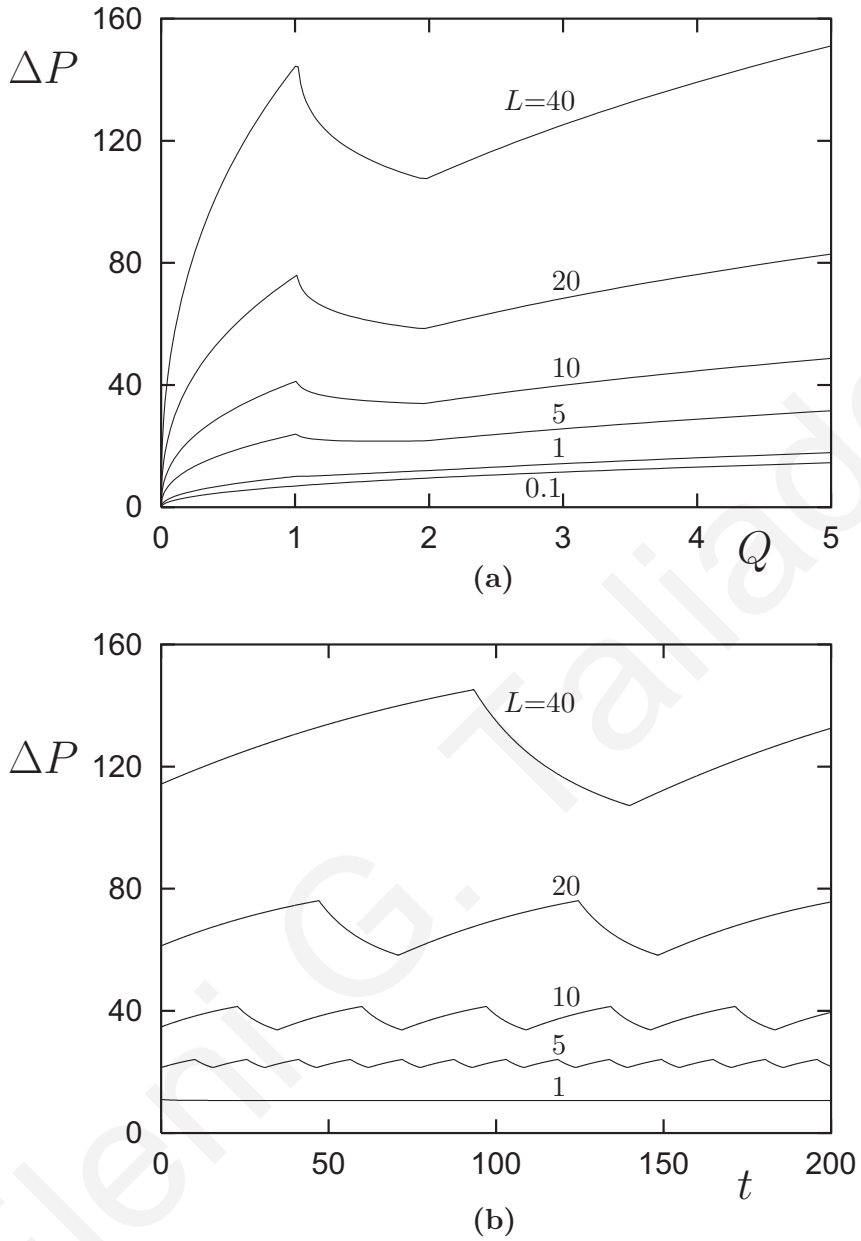

Figure 2.23: *Flow curves (a) and pressure oscillations (b) for different capillary lengths; Carreau flow (n=0.44), Re=0.01, Q=1.35 and L_b=80.*

the difference between its maximum and minimum values are reduced as the capillary length is decreased. Moreover, for very small capillary lengths the flow curve becomes monotonic, which implies that the flow is stable for all values of the volumetric flow rate. In other words, the hysteresis loop decreases in size and eventually vanishes as the capillary length is decreased. As a consequence, the amplitude and the period of the pressure drop oscillations decrease, as illustrated in Fig. 2.3b; for L=1, no oscillations are observed, since the flow is everywhere stable.

Figure 2.24 shows that the period and the amplitude of the pressure drop oscillations vary linearly with the capillary length, above the critical value at which the flow curve ceases to be monotonic. These results agree well with experiments on HDPEs [20, 39, 58, 74], regarding the size of the hysteresis loop and the amplitude and the period of the pressure oscillations. Unlike the experiments, however, our simulations do not predict the shift of the stick-slip regime to lower flow rates. This may be due to the fact that the pressure dependence of wall slip is not taken into account in the slip model [40]. The numerical simulations also showed that the capillary length has a slight effect on the waveform of the pressure oscillations.

As illustrated in Fig. 2.25, where the normalized pressure oscillations for L=5, 10 and 40 are compared, the increasing part of the oscillation increases slightly with the capillary length.

Assuming that the pressure drop corresponding to the very short capillary length L=0.1 (see Fig. 2.23a) is equal to the Bagley end correction, P_{end}, in Eq. (2.2), we calculated the wall shear stresses versus the apparent wall shear rate. Interestingly, the curves of the calculated wall shear stresses for all capillary lengths (L=1, 5, 10, 20 and 40) coincide, as shown in Fig. 2.26. The critical values of the wall shear stress are σ_{c2}=0.34 MPa and σ_{c3}=0.24 MPa, which give $(\sigma_{c2} - \sigma_{c3})$= 0.1 MPa. The values of σ_{c2} reported by Hatzikiriakos and Dealy [40] are in the range 0.22 - 0.50 MPa, while those of $(\sigma_{c2} - \sigma_{c3})$ are in the range 0.03-0.11 MPa.

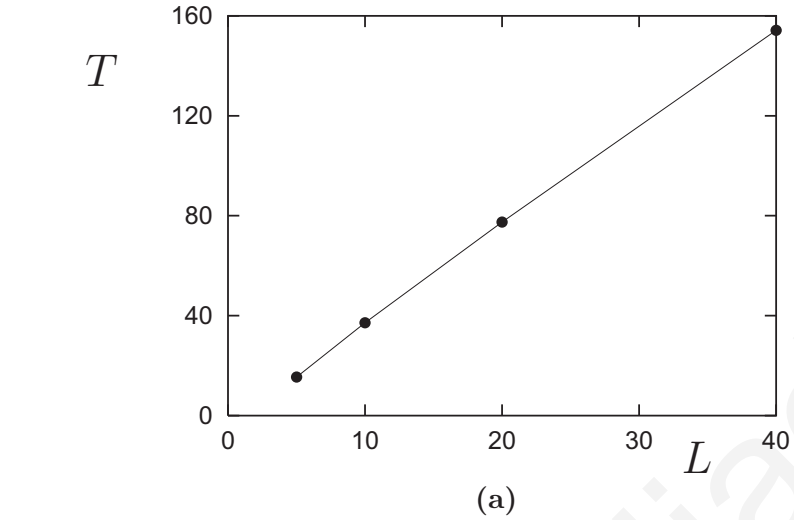

(a)

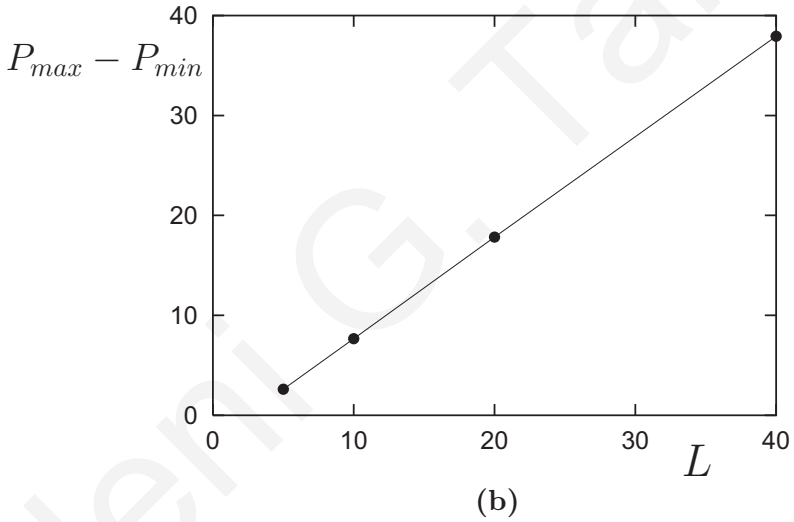

(b)

Figure 2.24: *Period (a) and amplitude (b) of the pressure oscillations as functions of the capillary length; Carreau flow (n=0.44), Re=0.01, Q=1.35 and L_b=80.*

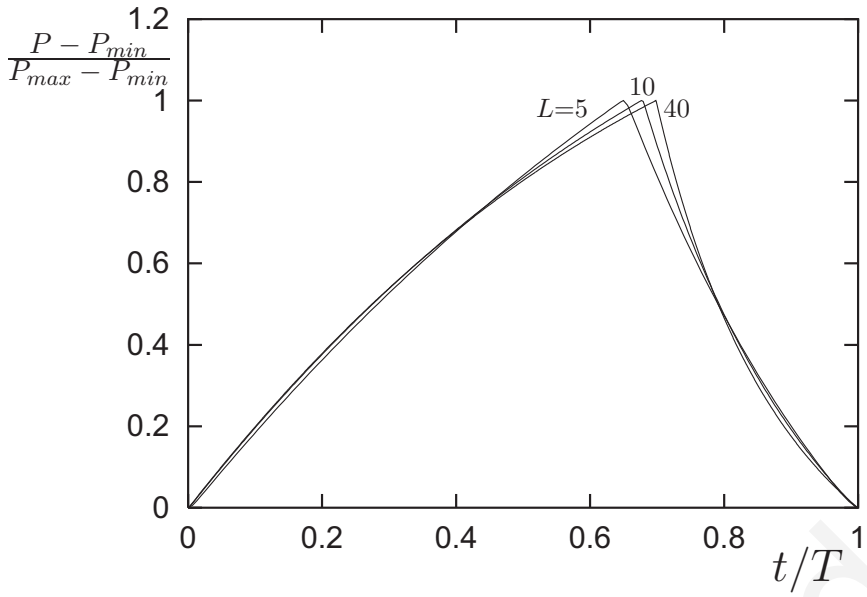

Figure 2.25: *Normalized pressure oscillations for different capillary lengths; Carreau flow (n=0.44), Re=0.01, Q=1.35 and L_b=80.*

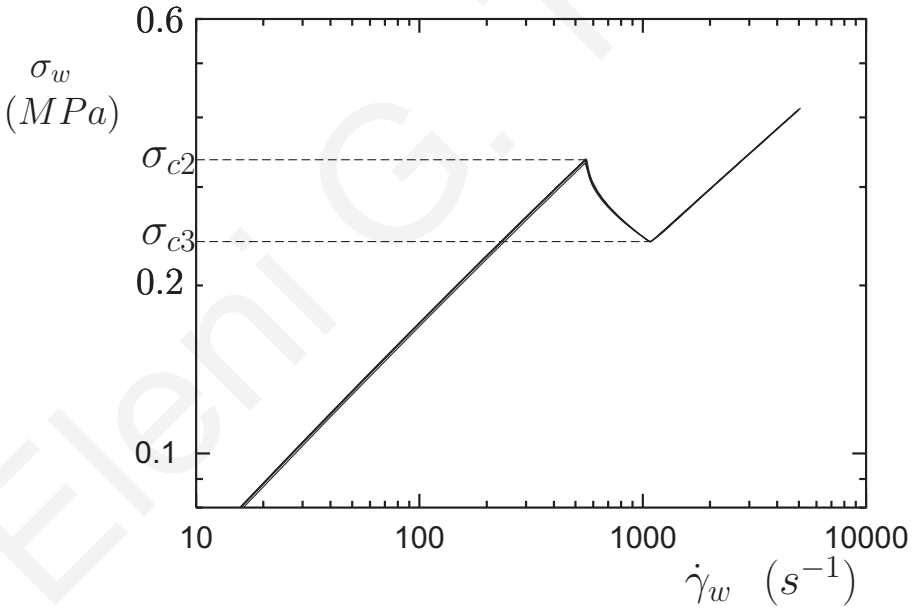

Figure 2.26: *Apparent wall shear stress versus the apparent wall shear rate for different capillary lengths: L=1, 5, 10, 20 and 40; Carreau flow (n=0.44) and Re=0.01.*

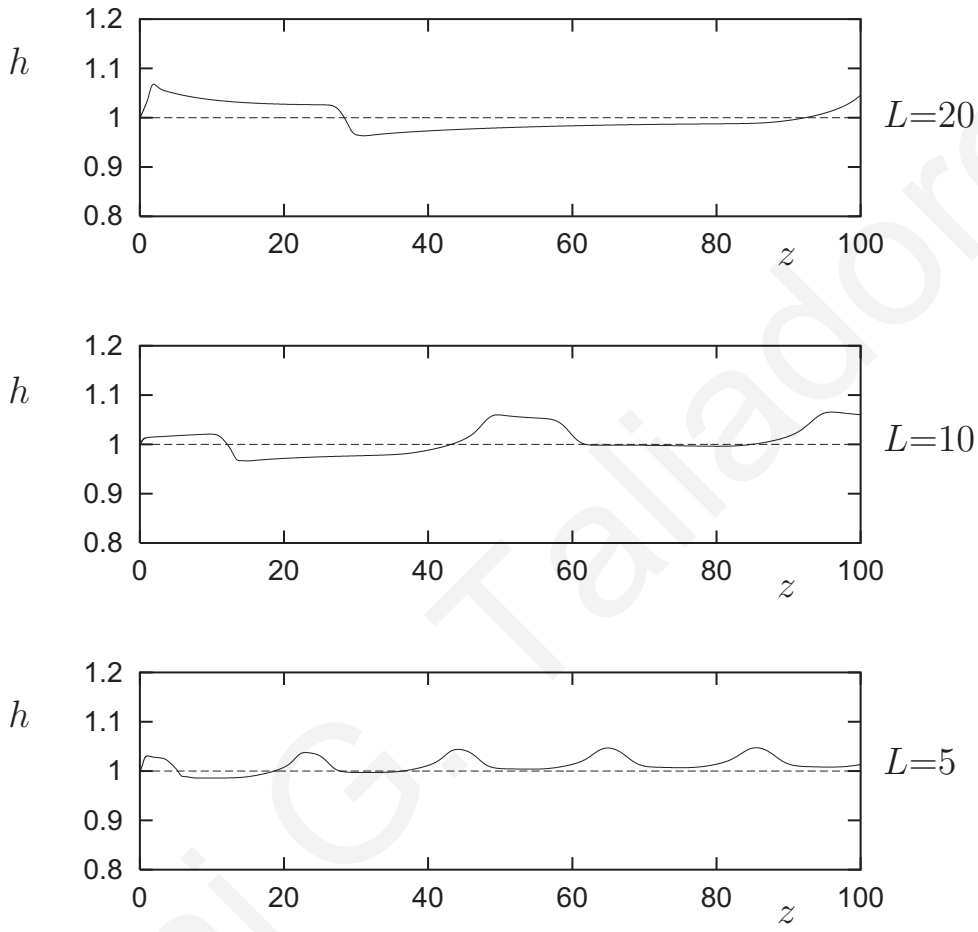

Figure 2.27: *Free surface oscillations at a pressure drop maximum for different capillary lengths; Carreau flow (n=0.44), Re=0.01 and L_b=80.*

Given the assumptions made in the present work, the agreement between simulations and experiments is rather good. As already mentioned, experimental observations on the effect of the capillary length on the value of σ_{c2} cover all possibilities. In some cases, σ_{c2} has been found to increase [20, 40, 74, 89] and in others to decrease [46, 22, 92], as L is increased. Our simulations agree with the experiments of Ramamurthy [69] and Wang and Drda [94, 95] in which σ_{c2} was found to be independent of L. Finally, the effect of the capillary length on the free-surface oscillations is illustrated in Fig. 2.27. Both the amplitude and the wavelength increase, and the waveform appears to change dramatically with the capillary length.

2.4 Conclusions

We used finite elements to simulate the time-dependent, compressible extrusion of a Carreau fluid in the full reservoir-capillary-extrudate geometry, assuming that slip occurs along the die wall following a nonmonotone slip law that is based on the experimental measurements of Hatzikiriakos and Dealy [39, 40].

The numerical simulations agree well with the following experimental observations: (a) the pressure and flow rate oscillations follow the hysteresis loop defined by the two branches of the flow curve, and the volumetric flow rate is characterized by instantaneous jumps between the two branches; (b) the amplitude and the period of the pressure oscillations increase linearly with the capillary length, since the hysteresis loop becomes larger; (c) for small capillary lengths, the pressure is a continuous monotonic function of Q, and no oscillations are observed; and (d) the period of the pressure and flow rate oscillations increases linearly with the reservoir length, while their amplitudes and waveforms are fairly constant. Nevertheless, the period of the pressure oscillations, when plotted versus the reservoir volume, appears to pass through

the origin, which is not the case with extrapolated experimental data [20, 40, 73, 74].

In agreement with certain experiments [58, 61, 96, 92], the period of the pressure oscillations passes through a minimum, when this is plotted versus the imposed volumetric flow rate. The compression part of the pressure oscillations is relatively reduced, as Q is increased.

The calculated value of the critical wall shear stress for the onset of the stick-slip instability, σ_{c2}=0.34 MPa, is in the range reported by Hatzikiriakos and Dealy [40]. This value was found to be independent of the capillary length, which is in agreement only with certain experiments [69, 94, 95]. Unlike experimental observations [20, 40], the stick-slip regime is not shifted to lower volumetric flow rates but remains constant as the capillary length is increased. This may be due to the fact that the slip equation we employed does not take into account the pressure dependence of wall slip and holds uniformly across the capillary.

Chapter 3

Numerical simulation of the extrusion of strongly compressible Newtonian liquids

3.1 Introduction

Foams are structured dispersions of gas bubbles in a small volume fraction of a liquid with the liquid as the continuous phase and the gas as the dispersed one[1]. Foamed products are useful in many different industrial applications. In the plastics industry, polyethylene, polystyrene and polypropylene foams are produced for thermal insulation, packaging applications, protecting and sporting equipment, and aircraft or automotive parts with high strength to weight ratio [59, 62]. Foamed polymer solutions are used widely in the petroleum industry as drilling fluids and in the hydraulic fracturing of hydrocarbon wells [27]. Metal foams also

[1]Some of the results presented in this chapter appear also in References [81, 83]

find applications in the automotive industry [7]. Aqueous polymer solutions foamed with nitrogen and/or carbon dioxide are used in fire-fighting technology for polar solvent and oil fires [27, 43]. Other applications can be found in the food and biopolymer industry, with products ranging from starch-based foams [97], cereal foods [56, 93] and aerated chocolates [27] to cosmetics and medical drugs [43].

In foam extrusion, a chemical foaming agent is mixed with the polymer to be extruded. The heat generated to melt the polymer decomposes the chemical foaming agent producing gas which is dispersed in the polymer melt. An alternative is to blow the polymer melt with an inert gas, such as carbon dioxide or nitrogen [59, 62, 98]. Upon exiting the die, the gas expands considerably. Expansion of extrudates is one of the most important phenomena of foam extrusion processing, resulting in products with a cellular foam structure [59, 60, 93]. This is a complex phenomenon caused by different mechanisms, such as phase transitions, nucleation and bubble growth and collapse [56, 59, 60] in addition to extrudate-swell. Important parameters that affect the final dimensions and quality of the extrudate are the die geometry, material properties, and processing environment [93].

In the polymer foam production industry, the expansion of the extrudate is usually described by the volume expansion ratio, which is also known as overall expansion ratio or foaming ratio. This is the ratio of the extrudate solid density to the bulk density. In the food industry, the radial expansion ratio is used instead. This is the ratio of the cross-sectional area of the extrudate to that of the die [77, 99]. In other words, the radial expansion ratio is the square of the well-known extrudate-swell ratio, which is defined as the ratio of the final extrudate diameter to that of the die. The axial expansion ratio, calculated by dividing the volume expansion by the radial expansion ratio, is also used [77]. The expansion ratios and the density are important properties of extruded foams. High expansion ratios and low unit

density are ideal for foams because of the reduced cost of the final product [99].

In general, polymer foams produced by conventional extrusion process exhibit high expansion ratios up to 100. Park and co-workers reported volume expansion ratios as high as 23 for microcellular high impact polystyrene (HIPS) foams [62], in the range of 1.5 - 20 for fine-cell HDPE foams [4], and up to 45 for biodegradable polyester foams [63]. For the extrusion of polypropylene foams blown with butane, Naguib et al. [59, 60] reported volume expansion ratios ranged from about 1 to 90, depending on the gas fraction, the temperature, and the talc content. Very recently, Lee et al. [51] reported volume expansion ratios ranging from 2.3 to 8.5 in the case of open-cell LDPE/PS sheet foams produced with an annular die. Xu et al. [98] reported volume expansion ratios up to 6 in direct extrusion foaming of a low density polypropylene. Large expansion ratios are also observed in the case of extruded biodegradable starch and cereal foams. Radial expansion ratios up to 62.4 have been reported [56, 97, 99].

Of particular interest to the present work is the phenomenon of the contraction of the extrudate after the initial expansion near the die exit, which is known to be detrimental to large expansion [60]. This contraction is attributed to the escape of gas through the exterior skin of the extruded foam [4, 59, 62]. Therefore, in order to produce low-density foams, gas diffusion must be prevented. In extrusion experiments with microcellular HIPS foams blown with carbon dioxide, Park et al. [62] observed that the diameter of the initially expanded foam at a relatively high temperature was about 2.2 times of the diameter of the finally contracted foam. By decreasing both the melt and nozzle temperatures, Park et al. [62] were able to achieve full expansion eliminating the contraction, which was attributed to the reduced gas diffusion through the frozen skin layer of the extrudate and the suppression of cell coalescence.

Naguib et al. [59, 60] studied the fundamental mechanisms governing the volume expansion behavior of extruded polypropylene foams blown with butane. Based on their experimental data, they reached the conclusion that either gas loss or polymer crystallization govern the final volume expansion ratio of the polypropylene foams and that the maximum expansion ratio was achieved when the governing mechanism changed from one to the other. They also noted that at higher temperatures, initial expansion is followed by an undesirable contraction and that as temperature is increased, initial expansion becomes larger but final expansion is reduced beyond an optimum temperature. The angle of initial expansion was found to increase with temperature, i.e. initial expansion becomes faster [59].

Extrudate contraction following the initial expansion has also been observed with extruded starch-based foams [24, 93, 97, 99] and cereal foods [56], resulting in increased densities and reduced expansions. Willett and Shogren [97] and Moraru and Kokini [56] attribute this phenomenon to the cooling rate, which is not rapid enough to prevent bubble collapse.

The objective of the present work is to study numerically the expansion of extruded foams in the so-called extrudate-swell flow and investigate whether the aforementioned phenomenon of extrudate contraction can be attributed to the compressibility of the foam. The latter is treated as a homogeneous fluid. In other words, the extrudate expansion of foamed liquids is studied at a macroscopic level. Bubble growth phenomena are taken into account implicitly by assuming that the foam is highly compressible. For other analyses, in which bubble growth is characterized at a microscopic level, the reader is referred to the paper by Wang et al. [93] and the references therein.

The knowledge of the rheological behavior of foamed fluids is essential in engineering applications. As stated by Reinelt and Kraynik [71], a complete theory of foam rheology does not

exist, since foam behavior involves a broad range of physical mechanisms acting over multiple length and time scales. Additional information concerning these physical mechanisms can also be found in the recent review article of Höhler and Cohen-Addad [43]. Rheological studies have shown that foam viscosity depends on properties, such as the foam expansion ratio, defined as the ratio of the volume of the foam to the volume of the foam liquid at atmospheric conditions, the bubble size distribution, and other properties of individual phases, i.e. the surface tension [23, 27]. In general, a foam behaves like a non-Newtonian fluid exhibiting shear thinning, yield stress and elastic behavior typical of emulsions [49]. The origin of the elastic behavior comes from the minimization of surface area, due to the surface tension that exists in the thin liquid films. The yield stress arises due to the internal structure of foam, which consists of bubbles separated by a matrix of thin films [49]. Yield stress was found to increase monotonically with the gas fraction (volume of contained gas/volume of foam), the surface tension, and decreasing bubble size [25, 48]. Typically, a Herschel-Bulkley model is fitted to the experimental data [27, 42].

In the present work, we concentrate our attention on the effects of compressibility assuming that the foam behaves as a homogeneous compressible Newtonian fluid with a viscosity independent of the pressure. The latter assumption is also a strong one; a correct simulation of foam flow has to include pressure-dependent viscosity [44]. Beverly and Tanner [10] were the first to solve numerically the compressible, axisymmetric Newtonian extrudate-swell problem. Their simulations showed that weak compressibility reduces the swelling of Newtonian fluids. The finite-element calculations of Georgiou [28] confirmed this result and showed that as compressibility increases, the extrudate-swell ratio passes through a minimum and then starts increasing rapidly, in agreement with experiments [4, 62, 63]. A second objective of the present work is to investigate this phenomenon further, given that liquid foams are highly

compressible.

First, the governing equations and boundary conditions for the compressible Newtonian extrudate-swell flow are presented and discussed. In order to study the effects of compressibility, two alternative equations of state, a linear and an exponential one, are used. A linear equation of state has been employed in previous numerical studies of the compressible extrudate-swell flow [10, 28], by Hatzikiriakos and Dealy [40] for a HDPE, and in our previous studies concerning the simulation of the stick-slip extrusion instability [29, 32]. Exponential equations of state have been employed, for example, by Ranganathan et al. [70] for a HDPE and, more recently, by Vinay et al. [90] in simulations of weakly compressible Bingham flows. It should be pointed out that taking into account only the pressure dependence of the density (and even that of viscosity) is not sufficient for modeling foam expansion with chemical or physical blowing agents, since these mechanisms involve chemical reaction or gas diffusion, respectively. Since foams are known to slip along the walls [5, 9, 23, 26, 27, 42, 48], in addition to the no-slip boundary condition at the wall, the possibility of slip by means of a linear slip equation is also considered. Then, the numerical method is briefly described and the numerical results are presented and discussed. Emphasis is given on the effects of compressibility on the expansion of the jet. The numerical results confirm previous reports that the swelling of the extrudate decreases initially as the compressibility of the fluid is increased and then increases considerably, in agreement with experimental observations. The numerical simulations also reveal that high compressibility may lead to a contraction of the extrudate after the initial expansion, similar to that observed experimentally with liquid foams or to decaying oscillations of the extrudate surface, provided that inertia is taken into account. Lastly, the conclusions are summarized and some possibilities for future work are given.

3.2 Governing equations

Since the equations and boundary conditions for the plane problem are similar, only the axisymmetric extrudate-swell flow is discussed. The flow is assumed to be laminar, compressible and isothermal, and gravity is neglected. Letting p, $\mathbf{v}$, and $\boldsymbol{\tau}$ denote the pressure, the velocity vector, and the viscous stress tensor, respectively, the continuity and the momentum equations are written as:

$$\frac{\partial \rho}{\partial t} + \nabla \cdot \rho \, \mathbf{v} = 0 \,, \tag{3.1}$$

$$\rho \left(\frac{\partial \mathbf{v}}{\partial t} + \mathbf{v} \cdot \nabla \mathbf{v} \right) = -\nabla p + \nabla \cdot \boldsymbol{\tau} \,, \tag{3.2}$$

where ρ is the density. For compressible Newtonian flow with the bulk viscosity neglected, the viscous stress tensor is given by

$$\boldsymbol{\tau} = \mu \left[(\nabla \mathbf{v}) + (\nabla \mathbf{v})^T \right] - \frac{2}{3} \mu \, \mathbf{I} \, \nabla \cdot \mathbf{v} \,, \tag{3.3}$$

where $\mathbf{I}$ is the unit tensor, μ is the viscosity, and the superscript T denotes the transpose. The viscosity is assumed to be constant and independent of the pressure.

The above equations are completed by a thermodynamic equation of state relating the density to the pressure. At constant temperature and low pressures, the density can be represented by the linear approximation

$$\rho = \rho_0 \left[1 + \beta \, (p - p_0) \right] \,, \tag{3.4}$$

where

$$\beta \equiv -\frac{1}{V_0} \left(\frac{\partial V}{\partial p} \right)_{p_0, T} \tag{3.5}$$

is the isothermal compressibility assumed to be constant, V is the specific volume, ρ_0 and V_0 are, respectively, the density and the specific volume at a reference pressure p_0, and T is the

temperature. For comparison purposes, the following exponential equation is also used:

$$\rho \;=\; \rho_0 \, e^{\beta \, (p \,-\, p_0)} \,. \tag{3.6}$$

This is equivalent to the linear equation of state for low pressures depending on the value of β. A disadvantage of this equation is the fast growth of the density (for high values of β). On the other hand, the linear model may lead to negative values of the density. Obviously more sophisticated equations of state should be used for highly compressible flows.

To non-dimensionalize the governing equations, we scale the lengths by the radius R, the velocity by the mean velocity U at the inlet of the capillary, the pressure and the stress components by $\mu U/R$, and the density by ρ_0. With these scalings, the continuity and momentum equations become

$$\frac{\partial \rho}{\partial t} \;+\; \nabla \cdot \rho \, \mathbf{v} \;=\; 0 \,, \tag{3.7}$$

and

$$Re \left(\frac{\partial \mathbf{v}}{\partial t} \;+\; \mathbf{v} \cdot \nabla \mathbf{v} \right) \;=\; -\nabla p \;+\; \nabla \cdot \boldsymbol{\tau} \,, \tag{3.8}$$

where all variables are now dimensionless, and Re is the Reynolds number defined as

$$Re \;\equiv\; \frac{\rho_0 \, U \, R}{\mu} \,. \tag{3.9}$$

The linear and the exponential equations of state respectively become

$$\rho \;=\; 1 \;+\; B \, p \tag{3.10}$$

and

$$\rho \;=\; e^{Bp} \,, \tag{3.11}$$

where B is the compressibility number,

$$B \;\equiv\; \frac{\beta \, \mu \, U}{R} \,, \tag{3.12}$$

and the reference pressure has been set to zero. The behavior of the two dimensionless equations of state is illustrated in Fig. 3.1. The two models are equivalent only if the pressure, p, and the compressibility number, B, are sufficiently low.

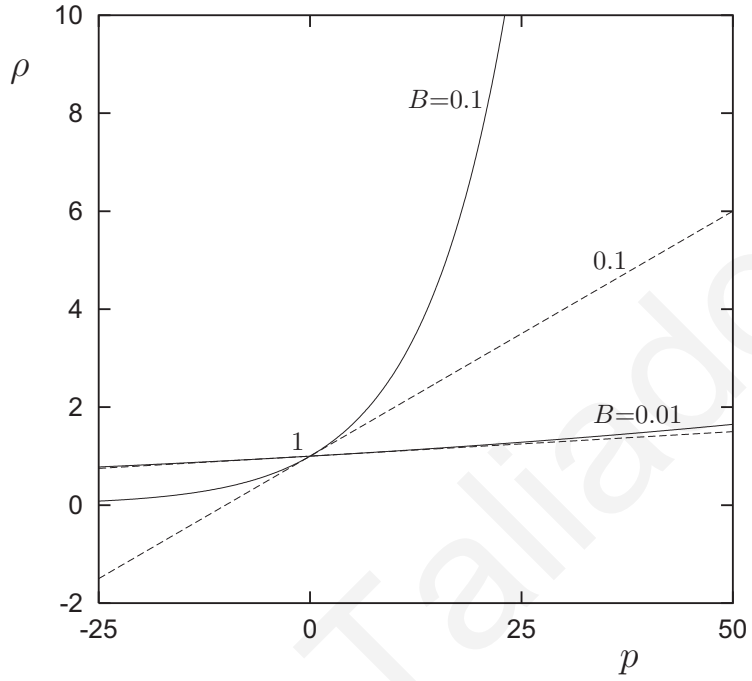

Figure 3.1: *Behavior of the linear (dashed) and exponential (solid) equations of state for B=0.01 and 0.1.*

The dimensionless boundary conditions of the flow are shown in Fig. 3.2. To include slip effects, a linear slip equation is employed, the dimensionless form of which is

$$\tau_w \;=\; \frac{1}{A}\, v_w \,, \tag{3.13}$$

where v_w is the dimensionless slip velocity, τ_w is the dimensionless shear stress at the wall, and A is a dimensionless slip number defined by

$$A \;\equiv\; \frac{\alpha\,\mu}{R} \,, \tag{3.14}$$

α being a slip parameter depending on the material properties for a given wall. Hence, along the capillary wall, the axial velocity, v_z, satisfies the slip equation (3.13), whereas the radial velocity, v_r, is zero.

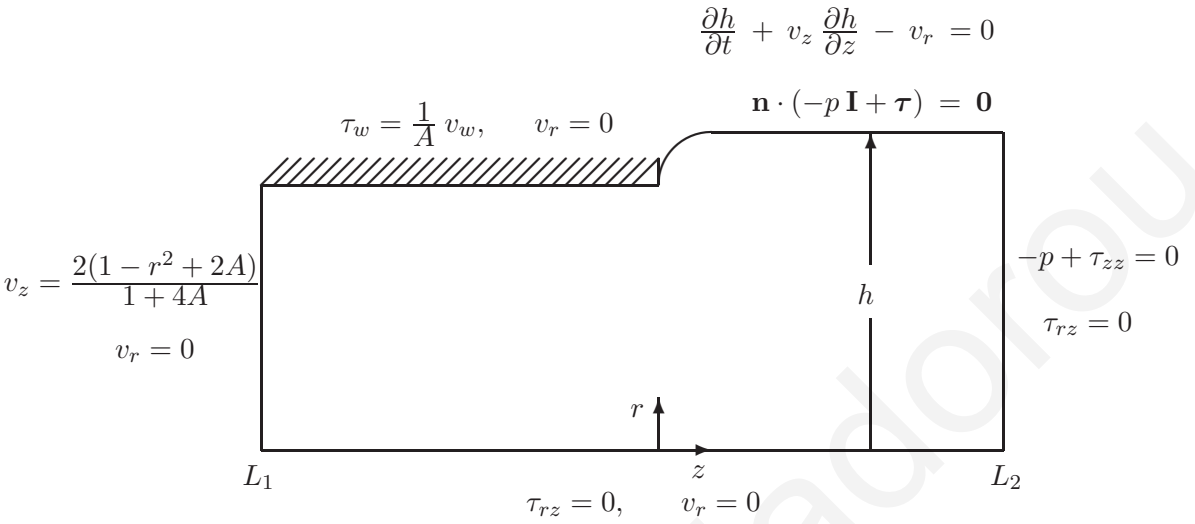

Figure 3.2: *Geometry and dimensionless boundary conditions for the axisymmetric extrudate-swell flow of a Newtonian fluid with slip at the wall.*

At the inlet plane, assumed to be taken far upstream the exit so that the flow can be taken as fully developed, v_r is zero and v_z is given by

$$v_z = \frac{2}{1 + 4A} (1 - r^2 + 2A) . \tag{3.15}$$

The above velocity profile satisfies the slip equation (3.13). The dimensionless slip velocity at the inlet plane is v_w=$4A/(1 + 4A)$. Setting A=0 leads to the well-known dimensionless Newtonian velocity profile corresponding to no slip.

The outflow plane is assumed to be far downstream from the die exit so that total normal stress and the shear stress vanish, $-p + \tau_{zz}$=0 and τ_{rz}=0. Along the axis of symmetry, the usual symmetry boundary conditions are used. Finally, on the free surface, it is assumed that

surface tension is zero and vanishing normal and tangential stresses are imposed. Additionally, the unknown position $h(z,t)$ of the free surface satisfies the kinematic condition:

$$\frac{\partial h}{\partial t} + v_z \frac{\partial h}{\partial z} - v_r = 0 . \tag{3.16}$$

In the case of the time-dependent calculations, the solution corresponding to a volumetric flow rate Q_0 at the inlet is used as the initial condition and at t=0 the volumetric flow rate is perturbed to Q=1.

3.3 Numerical simulations

The finite element formulation is used for solving the free-surface flow problem under study. The unknown position of the free surface is calculated simultaneously with the velocity and pressure fields (full-Newton method). The mesh is updated accordingly, using a spine scheme. The standard biquadratic-velocity (P^2-C^0) and bilinear-pressure (P^1-C^0) elements with a quadratic representation for the position h of the free surface are employed. For the spatial discretization, the standard Galerkin forms of the continuity, momentum and kinematic equations are used, while for the time discretization, the standard fully-implicit (Euler backward-difference) scheme has been chosen.

In order to check the convergence of the numerical results, we have constructed four meshes of different refinement near the singularity at the die exit. We have also considered three capillary lengths: L_1=5, 10 and 20. Unless otherwise indicated, the length of the extrudate region has been taken to be L_2=20. Table 3.1 shows the sizes of the elements adjacent to the singular point and the characteristics of all meshes used in the present work. In the beginning of this section, we will consider the steady-state creeping flow case. The dramatic effect of inertia will be discussed afterwards.

Table 3.1: *Mesh characteristics.*

Mesh	L_1	L_2	Size of smaller element	Number of elements	Number of unknowns
Mesh 1	5	20	0.04	3971	37208
Mesh 2	5	20	0.02	4641	43320
Mesh 3	5	20	0.01	5359	49864
Mesh 4	5	20	0.0045	6526	60490
Mesh 3	5	20	0.01	5359	49864
	10	20	0.01	6026	56012
	20	20	0.01	7268	67460
Mesh 3	5	10	0.01	3887	36168
	5	20	0.01	5359	49864
	5	40	0.01	6509	60564

3.4 Creeping flow

We first carried out simulations of the creeping, steady-state axisymmetric extrusion flow with no-slip along the capillary wall using the linear equation of state. The effects of mesh refinement on the centerline pressure and the position of the free surface, are illustrated in Figs. 3.3 and 3.4, respectively, where the results obtained with Meshes 1 and 3 for different compressibility numbers are compared. While the calculated centerline pressures practically coincide, the elevation of the free surface is overestimated with the coarser meshes for $B < 0.1$. This is more clearly shown in Fig. 3.5, where the extrudate-swell ratios, h_f, calculated with Meshes 1, 2 and 3 are compared. For $B > 0.1$, h_f is underestimated with the coarse meshes. Going back to Fig. 3.3, we note that the pressure increases with compressibility, which is expected, since the mass flow rate is increased. Test runs for the Poiseuille flow (i.e. with the extrudate region excluded) have shown that the method diverges at high values of B ($B \simeq 0.5$). This observation is useful, since it shows that the divergence of the method in the case of strongly compressible extrusion flow is not due to the sudden elevation of the free surface.

It is clear in Fig. 3.5 that weak compressibility leads to a small reduction of the extrudate-swell ratio, in agreement with earlier numerical studies [10, 28]. This reduction has been attributed to the compression of the extrudate downstream, given that the fluid is decompressed near the singularity at the die exit where the pressure is negative [28]. However, as compressibility increases, h_f passes through a minimum between B=0.02 and 0.03 and then increases steadily due to the increase of the mass flow rate. At high values of B, the angle of expansion increases and the elevation of the free surface is rapid (see Fig. 3.4). As already mentioned, the numerical method cannot converge for $B \simeq 0.12$. From Fig. 3.5, we conclude that the results for $B > 0.08$ should be ignored. In any case, the numerical results show

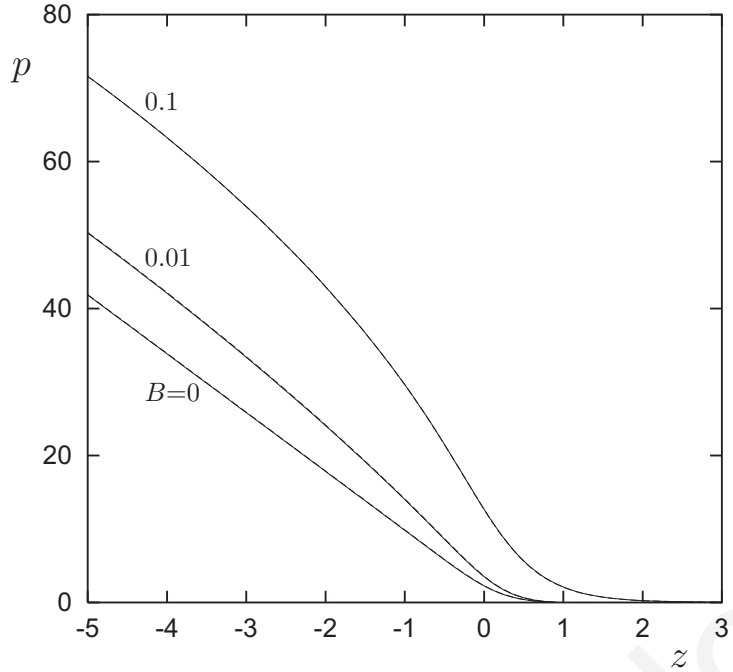

Figure 3.3: *Effect of mesh refinement on the centerline pressure in creeping axisymmetric flow with no-slip at the wall; results obtained with Meshes 1 (dashed) and 3 (solid) and* L_1*=5.*

that swelling increases considerably with compressibility, in agreement with foam extrusion experiments [4, 62, 63].

The expansion of the jet is further enhanced by increasing the capillary length, while it is reduced when slip occurs along the capillary wall. As illustrated in Fig. 3.6, the minimum of the extrudate-swell ratio is shifted to the left and higher extrudate-swell ratios are obtained when the length of the capillary, L_1, is increased, as more material is compressed. It should be noted that increasing the capillary length leads to a higher mass flow rate (since the velocity scale is the same), and therefore the mean velocity at the exit is higher. Figure 3.7 shows the effect of slip on the free surface profile for B=0.06. Swelling is reduced as slip is increased, which is consistent with experiments and theoretical studies.

Let us now look more closely at the numerical solution of strongly compressible flow. In

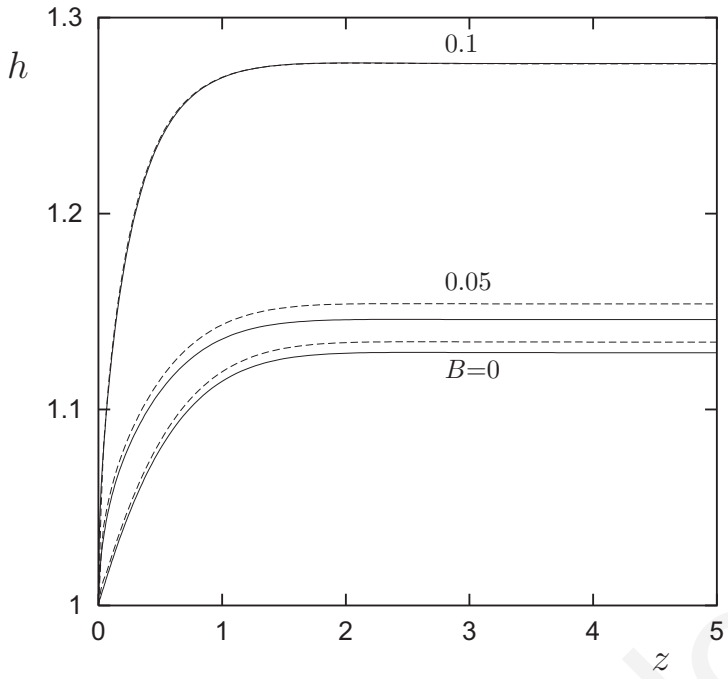

Figure 3.4: *Effect of mesh refinement on the position of the free surface in creeping axisymmetric flow with no-slip at the wall; results obtained with Meshes 1 (dashed) and 3 (solid) and* L_1*=5.*

Fig. 3.8, we see the finite element mesh, the velocity and pressure contours, and the streamlines obtained with Mesh 3 (L_1=10) for B=0.08. Two interesting observations are: (a) the free surface is almost vertical near the exit, and (b) there is a big region in the extrudate region where the pressure is negative, i.e. the density is less than the reference density. The negative pressures are swept out because of the convective nature of the flow.

The results with the exponential equation of state showed the importance of using a proper equation of state in the simulations. In Fig. 3.9, the centerline pressures from B=0 (incompressible flow) up to B=0.025, calculated with L_1=5, are plotted. The results for $B < 0.01$ are essentially the same as those obtained with the linear equation of state and shown in Fig. 3.3. For higher values of B, however, the pressure increases rapidly and the numerical method fails to converge for $B > 0.025$. In Fig. 3.10, the extrudate-swell ratios calculated

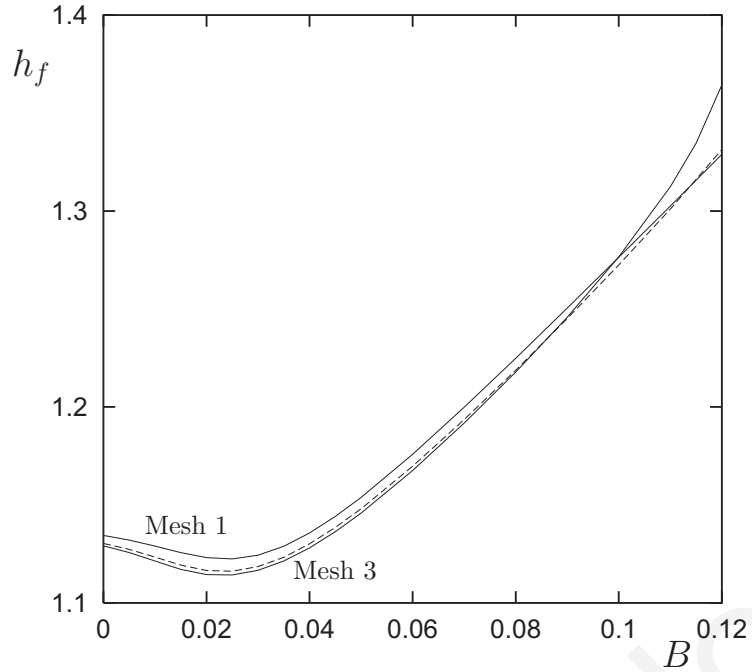

Figure 3.5: *Effect of mesh refinement on the extrudate-swell ratio in creeping axisymmetric flow with no-slip at the wall; results obtained with Meshes 1, 2 (dashed) and 3 and* L_1*=5.*

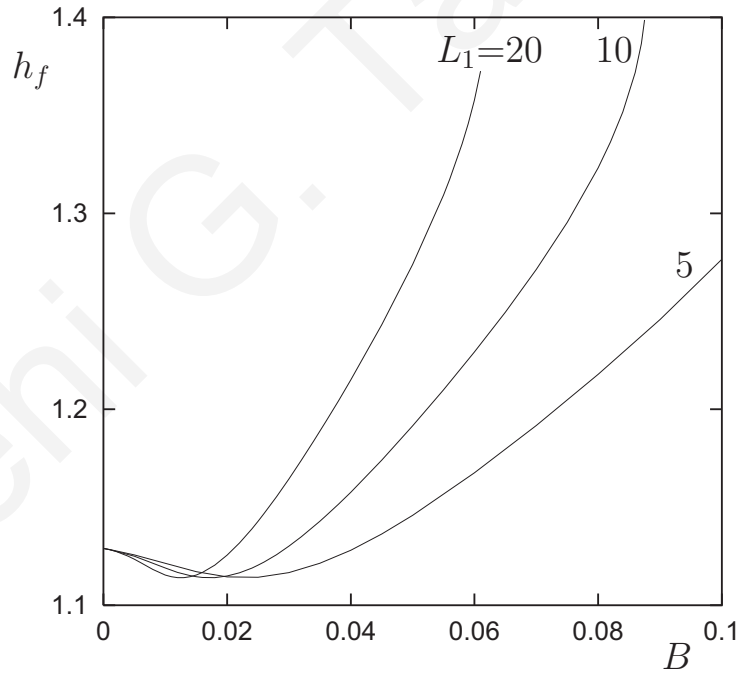

Figure 3.6: *Effect of the capillary length on the extrudate-swell ratio in creeping axisymmetric flow with no-slip at the wall.*

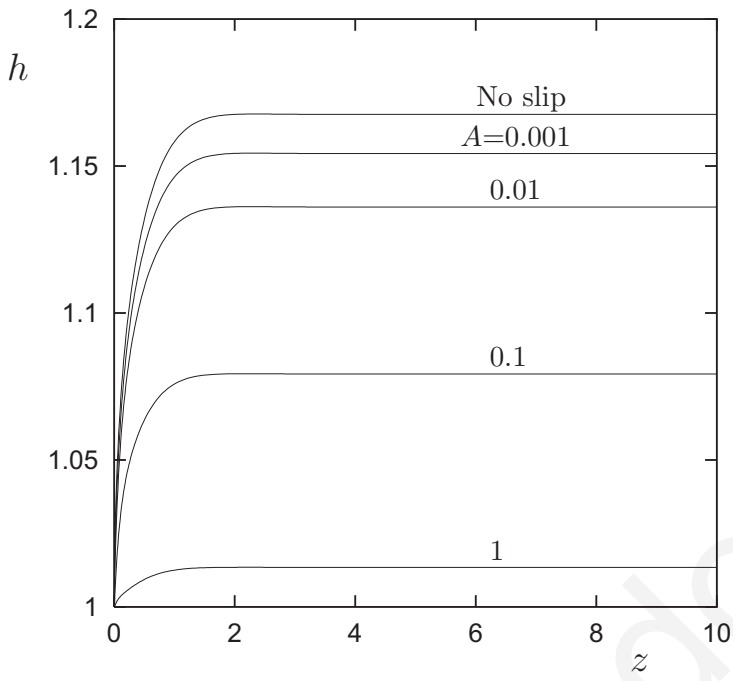

Figure 3.7: *Free surface profiles for B=0.06 and different slip numbers in creeping axisymmetric flow; Mesh 3 with L_1=5 and L_2=20.*

with the two equations of state are compared. Again, for $B < 0.01$, both equations yield essentially the same results. With the exponential equation of state, the minimum is again observed, but at a lower compressibility number. Just after the minimum, the extrudate-swell ratio increases considerably due to the dramatic increase of the pressure and, hence, the mass flow rate.

The numerical results for the planar compressible extrudate-swell flow are similar. In Fig. 3.11, we compare to their axisymmetric counterparts the extrudate swell ratios obtained with Mesh 3 and L_1=5. With the same mesh, simulations of the planar flow can be carried out for higher values of the compressibility number. Again, the extrudate swell ratio passes through a minimum, but at a higher compressibility number around B=0.05. It should be noted that for $B > 0.06$ the planar jet swells less than the axisymmetric one.

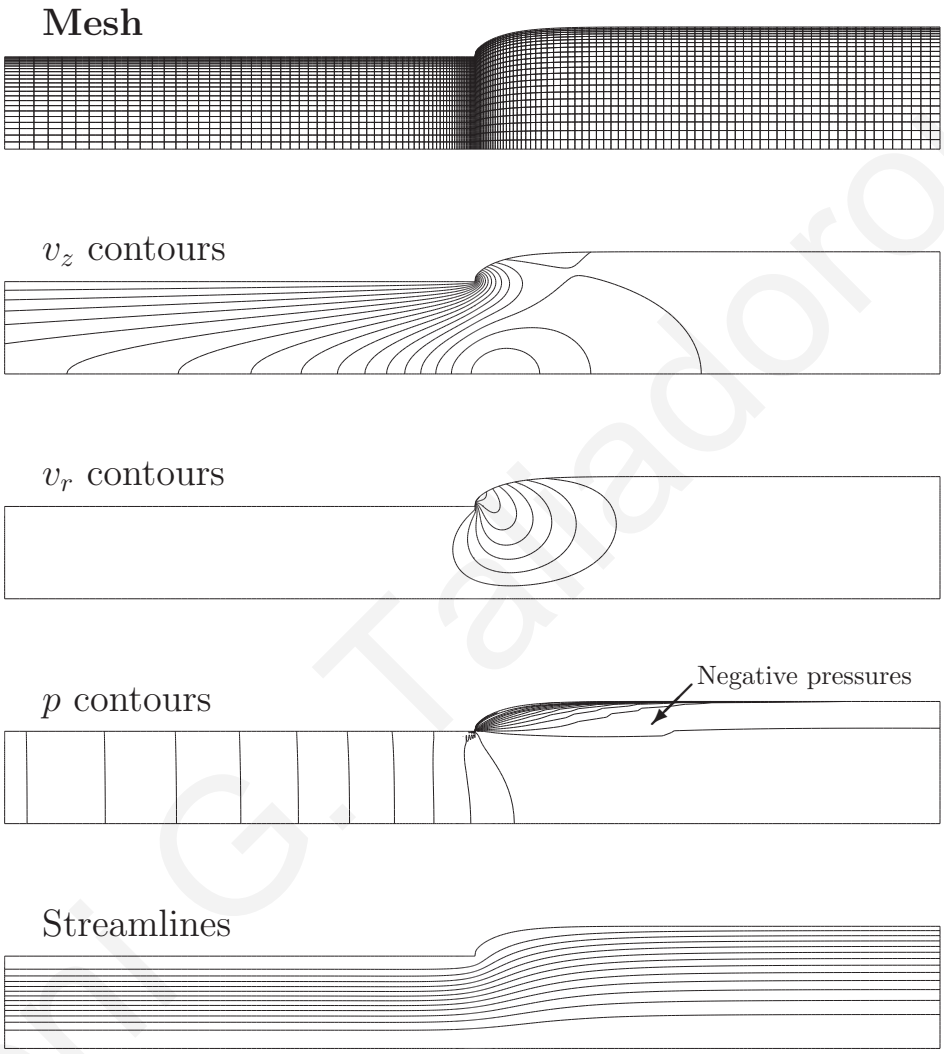

Figure 3.8: *Mesh and contours in creeping compressible axisymmetric extrudate-swell flow with no-slip at the wall; B=0.08, L_1=10 (only part of the domain is shown).*

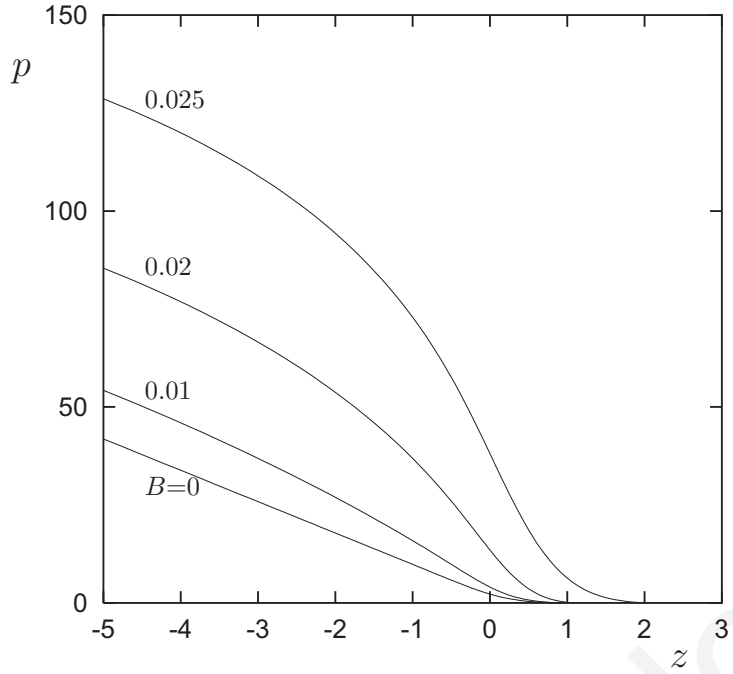

Figure 3.9: *Centerline pressures calculated with the exponential equation of state for different compressibility numbers; creeping axisymmetric flow with no slip at the wall, Mesh 3 with* L_1*=5.*

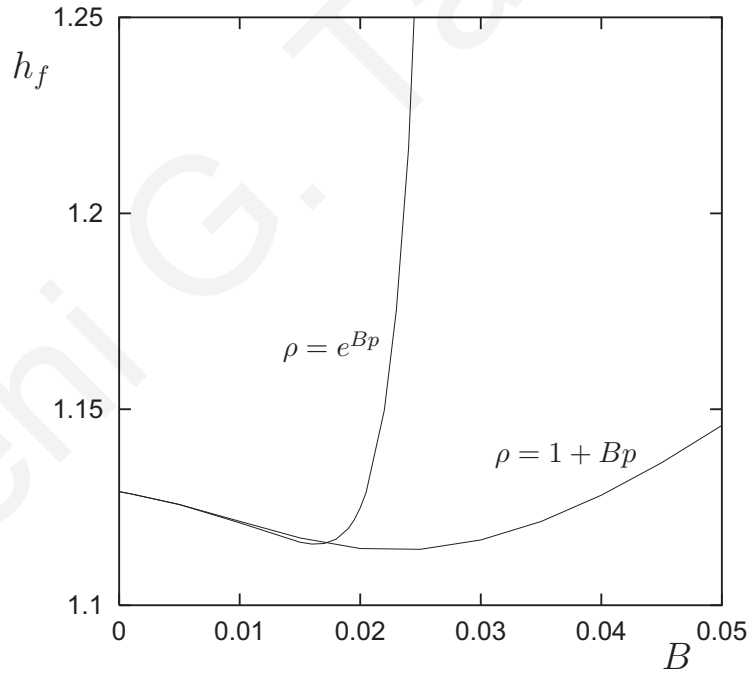

Figure 3.10: *Calculated extrudate-swell ratios with the two equations of state; creeping axisymmetric flow with no slip at the wall, Mesh 3 with* L_1*=5.*

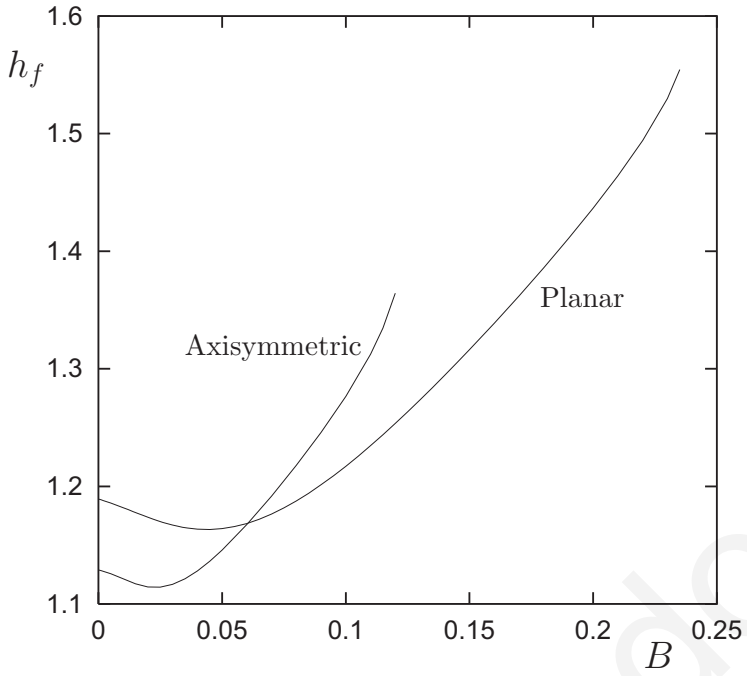

Figure 3.11: *Calculated extrudate-swell ratios for both the axisymmetric and planar extrudate-swell flows; creeping flow with no-slip at the wall, Mesh 3 with* L_1*=5.*

We have also studied the effect of compressibility on the pressure exit correction factor which gives the relative excess pressure loss above the Poiseuille fully-developed pressure loss. This is defined as follows [87]:

$$n_{ex} = \frac{\Delta P - \Delta P_0}{2\,\sigma_w} \tag{3.17}$$

where ΔP is the pressure drop between the inlet plane and the exit in the case of the extrudate swell flow, ΔP_0 is the pressure drop between the inlet plane and the exit of the capillary in the case of fully-developed Poiseuille flow, and σ_w is the wall shear stress corresponding to incompressible Poiseuille flow. In the present work, the pressure differences are taken along the centerline. The exit correction factors for both the planar and the axisymmetric flows are found to increase with compressibility, as shown in Fig. 3.12. The increase is more dramatic in the case of the axisymmetric flow. The convergence of these results has been checked

Table 3.2: *Convergence of the exit correction factor and the extrudate-swell ratio with mesh refinement.*

Mesh	Size of smaller element	Axisymmetric		Planar	
		n_{ex}	h_f	n_{ex}	h_f
Mesh 1	0.04	0.23603	1.1344	0.15139	1.1953
Mesh 2	0.02	0.23191	1.1303	0.14909	1.1908
Mesh 3	0.01	0.23021	1.1290	0.14816	1.1893
Mesh 4	0.0045	0.22855	1.1278	0.14725	1.1878

by using Meshes 1 to 4. In Table 3.2, the calculated exit correction factors for both the axisymmetric and planar incompressible flows are tabulated together with the corresponding extrudate-swell ratios. The convergence of n_{ex} with mesh refinement is illustrated in Fig. 3.13. It appears that the converged values of n_{ex} are about 0.227 for the axisymmetric jet and 0.147 for the planar one. These values, which are insensitive to the capillary length L_1 (for $L_1 > 3$), are much lower than those reported in the literature [54, 87]. However, as pointed out by Mitsoulis [54], who reported the value n_{ex}=0.235 for the axisymmetric jet, coarse meshes tend to overestimate n_{ex}, which is consistent with the present calculations. We believe that the meshes used in previous studies were rather coarse. Finally, as the meshsize is decreased the computed values of the extrudate-swell ratio (tabulated in Table 3.2) appear to approach nicely the converged values 1.1265 and 1.1863 reported by Georgiou and Boudouvis [31] for the axisymmetric and planar flows, respectively.

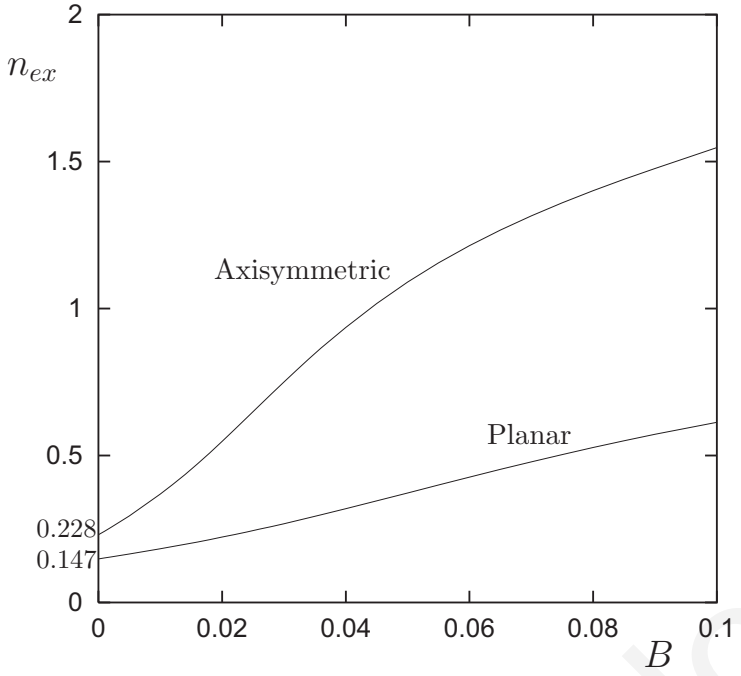

Figure 3.12: *Exit correction factors for both the axisymmetric and extrudate-swell flows versus the compressibility number; creeping flow with no-slip at the wall, Mesh 3 with* L_1*=5.*

3.5 Effect of inertia

It is well known that in the incompressible case (B=0), swelling is reduced as the Reynolds number is increased [34]. Our simulations showed that this is also the case with weakly compressible flows. At high compressibility numbers, however, the final extrudate-swell ratio increases sharply with the Reynolds number, as illustrated in Fig. 3.14, which shows results obtained with the no-slip boundary condition. In some intermediate range of compressibility numbers, the final extrudate-swell ratio appears to pass through a minimum.

The free surface profiles for nonzero Reynolds number look more exciting than the values of the final extrudate-swell ratio. In Figs. 3.15 and 3.16, the free-surface profiles for B=0.06 and B=0.08, respectively, and various Reynolds numbers are shown. We observe that the angle of expansion and the swelling increase with the Reynolds number and that the expan-

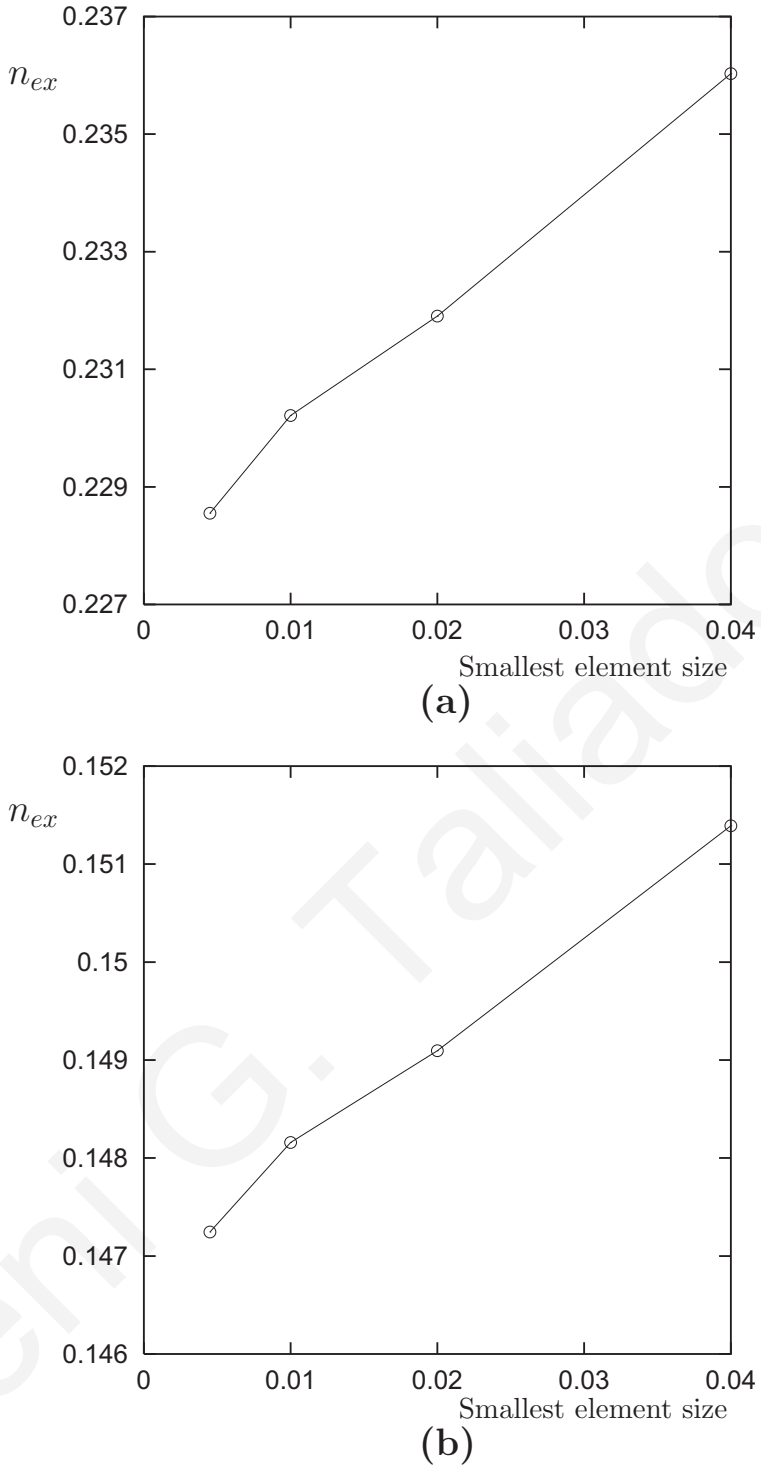

Figure 3.13: *Convergence of the exit pressure correction factor with mesh refinement: (a) Axisymmetric jet; (b) Planar jet; creeping flow with no-slip at the wall, Mesh 3 with L_1=5.*

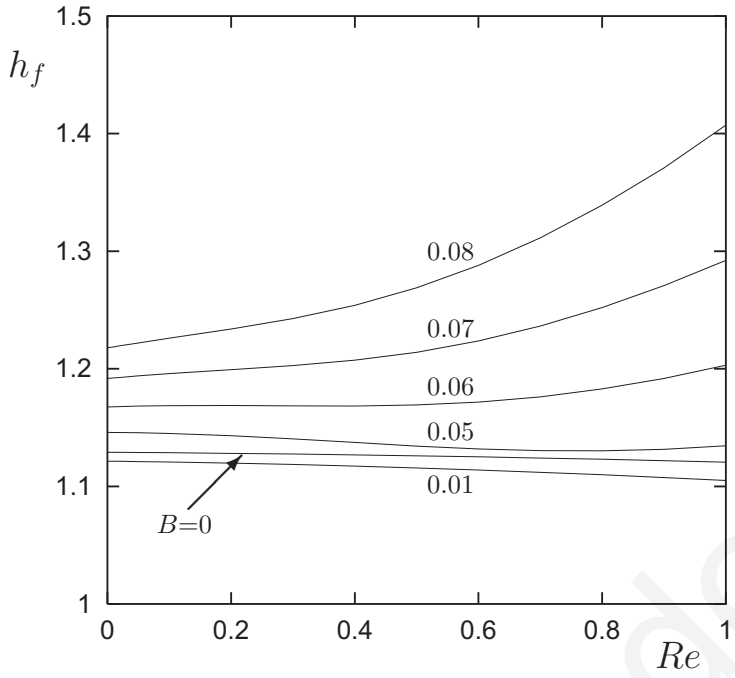

Figure 3.14: *Final extrudate-swell ratio vs Re for different compressibility numbers; axisymmetric flow with no-slip at the wall, Mesh 3 with L_1=5 and L_2=20.*

sion is followed by a weaker contraction. This behavior of the free surface agrees with the experimental observations on extruded polymer [4, 59, 60, 62], starch-based [24, 93, 97, 99] and cereal [56] foams. Therefore, the phenomenon of foam extrudate contraction can, at least partially, be attributed to the combined effect of the compressibility of the foam and inertia. As the Reynolds number is further increased, more decaying oscillations of the free surface are observed downstream. The same phenomenon is observed when the fluid is allowed to slip along the capillary wall. In Fig. 3.17, we plot the free surface profiles obtained for B=0.06, A=0.1 and various Reynolds numbers. A comparison with Fig. 15 shows again that slip reduces swelling and the amplitude of the free surface oscillations.

The effect of compressibility for a nonzero Reynolds number (Re=1) is illustrated in Fig. 3.18, where steady free surface profiles obtained with different values of B are shown. The free surface is monotonic in the incompressible case. As in the creeping flow, the angle of expansion

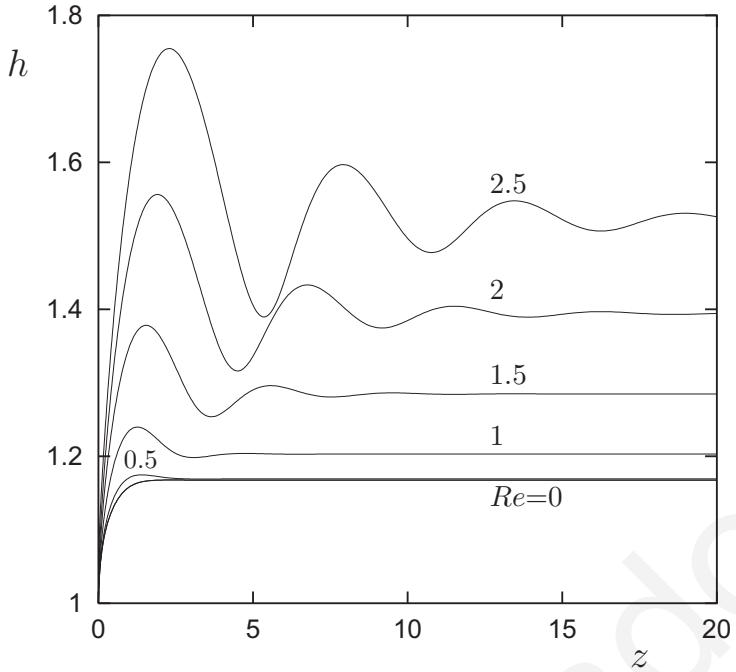

Figure 3.15: *Free surface profiles for B=0.06 and different Reynolds numbers; axisymmetric flow with no-slip at the wall, Mesh 3 with L_1=5 and L_2=20.*

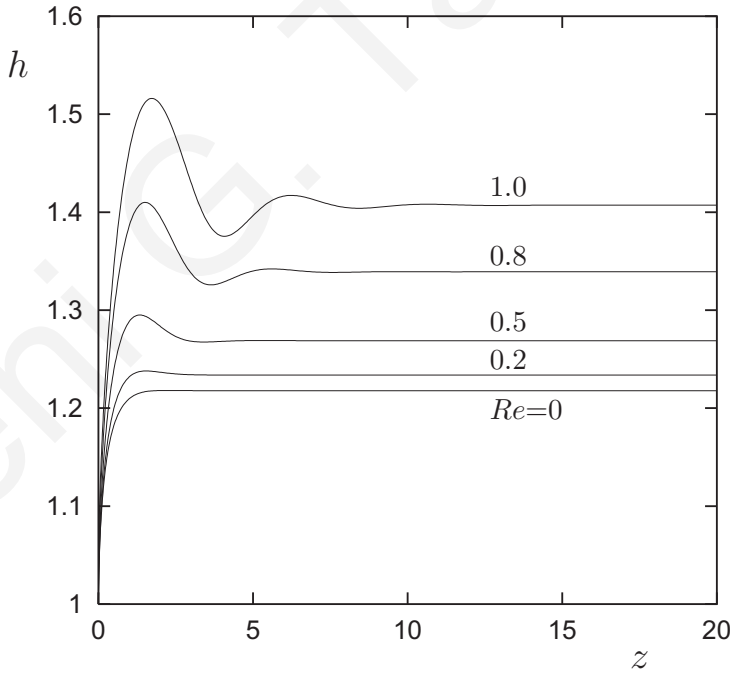

Figure 3.16: *Free surface profiles for B=0.08 and different Reynolds numbers; axisymmetric flow with no-slip at the wall, Mesh 3 with L_1=5 and L_2=20.*

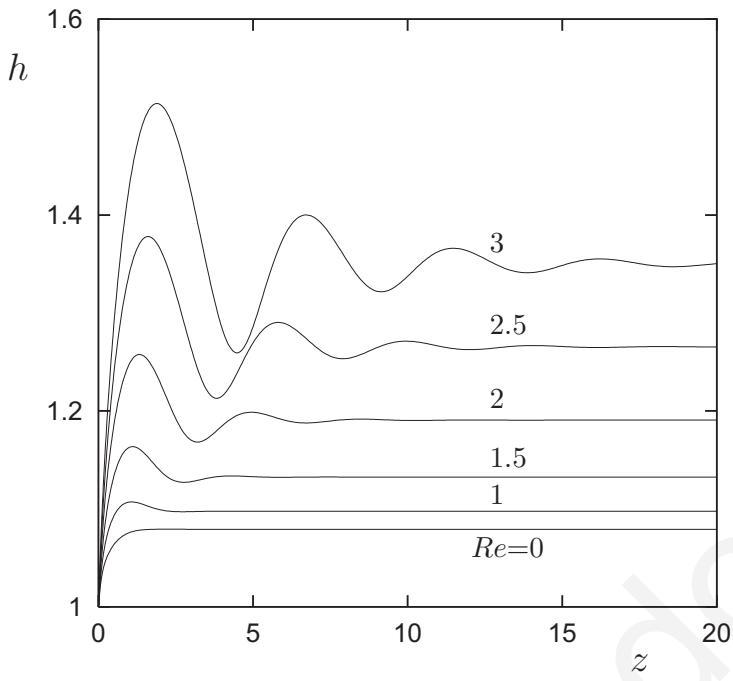

Figure 3.17: *Free surface profiles for B=0.06, A=0.1 and various Reynolds numbers; axisymmetric flow, Mesh 3 with L_1=5 and L_2=20.*

and swelling increase with B. A kink appears which grows with B. At higher compressibilities, there appear smaller decaying oscillations following the initial kink. Figure 3.19 shows the mesh and the axial velocity contours when B=0.06 and Re=2.5 (i.e. a rather extreme case). The sharp angle of expansion as well as the dense refinement of the mesh in the axial direction are clear.

Some checks have been considered in order to confirm that the calculated oscillating steady free surface profiles are not numerical artifacts. First, we verified that the solution does not depend on the length L_2 of the extrudate. Figure 3.20 shows comparisons of the free surface profiles obtained for B=0.06, various Reynolds numbers and L_2=10, 20 and 40. It is clear that the results coincide in all cases. In other words, the oscillatory nature of the steady-state solutions is not affected by the length of the extrudate.

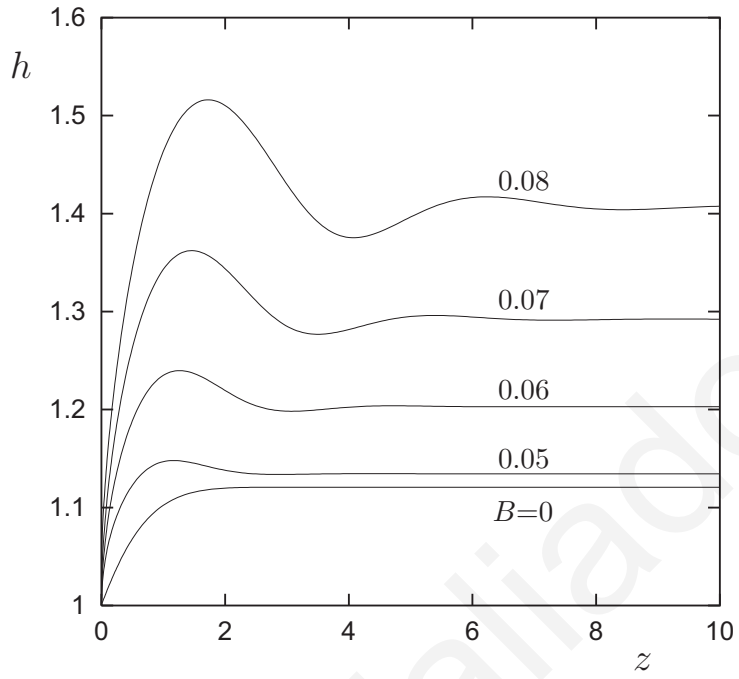

Figure 3.18: *Free surface profiles for Re=1 and different compressibility numbers; axisymmetric flow with no-slip at the wall, Mesh 3 with L_1=5 and L_2=20.*

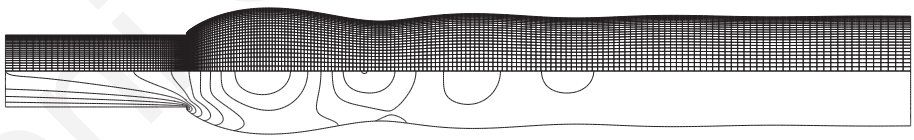

Figure 3.19: *Mesh and axial velocity contours for B=0.06 and Re=2.5; axisymmetric flow with no-slip at the wall, Mesh 3 with L_1=5 and L_2=20.*

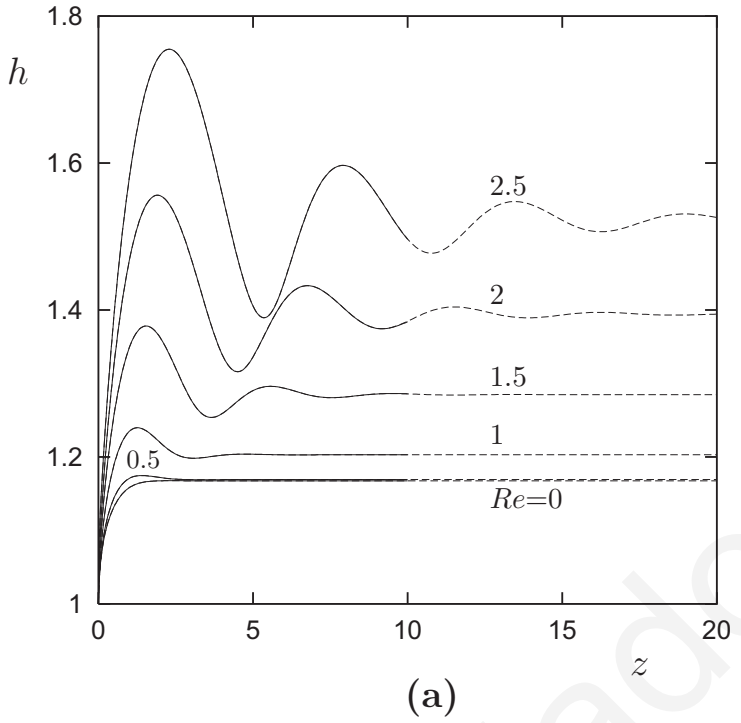

(a)

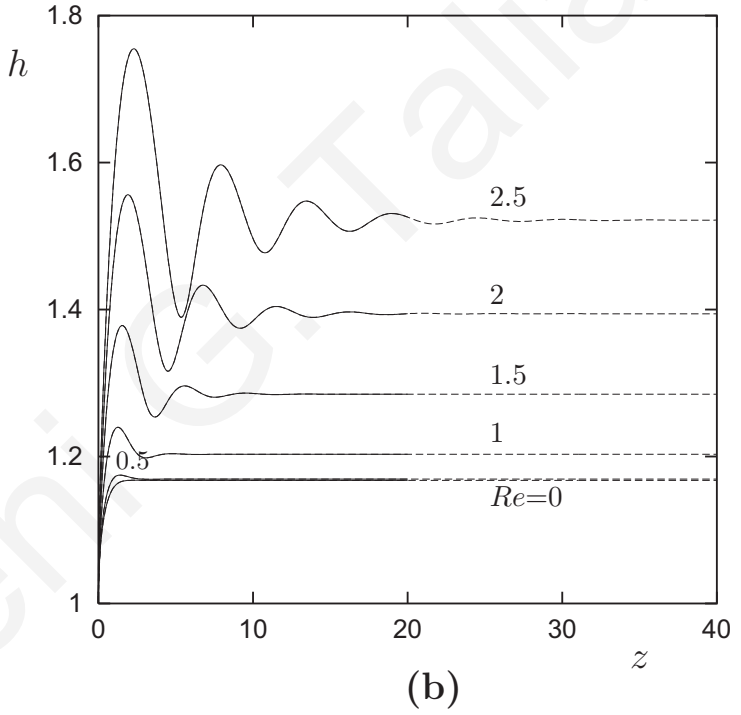

(b)

Figure 3.20: *Effect of the extrudate length on the steady free-surface profiles for B=0.06 and various Reynolds numbers: (a) Results for L_2=10 (solid) and 20 (dashed); (b) Results for L_2=20 (solid) and 40 (dashed); axisymmetric flow with no-slip at the wall, Mesh 3 with L_1=5.*

We have also checked the stability of the oscillatory steady-state solutions by means of time-dependent calculations. The steady-state solution at the volumetric flow rate Q_0=0.5 has been taken as the initial condition, and at t=0 the volumetric flow rate was set to Q=1. In all cases examined, the oscillatory steady-states have been found to be stable. A rather extreme example for B=0.06 and Re=2.5 is presented here. The free surface profiles for Q_0=0.5 and Q=1 are shown in Fig. 3.21. In Fig. 3.22, the evolution of the free surface to the new oscillatory steady state is shown. The large free surface profile overshoot, which is due to the sudden increase of the volumetric flow rate, propagates downstream and the new stable steady-state is finally reached.

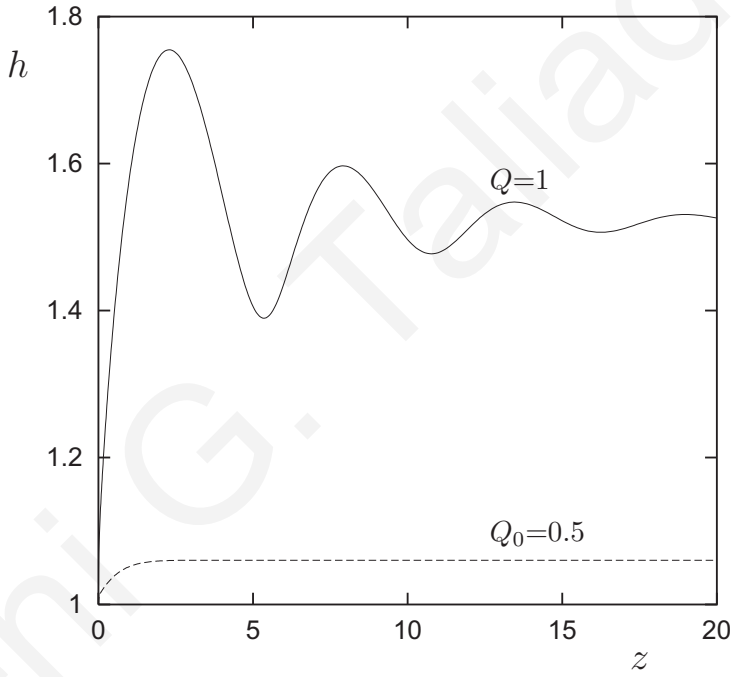

Figure 3.21: *Steady free surface profiles for B=0.06, Re=1 and Q_0=0.5 (initial condition) and Q=1 (new steady-state); axisymmetric flow with no-slip at the wall, Mesh 3 with L_1=5 and L_2=20.*

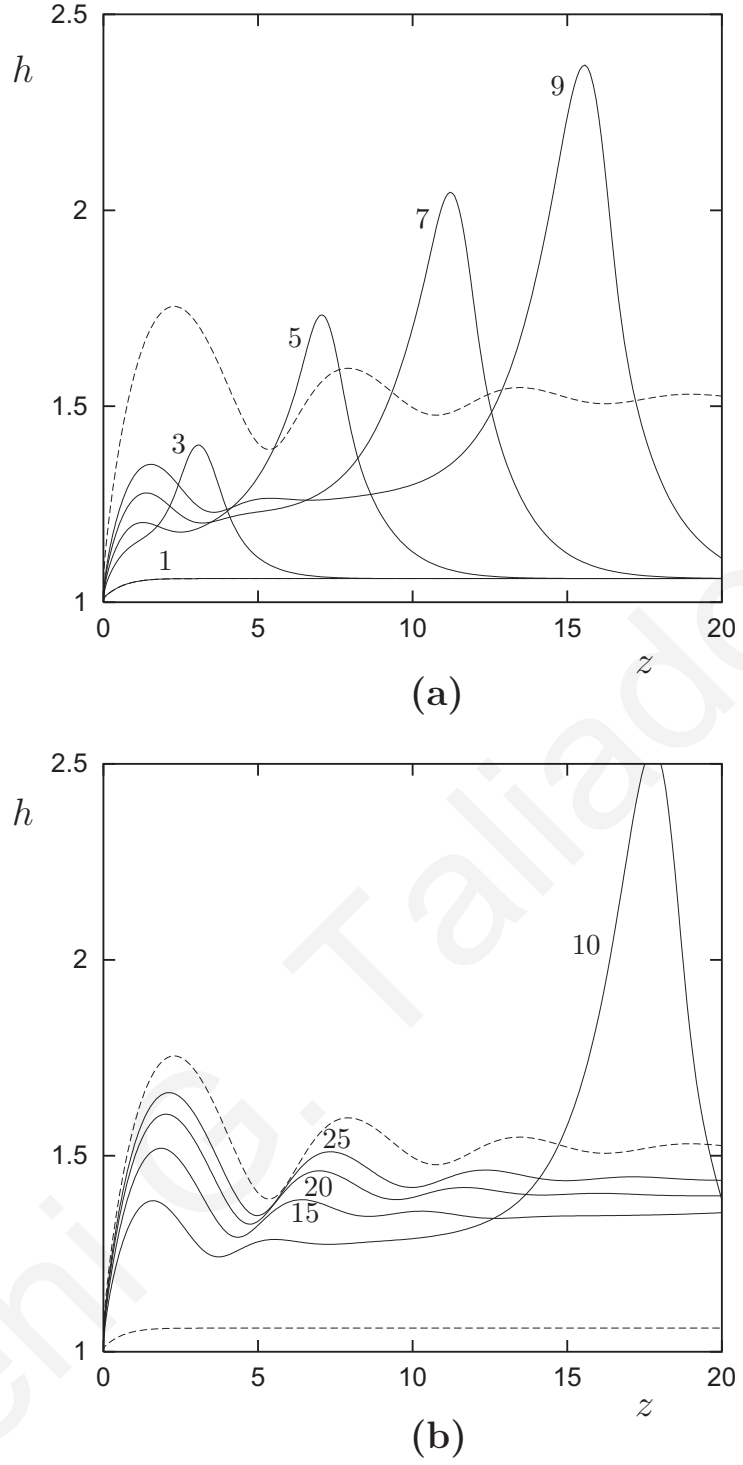

Figure 3.22: *Evolution of the free surface when perturbing the steady-state solution for B=0.06 and Re=2.5 from Q_0=0.5 to Q=1: (a) t=1, 3, 5, 7 and 9; (b) t=10, 15, 20, 25; the dashed lines show the initial and the final steady-state; axisymmetric flow with no-slip at the wall, Mesh 3 with L_1=5 and L_2=20.*

3.6 Conclusions

We have solved numerically the axisymmetric and plane extrudate-swell flows of a strongly compressible Newtonian fluid, and studied the effects of the compressibility and the equation of state, slip, geometry, and inertia on the expansion of the jet. In agreement with experimental observations [4, 62, 63], strong compressibility was found to enhance the expansion and the angle of separation of the jet. However, swelling initially decreases as compressibility is increased, which agrees with previous numerical studies [10, 28]. The expansion of the jet is further enhanced when the length of the capillary is increased, i.e. when more material is compressed. On the other hand, slip at the wall reduces swelling. The planar jet has been found to swell more than its axisymmetric counterpart only below a certain value of the compressibility number. The simulations with a linear and an exponential equation of state showed that swelling is accelerated in the latter case, which indicates the importance of using a more physically based equation of state. We are currently investigating this issue in conjuction with the use of a more realistic constitutive equation for liquid foams, such as the Herschel-Bulkley model with density-dependent parameters. Another consideration is the construction of the finite element mesh which needs to be improved in order to capture the high expansion ratios observed in foam extrusion experiments.

The numerical simulations for non-zero Reynolds number revealed that compressibility leads to a contraction of the jet after the initial expansion, a phenomenon that has been observed in extrusion experiments with polymer [4, 59, 60, 62], starch-based [24, 93, 97, 99] and cereal [56] foams. At higher Reynolds numbers, the steady-state free surface profiles become oscillatory, with the oscillations decaying downstream. These steady-state oscillatory solutions are not affected by the length of the extrudate region nor by the boundary condition along the

capillary wall (slip or no-slip). Their stability has been confirmed by means of time-dependent calculations.

Chapter 4

Perturbation solutions of Poiseuille flows of weakly compressible Newtonian liquids

4.1 Introduction

Laminar Poiseuille flows of weakly compressible fluids (i.e. flows corresponding to low Mach numbers) have been studied extensively in the past few decades due to their applications in many processes involving gas flows in long capillaries or at high speeds [88], such as gas flows in micro-electro-mechanical systems (MEMS) devices [2, 3, 12, 37], liquid flows in relatively long tubes, such as waxy crude oil transport [90] and polymer extrusion [29]. Numerical solutions of weakly compressible Poiseuille flows have been presented not only for Newtonian fluids [29, 33, 37, 38] but also for generalized Newtonian fluids, such as the Carreau fluid [29]

and the Bingham plastic [90], and viscoelastic fluids [6][1].

Perturbation and other approximate solutions have also been presented in the literature for Poiseuille flows of compressible Newtonian fluids, mostly under the assumption of ideal gas flow. Prud'homme et al. [67] employed a double perturbation expansion in terms of the radius to length ratio and the relative pressure drop to approximately solve the flow of an ideal gas in a long tube under the assumptions of purely axial flow (i.e. zero radial velocity component), no radial pressure gradient, and negligible gravity. Van den Berg et al. [8] investigated the compressible laminar Newtonian flow in a capillary using a one-dimensional perturbation analysis of radially symmetric flow and two lumped perturbation parameters which could not allow the isolation of the effects of compressibility, inertia, and bulk viscosity. The same approach has been adopted by Zohar et al. [101] to obtain a solution for subsonic gas flow through microtubes and channels with wall slip. As noted by Venerus [88], in the above studies the lubrication approximation is implicitly invoked due to the assumption of zero radial pressure gradient and the corresponding solutions are expected to be sufficiently accurate for slow flow or flow in long capillaries. Venerus [88] also pointed out that in the analyses of Prud'homme et al. [67] and van den Berg et al. [8], terms of different orders of the aspect ratio have been retained in the two components of the momentum equation, which leads to the violation of the compatibility condition for the equations of motion. Venerus [88] analyzed up to the second order the axisymmetric Poiseuille flow relaxing the lubrication approximation assumption using the streamfunction/vorticity formulation with a linear equation of state (relating the density to the pressure), and employing compressibility as the single perturbation parameter. In contrast with previous analyses, he found both a non-zero radial velocity and non-zero radial pressure gradient. Much earlier, Schwartz [75] studied the plane Poiseuille

[1]Some of the results presented in this chapter appear also in Reference [85]

flow using a fourth-order perturbation expansion in the parameter (Mach number)^2/Reynolds number. His perturbation scheme was based on the principle of slow variation, which implies that the flow properties vary slowly with distance along the channel for sufficiently small viscosity and/or mass flow rate. He also assumed that the fluid is a thermally perfect gas (i.e. the density is proportional to the pressure) and that the bulk viscosity is zero.

In the present work we derive second order perturbation solutions for both the planar and axisymmetric isothermal Poiseuille flows of weakly compressible Newtonian liquids. Following Venerus [88], a linear equation of state is employed and the isothermal compressibility is taken as the perturbation parameter. Moreover, both the shear and bulk viscosities are assumed to be constant (independent of the pressure) and the no-slip boundary condition is assumed along the wall. However, instead of using a vorticity/streamfunction formulation, only the primary unknown fields are perturbed in the present work.

The governing equations and the nondimensionalization are presented in section 4.2. The perturbation expansion method for the plane Poiseuille flow of a compressible Newtonian fluid is presented in section 4.3, where explicit analytical solutions for pressure, density, and velocity are obtained up to the second order. These agree (up to the second order) with the solution of Schwartz [75] at the exit of the channel. The derivation of the solution of the axisymmetric flow is provided in the Appendix. The results concerning the effects of compressibility, the Reynolds number, the aspect ratio, and the bulk viscosity on the velocity and pressure fields are presented and discussed in section 4.4. Finally some conclusions are drawn in section 4.5.

4.2 Governing equations

The constitutive equation of a compressible Newtonian fluid is

$$\boldsymbol{\tau} = \eta \left[\nabla \mathbf{u} + (\nabla \mathbf{u})^T\right] + \left(\kappa - \frac{2}{3}\,\eta\right) \nabla \cdot \mathbf{u}\, \mathbf{I} \tag{4.1}$$

where $\boldsymbol{\tau}$ is the viscous stress tensor, $\mathbf{u}$ is the velocity vector, $\nabla \mathbf{u}$ is the velocity gradient tensor, $\mathbf{I}$ is the unit tensor, η denotes the viscosity, and κ is the bulk (or dilatational) viscosity. In the present work, both η and κ are assumed to be constant, i.e. independent of pressure. Note that the bulk viscosity κ, which is very often neglected, is identically zero only for monoatomic gases at low density. This becomes important in polyatomic gases, in liquids containing gas bubbles [11], and in liquids in general [88].

We consider the steady, two-dimensional, planar isothermal Poiseuille flow of a weakly compressible Newtonian fluid under zero gravity and no slip at the walls, as illustrated in Fig. 4.1. Under these assumptions the continuity and the x- and y-components of the Navier-Stokes equation become:

$$\frac{\partial}{\partial x}\,(\,\rho\, u_x) \;+\; \frac{\partial}{\partial y}\,(\rho\, u_y) \;=\; 0\,, \tag{4.2}$$

$$\rho\,\left(u_x\,\frac{\partial\, u_x}{\partial\, x} \;+\; u_y\,\frac{\partial\, u_x}{\partial\, y}\right) = -\frac{\partial\, P}{\partial\, x} + \eta\,\left(\frac{\partial^2 u_x}{\partial x^2} + \frac{\partial^2 u_x}{\partial y^2}\right) + \left(\kappa + \frac{\eta}{3}\right)\left(\frac{\partial^2 u_y}{\partial x \partial y} + \frac{\partial^2 u_x}{\partial x^2}\right), \tag{4.3}$$

and

$$\rho\,\left(u_x\,\frac{\partial\, u_y}{\partial\, x} \;+\; u_y\,\frac{\partial\, u_y}{\partial\, y}\right) = -\frac{\partial\, P}{\partial\, y} \;+\eta\,\left(\frac{\partial^2 u_y}{\partial x^2} + \frac{\partial^2 u_y}{\partial y^2}\right) + \left(\kappa + \frac{\eta}{3}\right)\left(\frac{\partial^2 u_x}{\partial x \partial y} + \frac{\partial^2 u_y}{\partial y^2}\right) \tag{4.4}$$

where ρ is the fluid density, u_x and u_y are respectively the horizontal and transverse velocity components, and P is the pressure. The fluid density is assumed to obey a linear equation of state:

$$\rho \;= \rho_0[\,1 \;+\; \beta\,(P \;- P_0)], \tag{4.5}$$

where β is the isothermal compressibility,

$$\beta \equiv -\frac{1}{V_0}\left(\frac{\partial V}{\partial P}\right)_{P_0,T} \tag{4.6}$$

assumed to be constant, V is the specific volume, ρ_0 and V_0 are, respectively, the density and the specific volume at a reference pressure P_0, and T is the temperature. Taking the velocity,

$$U = \frac{\dot{M}}{\rho_0 H W}$$

where $\dot{M}$ is the mass flow rate, H is the channel width, and W is the unit length in the x-direction, as the characteristic velocity of the flow, we define the Mach number by

$$Ma \equiv \frac{U}{\sigma} \tag{4.7}$$

where

$$\sigma = \left[\gamma \left(\frac{\partial P}{\partial \rho}\right)_T\right]^{1/2} = \left(\frac{\gamma}{\beta \rho_0}\right)^{1/2} \tag{4.8}$$

is the speed of sound in the fluid, γ being the heat capacity ratio (or adiabatic index). In this work we consider subsonic flows so that $Ma \ll 1$.

To nondimensionalize the governing equations, we scale x by L, y by H, ρ by the reference density ρ_0, u_x by U, the transverse velocity u_y by UH/L, and the pressure by $3\eta LU/H^2$. The latter pressure scale is used so that the dimensionless pressure gradient along the domain, in the incompressible flow is equal to 1. For the sake of simplicity, in what follows we will use the same symbols (i.e. without stars) for all dimensionless variables. Using the above scalings, the dimensionless forms of the equation of state, the continuity equation and momentum equations become:

$$\rho = 1 + \varepsilon P\,, \tag{4.9}$$

$$\frac{\partial}{\partial x}(\rho u_x) + \frac{\partial}{\partial y}(\rho u_y) = 0\,, \tag{4.10}$$

$$\alpha\, Re\rho\, \left(u_x\, \frac{\partial\, u_x}{\partial\, x}\, +\, u_y\, \frac{\partial\, u_x}{\partial\, y}\right) = -3\frac{\partial\, P}{\partial\, x}\, + \alpha^2 \frac{\partial^2 u_x}{\partial x^2} + \frac{\partial^2 u_x}{\partial y^2} + \alpha^2\, \left(\chi + \frac{1}{3}\right)\left(\frac{\partial^2 u_y}{\partial x \partial y} + \frac{\partial^2 u_x}{\partial x^2}\right), \tag{4.11}$$

$$\alpha^3\, Re\, \rho\, \left(u_x\, \frac{\partial\, u_y}{\partial\, x}\, +\, u_y\, \frac{\partial\, u_y}{\partial\, y}\right)$$
$$= -3\frac{\partial\, P}{\partial\, y}\, + \alpha^4 \frac{\partial^2 u_y}{\partial x^2} + \alpha^2 \frac{\partial^2 u_y}{\partial y^2} + \alpha^2\, \left(\chi + \frac{1}{3}\right)\left(\frac{\partial^2 u_x}{\partial x \partial y} + \frac{\partial^2 u_y}{\partial y^2}\right), \tag{4.12}$$

where $\chi \equiv \kappa/\eta$ is the bulk-to-shear viscosity ratio, $\alpha \equiv H/L$ is the aspect ratio of the channel, and Re and ε are, respectively, the Reynolds and compressibility numbers, which are defined by

$$Re \equiv \frac{\rho_0 U H}{\eta} \tag{4.13}$$

and

$$\varepsilon \equiv \frac{3\eta\, \beta\, LU}{H^2}. \tag{4.14}$$

The Mach number takes the form

$$Ma \equiv \sqrt{\frac{\varepsilon\, \alpha\, Re}{3\, \gamma}}$$

The system of partial differential equations (4.10)-(4.12)is supplemented by appropriate boundary conditions, which are shown in Fig. 4.1. Along the wall, it is assumed that no slip occurs and the transverse velocity component vanishes (impermeable wall):

$$u_x(x,1) = u_y(x,1) = 0, \qquad 0 \leq\, x\, \leq\, 1. \tag{4.15}$$

Along the midplane, the usual symmetry conditions are employed:

$$\frac{\partial u_x}{\partial y}(x,0) = u_y(x,0) = 0, \qquad 0 \leq\, x\, \leq\, 1. \tag{4.16}$$

At the exit plane, the dimensionless mass flow rate is set at a value of 1.

$$\int_0^1 \rho\, u_x\, dy = 1. \tag{4.17}$$

Finally, the pressure is set to zero at $x = y = 1$:

$$P(1,1) = 0. \tag{4.18}$$

As in Venerus [88], no boundary conditions are specified at the inlet plane. For an interesting discussion on the inlet and outlet boundary conditions, the reader is referred to the articles of Poinsot and Lele [66] and Venerus [88].

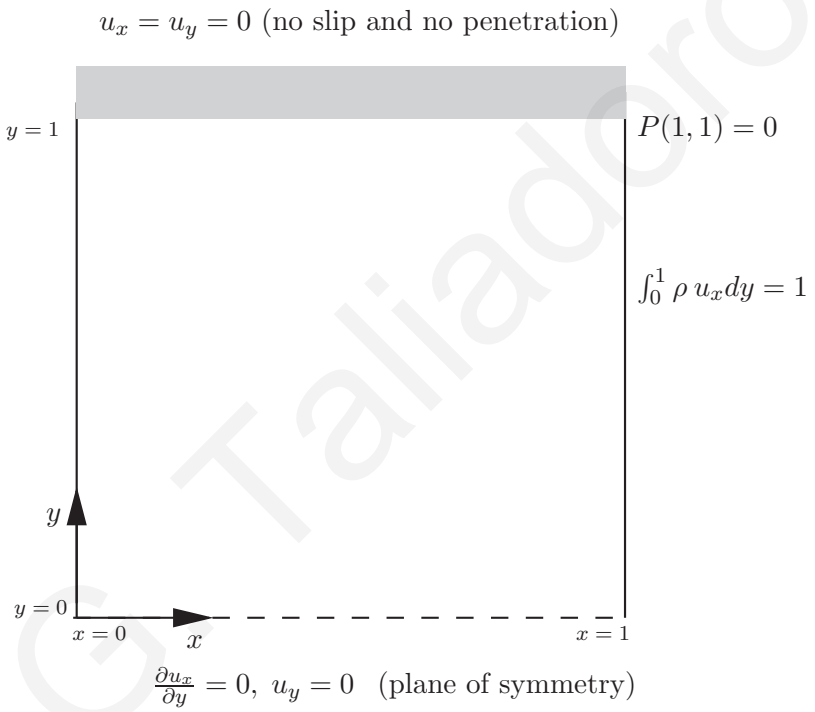

Figure 4.1: *Geometry and boundary conditions for the compressible plane Poiseuille flow (all variables are dimensionless).*

4.3 Perturbation solution

Equations (4.9)-(4.12) constitute a nonlinear system of PDEs that cannot be solved analytically. By using perturbation methods, approximate solutions of the flow can be obtained. As

already discussed, different perturbation parameters have been used in the literature. The compressibility number, ε, is chosen here as the perturbation parameter. This choice has also been made by Venerus [88] and Schwartz [75]. The latter author used the parameter (Mach number)^2/Reynolds number at x=1, which is equivalent to the compressibility number used here. Prud'homme et al. [67] employed a double perturbation expansion in terms of the aspect ratio and the relative pressure drop.

As already mentioned, perturbation is performed on all primary variables, ρ, P, u_x and u_y, using the compressibility number, ε, as the perturbation parameter:

$$\left.\begin{aligned} \rho &= \rho^{(0)} + \varepsilon\rho^{(1)} + \varepsilon^2\rho^{(2)} + O(\varepsilon^3) \\ u_y &= u_y^{(0)} + \varepsilon\, u_y^{(1)} + \varepsilon^2\, u_y^{(2)} + O(\varepsilon^3) \\ u_x &= u_x^{(0)} + \varepsilon\, u_x^{(1)} + \varepsilon^2\, u_x^{(2)} + O(\varepsilon^3) \\ P &= P^{(0)} + \varepsilon\, P^{(1)} + \varepsilon^2\, P^{(2)} + O(\varepsilon^3) \end{aligned}\right\} \tag{4.19}$$

Substituting the above expressions into the governing equations (4.9)-(4.12) and collecting terms of the same order in the perturbation parameter ε, we get a regular perturbation scheme. The solutions up to the second order are provided below. For the zero- and the first-order equations it is assumed that the transverse velocity u_y is zero throughout the domain. For the second-order equations it is assumed that $u_y = u_y(y)$ and that its second derivatives at the wall and the plane of symmetry are equal to zero.

Zero-order solution

The zero-order equations are:

$$\rho^{(0)} = 1,$$

$$\frac{\partial}{\partial x}\left[\rho^{(0)}u_x^{(0)}\right] + \frac{\partial}{\partial y}\left[\rho^{(0)}u_y^{(0)}\right] = 0,$$

$$\alpha Re\rho^{(0)}\left[u_x^{(0)}\frac{\partial u_x^{(0)}}{\partial x} + u_y^{(0)}\frac{\partial u_x^{(0)}}{\partial y}\right]$$

$$= -3\,\frac{\partial P^{(0)}}{\partial x} + \frac{\partial^2 u_x^{(0)}}{\partial y^2} + \alpha^2\,\frac{\partial^2 u_x^{(0)}}{\partial x^2} + \alpha^2\left(\chi+\frac{1}{3}\right)\left[\frac{\partial^2 u_y^{(0)}}{\partial x\partial y} + \frac{\partial^2 u_x^{(0)}}{\partial x^2}\right],$$

and

$$\alpha^3 Re\rho^{(0)}\left[u_x^{(0)}\,\frac{\partial u_y^{(0)}}{\partial x} + u_y^{(0)}\,\frac{\partial u_y^{(0)}}{\partial y}\right]$$

$$= -3\,\frac{\partial P^{(0)}}{\partial y} + \alpha^4\,\frac{\partial^2 u_y^{(0)}}{\partial x^2} + \alpha^2\,\frac{\partial^2 u_y^{(0)}}{\partial y^2} + \alpha^2\left(\chi+\frac{1}{3}\right)\left[\frac{\partial^2 u_x^{(0)}}{\partial x\partial y} + \frac{\partial^2 u_y^{(0)}}{\partial y^2}\right].$$

With the assumptions $u_y^{(0)}(x,y)$=0 and $P^{(0)}$(x=0)=1, the zero-order solution is easily obtained:

$$\rho^{(0)} = 1 \tag{4.20}$$

$$u_y^{(0)} = 0 \tag{4.21}$$

$$u_x^{(0)} = \frac{3}{2}(1 - y^2) \tag{4.22}$$

$$P^{(0)} = 1 - x \tag{4.23}$$

Obviously, the above solution is the solution of the incompressible Newtonian planar Poiseuille flow.

First-order solution

The first-order equations are:

$$\rho^{(1)} = P^{(0)}(x),$$

$$\frac{\partial}{\partial x}\left[\rho^{(0)}\,u_x^{(1)} + \rho^{(1)}\,u_x^{(0)}\right] + \frac{\partial}{\partial y}\left[\rho^{(0)}\,u_y^{(1)} + \rho^{(1)}\,u_y^{(0)}\right] = 0,$$

$$\alpha Re\rho^{(1)}\left[u_x^{(0)}\,\frac{\partial u_x^{(0)}}{\partial x} + u_y^{(0)}\,\frac{\partial u_x^{(0)}}{\partial y}\right]$$

$$+\alpha Re\rho^{(0)}\left[u_x^{(0)}\,\frac{\partial u_x^{(1)}}{\partial x} + u_x^{(1)}\,\frac{\partial u_x^{(0)}}{\partial x} + u_y^{(0)}\,\frac{\partial u_x^{(1)}}{\partial y} + u_y^{(1)}\,\frac{\partial u_x^{(0)}}{\partial y}\right]$$

$$= -3\,\frac{\partial P^{(1)}}{\partial x} + \frac{\partial^2 u_x^{(1)}}{\partial y^2} + \alpha^2\,\frac{\partial^2 u_x^{(1)}}{\partial x^2} + \alpha^2\left(\chi+\frac{1}{3}\right)\left[\frac{\partial^2 u_y^{(1)}}{\partial x\partial y} + \frac{\partial^2 u_x^{(1)}}{\partial x^2}\right],$$

and

$$\alpha^3 Re\rho^{(1)}\left[u_x^{(0)}\,\frac{\partial u_y^{(0)}}{\partial x}\;+\;u_y^{(0)}\,\frac{\partial u_y^{(0)}}{\partial y}\right]$$

$$+\,\alpha^3\,Re\,\rho^{(0)}\left[u_x^{(0)}\,\frac{\partial u_y^{(1)}}{\partial x}\;+\;u_x^{(1)}\,\frac{\partial u_y^{(0)}}{\partial x}\;+\;u_y^{(0)}\,\frac{\partial u_y^{(1)}}{\partial y}\;+\;u_y^{(1)}\,\frac{\partial u_y^{(0)}}{\partial y}\right]$$

$$=-3\,\frac{\partial P^{(1)}}{\partial y}\;+\alpha^4\;\frac{\partial^2 u_y^{(1)}}{\partial x^2}\;+\alpha^2\;\frac{\partial^2 u_y^{(1)}}{\partial y^2}\;+\;\alpha^2\,\left(\chi+\frac{1}{3}\right)\left[\frac{\partial^2 u_x^{(1)}}{\partial x\partial y}\;+\;\frac{\partial^2 u_y^{(1)}}{\partial y^2}\right].$$

Obviously, $\rho^{(1)}$=$P^{(0)}(x)$=$1-x$. Assuming that $u_y^{(1)}(x,y)$=0, we find from the continuity and the y-momentum equations that

$$u_x^{(1)}\;=\;-\frac{3}{2}\,(1-x)\,(1-y^2)\;+\;f(y)$$

and

$$P^{(1)}\;=\;\frac{1}{2}\alpha^2\,\left(\chi+\frac{1}{3}\right)(1-y^2)\;+\;g(x),$$

where $f(y)$ and $g(x)$ are unknown functions. Substituting into the x-momentum equation and separating variables we get

$$\frac{9}{4}\alpha\,Re\,(1-y^2)^2\;-f''(y)=-3\frac{\partial\,P^{(1)}}{\partial\,x}+3(1-x)=c$$

where c is a constant to be determined. Integrating the resulting ODEs and applying the boundary conditions $f'(0)$=$f(1)$=0 and $\int_0^1 f(y)dy$=0 for $u_x^{(1)}(x,y)$ and $P^{(1)}(1,1)$=0 for $P(x,y)$ we find that c=$54/35\alpha Re$ and the functions $g(x)$ and $f(y)$. The first-order solution reads:

$$\rho^{(1)}\;=\;1-x \tag{4.24}$$

$$u_y^{(1)}\;=\;0 \tag{4.25}$$

$$u_x^{(1)}\;=\;-\frac{3}{2}(1-x)(1-y^2)\;+\;\frac{3}{280}\alpha\,Re(1-y^2)(-5+28y^2-7y^4) \tag{4.26}$$

$$P^{(1)}\;=\;\frac{1}{2}\alpha^2\,\left(\chi+\frac{1}{3}\right)(1-y^2)-\frac{1}{2}(1-x)^2\;+\;\frac{18}{35}\alpha\,Re\,(1-x). \tag{4.27}$$

We observe that the first-order pressure is a function of both x and y. It should also be noted that the assumption of zero, first-order transverse velocity is made implicitly in the analysis of Venerus [88] for the axisymmetric flow, since simple functional forms for the first-order vorticity and streamfunction are assumed instead.

Second-order solution

The equations governing the second-order solution are:

$$\rho^{(2)} \;=\; P^{(1)}(x,y),$$

$$\frac{\partial}{\partial x}\left[\rho^{(0)}u_x^{(2)} \;+\; \rho^{(1)}u_x^{(1)} \;+\; \rho^{(2)}u_x^{(0)}\right] \;+\; \frac{\partial}{\partial y}\left[\rho^{(0)}u_y^{(2)} \;+\; \rho^{(1)}u_y^{(1)} \;+\; \rho^{(2)}u_y^{(0)}\right] \;=\; 0,$$

$$\begin{aligned}
&\alpha Re\rho^{(2)}\left[u_x^{(0)}\,\frac{\partial u_x^{(0)}}{\partial x} \;+\; u_y^{(0)}\,\frac{\partial u_x^{(0)}}{\partial y}\right]\\
&+\alpha Re\rho^{(1)}\left[u_x^{(0)}\,\frac{\partial u_x^{(1)}}{\partial x} \;+\; u_x^{(1)}\,\frac{\partial u_x^{(0)}}{\partial x} \;+\; u_y^{(0)}\,\frac{\partial u_x^{(1)}}{\partial y} \;+\; u_y^{(1)}\,\frac{\partial u_x^{(0)}}{\partial y}\right]\\
&+\alpha\,Re\,\rho^{(0)}\left[u_x^{(0)}\,\frac{\partial u_x^{(2)}}{\partial x} \;+\; u_x^{(1)}\,\frac{\partial u_x^{(1)}}{\partial x} \;+\; u_x^{(2)}\,\frac{\partial u_x^{(0)}}{\partial x} + u_y^{(0)}\,\frac{\partial u_x^{(2)}}{\partial y} \;+\; u_y^{(1)}\,\frac{\partial u_x^{(1)}}{\partial y} \;+\; u_y^{(2)}\,\frac{\partial u_x^{(0)}}{\partial y}\right]\\
&\qquad\qquad = \;-3\,\frac{\partial P^{(2)}}{\partial x} \;+\frac{\partial^2 u_x^{(2)}}{\partial y^2}+\;\alpha^2\,\frac{\partial^2 u_x^{(2)}}{\partial x^2}+\;\alpha^2\,\left(\chi+\frac{1}{3}\right)\,\left[\frac{\partial^2 u_y^{(2)}}{\partial x\partial y} \;+\; \frac{\partial^2 u_x^{(2)}}{\partial x^2}\right],
\end{aligned}$$

and

$$\begin{aligned}
&\alpha^3 Re\rho^{(2)}\left[u_x^{(0)}\,\frac{\partial u_y^{(0)}}{\partial x} \;+\; u_y^{(0)}\,\frac{\partial u_y^{(0)}}{\partial y}\right]\\
&+\alpha^3\,Re\,\rho^{(1)}\left[u_x^{(0)}\,\frac{\partial u_y^{(1)}}{\partial x} \;+\; u_x^{(1)}\,\frac{\partial u_y^{(0)}}{\partial x} \;+\; u_y^{(0)}\,\frac{\partial u_y^{(1)}}{\partial y} \;+\; u_y^{(1)}\,\frac{\partial u_y^{(0)}}{\partial y}\right]\\
&+\alpha^3\,Re\,\rho^{(0)}\left[u_x^{(0)}\,\frac{\partial u_y^{(2)}}{\partial x} \;+\; u_x^{(1)}\,\frac{\partial u_y^{(1)}}{\partial x} \;+\; u_x^{(2)}\,\frac{\partial u_y^{(0)}}{\partial x} \;+\; u_y^{(0)}\,\frac{\partial u_y^{(2)}}{\partial y} \;+\; u_y^{(1)}\,\frac{\partial u_y^{(1)}}{\partial y} \;+\; u_y^{(2)}\,\frac{\partial u_y^{(0)}}{\partial y}\right]\\
&\qquad\qquad = \;-3\,\frac{\partial P^{(2)}}{\partial y} \;+\alpha^2\,\frac{\partial^2 u_y^{(2)}}{\partial y^2} \;+\alpha^4\,\frac{\partial^2 u_y^{(2)}}{\partial x^2} \;+\; \alpha^2\,\left(\chi+\frac{1}{3}\right)\,\left[\frac{\partial^2 u_x^{(2)}}{\partial x\partial y}+\frac{\partial^2 u_y^{(2)}}{\partial y^2}\right].
\end{aligned}$$

For $\rho^{(2)}$ we simply have:

$$\rho^{(2)} \;=\; P^{(1)}(x,y) = \frac{1}{2}\alpha^2\,\left(\chi+\frac{1}{3}\right)(1-y^2) - \frac{1}{2}(1-x)^2 \;+\; \frac{18}{35}\alpha\,Re\,(1-x). \tag{4.28}$$

At this point the assumption of zero transverse velocity is relaxed, letting u_y to be a function of y, $u_y^{(2)}$=$u_y^{(2)}(y)$. Note again that in the analysis of Venerus [88] for the axisymmetric flow, the simplest expressions for the second-order vorticity and streamfunction are postulated instead. From the continuity and y-momentum equations we respectively get:

$$\begin{aligned} u_x^{(2)} &= \frac{9}{4}(1-x)^2(1-y^2) - \frac{3}{4}\alpha^2\left(\chi+\frac{1}{3}\right)(1-y^2)^2 \\ &\quad -\frac{3}{280}\alpha\, Re(1-x)(1-y^2)(67+28y^2-7y^4) + \frac{\partial u_y^{(2)}}{\partial y}(1-x) + F(y) \end{aligned} \tag{4.29}$$

and

$$\begin{aligned} P^{(2)} &= \frac{1}{3}\alpha^2\frac{\partial u_y^{(2)}}{\partial y} - \frac{3}{2}\alpha^2\left(\chi+\frac{1}{3}\right)(1-x)(1-y^2) \\ &\quad +\frac{1}{280}\alpha^3 Re\left(\chi+\frac{1}{3}\right)(1-y^2)(67+28y^2-7y^4) + G(x), \end{aligned} \tag{4.30}$$

where $F(y)$ and $G(x)$ are functions to be determined. Combining Eqs. (4.28)-(4.30) and the x-momentum equation leads to:

$$\begin{aligned} &\alpha\, Re\left[-3yu_y^{(2)} - \frac{3}{2}(1-y^2)\frac{\partial u_y^{(2)}}{\partial y} - \frac{27}{4}(1-x)(1-y^2)^2\right. \\ &\qquad\left. +\frac{9}{560}\alpha\, Re(1-y^2)^2(62+56y^2-14y^4)\right] \\ &= -3G'(x) - \frac{9}{2}(1-x)^2 + \frac{\partial^3 u_y^{(2)}}{\partial y^3}(1-x) + F''(y) - \frac{3}{280}\alpha Re(1-x)(-78-420y^2+210y^4) \\ &\qquad + \frac{9}{2}\alpha^2(1-y^2) + 3\alpha^2\left(\chi+\frac{1}{3}\right)(1-3y^2). \end{aligned} \tag{4.31}$$

Here, it is assumed that the terms involving both $(1-x)$ and y must be equal to a (scalar) multiple of $(1-x)$. Thus we can assume that

$$\frac{27}{4}\alpha\, Re(1-y^2)^2 + \frac{\partial^3 u_y^{(2)}}{\partial y^3} - \frac{3}{280}\alpha\, Re(-78-420y^2+210y^4) = \alpha\, Re\gamma. \tag{4.32}$$

where γ is new constant to be determined. Solving the above equation with the conditions $u_y^{(2)}(0)$=$u_y^{(2)}(1)$=0 and $\partial u_y^{(2)}/\partial y(1)$=$\partial^2 u_y^{(2)}/\partial y^2(0)$=0 yields γ=216/35 and the second-order

transverse velocity:

$$u_y^{(2)} = \frac{3}{140}\alpha\, Re\, y\,(1-y^2)^2(5-y^2). \tag{4.33}$$

Separating variables in Eq. (4.31) gives the following ODEs for $F(y)$ and $G(x)$:

$$\alpha Re\left[-3yu_y^{(2)} - \frac{3}{2}(1-y^2)\frac{\partial u_y^{(2)}}{\partial y} + \frac{9}{560}\alpha\, Re(1-y^2)^2(62+56y^2-14y^4)\right]$$
$$-F''(y) - \frac{9}{2}\alpha^2\,(1-y^2) - 3\alpha^2\left(\chi+\frac{1}{3}\right)(1-3y^2) = A \tag{4.34}$$

and

$$-3G'(x) - \frac{9}{2}(1-x)^2 + \alpha\, Re\,\gamma\,(1-x) \;=\; A. \tag{4.35}$$

where A is another constant to be determined. Integrating Eq. (4.34) and applying the conditions $F'(0)$=$F(1)$=0 and $\int_0^1 F(y)dy$=0 we find that

$$\begin{aligned} F(y) \;&=\; \alpha^2\left(\chi+\frac{1}{3}\right)\left(\frac{3}{20}-\frac{9}{10}y^2+\frac{3}{4}y^4\right) + \alpha^2\left(\frac{3}{40}-\frac{9}{20}y^2+\frac{9}{24}y^4\right) \\ &\quad -\frac{3}{431200}\alpha^2 Re^2(2193-11356y^2+2310y^4+12012y^6-5775y^8+616y^{10}) \end{aligned} \tag{4.36}$$

and

$$A \;=\; -\frac{18\alpha^2}{5} - \frac{6}{5}\alpha^2\left(\chi+\frac{1}{3}\right) + \frac{9132}{13475}\alpha^2\, Re^2. \tag{4.37}$$

Integrating now Eq. (4.35) and substituting A under the condition $P^{(2)}(1,1)$=0 we obtain

$$G(x) = \frac{1}{2}(1-x)^3 - \frac{6}{5}\alpha^2(1-x) - \frac{36}{35}\alpha\, Re(1-x)^2 + \frac{3044}{13475}\alpha^2 Re^2(1-x) - \frac{2}{5}\alpha^2\left(\chi+\frac{1}{3}\right)(1-x) \tag{4.38}$$

Thus, the second order solution reads:

$$\rho^{(2)} \;=\; \frac{1}{2}\alpha^2\,\left(\chi+\frac{1}{3}\right)(1-y^2) - \frac{1}{2}(1-x)^2 \;+\; \frac{18}{35}\alpha\, Re\,(1-x) \tag{4.39}$$

$$u_y^{(2)} \;=\; \frac{3}{140}\alpha\, Re\, y\,(1-y^2)^2(5-y^2) \tag{4.40}$$

$$\begin{aligned} u_x^{(2)} \;&=\; (1-y^2)\left[\frac{9}{4}(1-x)^2 - \frac{3}{280}\alpha\, Re\,(57+84y^2-21y^4)(1-x)\right. \\ &\quad \left. +\frac{3}{40}\alpha^2(1-5y^2) \;-\; \frac{3}{5}\alpha^2\left(\chi+\frac{1}{3}\right)\right. \end{aligned}$$

$$-\frac{3}{431200}\alpha^2\, Re^2(2193-9163y^2-6853y^4+5159y^6-616y^8)\Big] \quad (4.41)$$

$$\begin{aligned} P^{(2)} &= \frac{1}{2}(1-x)^3-\frac{6}{5}\alpha^2(1-x)-\frac{36}{35}\alpha\, Re(1-x)^2+\frac{3044}{13475}\alpha^2Re^2(1-x) \\ &\quad -\frac{1}{10}\alpha^2\left(\chi+\frac{1}{3}\right)(19-15y^2)(1-x) \\ &\quad +\frac{1}{280}\alpha^3Re(1-y^2)\left[2(5-28y^2+7y^4)+\left(\chi+\frac{1}{3}\right)(67+28y^2-7y^4)\right] \quad (4.42) \end{aligned}$$

Summarizing the results, the solution of the flow problem up to the second order is as follows:

$$\begin{aligned} \rho &= 1+\varepsilon(1-x)+\varepsilon^2\left[\frac{1}{2}\alpha^2\left(\chi+\frac{1}{3}\right)(1-y^2)-\frac{1}{2}(1-x)^2+\frac{18}{35}\alpha\, Re\,(1-x)\right] \\ &\quad +O(\varepsilon^3) \quad (4.43) \end{aligned}$$

$$u_y = \frac{3}{140}\varepsilon^2\alpha\, Re\, y\,(1-y^2)^2(5-y^2)+O(\varepsilon^3) \quad (4.44)$$

$$\begin{aligned} u_x &= \frac{3}{2}(1-y^2)\Big[1-\varepsilon(1-x)+\frac{1}{140}\varepsilon\alpha\, Re(-5+28y^2-7y^4)+\frac{3}{2}\varepsilon^2(1-x)^2 \\ &\quad -\frac{1}{140}\varepsilon^2\alpha\, Re(57+84y^2-21y^4)(1-x)+\frac{1}{20}\varepsilon^2\alpha^2(1-5y^2)-\frac{2}{5}\varepsilon^2\alpha^2\left(\chi+\frac{1}{3}\right) \\ &\quad -\frac{1}{215600}\varepsilon^2\alpha^2\, Re^2(2193-9163y^2-6853y^4+5159y^6-616y^8)\Big]+O(\varepsilon^3) \quad (4.45) \end{aligned}$$

$$\begin{aligned} P &= 1-x+\frac{1}{2}\varepsilon\alpha^2\left(\chi+\frac{1}{3}\right)(1-y^2)-\frac{1}{2}\varepsilon(1-x)^2+\frac{18}{35}\varepsilon\alpha\, Re\,(1-x)+\frac{1}{2}\varepsilon^2(1-x)^3 \\ &\quad -\frac{6}{5}\varepsilon^2\alpha^2(1-x)-\frac{36}{35}\varepsilon^2\alpha\, Re(1-x)^2+\frac{3044}{13475}\varepsilon^2\alpha^2Re^2(1-x) \\ &\quad -\frac{1}{10}\varepsilon^2\alpha^2\left(\chi+\frac{1}{3}\right)(19-15y^2)(1-x) \\ &\quad +\frac{1}{280}\varepsilon^2\,\alpha^3Re(1-y^2)\left[2(5-28y^2+7y^4)+\left(\chi+\frac{1}{3}\right)(67+28y^2-7y^4)\right] \\ &\quad +O(\varepsilon^3). \quad (4.46) \end{aligned}$$

The perturbation solution for the axisymmetric flow has been also derived and is provided in the Appendix B. This is the same as the solution reported by Venerus [88] who used a vorticity/streamfunction formulation instead of working with the primary flow variables.

The basic features of the velocity and pressure fields given in Eqs. (4.43)-(4.46) are the following:

(a) The transverse velocity, u_y, which depends only on the y coordinate, is zero at first order in ε (by assumption). At second order in ε, u_y is always positive, varies linearly with the aspect ratio and the Reynolds number, and is independent of the bulk viscosity.

(b) The horizontal velocity, u_x, deviates from the parabolic incompressible solution at first order in ε due to fluid inertia. At second order in ε, there is a reduction of the horizontal velocity that is independent of inertia and enhanced by the bulk viscosity, which does not alter its parabolicity.

(c) The pressure is a function of both x and y. The y-dependence at first order in ε becomes stronger as α^2 is increased (i.e. in short channels). It also increases with the bulk viscosity. (It should be noted that there is y-dependence even when the bulk viscosity vanishes). At second order in ε, the y-dependence of P is due not only to α and the bulk viscosity but also to inertia.

(d) The density is a decreasing function of both x and y. This is expected since the fluid is decompressed as it moves downstream and the density takes is lowest value at x=y=1. At the exit of the channel (x=1), for example,

$$\rho = 1 + \frac{1}{2}\varepsilon^2\,\alpha^2\,\left(\chi + \frac{1}{3}\right)(1-y^2).$$

Since at the exit of the channel only very small variations of ρ can be acceptable, it must be $\varepsilon\alpha \ll 1$.

In the compressible flow under study, the volumetric flow rate is an increasing function of x:

$$Q(x) \;=\; \int_0^1 u_x(x,y)\,dy \qquad \Longrightarrow$$

$$Q(x) = 1 - \varepsilon(1-x) + \frac{1}{70}\varepsilon^2\left[-28\alpha^2\,\left(\chi + \frac{1}{3}\right) - 36\,\alpha\,Re\,(1-x) \;+\; 105\,(1-x)^2\right] \;+\; O(\varepsilon^3). \tag{4.47}$$

In the special case $\alpha \ll 1$, one gets $Q(0) = 1 - \varepsilon + 3\,\varepsilon^2/2$ which is a parabola with a minimum at $\varepsilon^* = 1/3$. Since increasing ε leads to more compression, i.e. to a lower value at $Q(0)$, the perturbation solution is valid for $\varepsilon < 1/3$. The same conclusion is reached for the axisymmetric flow (see Appendix B) for which Venerus [88] reported that the compressibility parameter is limited to values $\varepsilon \leq 0.25$.

The present results agree up to the second order with the third-order results of Schwartz [75] at x=1 when x=1, χ=0 and α=3. It is interesting to note that employing the lubrication approximation would have led to the following simplified solution [33]

$$\left.\begin{aligned} \rho &= 1 + \varepsilon\, P \\ u_y &= 0 \\ u_x &= \tfrac{3}{2}\frac{(1-y^2)}{\sqrt{1+2\,\varepsilon\,(1-x)}} \\ P &= \frac{-1+\sqrt{1+2\,\varepsilon\,(1-x)}}{\varepsilon} \end{aligned}\right\} \tag{4.48}$$

Expanding the expressions of u_x and P as power series to second order in ε leads to the approximate solution

$$\left.\begin{aligned} \rho &= 1 + \varepsilon\,(1-x) - \tfrac{1}{2}\,\varepsilon^2\,(1-x)^2 + O(\varepsilon^3) \\ u_y &= 0 \\ u_x &= \tfrac{3}{2}(1-y^2)\left[1 - \varepsilon\,(1-x) + \tfrac{3}{2}\,\varepsilon^2\,(1-x)^2\right] + O(\varepsilon^3) \\ P &= 1 - x - \tfrac{1}{2}\,\varepsilon\,(1-x)^2 + \tfrac{1}{2}\,\varepsilon^2\,(1-x)^3 + O(\varepsilon^3) \end{aligned}\right\} \tag{4.49}$$

which involves only the compressibility parameter ε and agrees with the perturbation solution for $\alpha \ll 1$ and $Re \ll 1$.

The streamfunction, $\psi(x, y)$, defined by

$$\frac{\partial \psi}{\partial x} \equiv \rho u_y \quad \text{and} \quad \frac{\partial \psi}{\partial y} \equiv -\rho u_x \tag{4.50}$$

is found to be

$$\begin{aligned}\psi(x,y) &= \frac{1}{2}\,y\,\left(3-y^2\right)-\frac{3}{280}\varepsilon\,\alpha\,Re\,y(1-y^2)^2(5-y^2)\\ &\quad+\varepsilon^2\left[\frac{3}{40}\,\alpha^2\,y\,(1-y^2)^2+\frac{3}{20}\,\alpha^2(\,\chi+\frac{1}{3})\,y\,(1-y^2)^2\right.\\ &\quad+\frac{3}{140}\,\alpha\,Re\,y\,(1-y^2)^2(5-y^2)(1-x)\\ &\quad\left.+\frac{9}{431200}\alpha^2Re^2y(1-y^2)^2(-6579-1802y^2+1589y^4-168y^6)\right]\\ &\quad+O(\varepsilon^3). \end{aligned} \tag{4.51}$$

4.4 Results and discussion

The effects of all parameters involved in the solution, i.e. the compressibility number, ε, the aspect ratio, α, the Reynolds number, Re and the bulk viscosity, χ, have been studied. Mostly results for the planar compressible Poiseuille flow will be presented in this section, since the perturbation solution for the axisymmetric flow (Appendix) is that obtained by Venerus [88].

The effects of the Reynolds number and compressibility on the two velocity components are illustrated in Figs. 4.2 and 4.3, respectively. The deviation of the horizontal velocity profile from the incompressible solution relatively close to the exit at x=0.9 is shown in Fig. 4.2a for different Reynolds numbers (Re=0, 10, 100), α=0.01, and for the relatively high compressibility number ε=0.25. While for low Reynolds numbers it is parabolic, the deviation from the incompressible solution becomes sigmoidal at higher Reynolds numbers. The effect of the Reynolds number on the transverse velocity, u_y, is illustrated in Fig. 4.2b. It is clear from Eq. (4.44), that u_y is always positive, does not depend on the x coordinate and the

bulk viscosity χ, and increases linearly with the Reynolds number. Figure 4.3a shows the deviation of the horizontal velocity from the incompressible flow near the exit ($x = 0.9$) for different values of ε, Re=10 and α=0.01. It can be observed that the profile of u_x flattens as compressibility is increased. The effect of ε on the transverse velocity is shown in Fig. 4.3b. As expected, u_y increases quadratically with the compressibility number.

Figure 4.4 shows the transverse velocity profile in both the axisymmetric and planar cases for ε=0.25, α=0.1, $\alpha\, Re$=1 and $\alpha^2(\chi + 1/3)$=0. The axisymmetric result is of course identical to that of Venerus [88]. A more flattened profile is obtained in the planar case.

Figure 4.5 shows the deviation of the horizontal velocity from the incompressible solution at the entrance and the exit of the channel for Re=1, ε=0.1, χ=0, and two values of α (0.1 and 0.01). It is clear that the velocity is reduced and its profile flattens upstream. For $\alpha = 0.1$ (short channel) some small differences from the incompressible solution are observed at the exit of the channel. These vanish when the length of the channel is increased (α=0.01).

In Fig. 4.6, we show the pressure contours obtained with ε=0.25 and α=0.1 for the two cases considered by Venerus [88]: (a) αRe=1 and $\alpha^2(\chi + 1/3)$=0; (b) αRe=0 and $\alpha^2(\chi + 1/3)$=1. These are similar to their axisymmetric counterparts ([88]). When the channel is relatively short ($\alpha\, Re$=1, Fig. 4.6a) the flow is essentially incompressible and the pressure contours are practically vertical and equidistant. For longer channels ($\alpha\, Re$=0), however, the pressure contours are slightly parabolic as illustrated in Fig. 4.6b. Moreover the distance between the contours increases upstream, due to compressibility. As pointed out by Venerus [88] this effect is due to the bulk viscosity. Note that Venerus [88] does not specify the value of α which is taken here to be equal to 0.1. In Figure 4.7 we provide the pressure contours for the two complementary cases: (a) αRe=0 and $\alpha^2(\chi + 1/3)$=0; (b) αRe=1 and $\alpha^2(\chi + 1/3)$=1. Comparing Figs. 4.6 and 4.7, we deduce that the parameter $\alpha^2(\chi + 1/3)$ has a stronger effect

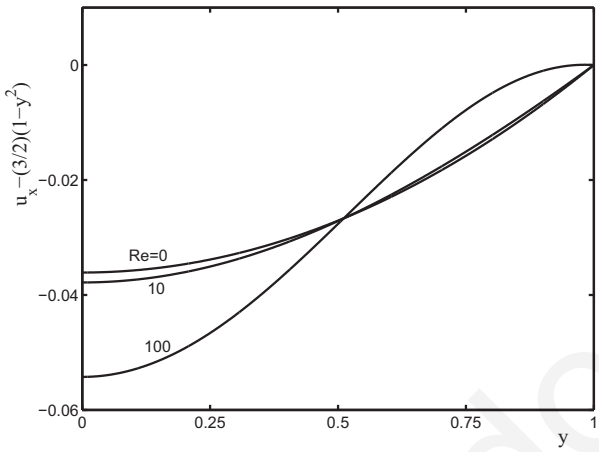

(a)

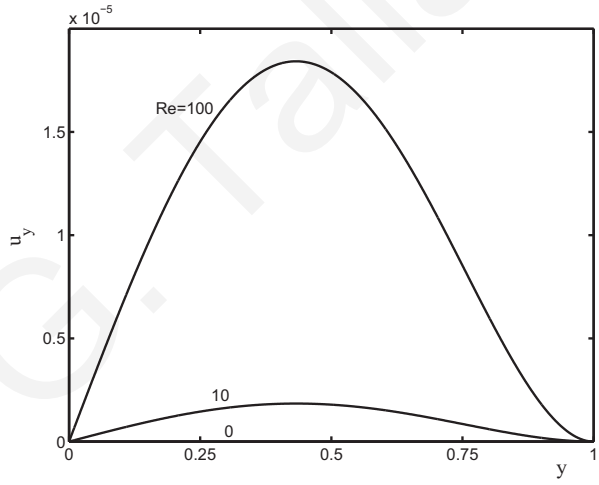

(b)

Figure 4.2: *Effect of the Reynolds number on the velocity components: (a) deviation of the horizontal velocity u_x from the incompressible profile; (b) transverse velocity u_y;* $\varepsilon = 0.25$, $\alpha = 0.01$, $\chi = 0$, *and* $x = 0.9$.

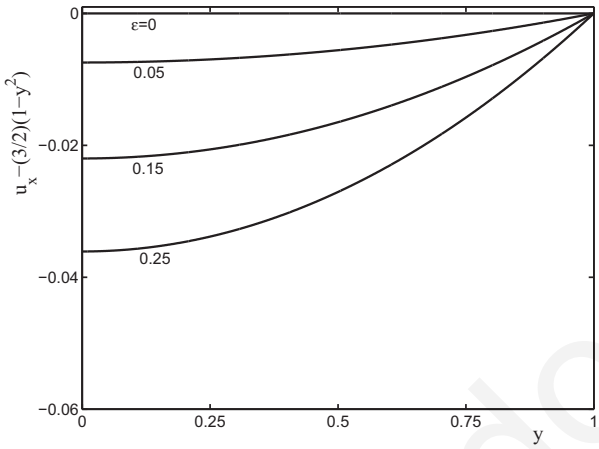

(*a*)

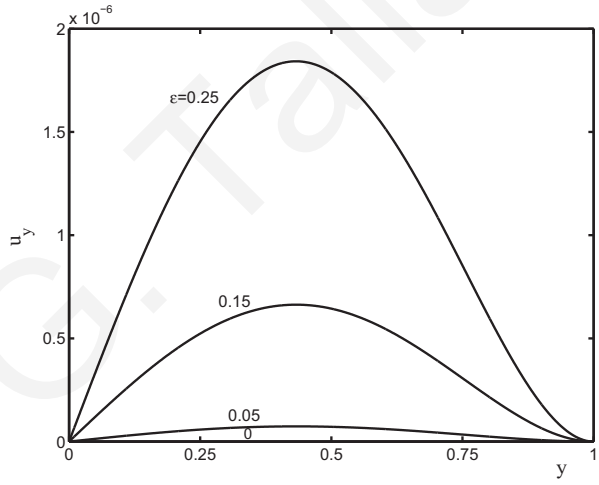

(*b*)

Figure 4.3: *Effect of compressibility on the velocity components: (a) deviation of the horizontal velocity u_x from the incompressible profile; (b) transverse velocity u_y; $Re = 10$, $\alpha = 0.01$, $\chi = 0$, and $x = 0.9$.*

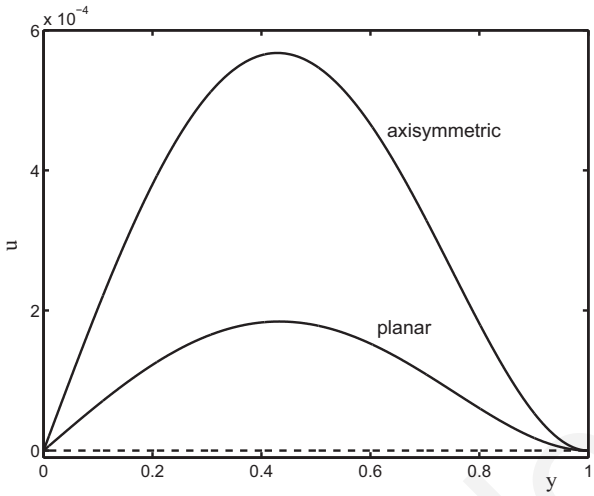

Figure 4.4: *Transverse velocity profiles for* $\varepsilon = 0.25$, $\alpha = 0.1$ *and* $\alpha\, Re = 1$.

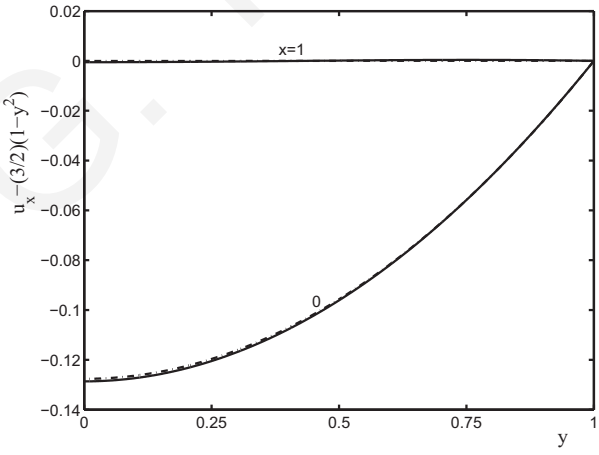

Figure 4.5: *Horizontal velocity field deviation from incompressible flow at* $x = 0$, *and* 1 *for* $\alpha = 0.1$ *(solid) and* $\alpha = 0.01$ *(dash-dot),* $Re = 1$, $\varepsilon = 0.1$, *and* $\chi = 0$.

on the pressure contours than αRe. The velocity contours for all cases considered in Figs. 4.6 and 4.7, are given in Figs. 4.8 and 4.9, respectively.

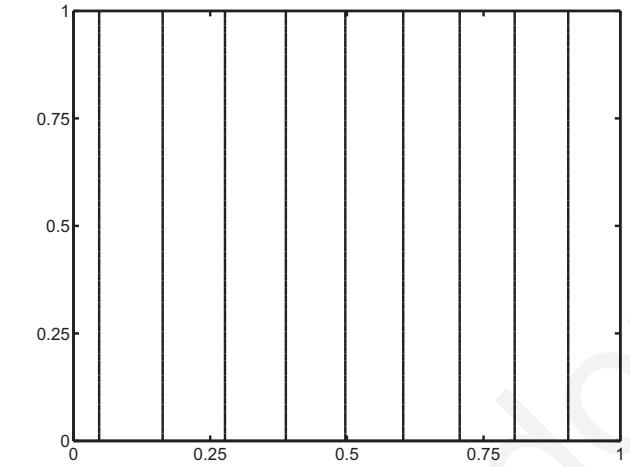

(a)

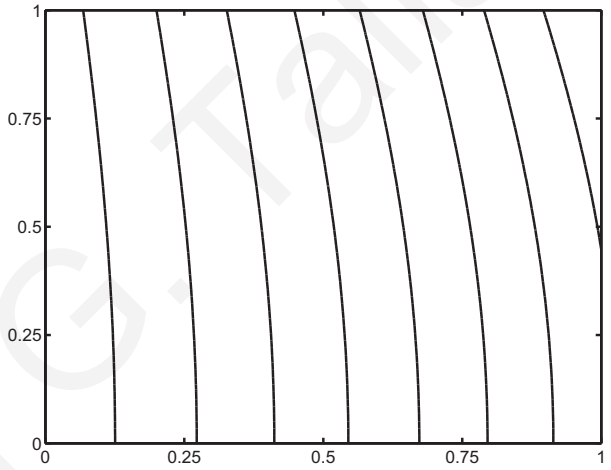

(b)

Figure 4.6: *Pressure field contours for plane Poiseuille flow (0.1, 0.2, ..., 0.9) with* $\varepsilon = 0.25$ *and* $\alpha = 0.1$*: (a)* $\alpha\, Re = 1$, $\alpha^2(\chi + 1/3) = 0$*; (b)* $\alpha\, Re = 0$, $\alpha^2(\chi + 1/3) = 1$.

Figure 4.10 shows the horizontal velocity field deviation from the incompressible solution at various distances from the inlet plane, as given by Eq. (4.45) with ε=0.25 and α=0.1 for two cases: (a) $\alpha\, Re$=1, $\alpha^2(\chi + 1/3)$=0 and (b) $\alpha\, Re$=0, $\alpha^2(\chi + 1/3)$=1. In Fig. 4.10a, where

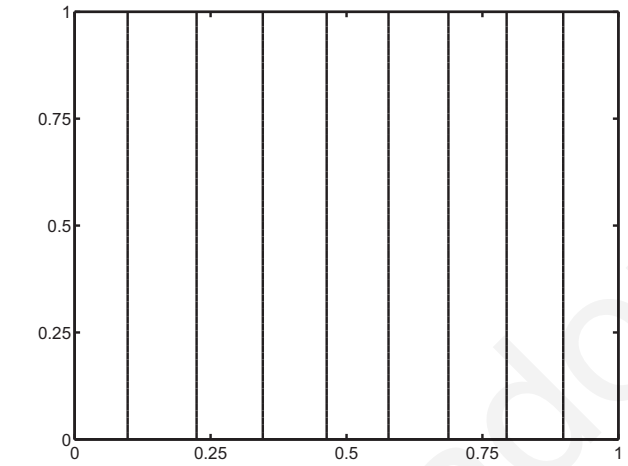

(a)

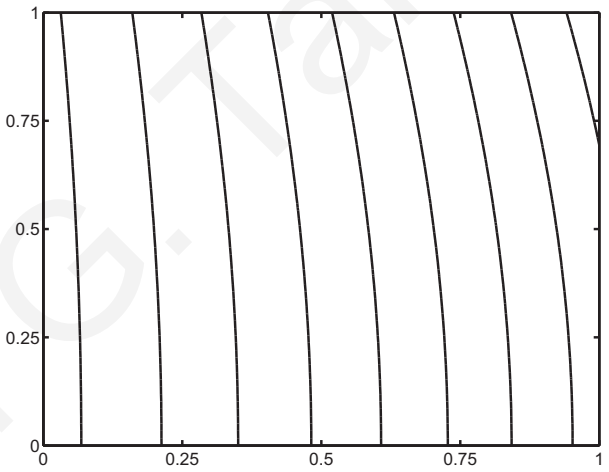

(b)

Figure 4.7: *Pressure field contours for plane Poiseuille flow (0.1, 0.2, ..., 0.9) with* $\varepsilon = 0.25$ *and* $\alpha = 0.1$*: (a)* $\alpha\, Re = 0$, $\alpha^2(\chi + 1/3) = 0$*; (b)* $\alpha\, Re = 1$, $\alpha^2(\chi + 1/3) = 1$.

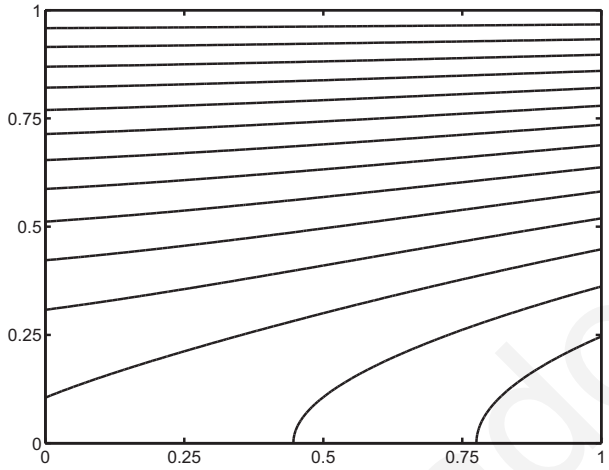

(a)

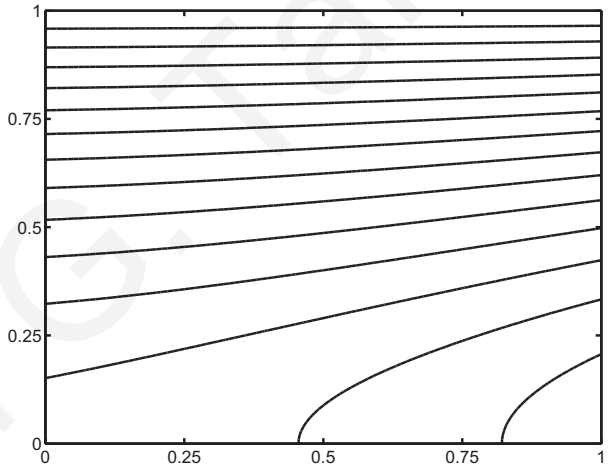

(b)

Figure 4.8: *Velocity field contours for plane Poiseuille flow (0.1, 0.2, ..., 1.4) with* $\varepsilon = 0.25$ *and* $\alpha = 0.1$*: (a)* $\alpha\, Re = 1$, $\alpha^2(\chi + 1/3) = 0$*; (b)* $\alpha\, Re = 0$, $\alpha^2(\chi + 1/3) = 1$.

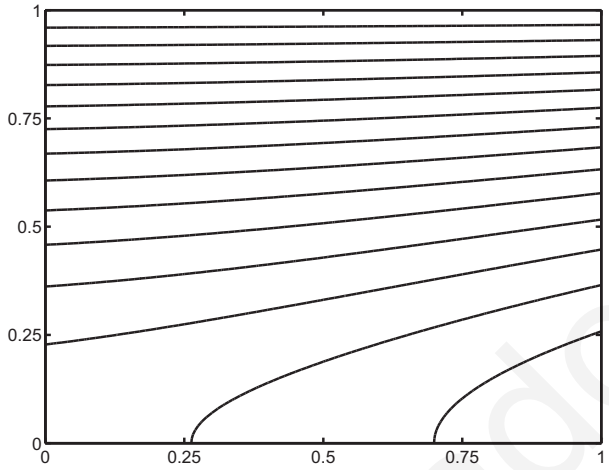

(a)

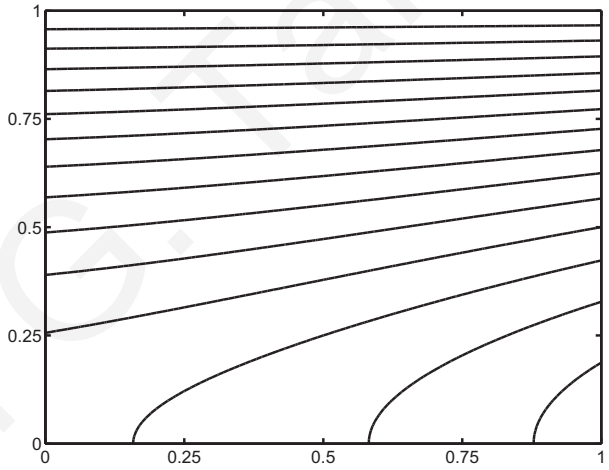

(b)

Figure 4.9: *Velocity field contours for plane Poiseuille flow (0.1, 0.2, ..., 1.4) with* $\varepsilon = 0.25$ *and* $\alpha = 0.1$*: (a)* $\alpha\, Re = 0$, $\alpha^2(\chi + 1/3) = 0$*; (b)* $\alpha\, Re = 1$, $\alpha^2(\chi + 1/3) = 1$.

the channel is relatively short the velocity profile flattens as the fluid moves downstream. For longer channels (Fig. 4.10b) the effect of the bulk viscosity is small and the horizontal velocity profile remains parabolic. These results which are similar to those of Venerus [88] for the axisymmetric case, are also consistent with the numerical results of Guo and Wu [37, 38]. Finally, Fig. 4.11 shows the two transverse velocity profiles obtained with (a) Re=100, ε=0.006 and (b) Re=0.01, ε=0.2 when α=3. The latter value of α was chosen in order to make comparisons with the results reported by Schwartz [75] at the exit x=1. The present results agree with those of Schwartz [75] up to the second order. According to Eq. (4.44), u_y is always positive which is not the case with the third-order solution of Schwartz [75]; this is valid only at the exit and yields negative values of u_y for small Reynolds numbers (Re=0.001).

4.5 Appendix: Compressible axisymmetric Poiseuille Flow

The two-dimensional perturbation solution of the compressible axisymmetric Poiseuille flow is derived in this Appendix. To nondimensionalize the equations, we scale z by L, r by R, the density by the reference density ρ_0, the axial velocity u_z by $U = \dot{M}/\rho_0\pi R^2$, the radial velocity u_r by UR/L, and the pressure by $8\eta LU/R^2$. The dimensionless forms of the governing equations are:

$$\rho \;=\; 1 \;+\; \varepsilon\, P\,, \tag{4.52}$$

$$\frac{1}{r}\frac{\partial}{\partial r}\,(r\,\rho\,u_r) \;+\; \frac{\partial}{\partial z}\,(\rho\,u_z) \;=\; 0\,, \tag{4.53}$$

$$\alpha\, Re\, \rho\, \left(u_r\,\frac{\partial\, u_z}{\partial\, r} \;+\; u_z\,\frac{\partial\, u_z}{\partial\, z}\right) = -8\,\frac{\partial\, P}{\partial\, z} \;+\; \frac{1}{r}\,\frac{\partial}{\partial\, r}\left(r\,\frac{\partial\, u_z}{\partial\, r}\right) + \alpha^2\,\frac{\partial^2 u_z}{\partial\, z^2}$$

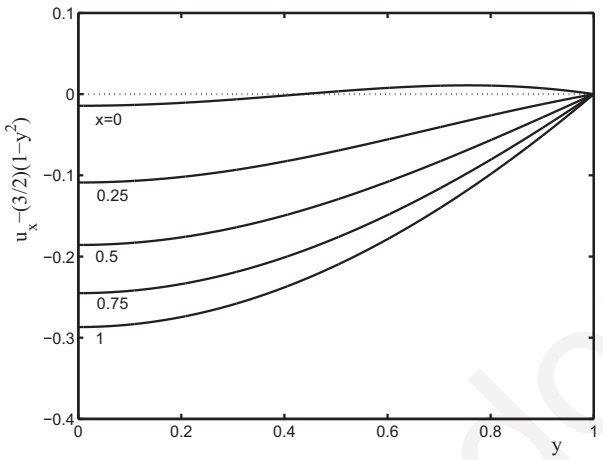

(a)

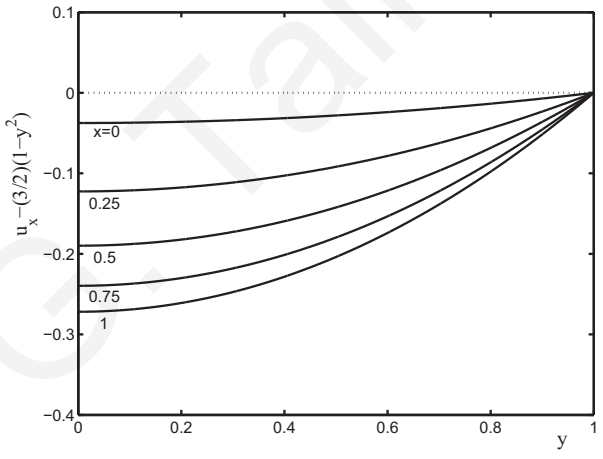

(b)

Figure 4.10: *Horizontal velocity field deviation from incompressible flow at various distances from the inlet plane for* $\varepsilon = 0.25$ *and* $\alpha = 0.1$*: (a)* $\alpha\, Re = 1$, $\alpha^2(\chi + 1/3) = 0$*; (b)* $\alpha\, Re = 0$, $\alpha^2(\chi + 1/3) = 1$.

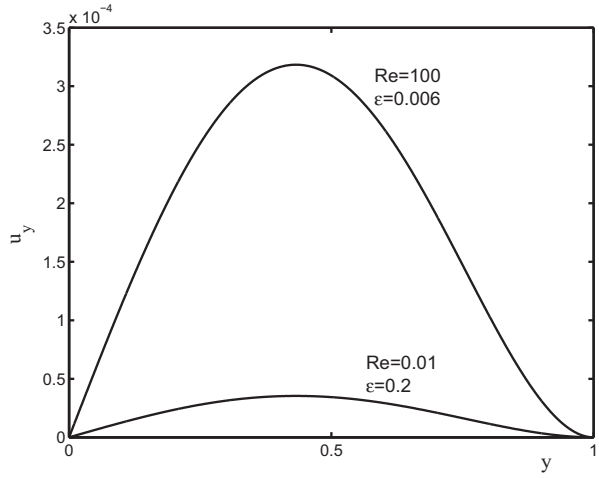

Figure 4.11: *Transverse velocity profiles of plane Poseuille flow with* $\alpha = 3$ *and the Reynolds and compressibility numbers used by Schwartz [75].*

$$+ \alpha^2 \left(\chi + \frac{1}{3}\right) \left[\frac{\partial}{\partial z}\left(\frac{1}{r}\frac{\partial}{\partial r}(r\,u_r)\right) + \frac{\partial^2 u_z}{\partial z^2}\right], \tag{4.54}$$

$$\alpha^3 \, Re \, \rho \left(u_r \frac{\partial u_r}{\partial r} + u_z \frac{\partial u_r}{\partial z}\right) = -8 \frac{\partial P}{\partial r} + \alpha^2 \frac{\partial}{\partial r}\left(\frac{1}{r}\frac{\partial}{\partial r}(r\,u_r)\right) + \alpha^4 \frac{\partial^2 u_r}{\partial z^2}$$
$$+ \alpha^2 \left(\chi + \frac{1}{3}\right) \left[\frac{\partial}{\partial r}\left(\frac{1}{r}\frac{\partial}{\partial r}(r\,u_r)\right) + \frac{\partial^2 u_z}{\partial r \partial z}\right] \tag{4.55}$$

where:

$$\chi \equiv \frac{\kappa}{\eta}, \quad \alpha \equiv \frac{R}{L}, \quad Re \equiv \frac{\rho_0 U R}{\eta}, \quad \text{and} \quad \varepsilon \equiv \frac{8\eta\beta L U}{R^2}.$$

The boundary conditions are similar to those used for the planar problem.

Writing the primary fields as expansions in the perturbation parameter ε,

$$\left.\begin{aligned} \rho &= \rho^{(0)} + \varepsilon\rho^{(1)} + \varepsilon^2\rho^{(2)} + O(\varepsilon^3) \\ u_r &= u_r^{(0)} + \varepsilon\, u_r^{(1)} + \varepsilon^2\, u_r^{(2)} + O(\varepsilon^3) \\ u_z &= u_z^{(0)} + \varepsilon\, u_z^{(1)} + \varepsilon^2\, u_z^{(2)} + O(\varepsilon^3) \\ P &= P^{(0)} + \varepsilon\, P^{(1)} + \varepsilon^2\, P^{(2)} + O(\varepsilon^3) \end{aligned}\right\}, \tag{4.56}$$

substituting in the governing equations, and following similar steps as for the planar problem, we obtain the solution of the flow up to the second order.

Zero-order solution

The zero-order equations are:

$$\rho^{(0)} \;=\; 1,$$

$$\frac{1}{r}\frac{\partial}{\partial r}\left[r\,\rho^{(0)}u_r^{(0)}\right] \;+\; \frac{\partial}{\partial z}\left[\rho^{(0)}u_z^{(0)}\right] \;=\; 0,$$

$$\alpha\,Re\,\rho^{(0)}\left[u_r^{(0)}\,\frac{\partial u_z^{(0)}}{\partial r} \;+\; u_z^{(0)}\,\frac{\partial u_z^{(0)}}{\partial z}\right]$$

$$= -8\,\frac{\partial P^{(0)}}{\partial z} + \frac{1}{r}\frac{\partial}{\partial r}\left(r\,\frac{\partial u_z^{(0)}}{\partial r}\right) + \alpha^2\,\frac{\partial^2 u_z^{(0)}}{\partial z^2} + \alpha^2\left(\chi+\frac{1}{3}\right)\left[\frac{\partial}{\partial z}\left(\frac{1}{r}\,\frac{\partial}{\partial r}\left(r\,u_r^{(0)}\right)\right) + \frac{\partial^2 u_z^{(0)}}{\partial z^2}\right],$$

and

$$\alpha^3\,Re\,\rho^{(0)}\left[u_r^{(0)}\,\frac{\partial u_r^{(0)}}{\partial r} \;+\; u_z^{(0)}\,\frac{\partial u_r^{(0)}}{\partial z}\right] \;=\; -8\,\frac{\partial P^{(0)}}{\partial r} + \alpha^2\,\frac{\partial}{\partial r}\left[\frac{1}{r}\,\frac{\partial}{\partial r}\left(ru_r^{(0)}\right)\right] + \alpha^4\,\frac{\partial^2 u_r^{(0)}}{\partial z^2}$$

$$+\,\alpha^2\left(\chi+\frac{1}{3}\right)\left[\frac{\partial}{\partial r}\left(\frac{1}{r}\,\frac{\partial}{\partial r}\left(r\,u_r^{(0)}\right)\right) \;+\; \frac{\partial^2 u_z^{(0)}}{\partial r\partial z}\right].$$

With the assumptions $\partial u_z^{(0)}/\partial r(0)=u_z^{(0)}(1)=0$, $P^{(0)}(z=1)=0$ and $P^{(0)}(z=0)=1$, we find the zero-order solution:

$$\rho^{(0)} \;=\; 1 \tag{4.57}$$

$$u_r^{(0)} \;=\; 0 \tag{4.58}$$

$$u_z^{(0)} \;=\; 2(1\,-\,r^2) \tag{4.59}$$

$$P^{(0)} \;=\; 1\,-\,z \tag{4.60}$$

First-order solution

The first-order equations are:

$$\rho^{(1)} \;=\; P^{(0)}(z) \;=\; 1-z,$$

$$\frac{1}{r}\frac{\partial}{\partial r}\left[r\,\left(\rho^{(0)}u_r^{(1)} \;+\; \rho^{(1)}u_r^{(0)}\right)\right] \;+\; \frac{\partial}{\partial z}\left[\rho^{(0)}u_z^{(1)} \;+\; \rho^{(1)}u_z^{(0)}\right] \;=\; 0,$$

$$\alpha\,Re\,\rho^{(1)}\left[u_r^{(0)}\,\frac{\partial u_z^{(0)}}{\partial r} \;+\; u_z^{(0)}\,\frac{\partial u_z^{(0)}}{\partial z}\right]$$

$$+\alpha Re\rho^{(0)}\left[u_r^{(0)}\,\frac{\partial u_z^{(1)}}{\partial r}\;+\;u_r^{(1)}\,\frac{\partial u_z^{(0)}}{\partial r}\;+\;u_z^{(0)}\,\frac{\partial u_z^{(1)}}{\partial z}\;+\;u_z^{(1)}\,\frac{\partial u_z^{(0)}}{\partial z}\right]$$
$$=-8\,\frac{\partial P^{(1)}}{\partial z}+\frac{1}{r}\,\frac{\partial}{\partial r}\left(r\,\frac{\partial u_z^{(1)}}{\partial r}\right)+\alpha^2\,\frac{\partial^2 u_z^{(1)}}{\partial z^2}+\alpha^2\,\left(\chi+\frac{1}{3}\right)\left[\frac{\partial}{\partial z}\left(\frac{1}{r}\,\frac{\partial}{\partial r}\left(r\,u_r^{(1)}\right)\right)\;+\;\frac{\partial^2 u_z^{(1)}}{\partial z^2}\right],$$

and

$$\alpha^3\,Re\,\rho^{(1)}\left[u_r^{(0)}\,\frac{\partial u_r^{(0)}}{\partial r}\;+\;u_z^{(0)}\,\frac{\partial u_r^{(0)}}{\partial z}\right]$$
$$+\alpha^3\,Re\,\rho^{(0)}\left[u_r^{(0)}\,\frac{\partial u_r^{(1)}}{\partial r}\;+\;u_r^{(1)}\,\frac{\partial u_r^{(0)}}{\partial r}\;+\;u_z^{(0)}\,\frac{\partial u_r^{(1)}}{\partial z}\;+\;u_z^{(1)}\,\frac{\partial u_r^{(0)}}{\partial z}\right]$$
$$=-8\,\frac{\partial P^{(1)}}{\partial r}\;+\alpha^2\,\frac{\partial}{\partial r}\left[\frac{1}{r}\,\frac{\partial}{\partial r}\,\left(ru_r^{(1)}\right)\right]+\alpha^4\;\frac{\partial^2 u_r^{(1)}}{\partial z^2}$$
$$+\alpha^2\,\left(\chi+\frac{1}{3}\right)\left[\frac{\partial}{\partial r}\left(\frac{1}{r}\,\frac{\partial}{\partial r}\left(r\,u_r^{(1)}\right)\right)\;+\;\frac{\partial^2 u_z^{(1)}}{\partial r\partial z}\right].$$

Assuming that $u_r^{(1)}(z,r)$=0, we find from the continuity and the r-momentum equations that

$$u_z^{(1)}\;=\;-2\,(1-z)\,(1-r^2)\;+\;f(r)$$

and

$$P^{(1)}\;=\;\frac{1}{4}\,\alpha^2\,\left(\chi+\frac{1}{3}\right)(1-r^2)\;+\;g(z)$$

where $f(r)$ and $g(z)$ are unknown functions. Substituting into the z-momentum equation and separating variables we get

$$4\alpha\,Re\,(1-r^2)^2\;-\;\frac{1}{r}\frac{\partial}{\partial\,r}\,(r\,f'(r))=-8\frac{\partial\,P^{(1)}}{\partial\,z}+\;\frac{1}{r}\frac{\partial}{\partial\,r}\left(4r^2(1-z)\right)=c$$

where c is a constant to be determined. Integrating the resulting ODEs and applying the boundary conditions $f'(0)$=$f(1)$=0 and $\int_0^1 rf(r)dr$=0 for $u_z^{(1)}(z,r)$ and $P^{(1)}(1,1)$=0 for $P(z,r)$, we find that c=$2\alpha Re$ and obtain the first-order solution:

$$\rho^{(1)}\;=\;1-z \tag{4.61}$$

$$u_r^{(1)}\;=\;0 \tag{4.62}$$

$$u_z^{(1)}\;=\;2(1\;-\;r^2)\left[-(1-z)-\frac{1}{36}\,\alpha\,Re\,(2-7r^2+2r^4)\right] \tag{4.63}$$

$$P^{(1)}\;=\;-\frac{1}{2}\,(1\;-\;z)^2\;+\;\frac{1}{4}\alpha\,Re\,(1-z)\;+\;\frac{1}{4}\alpha^2\,\left(\chi+\frac{1}{3}\right)(1\;-\;r^2). \tag{4.64}$$

Second-order solution

The second-order equations are:

$$\rho^{(2)} \;=\; P^{(1)}(z,r) = -\frac{1}{2}\,(1-z)^2 \;+\frac{1}{4}\,\alpha\,Re(1-z) + \frac{1}{4}\,\alpha^2\left(\chi+\frac{1}{3}\right)(1-r^2), \tag{4.65}$$

$$\frac{1}{r}\frac{\partial}{\partial r}\left[r\,\left(\rho^{(0)}u_r^{(2)} \;+\; \rho^{(1)}u_r^{(1)} \;+\; \rho^{(2)}u_r^{(0)}\right)\right] \;+\; \frac{\partial}{\partial z}\left[\rho^{(0)}u_z^{(2)} \;+\; \rho^{(1)}u_z^{(1)} \;+\; \rho^{(2)}u_z^{(0)}\right] \;=\; 0,$$

$$\alpha\;Re\;\rho^{(2)}\left[u_r^{(0)}\;\frac{\partial u_z^{(0)}}{\partial r} \;+\; u_z^{(0)}\frac{\partial u_z^{(0)}}{\partial z}\right]$$

$$+\alpha Re\rho^{(1)}\left[u_r^{(0)}\;\frac{\partial u_z^{(1)}}{\partial r} \;+\; u_r^{(1)}\;\frac{\partial u_z^{(0)}}{\partial r} \;+\; u_z^{(0)}\;\frac{\partial u_z^{(1)}}{\partial z} \;+\; u_z^{(1)}\;\frac{\partial u_z^{(0)}}{\partial z}\right]$$

$$+\alpha Re\rho^{(0)}\left[u_r^{(0)}\;\frac{\partial u_z^{(2)}}{\partial r} \;+\; u_r^{(1)}\;\frac{\partial u_z^{(1)}}{\partial r} \;+\; u_r^{(2)}\;\frac{\partial u_z^{(0)}}{\partial r} \;+\; u_z^{(0)}\;\frac{\partial u_z^{(2)}}{\partial z} \;+\; u_z^{(1)}\;\frac{\partial u_z^{(1)}}{\partial z} \;+\; u_z^{(2)}\;\frac{\partial u_z^{(0)}}{\partial z}\right]$$

$$= -8\,\frac{\partial P^{(2)}}{\partial z} + \frac{1}{r}\,\frac{\partial}{\partial r}\left(r\;\frac{\partial u_z^{(2)}}{\partial r}\right) + \alpha^2\,\frac{\partial^2 u_z^{(2)}}{\partial z^2} + \alpha^2\,\left(\chi+\frac{1}{3}\right)\left[\frac{\partial}{\partial z}\left(\frac{1}{r}\,\frac{\partial}{\partial r}\left(r\,u_r^{(2)}\right)\right) \;+\; \frac{\partial^2 u_z^{(2)}}{\partial z^2}\right],$$

and

$$\alpha^3\;Re\;\rho^{(2)}\left[u_r^{(0)}\;\frac{\partial u_r^{(0)}}{\partial r} \;+\; u_z^{(0)}\;\frac{\partial u_r^{(0)}}{\partial z}\right]$$

$$+\alpha^3 Re\rho^{(1)}\left[u_r^{(0)}\;\frac{\partial u_r^{(1)}}{\partial r} \;+\; u_r^{(1)}\;\frac{\partial u_r^{(0)}}{\partial r} \;+\; u_z^{(0)}\;\frac{\partial u_r^{(1)}}{\partial z} \;+\; u_z^{(1)}\;\frac{\partial u_r^{(0)}}{\partial z}\right]$$

$$+\,\alpha^3\,Re\,\rho^{(0)}\left[u_r^{(0)}\;\frac{\partial u_r^{(2)}}{\partial r} \;+\; u_r^{(1)}\;\frac{\partial u_r^{(1)}}{\partial r} \;+\; u_r^{(2)}\;\frac{\partial u_r^{(0)}}{\partial r} \;+\; u_z^{(0)}\;\frac{\partial u_r^{(2)}}{\partial z} \;+\; u_z^{(1)}\;\frac{\partial u_r^{(1)}}{\partial z} \;+\; u_z^{(2)}\;\frac{\partial u_r^{(0)}}{\partial z}\right]$$

$$= -8\frac{\partial P^{(2)}}{\partial r} + \alpha^2\frac{\partial}{\partial r}\left[\frac{1}{r}\;\frac{\partial}{\partial r}\;\left(ru_r^{(2)}\right)\right] + \alpha^4\frac{\partial^2 u_r^{(2)}}{\partial z^2} + \alpha^2\,\left(\chi+\frac{1}{3}\right)\left[\frac{\partial}{\partial r}\left(\frac{1}{r}\,\frac{\partial}{\partial r}\left(r\,u_r^{(2)}\right)\right) \;+\; \frac{\partial^2 u_z^{(2)}}{\partial r\partial z}\right].$$

Now under the assumption that $u_r^{(2)}$=$u_r^{(2)}(r)$, from the continuity and r-momentum equations we get, respectively:

$$\begin{aligned} u_z^{(2)} \;&=\; 3(1-r^2)(1-z)^2 - \frac{1}{2}\alpha^2\left(\chi+\frac{1}{3}\right)(1-r^2)^2 + \frac{1}{r}\frac{\partial\,(ru_r^{(2)})}{\partial\,r}(1-z) \\ &\quad + \frac{\alpha\,Re}{18}(1-r^2)(-7-7r^2+2r^4)(1-z) + F(r) \end{aligned} \tag{4.66}$$

and

$$P^{(2)} = \frac{1}{8}\alpha^2\left(\frac{1}{r}\frac{\partial\,(ru_r^{(2)})}{\partial\,r}\right) - \frac{3}{4}\alpha^2\left(\chi+\frac{1}{3}\right)(1-r^2)(1-z) - \frac{1}{144}\alpha^3 Re\left(\chi+\frac{1}{3}\right)(1-r^2)(-7-7r^2+2r^4) + G(z), \quad (4.67)$$

where $F(r)$ and $G(z)$ are functions to be determined. Combining Eqs. (4.65)-(4.67) with the z-momentum equation leads to:

$$\begin{aligned}
&\alpha\, Re\left\{-4ru_r^{(2)} - 12(1-r^2)^2(1-z) - 2(1-r^2)\left[\frac{1}{r}\frac{\partial\,(ru_r^{(2)})}{\partial\,r}\right]\right. \\
&\qquad\left. + \frac{1}{9}\alpha\, Re(1-r^2)^2(-4r^4+14r^2+5)\right\} \\
&= 6\alpha^2(1-r^2) - \frac{1}{2}\alpha^2\left(\chi+\frac{1}{3}\right)(-8+16r^2) - 8G'(z) - 12(1-z)^2 \\
&+ \frac{1}{r}\frac{\partial}{\partial\,r}\left[r\frac{\partial}{\partial r}\left(\frac{1}{r}\frac{\partial\,(ru_r^{(2)})}{\partial\,r}\right)\right](1-z) + \frac{1}{r}\frac{\partial}{\partial\,r}(rF'(r)) + 4\alpha\, Re\, r^2(2-r^2)(1-z). \quad (4.68)
\end{aligned}$$

In order to separate variables, we demand that the terms involving both $(1-z)$ and r must be equal to a (scalar) multiple of $(1-z)$. Thus, we assume that

$$4\alpha\, Re\, r^2(2-r^2) + \frac{1}{r}\frac{\partial}{\partial\,r}\left[r\frac{\partial}{\partial r}\left(\frac{1}{r}\frac{\partial\,(ru_r^{(2)})}{\partial\,r}\right)\right] + 12\alpha\, Re(1-r^2)^2 = 4\alpha\, Re\gamma. \quad (4.69)$$

where γ is new constant to be determined. Solving the above equation under the conditions $u_r^{(2)}(0)=\partial u_r^{(2)}/\partial r(0)=0$ and $u_r^{(2)}(1)=\partial u_r^{(2)}/\partial r(1)=0$ yields $\gamma=2$ and the second-order radial velocity:

$$u_r^{(2)} = \frac{1}{36}\alpha\, Re\, r\,(1-r^2)^2(4-r^2). \quad (4.70)$$

Separating variables in Eq. (4.68) gives the following ODEs for $F(r)$ and $G(z)$:

$$\begin{aligned}
&\alpha Re\left[-4ru_r^{(2)} - 2(1-r^2)\left(\frac{1}{r}\frac{\partial\,(ru_r^{(2)})}{\partial\,r}\right) - \frac{1}{9}\,\alpha\, Re(-5-4r^2+27r^4-22r^6+4r^8)\right] \\
&\qquad -6\alpha^2(1-r^2) + \frac{\alpha^2}{2}\left(\chi+\frac{1}{3}\right)(-8+16r^2) - \frac{1}{r}\frac{\partial}{\partial\,r}(rF'(r)) = A \quad (4.71)
\end{aligned}$$

and

$$-8G'(z) - 12(1-z)^2 + 4\alpha\, Re\, \gamma(1-z) \;=\; A. \tag{4.72}$$

where A is another constant to be determined. Integrating Eq. (4.71) and applying the conditions $F(1)=0$ and $\int_0^1 rF(r)dr=0$ we find that

$$\begin{aligned} F(r) \;&=\; \frac{\alpha^2\, Re^2}{9}\left(\frac{43}{2400} - \frac{5}{12}r^2 + \frac{11}{8}r^4 - \frac{3}{2}r^6 + \frac{19}{32}r^8 - \frac{7}{100}r^{10}\right) \\ &\quad + \alpha^2\left(\frac{1}{8} - \frac{1}{2}r^2 + \frac{3}{8}r^4\right) + \alpha^2\left(\chi + \frac{1}{3}\right)\left(-\frac{2}{3}r^2 + \frac{1}{2}r^4 + \frac{1}{6}\right) \end{aligned} \tag{4.73}$$

and

$$A \;= 4\left[-\alpha^2 - \frac{1}{3}\,\alpha^2\left(\chi + \frac{1}{3}\right) + \frac{2}{27}\,\alpha^2\, Re^2\right]. \tag{4.74}$$

Integrating now Eq. (4.72) and substituting A under the condition $P^{(2)}(1,1)=0$ we obtain

$$G(z) = \frac{1}{2}(1-z)^3 - \frac{1}{2}\alpha^2(1-z) - \frac{1}{2}\alpha Re(1-z)^2 + \frac{1}{27}\alpha^2 Re^2(1-z) - \frac{1}{6}\alpha^2\left(\chi + \frac{1}{3}\right)(1-z) \tag{4.75}$$

Hence, the second order solution reads:

$$\rho^{(2)} \;=\; -\frac{1}{2}\,(1-z)^2 \;+ \frac{1}{4}\,\alpha\, Re(1-z) + \frac{1}{4}\,\alpha^2\left(\chi + \frac{1}{3}\right)(1-r^2) \tag{4.76}$$

$$u_r^{(2)} \;=\; \frac{1}{36}\alpha\, Re\, r\,(1-r^2)^2(4-r^2) \tag{4.77}$$

$$\begin{aligned} u_z^{(2)} \;&=\; 2(1-r^2)\left[\frac{3}{2}(1-z)^2 - \frac{1}{6}\alpha^2\left(\chi + \frac{1}{3}\right)\right. \\ &\qquad -\frac{1}{12}\alpha\, Re(1+7r^2-2r^4)(1-z) + \frac{1}{16}\alpha^2(1-3r^2) \\ &\qquad \left. +\frac{1}{43200}\alpha^2\, Re^2(43 - 957r^2 + 2343r^4 - 1257r^6 + 168r^8)\right] \end{aligned} \tag{4.78}$$

$$\begin{aligned} P^{(2)} \;&=\; \frac{1}{2}(1-z)^3 - \frac{1}{12}\alpha^2\left(\chi + \frac{1}{3}\right)(11-9r^2)(1-z) - \frac{1}{2}\alpha\, Re(1-z)^2 \\ &\quad - \frac{1}{2}\alpha^2(1-z) + \frac{1}{27}\alpha^2 Re^2(1-z) \\ &\quad + \frac{1}{144}\alpha^3\, Re(1-r^2)\left[(4 - 14r^2 + 4r^4) + \left(\chi + \frac{1}{3}\right)(7 + 7r^2 - 2r^4)\right]. \end{aligned} \tag{4.79}$$

Thus, the solution of the flow up to the second order is as follows:

$$\begin{aligned}
\rho &= 1+\varepsilon(1-z) \\
&\quad +\varepsilon^2\left[-\frac{1}{2}(1-z)^2 + \frac{1}{4}\alpha\, Re(1-z) + \frac{1}{4}\alpha^2\left(\chi+\frac{1}{3}\right)(1-r^2)\right] + O(\varepsilon^3) \quad (4.80)\\
u_r &= \frac{1}{36}\varepsilon^2\alpha\, Re\, r\,(1-r^2)^2(4-r^2) + O(\varepsilon^3) \quad (4.81)\\
u_z &= 2(1-r^2)\left[1-\varepsilon(1-z)-\frac{1}{36}\varepsilon\alpha\, Re(2-7r^2+2r^4)+\frac{3}{2}\varepsilon^2(1-z)^2\right. \\
&\quad -\frac{1}{12}\varepsilon^2\alpha\, Re(1+7r^2-2r^4)(1-z)+\frac{1}{16}\varepsilon^2\alpha^2(1-3r^2)-\frac{1}{6}\varepsilon^2\alpha^2\left(\chi+\frac{1}{3}\right) \\
&\quad \left.+\frac{1}{43200}\varepsilon^2\alpha^2\, Re^2(43-957r^2+2343r^4-1257r^6+168r^8)\right] + O(\varepsilon^3) \quad (4.82)\\
P &= (1-z)-\frac{1}{2}\varepsilon\,(1-z)^2 + \frac{1}{4}\varepsilon\,\alpha\, Re\,(1-z) \\
&\quad +\frac{1}{4}\varepsilon\,\alpha^2\left(\chi+\frac{1}{3}\right)(1-r^2)+\frac{1}{2}\varepsilon^2(1-z)^3 \\
&\quad -\frac{1}{12}\varepsilon^2\alpha^2\left(\chi+\frac{1}{3}\right)(11-9r^2)(1-z) \\
&\quad -\frac{1}{2}\varepsilon^2\alpha\, Re(1-z)^2-\frac{1}{2}\alpha^2(1-z)+\frac{1}{27}\varepsilon^2\alpha^2 Re^2(1-z) \\
&\quad +\frac{1}{144}\varepsilon^2\alpha^3\, Re(1-r^2)\left[(4-14r^2+4r^4)+\left(\chi+\frac{1}{3}\right)(7+7r^2-2r^4)\right] \\
&\quad + O(\varepsilon^3). \quad (4.83)
\end{aligned}$$

The streamfunction, defined by

$$\frac{\partial\psi}{\partial r} \equiv \rho r u_z \quad \text{and} \quad \frac{\partial\psi}{\partial z} \equiv -\rho r u_r \quad (4.84)$$

is given by

$$\begin{aligned}
\psi(r,z) &= \frac{1}{2}\,r^2\left(2-r^2\right) - \frac{1}{72}\varepsilon\,\alpha\, Re\, r^2(1-r^2)^2(4-r^2) + \varepsilon^2\left[\frac{1}{16}\,\alpha^2\,r^2\,(1-r^2)^2\right. \\
&\quad +\frac{1}{12}\,\alpha^2\left(\chi+\frac{1}{3}\right)\,r^2\,(1-r^2)^2+\frac{1}{36}\,\alpha\, Re\, r^2\,(1-r^2)^2(4-r^2)(1-z) \\
&\quad \left.+\frac{1}{43200}\alpha^2\, Re^2\, r^2\,(1-r^2)^2(43-414r^2+229r^4-28r^6)\right] + O(\varepsilon^3). \quad (4.85)
\end{aligned}$$

Finally, the volumetric flow rate across the tube,

$$Q(z) = 2\int_0^1 u_z(r,z)rdr,$$

is

$$Q(z) = 1 - \varepsilon(1-z) + \frac{1}{48}\varepsilon^2\left[-8\alpha^2\left(\chi + \frac{1}{3}\right) - 6\alpha Re(1-z) + 72(1-z)^2\right] + O(\varepsilon^3). \quad (4.86)$$

Chapter 5

Weakly compressible Poiseuille flows of a Herschel-Bulkley fluid

5.1 Introduction

Laminar Poiseuille flows of weakly compressible materials have gained interest in the past two decades due to their applications in many processes involving liquid flows in relatively long tubes, such as waxy crude oil transport [15, 90] and polymer extrusion [29, 32]. Numerical solutions of weakly compressible Poiseuille flows have been reported for Newtonian fluids [32], generalized Newtonian fluids, such as the Carreau fluid [29] and the Bingham plastic [90], as well as for viscoelastic fluids [6][1].

The objective of the present work is to solve approximately the plane and axisymmetric Poiseuille flows of weakly compressible fluids with yield stress, i.e. fluids obeying the Herschel-Bulkley constitutive equation, and investigate the effects of compressibility by means of two

[1]Some of the results presented in this chapter appear also in Reference [84]

different equations of state, i.e. a linear and an exponential one. A linear equation of state has been employed in previous numerical studies of the extrudate swell flow [10, 28] by Hatzikiriakos anf Dealy [40] for HDPE, also for laminar capillary flow by Venerus [88] for compressible Newtonian fluids, and in our previous studies concerning the simulation of the stick-slip extrusion instability [29, 32]. Exponential equations of state have been employed, for example, by Ranganathan et al. [70] for a HDPE and, more recently, by Vinay et al. [90] in simulations of weakly compressible Bingham flows.

The paper is organized as follows. In section 5.2, the governing equations for the axisymmetric Poiseuille flow are presented and the assumptions under which these are simplified are discussed. Analytical and semi-analytical results are presented for both the incompressible and compressible flows of a Herschel-Bulkley fluid and the numerical method is briefly discussed. In section 5.3, the numerical results for the compressible flows of Newtonian, power-law, Bingham, and Herschel-Bulkley fluids with both linear and exponential equations of state are compared and the effects of the compressibility and the yield stress are investigated. Finally, section 5.4 contains the conclusions.

5.2 Governing equations

Let us consider the steady, compressible axisymmetric Poiseuille flow of a generalized Newtonian fluid. The geometry of the flow is given in Fig. 5.1. Assuming that the flow is creeping and neglecting gravity, the momentum equation is reduced to

$$-\nabla p + \nabla \cdot \boldsymbol{\tau} = 0 \tag{5.1}$$

where p is the pressure and $\boldsymbol{\tau}$ is the stress tensor. Let us also denote the velocity vector by $\mathbf{u}$ and the rate-of-strain tensor by $\dot{\boldsymbol{\gamma}}$, i.e.

$$\dot{\boldsymbol{\gamma}} \equiv \nabla \mathbf{u} + (\nabla \mathbf{u})^T , \tag{5.2}$$

where $\nabla \mathbf{u}$ is the velocity-gradient tensor, and the superscript T denotes its transpose. Under the assumption of zero bulk viscosity, which implies that the viscosity forces are only due to shear and not to volume variations [90], the viscous stress tensor for a generalized Newtonian fluid is defined by a constitutive equation of the following general form:

$$\boldsymbol{\tau} = \eta(\dot{\gamma}) \left(\dot{\boldsymbol{\gamma}} - \frac{2}{3} \nabla \cdot \mathbf{u}\, \mathbf{I} \right) , \tag{5.3}$$

where $\mathbf{I}$ is the identity tensor, and η is the viscosity which depends on the magnitude $\dot{\gamma}$ of the rate-of-strain tensor:

$$\dot{\gamma} = \sqrt{\frac{1}{2} II_{\dot{\boldsymbol{\gamma}}}} = \sqrt{\frac{1}{2} \dot{\boldsymbol{\gamma}} : \dot{\boldsymbol{\gamma}}} \tag{5.4}$$

II being the second invariant of a tensor.

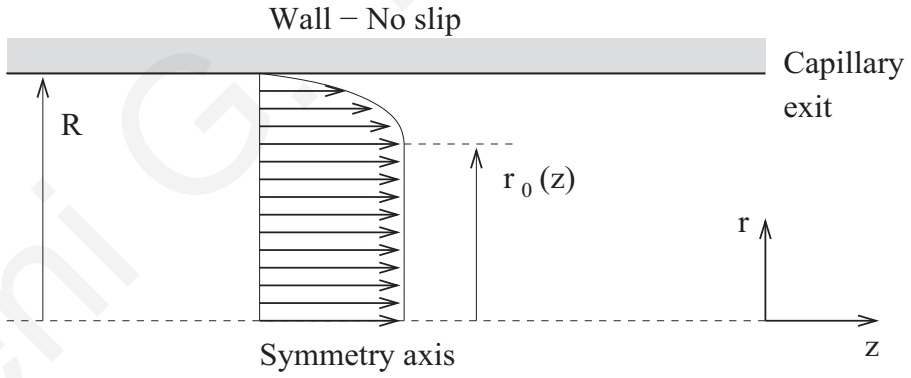

Figure 5.1: *Geometry of compressible axisymmetric Poiseuille flow of a Herschel-Bulkley fluid.*

The tensorial form of the Herschel-Bulkley constitutive equation is:

$$\begin{cases} \dot{\boldsymbol{\gamma}} \;=\; \mathbf{0}\,, & \tau \le \tau_0 \\ \boldsymbol{\tau} \;=\; \left(\frac{\tau_0}{\dot{\gamma}} \;+\; k\,\dot{\gamma}^{n-1}\right)\dot{\boldsymbol{\gamma}}\,, & \tau \ge \tau_0 \end{cases} \tag{5.5}$$

where τ_0 is the yield stress, k is the consistency index, n is the power law exponent, and τ is the magnitude of the stress tensor. The power-law fluid and the Bingham plastic are the special cases of the Herschel-Bulkley model for τ_0=0 and n=1, respectively.

For a weakly compressible flow, we can assume that the radial velocity component is zero. This assumption is consistent up to first order with Newtonian perturbation solutions in terms of compressibility [75, 88]. When u_r=0 the expression for $\dot{\gamma}$ is simplified as follows:

$$\dot{\gamma} \;=\; \sqrt{2\left(\frac{\partial u_z}{\partial z}\right)^2 \;+\; \left(\frac{\partial u_z}{\partial r}\right)^2} \tag{5.6}$$

We further assume that $\partial u_z/\partial z \ll 1$ so that the second term in the RHS of Eq. (5.3) is negligible and

$$\dot{\gamma} \;\simeq\; \left|\frac{\partial u_z}{\partial r}\right|\,. \tag{5.7}$$

Then from the r-momentum equation it is deduced that p=$p(z)$ and the z-momentum equation is reduced to

$$-\frac{dp}{dz} \;+\; \frac{1}{r}\,\frac{\partial}{\partial r}\left(r\tau_{rz}\right) \;=0 \tag{5.8}$$

where the pressure gradient is also a function of z. It should be noted that the above assumptions are valid when the radius of the tube is much smaller than its length [91]. Equation (5.5) is simplified as follows

$$\begin{cases} \frac{\partial u_z}{\partial r} \;=\; 0\,, & |\tau_{rz}| \le \tau_0 \\ \tau_{rz} \;=\; -\tau_0 \;+\; k\,\left(-\frac{\partial u_z}{\partial r}\right)^n\,, & |\tau_{rz}| \ge \tau_0 \end{cases} \tag{5.9}$$

Being a function of the pressure, the density also varies across the tube, i.e. ρ=$\rho(z)$. For the mass to be conserved, it must be

$$2\pi\rho(z)\int_0^R u_z(r,z)\,r dr \;=\; \text{const.}$$

or

$$\rho(z)\,Q(z) \;=\; Q_0 \tag{5.10}$$

where $Q(z)$ is the volumetric flow rate and Q_0=$Q(0)$.

In the following subsections we will first discuss the one-dimensional incompressible and then the two-dimensional compressible axisymmetric Poiseuille flow of a Herschel-Bulkley fluid. The equations for the planar compressible Poiseuille flow are given in the Appendix.

5.2.1 Incompressible axisymmetric Poiseuille flow

The solution of the incompressible Poiseuille flow of a Herschel-Bulkley fluid is straightforward and well known. However, it is presented here in order to show the analogy with the weakly compressible solution and to introduce the non-dimensionalization of the problem. In incompressible flow, the pressure gradient and the density are constant and the axial velocity component depends only on the radial coordinate [45]:

$$u_z(r) \;=\; \frac{n}{2^{1/n}\,(n+1)\,k^{1/n}}\,\left(-\frac{dp}{dz}\right)^{1/n}\begin{cases} (R\;-\;r_0)^{1/n+1}\,, & 0\le r\le r_0 \\ \left[(R\;-\;r_0)^{1/n+1}\;-\;(r\;-\;r_0)^{1/n+1}\right]\,, & r_0\le r\le R \end{cases} \tag{5.11}$$

where R is the capillary radius, $(-dp/dz)$ is the constant pressure gradient, and

$$r_0 \;=\; \frac{2\tau_0}{(-dp/dz)} < R \tag{5.12}$$

denotes the yield point, i.e. the point at which the material yields. Note that flow occurs only if $(-dp/dz) > 2\tau_0/R$. The volumetric flow rate is given by

$$Q \;=\; \frac{\pi\, n}{2^{1/n}\,(3n+1)\,k^{1/n}}\,\left(-\frac{dp}{dz}\right)^{1/n}\,R^{1/n+3}\left(1\;-\;\frac{r_0}{R}\right)^{1/n+1} \left\{1\;+\;\frac{2n}{2n\;+\;1}\,\frac{r_0}{R}\,\left[1\;+\;\frac{n}{n\;+\;1}\,\frac{r_0}{R}\right]\right\}. \tag{5.13}$$

In the cases of a Bingham plastic (n=1) and a power-law fluid (τ_0=0, r_0=0), Eq. (5.13) is reduced to

$$Q \;=\; \frac{\pi}{8\,\kappa}\,\left(-\frac{dp}{dz}\right)\,R^4\,\left[1\;-\;\frac{4}{3}\,\frac{r_0}{R}\;+\;\frac{1}{3}\left(\frac{r_0}{R}\right)^4\right] \tag{5.14}$$

and

$$Q \;=\; \frac{\pi\, n}{2^{1/n}\,(3n+1)\,k^{1/n}}\,\left(-\frac{dp}{dz}\right)^{1/n}\,R^{1/n+3} \tag{5.15}$$

respectively.

In what follows, it is preferable to work with dimensionless equations. Lengths are scaled by the tube radius, R, the velocity by the mean velocity, V_0, in the capillary, and the pressure by kV_0^n/R^n. With these scalings, the dimensionless velocity profile is written as follows

$$u_z(r) = \frac{n}{2^{1/n}(n+1)}\left(-\frac{dp}{dz}\right)^{1/n}\begin{cases}(1\;-\;r_0)^{1/n+1}\,, & 0\le r\le r_0\\ \left[(1\;-\;r_0)^{1/n+1}\;-\;(r\;-\;r_0)^{1/n+1}\right]\,, & r_0\le r\le 1\end{cases} \tag{5.16}$$

where all quantities are now dimensionless,

$$r_0 \;=\; \frac{2\,Bn}{(-dp/dz)} < 1 \tag{5.17}$$

and

$$Bn \;=\; \frac{\tau_0 R^n}{kV_0^n} \tag{5.18}$$

is the Bingham number. The dimensionless version of the constitutive equation, i.e. of Eq. (5.9), is:

$$\begin{cases}\dfrac{\partial u_z}{\partial r} \;=\; 0\,, & |\tau_{rz}|\le Bn\\[2ex] \tau_{rz} \;=\; -Bn\;+\;\left(-\dfrac{\partial u_z}{\partial r}\right)^n\,, & |\tau_{rz}|\ge Bn\end{cases} \tag{5.19}$$

Moreover, the dimensionless pressure-gradient is a solution of the following equation:

$$2^{1/n}\,\frac{3n+1}{n}\,\left(-\frac{dp}{dz}\right)^3 \;=\; \left[\left(-\frac{dp}{dz}\right) \;-\; 2\,Bn\right]^{1/n+1} \left[\left(-\frac{dp}{dz}\right)^2 + \frac{4n\,Bn}{2n+1}\,\left(-\frac{dp}{dz}\right) + \frac{8\,n^2\,Bn^2}{(n+1)(2n+1)}\right]. \tag{5.20}$$

In the case of a power-law fluid (Bn=0), the solution of Eq. (5.20) is simply

$$\left(-\frac{dp}{dz}\right) \;=\; 2\,\left(\frac{3n+1}{n}\right)^n. \tag{5.21}$$

In the case of a Bingham-plastic (n=1), Eq. (5.20) is reduced to

$$3\,\left(-\frac{dp}{dz}\right)^4 \;-\; 8\,(Bn+3)\,\left(-\frac{dp}{dz}\right)^3 \;+\; 16\,Bn^4 \;=\; 0 \tag{5.22}$$

It should be noted that flow occurs only if $(-dp/dz) > 2Bn$. For given values of Bn and n, Eq. (5.20) is easily solved for the pressure gradient using the Newton-Raphson method, and then the velocity profile can be constructed using Eq. (5.16). In Fig. 5.2, the velocity profiles calculated for n=0.5 and various Bingham numbers are shown. In Fig. 5.3, the velocity profiles obtained with $Bn = 10$ and $n = 0.5$, 1 and 1.5 are compared. With fixed volumetric flow rate, the size of the yielded region is reduced as the power-law exponent is increased. This is also shown in Fig. 5.4, where the yield point r_0 is plotted as a function of the Bingham number for various values of n.

5.2.2 Compressible axisymmetric Poiseuille flow

In the case of compressible flow, the pressure gradient and the density are functions of z and so are r_0 and the volumetric flow rate. It is easily deduced then that the dimensionless axial velocity (scaled by the mean velocity, V_0, at the exit of the capillary) is given by

$$u_z(r,z) = \frac{n}{2^{1/n}(n+1)}\left(-\frac{dp}{dz}\right)^{1/n}(z)\begin{cases} [1 \;-\; r_0(z)]^{1/n+1}\,, & 0 \le r \le r_0 \\ \left\{[1 \;-\; r_0(z)]^{1/n+1} \;-\; [r \;-\; r_0(z)]\right)^{1/n+1}\Big\}\,, & r_0 \le r \le 1 \end{cases} \tag{5.23}$$

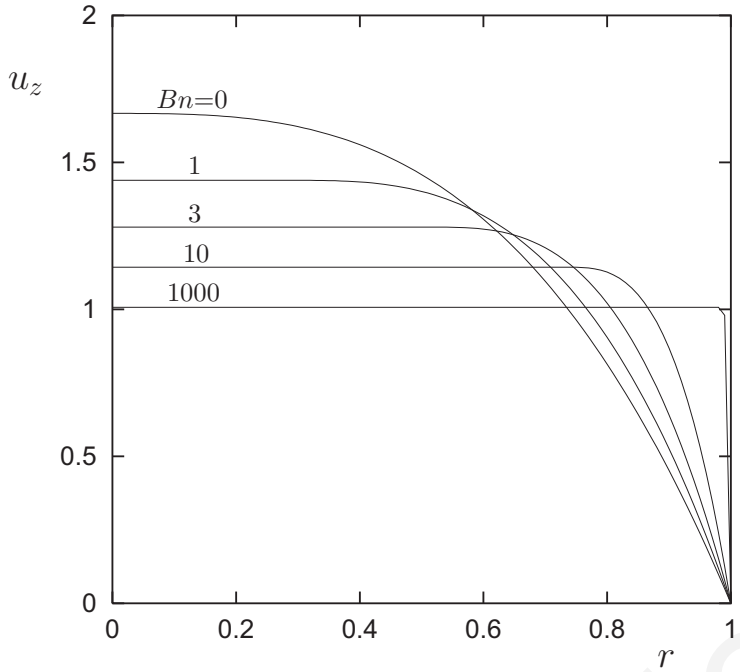

Figure 5.2: *Velocity profiles for the axisymmetric incompressible Poiseuille flow of a Herschel-Bulkley fluid with n=0.5 and various Bingham numbers.*

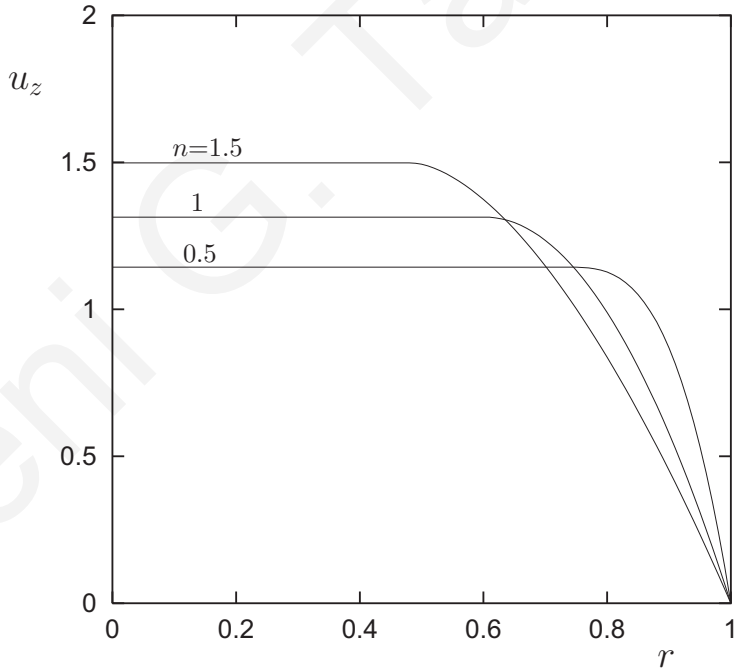

Figure 5.3: *Velocity profiles for the axisymmetric incompressible Poiseuille flow of a Herschel-Bulkley fluid with Bn=10 and various values of the power-law exponent.*

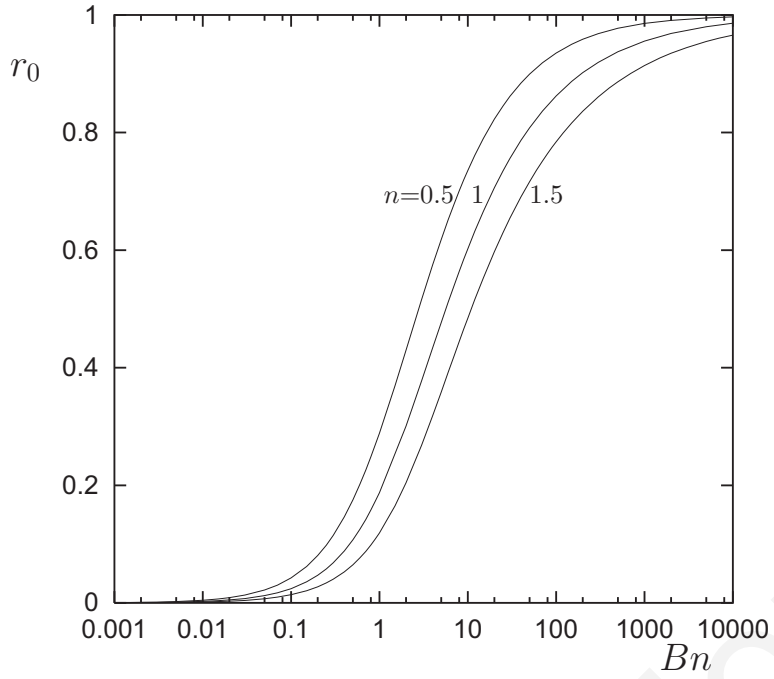

Figure 5.4: *Position of the yield point in axisymmetric incompressible Poiseuille flow of Herschel-Bulkley fluids.*

where

$$r_0(z) \;=\; \frac{2\,Bn}{(-dp/dz)(z)}\,. \tag{5.24}$$

It is clear that at the capillary exit (z=0), Eqs. (5.23) and (5.24) give the incompressible flow solution.

It should be pointed out that in steady compressible Poiseuille flow $r_0(z)$ is just a convenient idealization and not a real yield point. Since the axial velocity varies along the tube, $\partial u_z/\partial z > 0$ and thus $\dot{\gamma}$ is nonzero, which implies that unyielded regions cannot exist. Hence, $r_0(z)$ will be referred to as the pseudo-yield point. The fact that the classical plug region flow cannot be obtained in a compressible case was first emphasized by Vinay et al. [90]. However, these authors also calculated steady-state velocity profiles at the inlet and the outlet of the tube with the plug region at the center corresponding to half the pipe radius.

The pressure gradient $(-dp/dz)(z)$ across the capillary, i.e. for $z \leq 0$, can be calculated using

the conservation of mass, i.e. Eq. (5.10). It turns out that the pressure gradient is a solution of the following equation

$$2^{1/n}\,\frac{3n+1}{n\,\rho(p)}\,\left(-\frac{dp}{dz}\right)^3 \;=\; \left[\left(-\frac{dp}{dz}\right) \;-\; 2\,Bn\right]^{1/n+1} \left[\left(-\frac{dp}{dz}\right)^2 + \frac{4n\,Bn}{2n+1}\,\left(-\frac{dp}{dz}\right) + \frac{8\,n^2\,Bn^2}{(n+1)(2n+1)}\,\right] \tag{5.25}$$

which involves the pressure-dependent density of the fluid. The pressure gradient is obviously a function of p and is expected to decrease upstream.

The pressure dependence of the density is taken into account by means of a thermodynamic equation of state. At constant temperature and low pressures, the density can be represented by the linear approximation

$$\rho \;=\; \rho_0\,\left[1 \;+\; \beta\,(p \;-\; p_0)\,\right]\,, \tag{5.26}$$

where $\beta \equiv -(\partial\upsilon/\partial p)_{p_0,T}/\upsilon_0$ is the isothermal compressibility assumed to be constant, υ is the specific volume, ρ_0 and υ_0 are, respectively, the density and the specific volume at a reference pressure p_0, and T is the temperature. For comparison purposes, the following exponential equation is also used:

$$\rho \;=\; \rho_0\,e^{\beta\,(p\,-\,p_0)}\,. \tag{5.27}$$

This is equivalent to the linear equation of state for sufficiently small values of β and low pressures. A disadvantage of this equation is the fast growth of the density (for high values of β). On the other hand, the linear model may lead to negative values of the density. Obviously more sophisticated equations of state should be used for highly compressible flows. The equations of state are nondimensionalized scaling the density ρ by ρ_0 and the pressure as above. We thus get

$$\rho \;=\; 1 \;+\; B\,p \tag{5.28}$$

and

$$\rho \;=\; e^{Bp}\,, \tag{5.29}$$

where the reference pressure, p_0, has been set to zero, and B is the compressibility number,

$$B \;\equiv\; \frac{\beta\, k\, V_0^n}{R^n}\,. \tag{5.30}$$

The Mach number is defined by $Ma{=}V_0/c$, where c is the speed of sound in the fluid. In the present work, we consider subsonic flows such that $Ma \ll 1$.

Equation (5.25) can be integrated analytically in the case of a power-law fluid ($Bn{=}0$). With the linear equation of state one finds

$$p(z) \;=\; \frac{1}{B}\left\{[1 \;-\; 2\,(n+1)\,(1/n+3)^n\,Bz]^{1/(n+1)} \;-\; 1\right\} \tag{5.31}$$

and

$$u_z(r,z) \;=\; \frac{(3n+1)\,\left(1 \;-\; r^{1/n+1}\right)}{(n+1)\,[1 \;-\; 2\,(n+1)\,(1/n+3)^n\,Bz]^{1/(n+1)}} \tag{5.32}$$

Similarly, with the exponential equation of state one gets:

$$p(z) \;=\; \frac{1}{nB}\ln\left[1 \;-\; 2\,n\,(1/n+3)^n\,Bz\right] \tag{5.33}$$

and

$$u_z(r,z) \;=\; \frac{(3n+1)\,\left(1 \;-\; r^{1/n+1}\right)}{(n+1)\,[1 \;-\; 2\,n\,(1/n+3)^n\,Bz]^{1/n}} \tag{5.34}$$

Nevertheless, in the general case the pressure gradient and the pressure are calculated numerically.

Once the pressure $p(z)$ is known at a point (e.g. $p(0){=}0$), the pressure gradient $(-dp/dz)(z)$ can be calculated from Eq. (5.25), using the Newton-Raphson method, as before. Hence, we can write

$$-\frac{dp}{dz} \;=\; f(p)\,, \tag{5.35}$$

where the function f is implicitly known. If the pressure p_i at a point z_i is given, then the point z_{i+1} at which the pressure becomes p_{i+1}=p_i+Δp can be found by integrating the above equation:

$$z_{i+1} \;=\; z_i \;-\; \int_{p_i}^{p_i+\Delta p} \frac{dp}{f(p)}\,. \tag{5.36}$$

The integral in the RHS of the above equation was calculated using the composite Simpson's rule with 101 points and Δp=0.1. At each integration point, the pressure is known and the corresponding pressure gradient is calculated solving Eq. (5.25). It is also clear that we start at the channel exit (z_0=0) and march to the left, up to any desired distance upstream. The numerical code has been tested against the analytical expressions for the pressure distribution in the case of a power-law fluid.

5.3 Numerical results

Numerical results have been obtained using both the linear and exponential equations of state in order to investigate the effects of compressibility in Poiseuille flow of fluids with a yield stress. The effects of the three dimensionless parameters controlling the flow, i.e. the Bingham number, the compressibility number, and the power-law exponent have also been studied.

The pressure distributions for a Newtonian, a power-law, a Bingham and a Herschel-Bulkley fluid obtained using both the equations of state for $B = 0$, 0.01 and 0.1 are shown in Fig. 5.5. Note that the latter value of B is very high and corresponds to a highly compressible flow; it is used here only for illustration purposes. It is clear that the pressure gradient and the pressure required to drive the flow are reduced as compressibility is increased and increase with the Bingham number and the power-law exponent. The two equations of state give

essentially the same results only for sufficiently low compressibility numbers and/or near the die exit. Therefore, a careful selection of the equation of state is necessary when one studies compressible Poiseuille flow in very long channels.

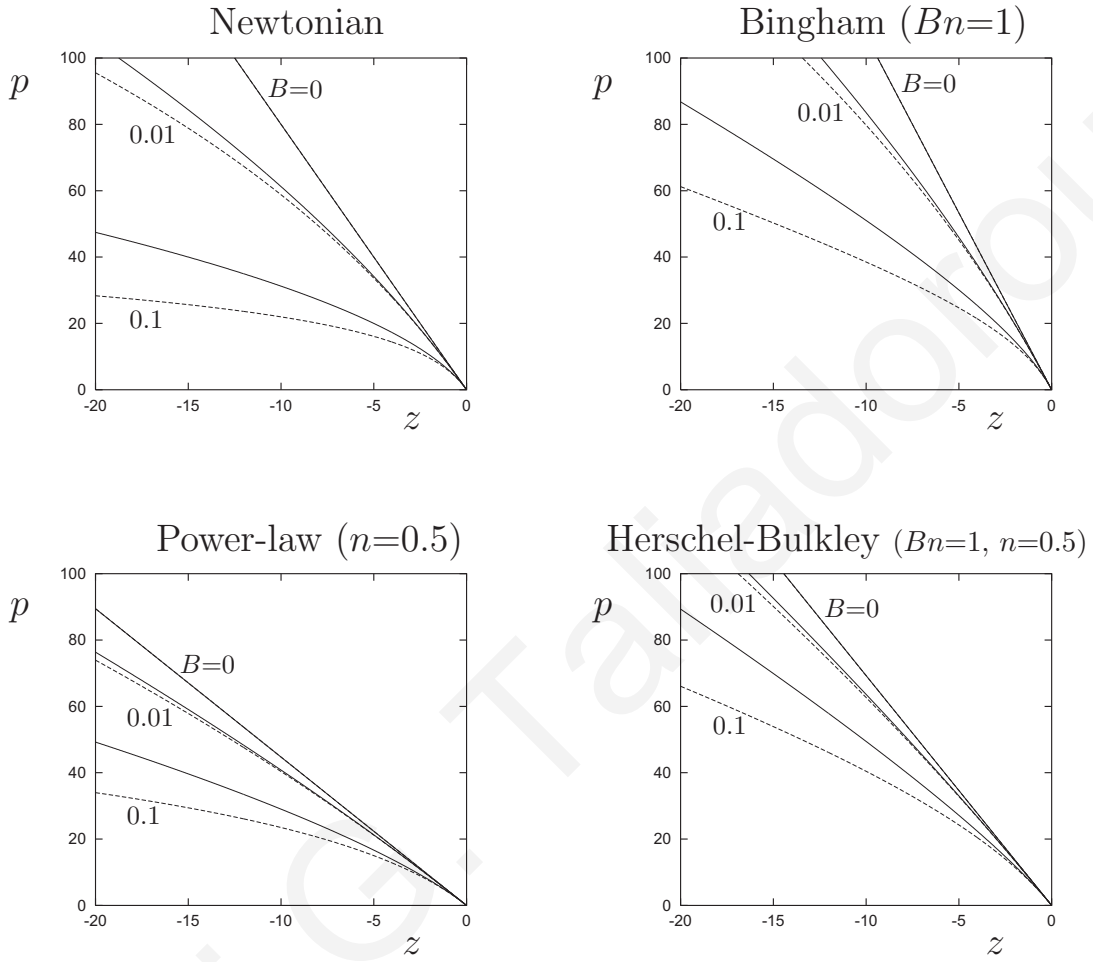

Figure 5.5: *Pressure distributions for four different fluids obtained with the linear (solid) and the exponential (dashed) equations of state in axisymmetric Poiseuille flow with B=0 (incompressible flow), 0.01 and 0.1.*

Once the pressure gradient is known as a function of z, the two-dimensional axial velocity can be constructed by means of Eq. (5.23). The velocity contours corresponding to the flows of Fig. 5.5 are shown in Fig. 5.6. Since the density becomes higher, the flow decelerates

upstream and forces the higher contours to bend towards the symmetry axis. In the case of fluids with a yield stress, this phenomenon is more abrupt, since just before the disappearance of a contour line, this is vertical to the symmetry plane and extends up to the corresponding pseudo-yield point. The results for the Bingham plastic (n=1) and the Herschel-Bulkley fluid (n=0.5) are quite similar. We can clearly observe that the pseudo-yield point moves towards the wall as we move upstream. The velocity profiles for the four fluids at z=0, -10 and -20 obtained using the linear equation of state with B=0.1 are given in Fig. 5.7. As already mentioned, the presence of unyielded regions in steady compressible viscoplastic flow is only an idealization. However, regions of plug-like flow may still exist as indicated by the steady-state numerical results of Vinay et al. [90].

The effect of the equation of state in the case of a Bingham fluid (Bn=10) is illustrated in Fig. 5.8a, where the pressure distributions calculated with B=0 and 0.01 using both equations are plotted. The velocity profile at the capillary exit is shown in Fig. 5.8b. In Fig. 5.9, the positions of the pseudo-yield point calculated using both equations of state for three compressibility numbers are shown. In the incompressible flow, the yield point is, of course, independent of the axial distance. In the compressible flow, r_0 moves towards the wall as we move upstream, which implies that the size of the plug-like region increases. This phenomenon is better observed in the exponential case due to the faster increase of the density. In Fig. 5.10, we plot the velocity contours of a Bingham fluid with $Bn = 10$ and $B = 0$, 0.01 and 0.02 using both equations of state. Upstream, the velocity reduces rapidly in the case of the exponential equation of state, which is expected because of the faster increase of the density. As a result, the velocity contours are crowded towards the exit plane. In Fig. 5.11, we plot the velocity profiles at different distances from the capillary exit of a Bingham fluid with Bn=10 and B=0.01 using again both equations of state.

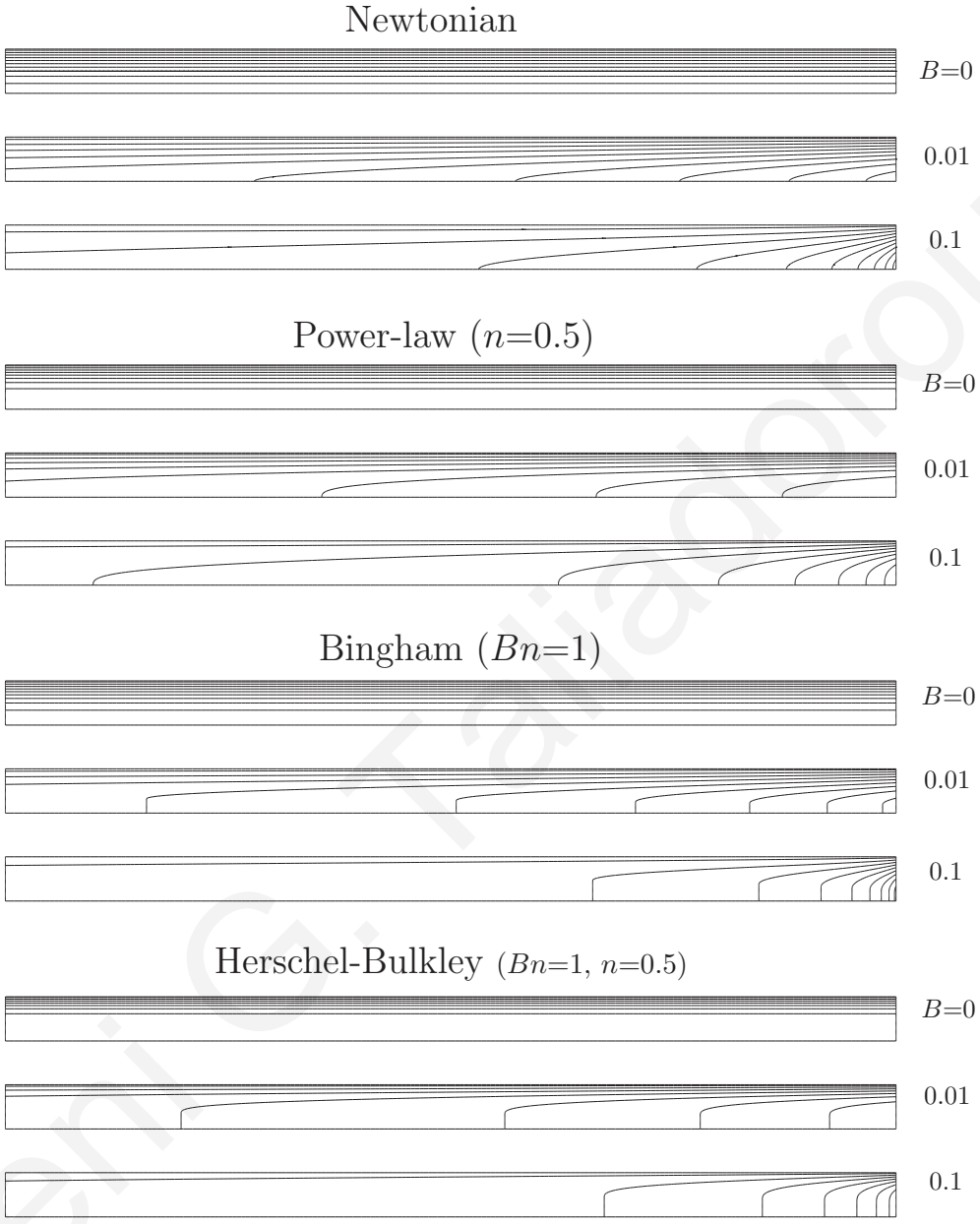

Figure 5.6: *Velocity contours for four different fluids obtained for the axisymmetric Poiseuille flow with the linear equation of state with B=0 (incompressible flow), 0.01 and 0.1.*

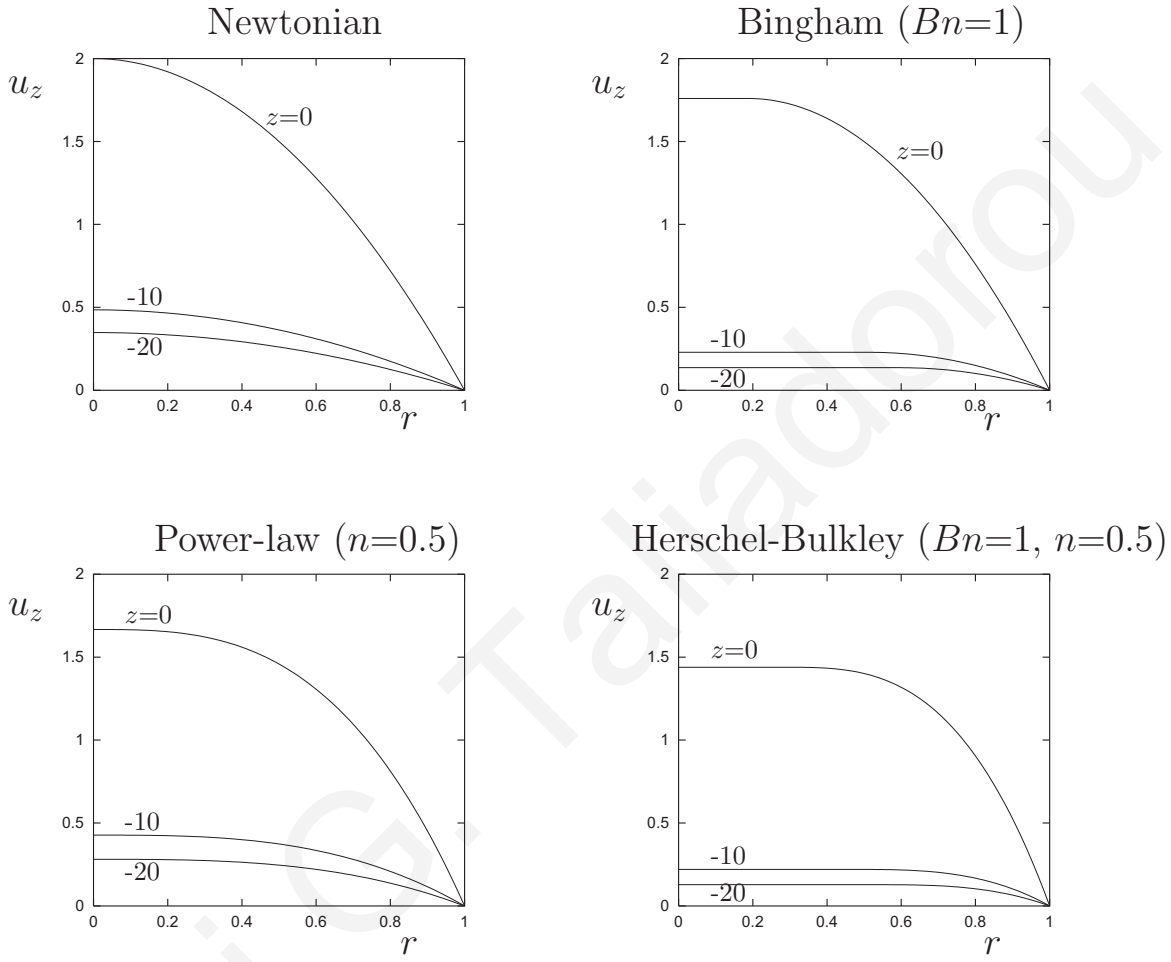

Figure 5.7: *Velocity profiles at z=0, -10 and -20 for four different fluids obtained with the linear equation of state in axisymmetric Poiseuille flow with B=0.1.*

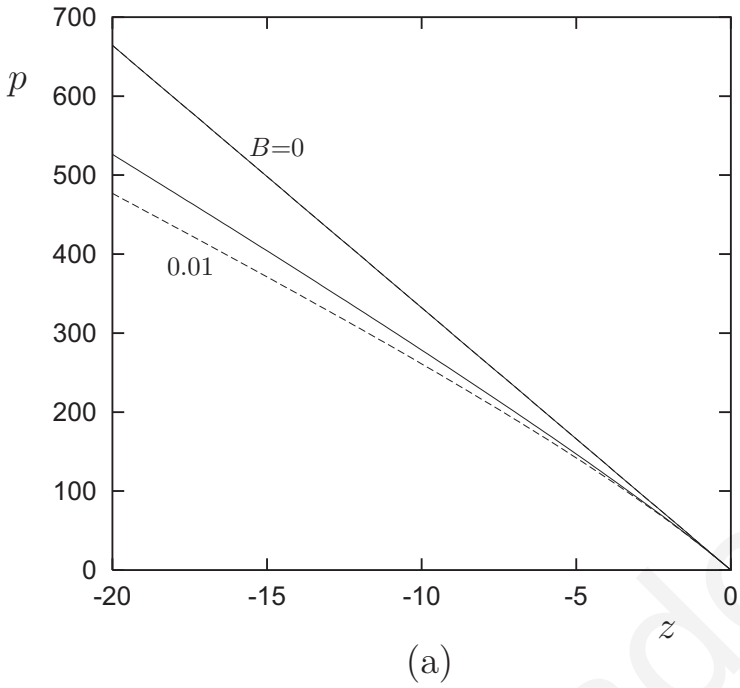

(a)

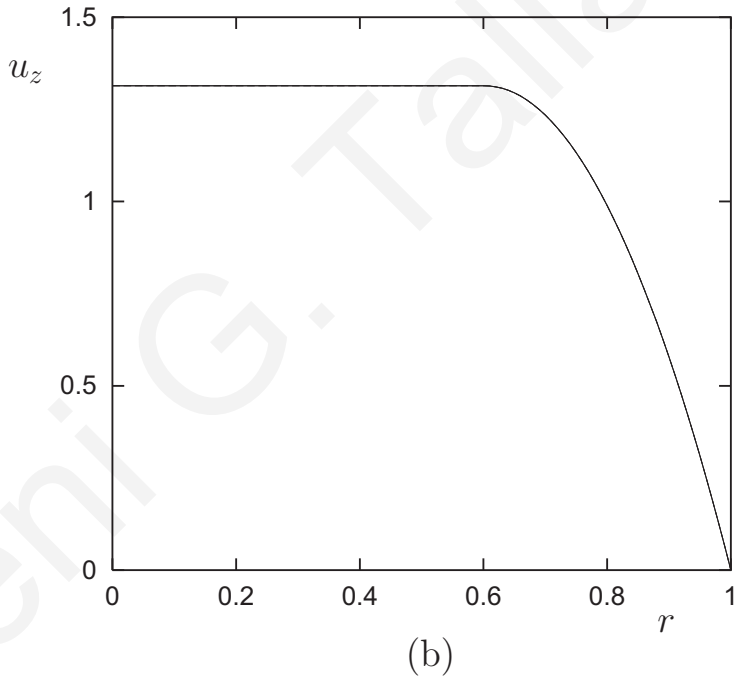

(b)

Figure 5.8: *(a) Pressure distributions in axisymmetric Poiseuille flow of a Bingham fluid with Bn=10, and B=0 and 0.01, and the linear (solid) and the exponential (dashed) equations of state; (b) Velocity profile at the capillary exit.*

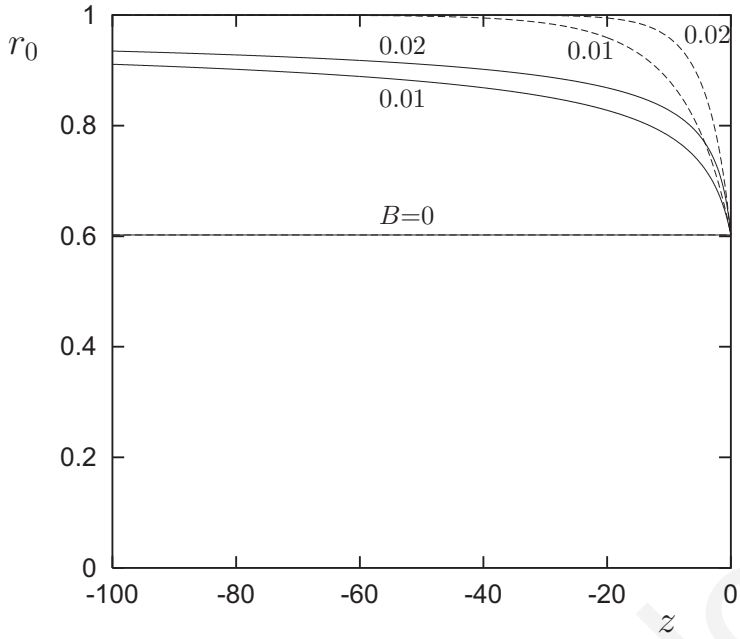

Figure 5.9: *Position of the pseudo-yield point in axisymmetric Poiseuille flow of a Bingham fluid for Bn=10 and various compressibility numbers. The solid lines correspond to the linear equation of state and the dashed ones to the exponential one.*

Figure 5.12 shows the effects of the Bingham number on the pressure distribution and the position of the pseudo-yield point in the case of Bingham flow (n=1) using the linear equation of state with B=0.01. We observe that the pressure increases upstream and the pseudo-yield point moves faster towards the wall as the Bingham number increases. This is more clearly shown in Fig. 5.13, where the velocity contours for different Bingham numbers are shown. As the Bn is increased the unyielded region moves towards the exit of the die.

5.4 Conclusions

We have derived approximate semi-analytical solutions of the axisymmetric and plane Poiseuille flows of weakly compressible Herschel-bulkley fluid. The two-dimensional axial velocity is given by an expression similar to that for the incompressible flow, with the pressure-gradient

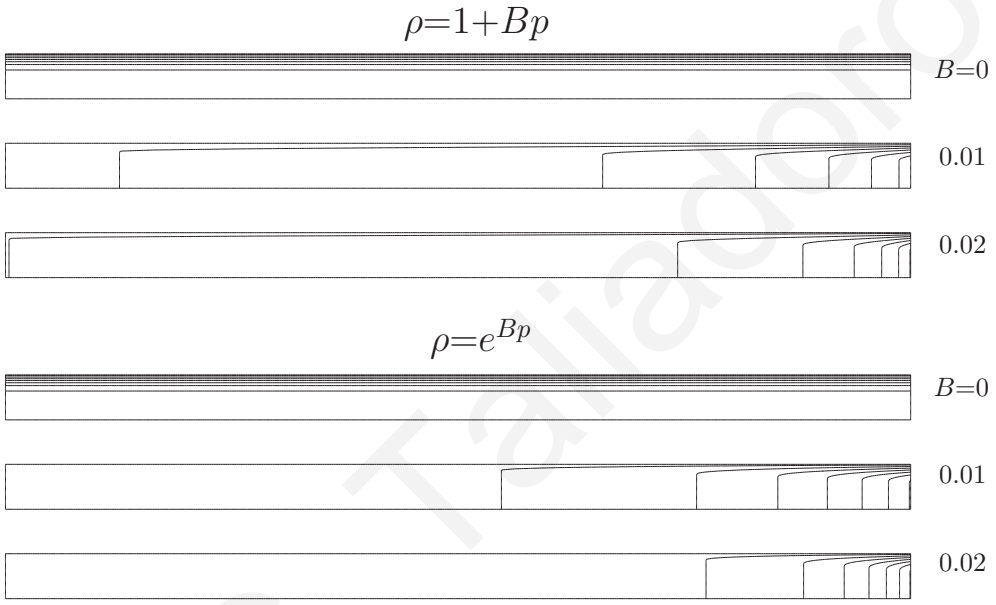

Figure 5.10: *Velocity contours in axisymmetric Poiseuille flow of a Bingham fluid with Bn=10 and different compressibility numbers using the linear and the exponential equations of state.*

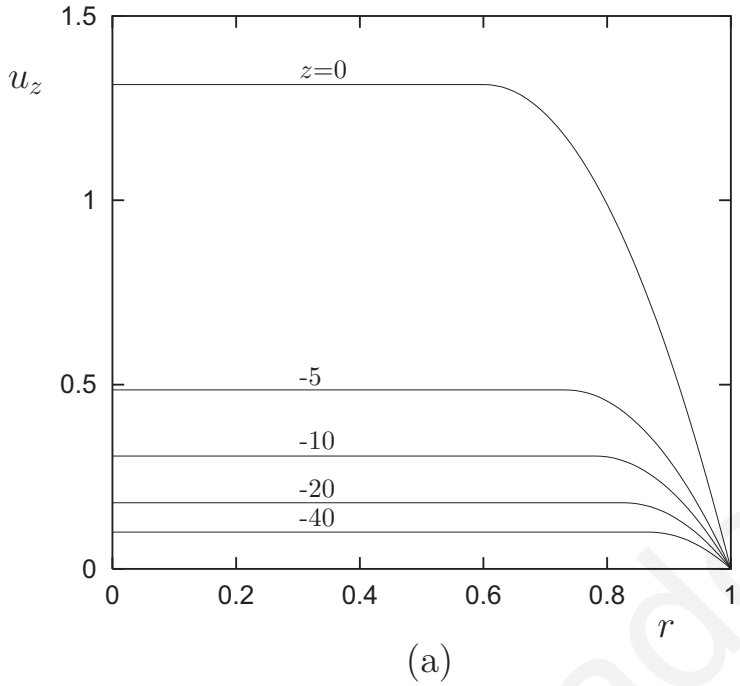

(a)

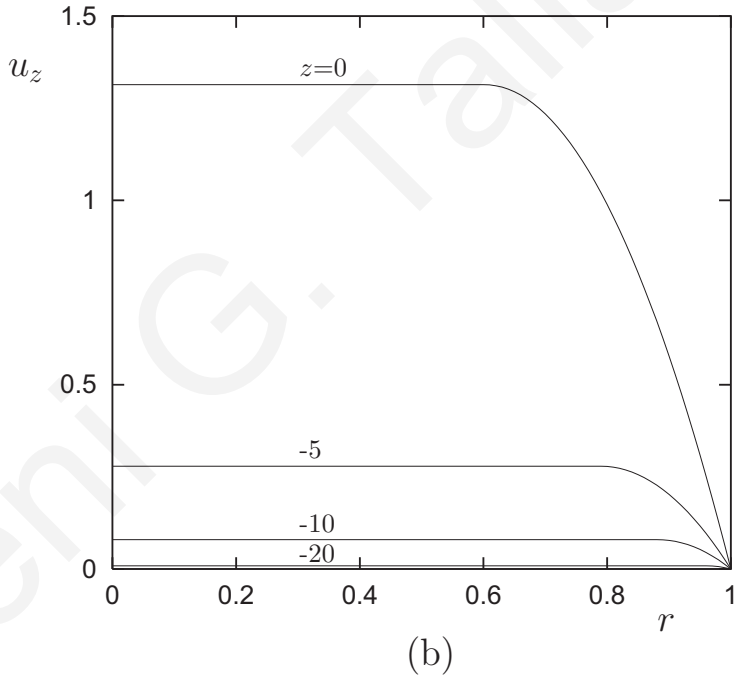

(b)

Figure 5.11: *Velocity profiles at different distances from the capillary exit in axisymmetric Poiseuille flow of a Bingham fluid with Bn=10 and B=0.01: (a) Linear equation of state; (b) Exponential equation of state.*

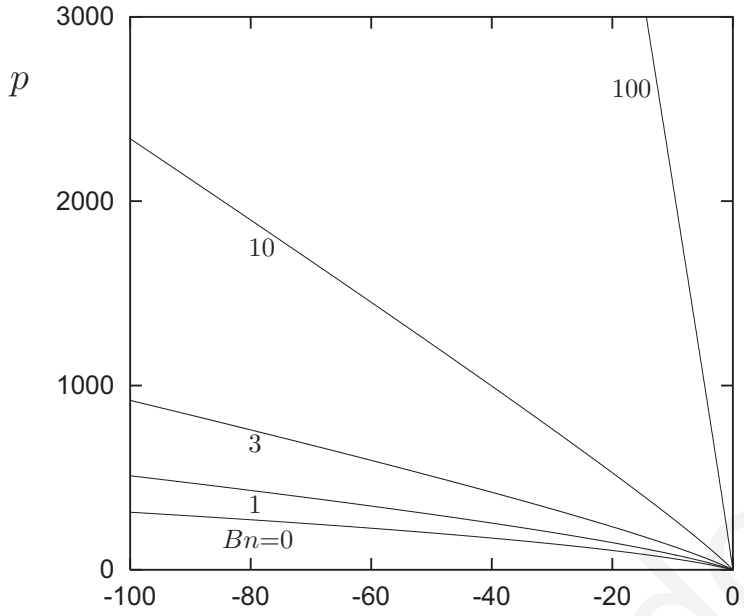

(a)

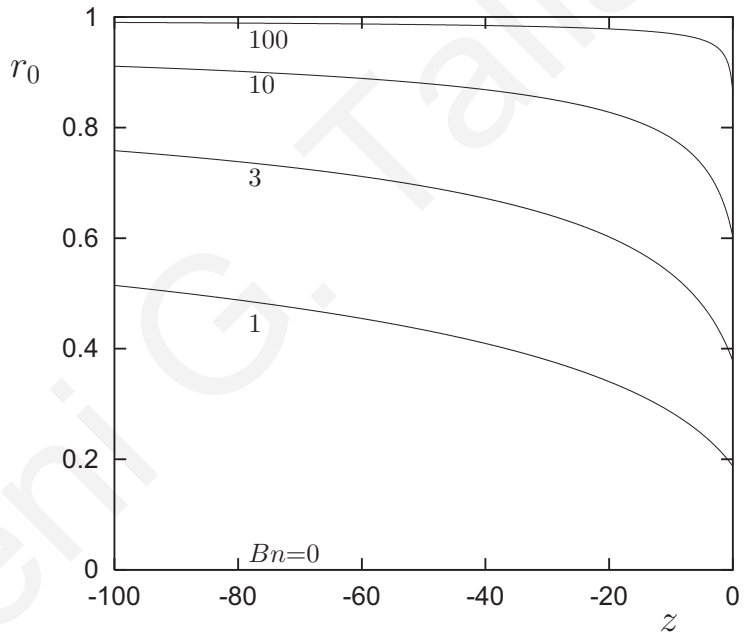

(b)

Figure 5.12: *Effect of the Bingham number in axisymmetric Poiseuille flow of a Bingham fluid with the linear equation of state and B=0.01: (a) Pressure distribution; (b) Position of the yield point.*

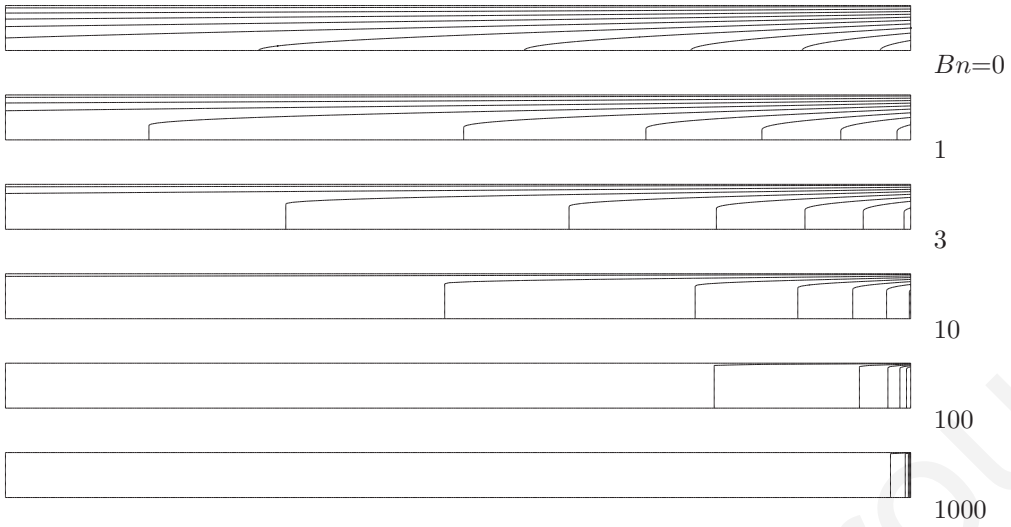

Figure 5.13: *Effect of the Bingham number on the velocity contours in axisymmetric compressible Poiseuille flow of a Bingham fluid; linear equation of state, B=0.01.*

and the yield stress point assumed to be functions of the axial coordinate. The pressure gradient is calculated by means of numerical integration starting at the exit of the tube and marching upstream. The effects of compressibility have been studied by using a linear and an exponential equation of state. The effects of the yield stress and the power-law exponent on the pressure gradient and the velocity have also been investigated. Our calculations lead to the following conclusions:

(a) The pressure required to drive the flow for a given tube length is reduced with compressibility.

(b) The linear and the exponential equations of state give similar predictions only for sufficiently low compressibility numbers and/or for short tubes. Hence, the equation of state should be chosen very carefully in numerical simulations of compressible flow in long tubes.

(c) The two-dimensional axial velocity is characterized by plug-like regions the size of which increases upstream, in agreement with the more sophisticated numerical simulations of Vinay et al. [90].

(d) With the exponential equation of state, the upstream growth of the pseudo-unyielded region is much faster than with the linear equation of state.

5.5 Appendix: Compressible plane Poiseuille flow

In plane Poiseuille flow, lengths are scaled by the channel-halfwidth, H, the velocity by the mean velocity, V_0, at the exit of the channel, and the pressure by kV_0^n/H^n. Under the same assumptions used for the axisymmetric flow, the dimensionless velocity profile in the case of compressible plane flow is written as follows

$$u_x(x,y) \;=\; \frac{n}{n+1}\left(-\frac{dp}{dx}\right)^{1/n}(x)\begin{cases}\left[1 \;-\; y_0(x)\right]^{1/n+1}, & 0 \le y \le y_0\\ \left\{\left[1 \;-\; y_0(x)\right]^{1/n+1} \;-\; \left[y \;-\; y_0(x)\right]\right)^{1/n+1}\Big\}, & y_0 \le y \le 1\end{cases} \tag{5.37}$$

where

$$y_0(x) \;=\; \frac{Bn}{(-dp/dx)(x)} \tag{5.38}$$

and

$$Bn \;=\; \frac{\tau_0 H^n}{kV_0^n} \tag{5.39}$$

is the Bingham number. The dimensionless pressure-gradient is a solution of the following equation:

$$\frac{2n+1}{n\,\rho(p)}\left(-\frac{dp}{dx}\right)^2 \;=\; \left[\left(-\frac{dp}{dx}\right) \;-\; Bn\right]^{1/n+1}\left[\frac{n}{n+1}\,Bn \;+\; \left(-\frac{dp}{dx}\right)\right]. \tag{5.40}$$

It is clear that at the channel exit (x=0), Eqs. (5.37) and (5.38) yield the solution for incompressible flow.

In the case of a power-law fluid, the solution of Eq. (5.40) is simply

$$\left(-\frac{dp}{dx}\right) \;=\; \left(\frac{2n+1}{n\,\rho(p)}\right)^n. \tag{5.41}$$

In the case of a Bingham-plastic, Eq. (5.40) is reduced to

$$2\left(-\frac{dp}{dx}\right)^3 - 3\,(Bn+\frac{2}{\rho(p)})\left(-\frac{dp}{dx}\right)^2 + Bn^3 = 0\,, \tag{5.42}$$

which has the following solution:

$$\left(-\frac{dp}{dx}\right) = \left(\frac{Bn}{2} + \frac{1}{\rho(p)}\right)\left[1 + 2\cos\left[\frac{1}{3}\cos^{-1}\left\{1 - \frac{2Bn^3}{\left(Bn + \frac{2}{\rho(p)}\right)^3}\right\}\right]\right]. \tag{5.43}$$

In Figs. 5.14-5.23 some representative results for the compressible plane Poiseuille flow are provided.

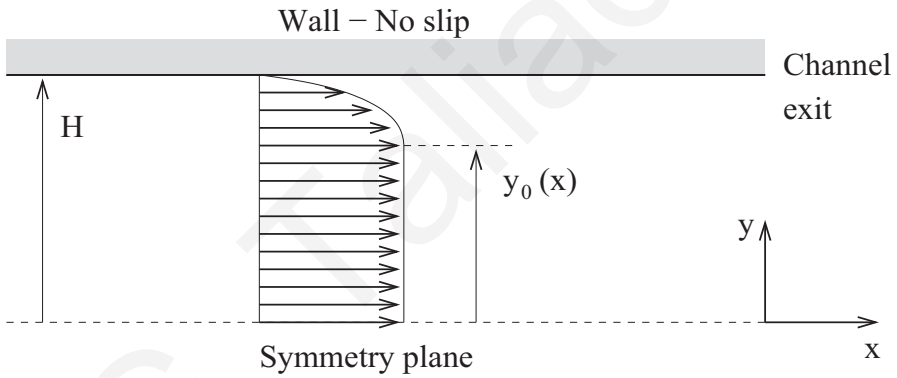

Figure 5.14: *Geometry of compressible plane Poiseuille flow of a Herschel-Bulkley fluid.*

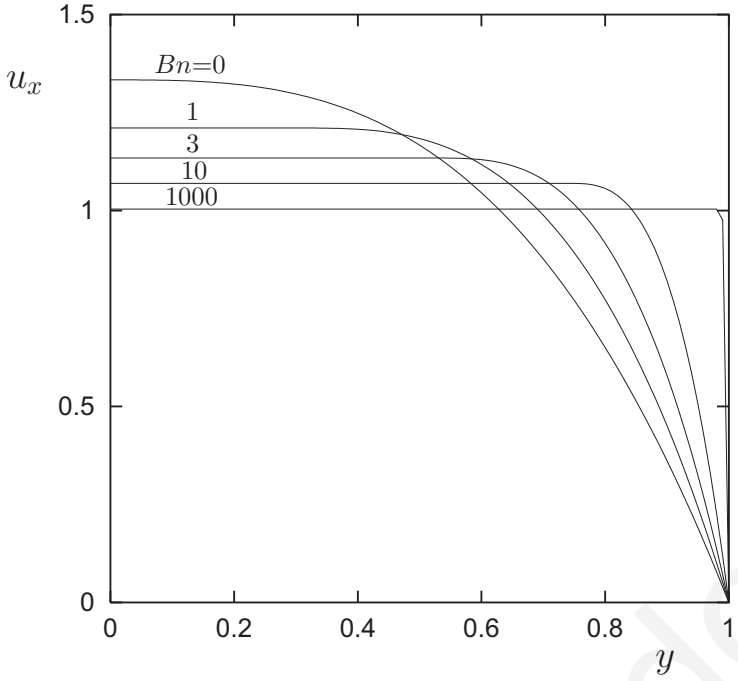

Figure 5.15: *Velocity profiles for the plane incompressible Poiseuille flow of a Herschel-Bulkley fluid with n=0.5 and various Bingham numbers.*

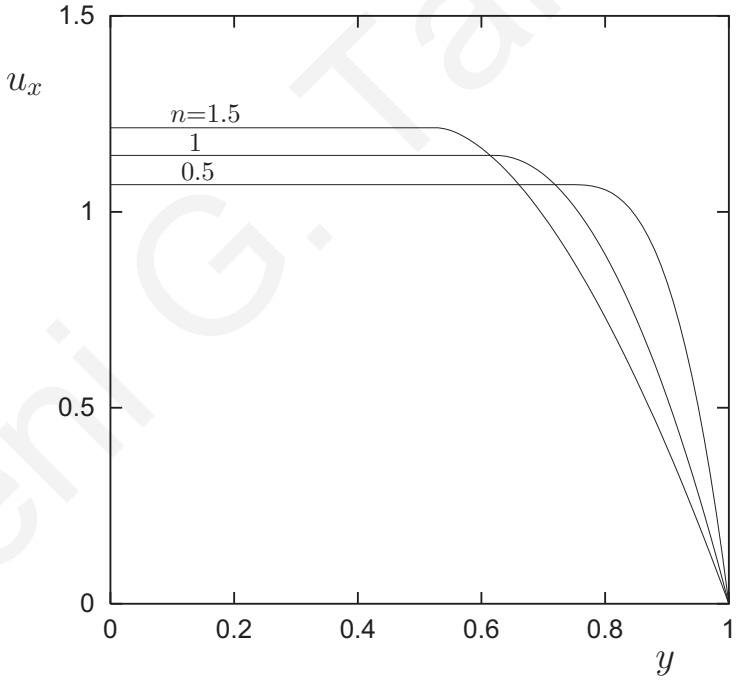

Figure 5.16: *Velocity profiles for the plane incompressible Poiseuille flow of a Herschel-Bulkley fluid with Bn=10 and various values of the power-law exponent.*

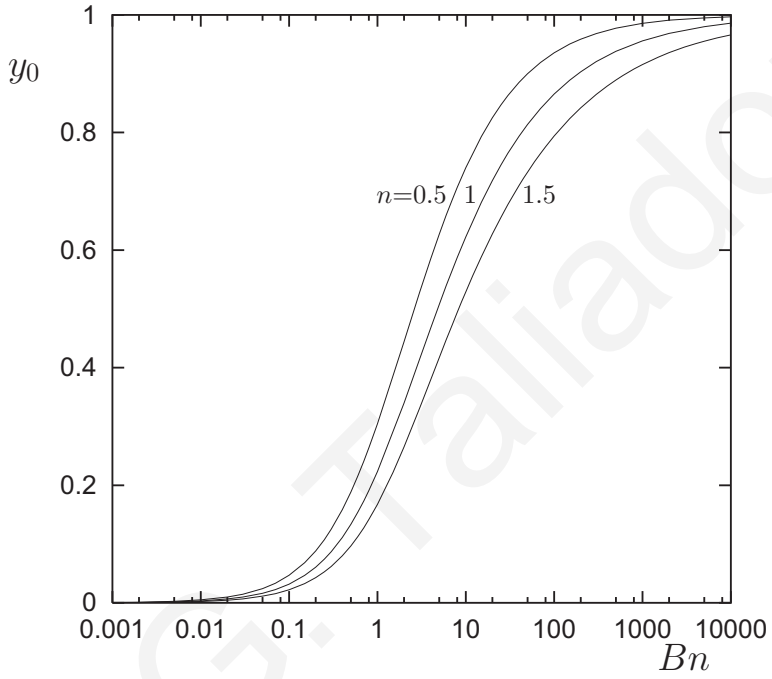

Figure 5.17: *Position of the yield point in plane incompressible Poiseuille flow of Herschel-Bulkley fluids.*

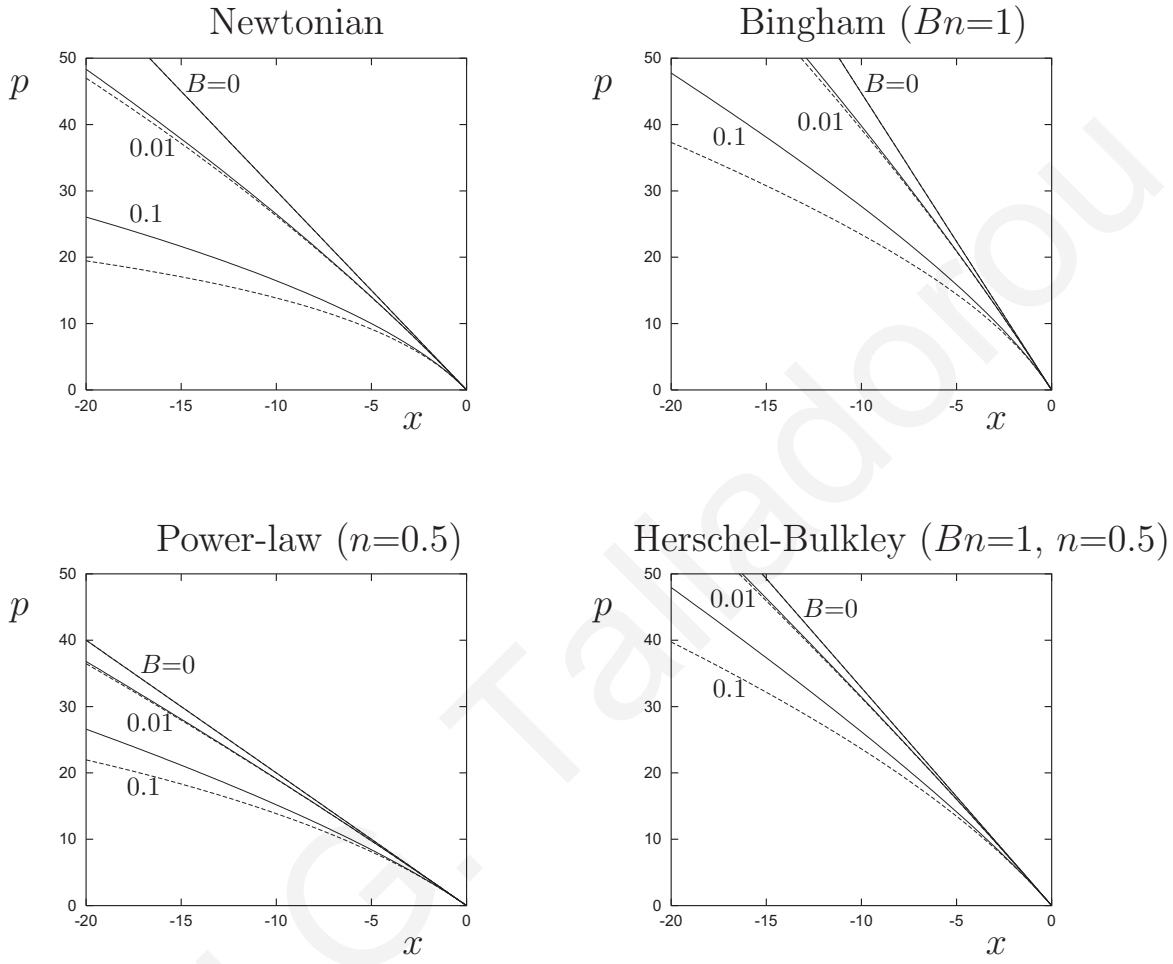

Figure 5.18: *Pressure distributions for four different fluids obtained with the linear (solid) and the exponential (dashed) equations of state with B=0 (incompressible flow), 0.01 and 0.1.*

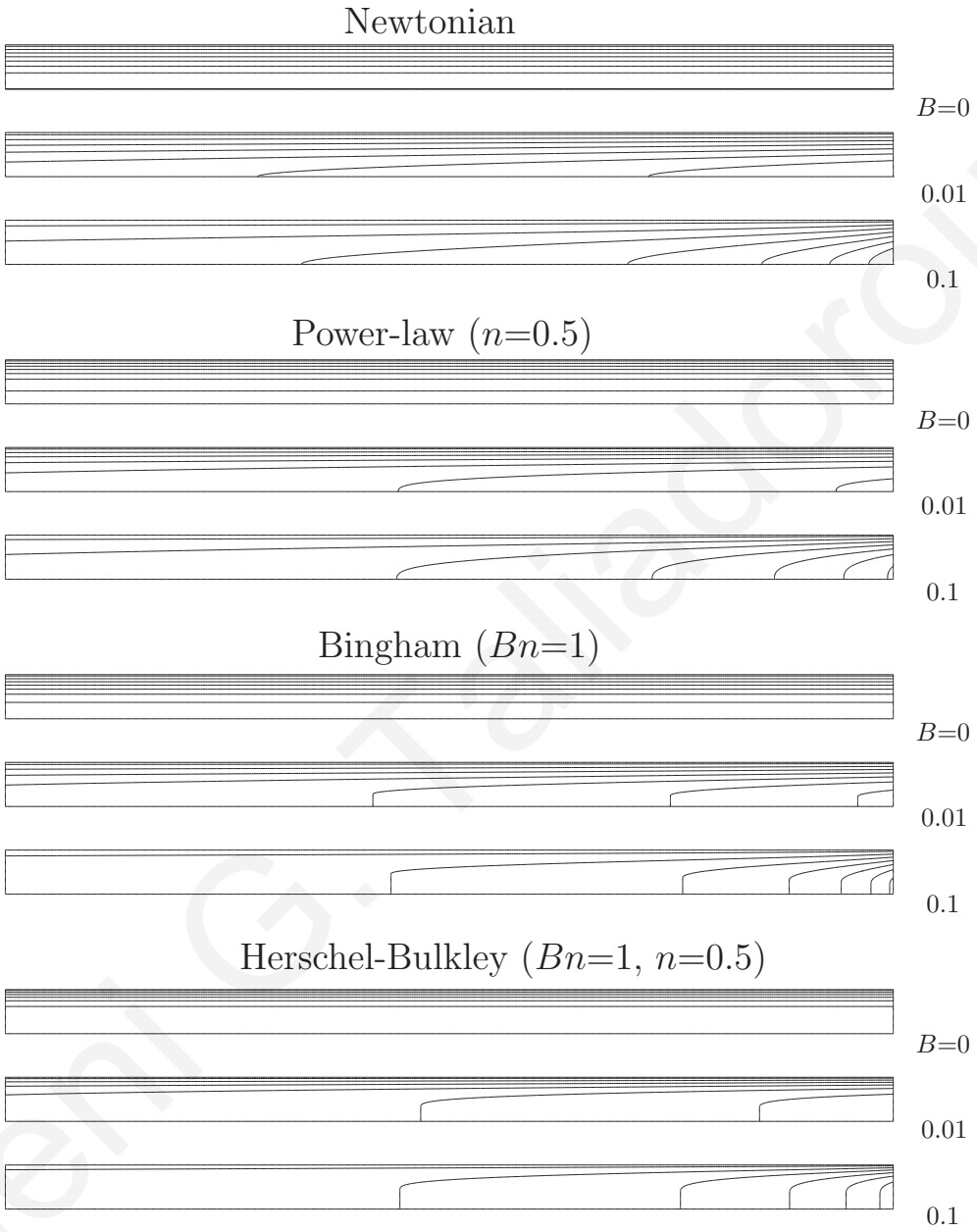

Figure 5.19: *Velocity contours for four different fluids obtained with the linear equation of state with B=0 (incompressible flow), 0.01 and 0.1.*

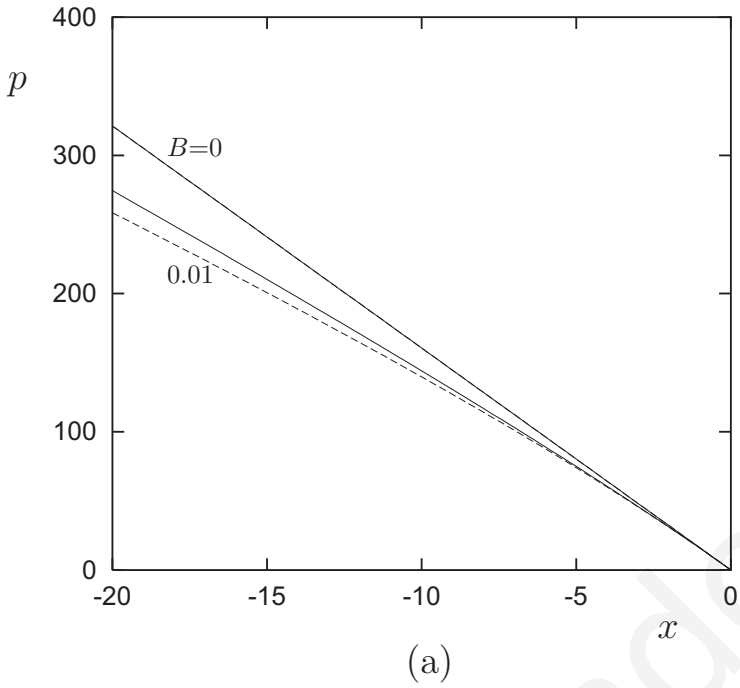

(a)

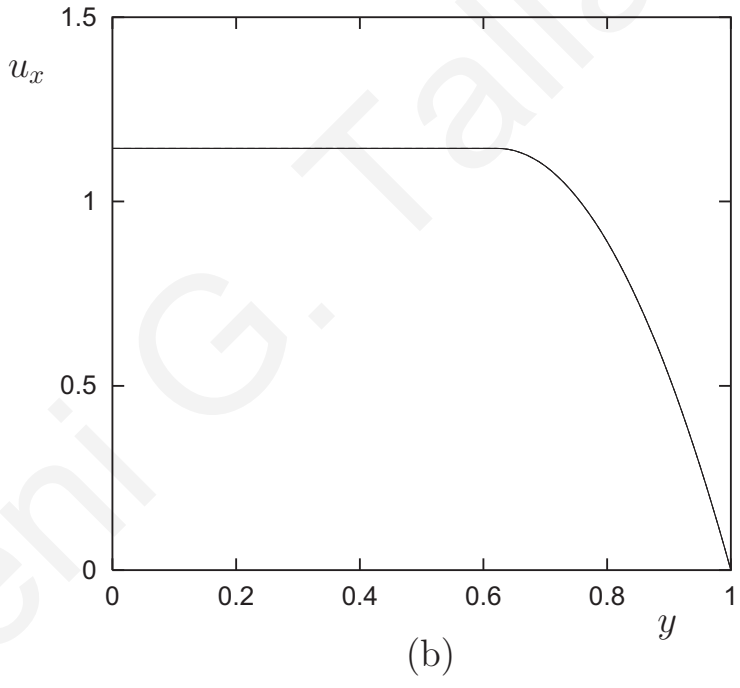

(b)

Figure 5.20: *(a) Pressure distributions in plane Poiseuille flow of a Bingham fluid with Bn=10 and B=0 and 0.01, using the linear (solid) and the exponential (dashed) equations of state; (b) Velocity profile at the channel exit.*

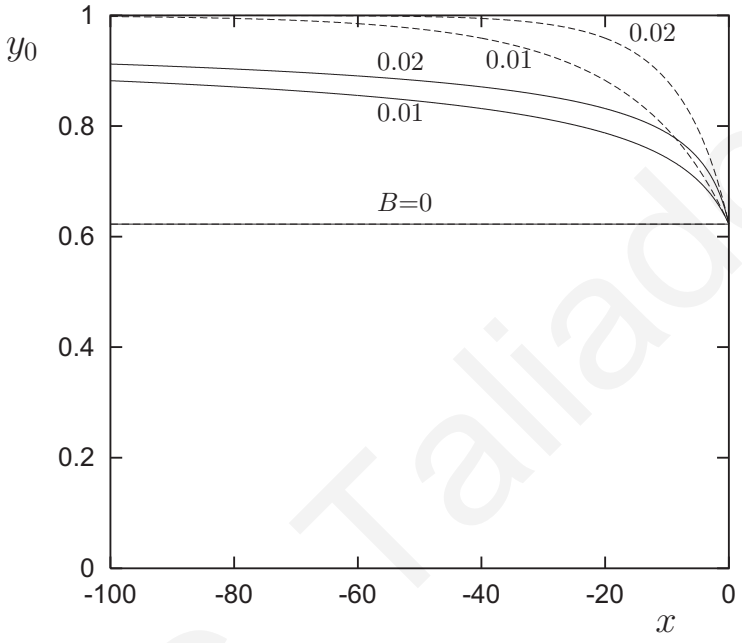

Figure 5.21: *Position of the pseudo-yield point in plane Poiseuille flow of a Bingham fluid for Bn=10 and various compressibility numbers. The solid lines correspond to the linear equation of state and the dashed ones to the exponential one.*

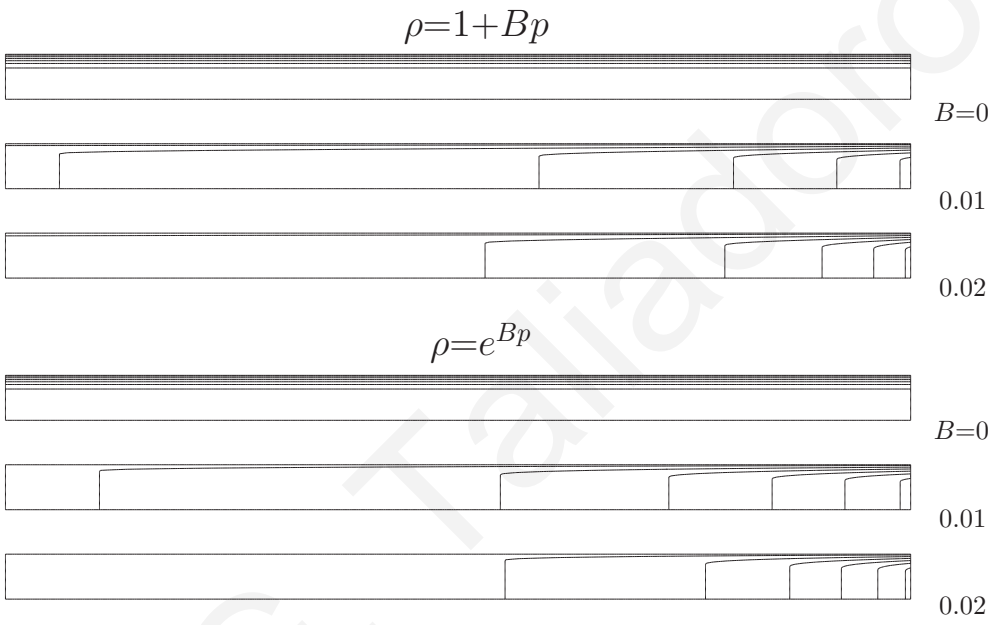

Figure 5.22: *Velocity contours in plane Poiseuille flow of a Bingham fluid with Bn=10 and different compressibility numbers using the linear and the exponential equation of state.*

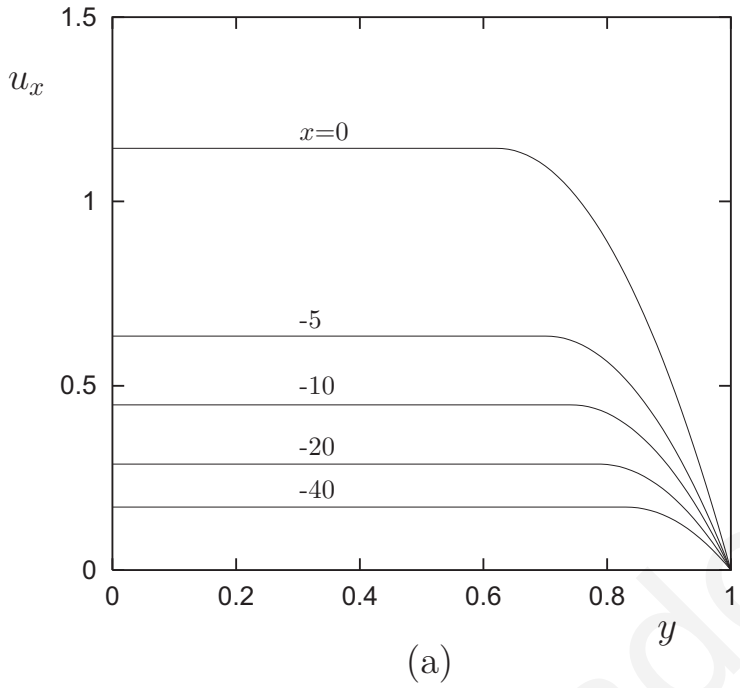

(a)

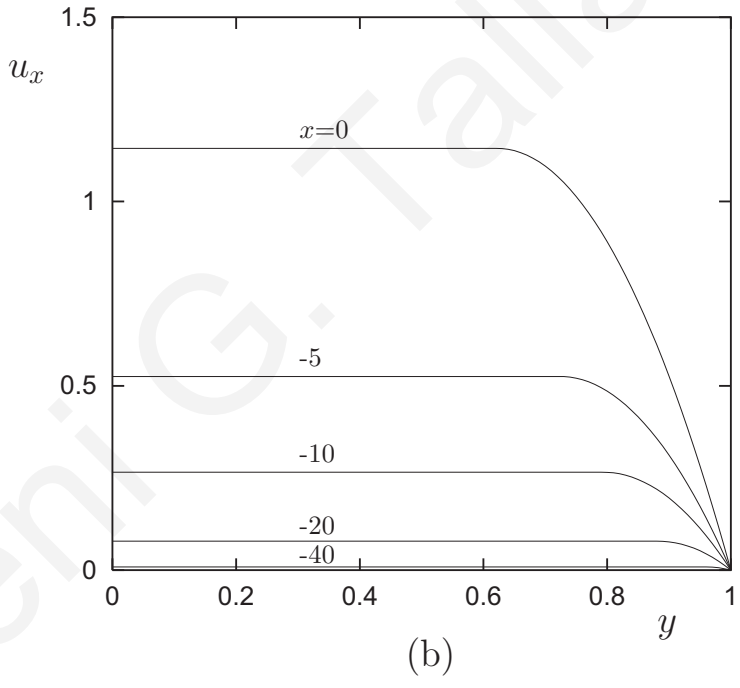

(b)

Figure 5.23: *Velocity profiles at different distances from the channel exit in plane Poiseuille flow of a Bingham fluid with Bn=10 and B=0.01: (a) Linear equation of state; (b) Exponential equation of state.*

Chapter 6

Summary and Future work

In this thesis, we have solved some weakly compressible Newtonian and generalized Newtonian flows using numerical (finite-element) and perturbation solution methods. In Chapter 2, we considered the time-dependent, compressible extrusion of a Carreau fluid over the reservoir-die-extrudate region using finite elements in space and a fully-implicit scheme in time. The objective was to simulate and investigate numerically the so-called stick-slip instability observed during the extrusion of polymer melts. A nonmonotonic slip law based on experimental data on polyethylene melts was assumed to hold along the die wall and the velocity at the entrance of the reservoir was taken to be fixed and uniform. As in the case of the extrudate-swell flow, the combination of compressibility and nonlinear slip leads to self-sustained oscillations of the pressure drop and of the mass flow rate in the unstable regime. The effects of the reservoir volume, the imposed flow rate, and the capillary length on the amplitude and the frequency of the pressure and free surface oscillations have been studied and comparisons were made with experimental observations. The numerical simulations agree well with the following experimental observations: (a) the pressure and flow rate oscillations follow the hysteresis loop defined by the two branches of the flow curve, and the

volumetric flow rate is characterized by instantaneous jumps between the two branches; (b) the amplitude and the period of the pressure oscillations increase linearly with the capillary length, since the hysteresis loop becomes larger; (c) for small capillary lengths, the pressure is a continuous monotonic function of Q, and no oscillations are observed; and (d) the period of the pressure and flow rate oscillations increases linearly with the reservoir length, while their amplitudes and waveforms are fairly constant. Nevertheless, the period of the pressure oscillations, when plotted versus the reservoir volume, appears to pass through the origin, which is not the case with extrapolated experimental data [20, 40, 73, 74]. In agreement with certain experiments [58, 61, 96, 92], the period of the pressure oscillations passes through a minimum, when this is plotted versus the imposed volumetric flow rate. The compression part of the pressure oscillations is relatively reduced, as Q is increased.

In Chapter 3, the axisymmetric and plane extrusion flows of a liquid foam were simulated assuming that the foam is a homogeneous compressible Newtonian fluid that slips along the walls. Compressibility effects were investigated using both a linear and an exponential equation of state. The numerical results confirm previous reports that the swelling of the extrudate decreases initially as the compressibility of the fluid is increased and then increases considerably. The latter increase was sharper in the case of the exponential equation of state, which indicates the importance of using an appropriate equation of state in foam flow simulations. In the case of non-zero inertia, high compressibility was found to lead to a contraction of the extrudate after the initial expansion, similar to that observed experimentally with liquid foams, and to subsequent decaying oscillations of the extrudate surface. The time-dependent calculations show that the latter oscillatory steady-state solutions are stable. These steady-state latter oscillatory solutions were not affected by the length of the extrudate region nor by the boundary condition along the wall.

In Chapter 4, we have solved both the planar and axisymmetric isothermal Poiseuille flows of weakly compressible Newtonian liquids with constant shear and bulk viscosities up to the second-order using the perturbation method. A linear equation of state was assumed and a perturbation analysis of the primary flow variables was performed using compressibility as the perturbation parameter. The effects of compressibility, the bulk viscosity, the aspect ratio, and the Reynolds number on the velocity and pressure fields were studied and comparisons were made with available analytical results [33, 75, 88].

Finally in Chapter 5, we have derived approximate semi-analytical solutions of the steady, creeping, weakly compressible plane and axisymmetric Poiseuille flows of a Herschel-Bulkley fluid. Since the flow is weakly compressible, the radial velocity component is assumed to be zero and the derivatives of the axial velocity with respect to the axial direction are assumed to be much smaller than those with respect to the radial direction. The axial velocity is then given by an expression similar to that holding for the incompressible flow, the only difference being that the pressure gradient was a function of the axial coordinate and satisfies a non-linear equation involving the density of the fluid. A linear as well as an exponential equation of state, relating the density of the fluid to the pressure, were considered to study the effects of compressibility. Both equations of state gave similar predictions for sufficiently low compressibility numbers and/or for short tube. The pressure distribution along the flow direction was calculated by means of numerical integration and the two-dimensional axial velocity can then be constructed. The effects of compressibility, equation of state, the Bingham number and the power-law exponent on the solutions were investigated.

As is always the case, many questions regarding the above problems are still open. Here are some suggestions for future work.

1. In the two-dimensional numerical study of the stick-slip extrusion instability (Chapter

2), it has been assumed that the inlet boundary is fixed which is not true since the piston is moving. It will be interesting to solve the problem taking the motion of the piston into account, i.e. employing a moving mesh that is updated at every time step.

2. In the case of the numerical simulation of the extrusion of strongly compressible Newtonian liquids (Chapter 3), another direction for research is the study of effects of compressibility and equation of state with a different constitutive equation, such as Bingham plastic. Assuming that slip occurs along the wall will also make the simulation of foam flow more realistic.

3. In the perturbation solutions of Poiseuille flows of weakly compressible Newtonian liquids (Chapter 4), other interesting directions are: (a) the solution of the annular Poiseuille flow; and (b) the perturbation solution for fluids with yield stress, such as Bingham plastics and Herschel-Bulkley fluids.

4. Finally, the work on weakly compressible Poiseuille flows of a Herschel-Bulkley fluid (Chapter 5) can be naturally extended to time-dependent two dimensional finite-element simulations.

Appendix A

Compressible planar Poiseuille flow

In this appendix the perturbation solution of the planar compressible Poiseuille flow is presented. To nondimensionalize the governing equations, we scale x by L, y by H, ρ by the reference density ρ_0, u_x by U, the transverse velocity u_y by UH/L, and the pressure by $3\eta LU/H^2$. The latter pressure scale is used so that the dimensionless pressure gradient along the domain, in the incompressible flow is equal to 1. For the sake of simplicity, in what follows we will use the same symbols (i.e. without stars) for all dimensionless variables. Using the above scalings, the dimensionless forms of the equation of state, the continuity equation and momentum equations become:

$$\rho \;=\; 1 \;+\; \varepsilon\, P\,, \tag{A.1}$$

$$\frac{\partial}{\partial x}\,(\,\rho\, u_x) \;+\; \frac{\partial}{\partial y}\,(\rho\, u_y) \;=\; 0\,, \tag{A.2}$$

$$\alpha\, Re\rho\,\left(u_x\,\frac{\partial\, u_x}{\partial\, x} \;+\; u_y\,\frac{\partial\, u_x}{\partial\, y}\right) = -3\frac{\partial\, P}{\partial\, x} \;+\alpha^2\frac{\partial^2 u_x}{\partial x^2} + \frac{\partial^2 u_x}{\partial y^2} + \alpha^2\,\left(\chi + \frac{1}{3}\right)\left(\frac{\partial^2 u_y}{\partial x \partial y} + \frac{\partial^2 u_x}{\partial x^2}\right), \tag{A.3}$$

$$\begin{aligned}\alpha^3\, Re\,\rho\,&\left(u_x\,\frac{\partial\, u_y}{\partial\, x} \;+\; u_y\,\frac{\partial\, u_y}{\partial\, y}\right)\\ &= -3\frac{\partial\, P}{\partial\, y} \;+\alpha^4\frac{\partial^2 u_y}{\partial x^2} + \alpha^2\frac{\partial^2 u_y}{\partial y^2} + \alpha^2\,\left(\chi + \frac{1}{3}\right)\left(\frac{\partial^2 u_x}{\partial x \partial y} + \frac{\partial^2 u_y}{\partial y^2}\right),\end{aligned} \tag{A.4}$$

where $\chi \equiv \kappa/\eta$ is the bulk-to-shear viscosity ratio, $\alpha \equiv H/L$ is the aspect ratio of the channel, and Re and ε are, respectively, the Reynolds and compressibility numbers, which are defined by

$$Re \equiv \frac{\rho_0 U H}{\eta} \tag{A.5}$$

and

$$\varepsilon \equiv \frac{3\eta\,\beta\,LU}{H^2}. \tag{A.6}$$

Perturbation Method

Perturbation is performed on all primary variables, ρ, P, u_x and u_y, using the compressibility number, ε, as the perturbation parameter:

$$\left.\begin{aligned} \rho &= \rho^{(0)} + \varepsilon\rho^{(1)} + \varepsilon^2\rho^{(2)} + O(\varepsilon^3) \\ u_y &= u_y^{(0)} + \varepsilon\, u_y^{(1)} + \varepsilon^2\, u_y^{(2)} + O(\varepsilon^3) \\ u_x &= u_x^{(0)} + \varepsilon\, u_x^{(1)} + \varepsilon^2\, u_x^{(2)} + O(\varepsilon^3) \\ P &= P^{(0)} + \varepsilon\, P^{(1)} + \varepsilon^2\, P^{(2)} + O(\varepsilon^3) \end{aligned}\right\} \tag{A.7}$$

Substituting these equations in the governing equations and collecting the terms of the same order in ε we obtain the equations of the flow up to the second order.

Equation of state

By substituting in

$$\rho = 1 + \varepsilon P$$

and collecting the terms of the same order of the perurbation parameter we get:

$$\rho^{(0)} + \varepsilon\rho^{(1)} + \varepsilon^2\rho^{(2)} = 1 + \varepsilon P^{(0)} + \varepsilon^2 P^{(1)} + \varepsilon^3 P^{(2)}$$

Thus,

$$\rho^{(0)} = 1, \quad \rho^{(1)} = P^{(0)} \quad \text{and} \quad \rho^{(2)} = P^{(1)}$$

Continuity Equation

Substituting into

$$\frac{\partial}{\partial x}(\rho u_x) + \frac{\partial}{\partial y}(\rho u_y) = 0$$

we get

$$\frac{\partial}{\partial x}\left[(\rho^{(0)} + \varepsilon\rho^{(1)} + \varepsilon^2\rho^{(2)} + ...)(u_x^{(0)} + \varepsilon u_x^{(1)} + \varepsilon^2 u_x^{(2)} + ...)\right]$$

$$+\frac{\partial}{\partial y}\left[(\rho^{(0)} + \varepsilon\rho^{(1)} + \varepsilon^2\rho^{(2)} + ...)(u_y^{(0)} + \varepsilon u_y^{(1)} + \varepsilon^2 u_y^{(2)} + ...)\right] = 0$$

$\Longrightarrow$

$$\frac{\partial}{\partial x}\left[\rho^{(0)}u_x^{(0)} + \varepsilon\left(\rho^{(0)}u_x^{(1)} + \rho^{(1)}u_x^{(1)}\right) + \varepsilon^2\left(\rho^{(0)}u_x^{(2)} + \rho^{(1)}u_x^{(1)} + \rho^{(2)}u_x^{(0)}\right)\right]$$

$$+\frac{\partial}{\partial y}\left[\rho^{(0)}u_y^{(0)} + \varepsilon\left(\rho^{(0)}u_y^{(1)} + \rho^{(1)}u_y^{(0)}\right) + \varepsilon^2\left(\rho^{(0)}u_y^{(2)} + \rho^{(1)}u_y^{(1)} + \rho^{(2)}u_y^{(0)}\right)\right] + O(\varepsilon^3) = 0$$

Thus we have

Zero - order

$$\frac{\partial}{\partial x}\left(\rho^{(0)}u_x^{(0)}\right) + \frac{\partial}{\partial y}\left(\rho^{(0)}u_y^{(0)}\right) = 0$$

First - order

$$\frac{\partial}{\partial x}\left(\rho^{(0)}u_x^{(1)} + \rho^{(1)}u_x^{(0)}\right) + \frac{\partial}{\partial y}\left(\rho^{(0)}u_y^{(1)} + \rho^{(1)}u_y^{(0)}\right) = 0$$

Second - order

$$\frac{\partial}{\partial x}\left(\rho^{(0)}u_x^{(2)} + \rho^{(1)}u_x^{(1)} + \rho^{(2)}u_x^{(0)}\right) + \frac{\partial}{\partial y}\left(\rho^{(0)}u_y^{(2)} + \rho^{(1)}u_y^{(1)} + \rho^{(2)}u_y^{(0)}\right) = 0$$

x-component of the momentum equation

Substituting into

$$\alpha Re\rho\left(u_x\frac{\partial u_x}{\partial x} + u_y\frac{\partial u_x}{\partial y}\right) = -3\frac{\partial P}{\partial x} + \alpha^2\frac{\partial^2 u_x}{\partial x^2} + \frac{\partial^2 u_x}{\partial y^2} + \alpha^2\left(\chi + \frac{1}{3}\right)\left[\frac{\partial^2 u_y}{\partial x\partial y} + \frac{\partial^2 u_x}{\partial x^2}\right]$$

we get

$$\alpha Re\left(\rho^{(0)} + \varepsilon\rho^{(1)} + \varepsilon^2\rho^{(2)} + ...\right)\left[\left(u_x^{(0)} + \varepsilon u_x^{(1)} + \varepsilon^2 u_x^{(2)} + ...\right)\frac{\partial}{\partial x}\left(u_x^{(0)} + \varepsilon u_x^{(1)} + \varepsilon^2 u_x^{(2)} + ...\right)\right.$$

$$+\left(u_y^{(0)}+\varepsilon u_y^{(1)}+\varepsilon^2 u_y^{(2)}+...\right)\frac{\partial}{\partial y}\left(u_x^{(0)}+\varepsilon u_x^{(1)}+\varepsilon^2 u_x^{(2)}+...\right)\Bigg]$$

$$=-3\frac{\partial}{\partial x}\left(P^{(0)}+\varepsilon P^{(1)}+\varepsilon^2 P^{(2)}+...\right)+\alpha^2\frac{\partial^2}{\partial x^2}\left(u_x^{(0)}+\varepsilon u_x^{(1)}+\varepsilon^2 u_x^{(2)}+...\right)$$

$$+\frac{\partial^2}{\partial y^2}\left(u_x^{(0)}+\varepsilon u_x^{(1)}+\varepsilon^2 u_x^{(2)}+...\right)$$

$$+\alpha^2\left(\chi+\frac{1}{3}\right)\left[\frac{\partial^2}{\partial x\partial y}\left(u_y^{(0)}+\varepsilon u_y^{(1)}+\varepsilon^2 u_y^{(2)}+...\right)+\frac{\partial^2}{\partial x^2}\left(u_x^{(0)}+\varepsilon u_x^{(1)}+\varepsilon^2 u_x^{(2)}+...\right)\right]$$

$\Longrightarrow$

$$\alpha Re\left(\rho^{(0)}+\varepsilon\rho^{(1)}+\varepsilon^2\rho^{(2)}\right)\Bigg[\left(u_x^{(0)}\frac{\partial u_x^{(0)}}{\partial x}+u_y^{(0)}\frac{\partial u_x^{(0)}}{\partial y}\right)$$

$$+\varepsilon\left(u_x^{(0)}\frac{\partial u_x^{(1)}}{\partial x}+u_x^{(1)}\frac{\partial u_x^{(0)}}{\partial x}+u_y^{(0)}\frac{\partial u_x^{(1)}}{\partial y}+u_y^{(1)}\frac{\partial u_x^{(0)}}{\partial y}\right)$$

$$+\varepsilon^2\left(u_x^{(0)}\frac{\partial u_x^{(2)}}{\partial x}+u_x^{(1)}\frac{\partial u_x^{(1)}}{\partial x}+u_x^{(2)}\frac{\partial u_x^{(0)}}{\partial x}+u_y^{(0)}\frac{\partial u_x^{(2)}}{\partial y}+u_y^{(1)}\frac{\partial u_x^{(1)}}{\partial y}+u_y^{(2)}\frac{\partial u_x^{(0)}}{\partial y}\right)\Bigg]$$

$$=-3\frac{\partial}{\partial x}\left(P^{(0)}+\varepsilon P^{(1)}+\varepsilon^2 P^{(2)}\right)+\alpha^2\frac{\partial^2}{\partial x^2}\left(u_x^{(0)}+\varepsilon u_x^{(1)}+\varepsilon^2 u_x^{(2)}\right)+\frac{\partial^2}{\partial y^2}\left(u_x^{(0)}+\varepsilon u_x^{(1)}+\varepsilon^2 u_x^{(2)}\right)$$

$$+\alpha^2\left(\chi+\frac{1}{3}\right)\left[\left(\frac{\partial^2 u_y^{(0)}}{\partial x\partial y}+\frac{\partial^2 u_x^{(0)}}{\partial x^2}\right)+\varepsilon\left(\frac{\partial^2 u_y^{(1)}}{\partial x\partial y}+\frac{\partial^2 u_x^{(1)}}{\partial x^2}\right)+\varepsilon^2\left(\frac{\partial^2 u_y^{(2)}}{\partial x\partial y}+\frac{\partial^2 u_x^{(2)}}{\partial x^2}\right)\right]+\ O(\varepsilon^3)$$

Thus we get:

Zero - order

$$\alpha Re\rho^{(0)}\left[u_x^{(0)}\frac{\partial u_x^{(0)}}{\partial x}+u_y^{(0)}\frac{\partial u_x^{(0)}}{\partial y}\right]=-3\frac{\partial P^{(0)}}{\partial x}+\alpha^2\frac{\partial^2 u_x^{(0)}}{\partial x^2}+\frac{\partial^2 u_x^{(0)}}{\partial y^2}+\alpha^2\left(\chi+\frac{1}{3}\right)\left[\frac{\partial^2 u_y^{(0)}}{\partial x\partial y}+\frac{\partial^2 u_x^{(0)}}{\partial x^2}\right]$$

First - order

$$\alpha Re\rho^{(1)}\left[u_x^{(0)}\frac{\partial u_x^{(0)}}{\partial x}+u_y^{(0)}\frac{\partial u_x^{(0)}}{\partial y}\right]+\alpha Re\rho^{(0)}\left[u_x^{(0)}\frac{\partial u_x^{(1)}}{\partial x}+u_x^{(1)}\frac{\partial u_x^{(0)}}{\partial x}+u_y^{(0)}\frac{\partial u_x^{(1)}}{\partial y}+u_y^{(1)}\frac{\partial u_x^{(0)}}{\partial y}\right]$$

$$=-3\frac{\partial P^{(1)}}{\partial x}+\alpha^2\frac{\partial^2 u_x^{(1)}}{\partial x^2}+\frac{\partial^2 u_x^{(1)}}{\partial y^2}+\alpha^2\left(\chi+\frac{1}{3}\right)\left[\frac{\partial^2 u_y^{(1)}}{\partial x\partial y}+\frac{\partial^2 u_x^{(1)}}{\partial x^2}\right]$$

Second - order

$$\alpha Re\rho^{(2)}\left[u_x^{(0)}\frac{\partial u_x^{(0)}}{\partial x}+u_y^{(0)}\frac{\partial u_x^{(0)}}{\partial y}\right]+\alpha Re\rho^{(1)}\left[u_x^{(0)}\frac{\partial u_x^{(1)}}{\partial x}+u_x^{(1)}\frac{\partial u_x^{(0)}}{\partial x}+u_y^{(0)}\frac{\partial u_x^{(1)}}{\partial y}+u_y^{(1)}\frac{\partial u_x^{(0)}}{\partial y}\right]$$

$$+\alpha Re\rho^{(0)}\left[u_x^{(0)}\frac{\partial u_x^{(2)}}{\partial x}+u_x^{(1)}\frac{\partial u_x^{(1)}}{\partial x}+u_x^{(2)}\frac{\partial u_x^{(0)}}{\partial x}+u_y^{(0)}\frac{\partial u_x^{(2)}}{\partial y}+u_y^{(1)}\frac{\partial u_x^{(1)}}{\partial y}+u_y^{(2)}\frac{\partial u_x^{(0)}}{\partial y}\right]$$

$$= -3\frac{\partial P^{(2)}}{\partial x} + \alpha^2\frac{\partial^2 u_x^{(2)}}{\partial x^2} + \frac{\partial^2 u_x^{(2)}}{\partial y^2} + \alpha^2\left(\chi + \frac{1}{3}\right)\left[\frac{\partial^2 u_y^{(2)}}{\partial x \partial y} + \frac{\partial^2 u_x^{(2)}}{\partial x^2}\right]$$

y-component of the momentum equation

As above, substituting into

$$\alpha^3 Re\rho\left(u_x\frac{\partial u_y}{\partial x} + u_y\frac{\partial u_y}{\partial y}\right) = -3\frac{\partial P}{\partial y} + \alpha^4\frac{\partial^2 u_y}{\partial x^2} + \alpha\frac{\partial^2 u_y}{\partial y^2} + \alpha^2\left(\chi + \frac{1}{3}\right)\left[\frac{\partial^2 u_x}{\partial x \partial y} + \frac{\partial^2 u_y}{\partial y^2}\right]$$

we get

$$\alpha^3 Re\left(\rho^{(0)} + \varepsilon\rho^{(1)} + \varepsilon^2\rho^{(2)} + ...\right)\left[\left(u_x^{(0)} + \varepsilon u_x^{(1)} + \varepsilon^2 u_x^{(2)} + ...\right)\frac{\partial}{\partial x}\left(u_y^{(0)} + \varepsilon u_y^{(1)} + \varepsilon^2 u_y^{(2)} + ...\right)\right.$$
$$\left. + \left(u_y^{(0)} + \varepsilon u_y^{(1)} + \varepsilon^2 u_y^{(2)} + ...\right)\frac{\partial}{\partial y}\left(u_y^{(0)} + \varepsilon u_y^{(1)} + \varepsilon^2 u_y^{(2)} + ...\right)\right]$$
$$= -3\frac{\partial}{\partial y}\left(P^{(0)} + \varepsilon P^{(1)} + \varepsilon^2 P^{(2)} + ...\right) + \alpha^4\frac{\partial^2}{\partial x^2}\left(u_y^{(0)} + \varepsilon u_y^{(1)} + \varepsilon^2 u_y^{(2)} + ...\right)$$
$$+\alpha\frac{\partial}{\partial y^2}\left(u_y^{(0)} + \varepsilon u_y^{(1)} + \varepsilon^2 u_y^{(2)} + ...\right)$$
$$+\alpha^2\left(\chi + \frac{1}{3}\right)\left[\frac{\partial^2}{\partial x \partial y}\left(u_x^{(0)} + \varepsilon u_x^{(1)} + \varepsilon^2 u_x^{(2)} + ...\right) + \frac{\partial^2}{\partial y^2}\left(u_y^{(0)} + \varepsilon u_y^{(1)} + \varepsilon^2 u_y^{(2)} + ...\right)\right]$$

$\Longrightarrow$

$$\alpha^3 Re\left(\rho^{(0)} + \varepsilon\rho^{(1)} + \varepsilon^2\rho^{(2)}\right)\left[\left(u_x^{(0)}\frac{\partial u_y^{(0)}}{\partial x} + u_y^{(0)}\frac{\partial u_y^{(0)}}{\partial y}\right)\right.$$
$$+\varepsilon\left(u_x^{(0)}\frac{\partial u_y^{(1)}}{\partial x} + u_x^{(1)}\frac{\partial u_y^{(0)}}{\partial x} + u_y^{(0)}\frac{\partial u_y^{(1)}}{\partial y} + u_y^{(1)}\frac{\partial u_y^{(0)}}{\partial y}\right)$$
$$\left.+\varepsilon^2\left(u_x^{(0)}\frac{\partial u_y^{(2)}}{\partial x} + u_x^{(1)}\frac{\partial u_y^{(1)}}{\partial x} + u_x^{(2)}\frac{\partial u_y^{(0)}}{\partial x} + u_y^{(0)}\frac{\partial u_y^{(2)}}{\partial y} + u_y^{(1)}\frac{\partial u_y^{(1)}}{\partial y} + u_y^{(2)}\frac{\partial u_y^{(0)}}{\partial y}\right)\right]$$
$$= -3\frac{\partial}{\partial y}\left(P^{(0)} + \varepsilon P^{(1)} + \varepsilon^2 P^{(2)}\right) + \alpha^4\frac{\partial^2}{\partial x^2}\left(u_y^{(0)} + \varepsilon u_y^{(1)} + \varepsilon^2 u_y^{(2)}\right) + \alpha\frac{\partial^2}{\partial y^2}\left(u_y^{(0)} + \varepsilon u_y^{(1)} + \varepsilon^2 u_y^{(2)}\right)$$
$$+\alpha^2\left(\chi + \frac{1}{3}\right)\left[\left(\frac{\partial^2 u_x^{(0)}}{\partial x \partial y} + \frac{\partial^2 u_y^{(0)}}{\partial y^2}\right) + \varepsilon\left(\frac{\partial^2 u_x^{(1)}}{\partial x \partial y} + \frac{\partial^2 u_y^{(1)}}{\partial y^2}\right) + \varepsilon^2\left(\frac{\partial^2 u_x^{(2)}}{\partial x \partial y} + \frac{\partial^2 u_y^{(2)}}{\partial y^2}\right)\right] + O(\varepsilon^3)$$

Thus we have:

Zero - order

$$\alpha^3 Re\rho^{(0)}\left[u_x^{(0)}\frac{\partial u_y^{(0)}}{\partial x} + u_y^{(0)}\frac{\partial u_y^{(0)}}{\partial y}\right] = -3\frac{\partial P^{(0)}}{\partial y} + \alpha^4\frac{\partial^2 u_y^{(0)}}{\partial x^2} + \alpha\frac{\partial^2 u_y^{(0)}}{\partial y^2} + \alpha^2\left(\chi + \frac{1}{3}\right)\left[\frac{\partial^2 u_x^{(0)}}{\partial x \partial y} + \frac{\partial^2 u_y^{(0)}}{\partial y^2}\right]$$

First - order

$$\alpha^3 Re\rho^{(1)}\left[u_x^{(0)}\frac{\partial u_y^{(0)}}{\partial x}+u_y^{(0)}\frac{\partial u_y^{(0)}}{\partial y}\right]+\alpha^3 Re\rho^{(0)}\left[u_x^{(0)}\frac{\partial u_y^{(1)}}{\partial x}+u_x^{(1)}\frac{\partial u_y^{(0)}}{\partial x}+u_y^{(0)}\frac{\partial u_y^{(1)}}{\partial y}+u_y^{(1)}\frac{\partial u_y^{(0)}}{\partial y}\right]$$
$$=-3\frac{\partial P^{(1)}}{\partial y}+\alpha^4\frac{\partial^2 u_y^{(1)}}{\partial x^2}+\alpha\frac{\partial^2 u_y^{(1)}}{\partial y^2}+\alpha^2\left(\chi+\frac{1}{3}\right)\left[\frac{\partial^2 u_x^{(1)}}{\partial x\partial y}+\frac{\partial^2 u_y^{(1)}}{\partial y^2}\right]$$

Second - order

$$\alpha^3 Re\rho^{(2)}\left[u_x^{(0)}\frac{\partial u_y^{(0)}}{\partial x}+u_y^{(0)}\frac{\partial u_y^{(0)}}{\partial y}\right]+\alpha^3 Re\rho^{(1)}\left[u_x^{(0)}\frac{\partial u_y^{(1)}}{\partial x}+u_x^{(1)}\frac{\partial u_y^{(0)}}{\partial x}+u_y^{(0)}\frac{\partial u_y^{(1)}}{\partial y}+u_y^{(1)}\frac{\partial u_y^{(0)}}{\partial y}\right]$$
$$+\alpha^3 Re\rho^{(0)}\left[u_x^{(0)}\frac{\partial u_y^{(2)}}{\partial x}+u_x^{(1)}\frac{\partial u_y^{(1)}}{\partial x}+u_x^{(0)}\frac{\partial u_y^{(1)}}{\partial x}+u_y^{(2)}\frac{\partial u_y^{(0)}}{\partial y}+u_y^{(1)}\frac{\partial u_y^{(1)}}{\partial y}+u_y^{(2)}\frac{\partial u_y^{(0)}}{\partial y}\right]$$
$$=-3\frac{\partial P^{(2)}}{\partial y}+\alpha^4\frac{\partial^2 u_y^{(2)}}{\partial x^2}+\alpha\frac{\partial^2 u_y^{(2)}}{\partial y^2}+\alpha^2\left(\chi+\frac{1}{3}\right)\left[\frac{\partial^2 u_x^{(2)}}{\partial x\partial y}+\frac{\partial^2 u_y^{(2)}}{\partial y^2}\right]$$

Zero-order solution

Using the zero-order equation of state,

$$\rho^{(0)} = 1 \tag{A.8}$$

the continuity equation

$$\frac{\partial}{\partial x}\left[\rho^{(0)}u_x^{(0)}\right] + \frac{\partial}{\partial y}\left[\rho^{(0)}u_y^{(0)}\right] = 0 \tag{A.9}$$

and the assumption

$$u_y^{(0)}(x,y) = 0 \tag{A.10}$$

we get

$$u_x^{(0)} = u_x^{(0)}(y) \tag{A.11}$$

Now, from the y-component of the momentum equation

$$\alpha^3\, Re\, \rho^{(0)}\left[u_x^{(0)}\,\frac{\partial u_y^{(0)}}{\partial x} + u_y^{(0)}\,\frac{\partial u_y^{(0)}}{\partial y}\right]$$
$$=-3\,\frac{\partial P^{(0)}}{\partial y}+\alpha^4\,\frac{\partial^2 u_y^{(0)}}{\partial x^2}+\alpha^2\,\frac{\partial^2 u_y^{(0)}}{\partial y^2}+\alpha^2\left(\chi+\frac{1}{3}\right)\left[\frac{\partial^2 u_x^{(0)}}{\partial x\partial y}+\frac{\partial^2 u_y^{(0)}}{\partial y^2}\right]$$

and Eqs. (A.8)-(A.11) we find that

$$P^{(0)} = P^{(0)}(x) \tag{A.12}$$

Substituting into the x-momentum equation

$$\alpha\, Re\, \rho^{(0)} \left[u_x^{(0)} \frac{\partial u_x^{(0)}}{\partial x} + u_y^{(0)} \frac{\partial u_x^{(0)}}{\partial y} \right] = -3 \frac{\partial P^{(0)}}{\partial x} + \frac{\partial^2 u_x^{(0)}}{\partial y^2} + \alpha^2 \frac{\partial^2 u_x^{(0)}}{\partial x^2} + \alpha^2 \left(\chi + \frac{1}{3} \right) \left[\frac{\partial^2 u_y^{(0)}}{\partial x \partial y} + \frac{\partial^2 u_x^{(0)}}{\partial x^2} \right]$$

we get

$$3 \frac{\partial P^{(0)}}{\partial x} = \frac{\partial^2 u_x^{(0)}}{\partial y^2} = c \tag{A.13}$$

where c is a constant to be determined. Integrating the resulting ODEs and applying the boundary conditions $P^{(0)}(0)$=1 and $P^{(0)}(1)$=0 for $P(x)$ we obtain the zero-order solution for the pressure, which reads:

$$P^{(0)} = 1 - x \tag{A.14}$$

From equations (A.13) and (A.14) we have

$$-3 = \frac{\partial^2 u_x^{(0)}}{\partial y^2}$$

and by integrating twice and applying the conditions $\partial u_x^{(0)}/\partial y(0)$=0 and $u_x^{(0)}(1)$=0 we obtain the zero-order solution for the velocity

$$u_x^{(0)} = \frac{3}{2}(1 - y^2) \tag{A.15}$$

Thus the zero-order solution is:

$$\rho^{(0)} = 1 \tag{A.16}$$

$$u_y^{(0)} = 0 \tag{A.17}$$

$$u_x^{(0)} = \frac{3}{2}(1 - y^2) \tag{A.18}$$

$$P^{(0)} = 1 - x \tag{A.19}$$

The assumptions we have used are:

$$\partial u_x^{(0)}/\partial y(0) = u_x^{(0)}(1) = 0$$

$$u_y^{(0)}(x,y) = 0$$

$$P^{(0)}(0) = 1, P^{(0)}(1) = 0$$

First-order solution

From the equation of state we obtain,

$$\rho^{(1)} \;=\; P^{(0)}(x) \quad \Longrightarrow \quad \rho^{(1)} = 1 - x. \tag{A.20}$$

Now, from the continuity equation

$$\frac{\partial}{\partial x}\left[\rho^{(0)}\, u_x^{(1)} + \rho^{(1)}\, u_x^{(0)}\right] \;+\; \frac{\partial}{\partial y}\left[\rho^{(0)}\, u_y^{(1)} + \rho^{(1)}\, u_y^{(0)}\right] \;=\; 0,$$

using $\rho^{(0)}$=1, $u_y^{(0)}$=0, $u_x^{(0)}$=3/2(1 − y^2), $u_y^{(1)}$=0 and integrating we get

$$u_x^{(1)} = -\frac{3}{2}(1-x)(1-y^2) + f(y) \tag{A.21}$$

where $f(y)$ is unknown function. From the y-momentum

$$\begin{aligned}
&\alpha\, Re\, \rho^{(1)} \left[u_x^{(0)}\, \frac{\partial u_x^{(0)}}{\partial x} \;+\; u_y^{(0)}\, \frac{\partial u_x^{(0)}}{\partial y}\right] \\
&+\alpha\, Re\, \rho^{(0)} \left[u_x^{(0)}\, \frac{\partial u_x^{(1)}}{\partial x} \;+\; u_x^{(1)}\, \frac{\partial u_x^{(0)}}{\partial x} \;+\; u_y^{(0)}\, \frac{\partial u_x^{(1)}}{\partial y} \;+\; u_y^{(1)}\, \frac{\partial u_x^{(0)}}{\partial y}\right] \\
&\quad = -3\, \frac{\partial P^{(1)}}{\partial x} + \frac{\partial^2 u_x^{(1)}}{\partial y^2} + \;\alpha^2\, \frac{\partial^2 u_x^{(1)}}{\partial x^2} + \;\alpha^2\, \left(\chi + \frac{1}{3}\right) \left[\frac{\partial^2 u_y^{(1)}}{\partial x \partial y} \;+\; \frac{\partial^2 u_x^{(1)}}{\partial x^2}\right]
\end{aligned} \tag{A.22}$$

and using all the above and integrating with respect to y, we get:

$$P^{(1)} = \frac{1}{2}\alpha^2(\chi + \frac{1}{3})(1-y^2) + g(x) \tag{A.23}$$

where $g(x)$ is an unknown function. By substituting in the x-momentum equation,

$$\alpha^3\, Re\, \rho^{(1)} \left[u_x^{(0)}\, \frac{\partial u_y^{(0)}}{\partial x} \;+\; u_y^{(0)}\, \frac{\partial u_y^{(0)}}{\partial y}\right]$$

$$+\alpha^3\, Re\, \rho^{(0)} \left[u_x^{(0)}\, \frac{\partial u_y^{(1)}}{\partial x} \;+\; u_x^{(1)}\, \frac{\partial u_y^{(0)}}{\partial x} \;+\; u_y^{(0)}\, \frac{\partial u_y^{(1)}}{\partial y} \;+\; u_y^{(1)}\, \frac{\partial u_y^{(0)}}{\partial y} \right]$$
$$= -3\, \frac{\partial P^{(1)}}{\partial y} \;+\alpha^4\; \frac{\partial^2 u_y^{(1)}}{\partial x^2} \;+\alpha^2\; \frac{\partial^2 u_y^{(1)}}{\partial y^2} \;+\; \alpha^2 \left(\chi + \frac{1}{3}\right) \left[\frac{\partial^2 u_x^{(1)}}{\partial x \partial y} \;+\; \frac{\partial^2 u_y^{(1)}}{\partial y^2} \right],$$

we have

$$\frac{9}{4}\alpha Re(1-y^2)^2 = \frac{\partial P^{(1)}}{\partial x} + 3(1-x) + f''(y)$$

By separating variables we obtain the follow expressions

$$\frac{9}{4}\alpha\, Re\, (1-y^2)^2 \;- f''(y) = -3\frac{\partial\, P^{(1)}}{\partial\, x} + 3(1-x) = c$$

where c is a constant to be determined. Integrating the first ODE twice leads to

$$f(y) = \frac{9}{4}\alpha Re \left(\frac{1}{2}y^2 - \frac{1}{6}y^4 + \frac{1}{30}y^6\right) - \frac{1}{2}c_1 y^2 + c_2 \tag{A.24}$$

Applying $f'(0)$=$f(1)$=0 we obtain

$$0 = \frac{33}{40}\alpha Re - \frac{1}{2}c_1 + c_2 \tag{A.25}$$

where c_1 and c_2 are contstants to be determined. Also, by applying $\int_0^1 f(y)dy$=0 we get

$$\frac{87}{280}\alpha Re - \frac{1}{6}c_1 + c_2 = 0 \tag{A.26}$$

Now, from Eqs. (A.25) and (A.26)

$$c_1 = \frac{54}{35}\alpha Re \quad \text{and} \quad c_2 = -\frac{3}{56}\alpha Re$$

and by substituting in Eq. (A.24), we find:

$$f(y) = \frac{3}{280}\alpha Re(1-y^2)(-5+28y^2-7y^4) \tag{A.27}$$

Substituting now $f(y)$ into Eq. (A.21) we obtain the first-order velocity component

$$u_x^{(1)} = -\frac{3}{2}(1-x)(1-y^2) + \frac{3}{280}\alpha Re(1-y^2)(-5+28y^2-7y^4). \tag{A.28}$$

From the $x-$momentum we find that

$$g(x) = \frac{3}{2}x(2-x) - \frac{54}{35}\alpha Rex + \kappa$$

where κ is to be determined. By substituting in Eq. (A.23) and using $P^{(1)}(1,1)$=0,

$$\kappa = \frac{18}{35}\alpha Re - \frac{1}{2}$$

and the solution for the pressure is

$$P^{(1)} = \frac{1}{2}\alpha^2\left(\chi + \frac{1}{3}\right)(1-y^2) - \frac{1}{2}(1-x)^2 + \frac{18}{35}\alpha Re(1-x). \tag{A.29}$$

The first-order solution, reads:

$$\rho^{(1)} = 1-x \tag{A.30}$$

$$u_y^{(1)} = 0 \tag{A.31}$$

$$u_x^{(1)} = -\frac{3}{2}(1-x)(1-y^2) + \frac{3}{280}\alpha\, Re(1-y^2)(-5+28y^2-7y^4) \tag{A.32}$$

$$P^{(1)} = \frac{1}{2}\alpha^2\left(\chi + \frac{1}{3}\right)(1-y^2) - \frac{1}{2}(1-x)^2 + \frac{18}{35}\alpha\, Re\,(1-x). \tag{A.33}$$

The assumptions we have used are:

$$f'(0) = f(1) = \int_0^1 f(y)dy = 0$$

$$u_y^{(1)}(x,y) = 0$$

$$P^{(1)}(1,1) = 0$$

Second-order solution

For $\rho^{(2)}$ we simply have:

$$\rho^{(2)} = P^{(1)}(x,y) \quad \Longrightarrow \quad \rho^{(2)} = \frac{1}{2}\alpha^2\left(\chi + \frac{1}{3}\right)(1-y^2) - \frac{1}{2}(1-x)^2 + \frac{18}{35}\alpha\, Re\,(1-x) \tag{A.34}$$

Now, from the continuity equation

$$\frac{\partial}{\partial x}\left[\rho^{(0)}u_x^{(2)} + \rho^{(1)}u_x^{(1)} + \rho^{(2)}u_x^{(0)}\right] + \frac{\partial}{\partial y}\left[\rho^{(0)}u_y^{(2)} + \rho^{(1)}u_y^{(1)} + \rho^{(2)}u_y^{(0)}\right] = 0,$$

we have

$$u_x^{(2)} = \frac{9}{4}(1-x)^2(1-y^2) - \frac{3}{4}\alpha^2\left(\chi+\frac{1}{3}\right)(1-y^2)^2$$
$$-\frac{3}{280}\alpha Re(1-x)(1-y^2)(67+28y^2-7y^4)+\frac{\partial u_y^{(2)}}{\partial y}(1-x)+F(y) \quad \text{(A.35)}$$

where $F(y)$ is a function to be determined. At this point the assumption of zero transverse velocity is relaxed, letting u_y to be a function of y, $u_y^{(2)}=u_y^{(2)}(y)$. From the y-momentum equation

$$\alpha^3\, Re\, \rho^{(2)}\left[u_x^{(0)}\,\frac{\partial u_y^{(0)}}{\partial x} + u_y^{(0)}\,\frac{\partial u_y^{(0)}}{\partial y}\right]$$
$$+\alpha^3\, Re\, \rho^{(1)}\left[u_x^{(0)}\,\frac{\partial u_y^{(1)}}{\partial x} + u_x^{(1)}\,\frac{\partial u_y^{(0)}}{\partial x} + u_y^{(0)}\,\frac{\partial u_y^{(1)}}{\partial y} + u_y^{(1)}\,\frac{\partial u_y^{(0)}}{\partial y}\right]$$
$$+\alpha^3\, Re\, \rho^{(0)}\left[u_x^{(0)}\,\frac{\partial u_y^{(2)}}{\partial x} + u_x^{(1)}\,\frac{\partial u_y^{(1)}}{\partial x} + u_x^{(2)}\,\frac{\partial u_y^{(0)}}{\partial x} + u_y^{(0)}\,\frac{\partial u_y^{(2)}}{\partial y} + u_y^{(1)}\,\frac{\partial u_y^{(1)}}{\partial y} + u_y^{(2)}\,\frac{\partial u_y^{(0)}}{\partial y}\right]$$
$$= -3\frac{\partial P^{(2)}}{\partial y}+\alpha^2\frac{\partial^2 u_y^{(2)}}{\partial y^2}+\alpha^4\frac{\partial^2 u_y^{(2)}}{\partial x^2}+\alpha^2\left(\chi+\frac{1}{3}\right)\left[\frac{\partial^2 u_x^{(2)}}{\partial x\partial y}+\frac{\partial^2 u_y^{(2)}}{\partial y^2}\right]$$

we have

$$3\frac{\partial P^{(2)}}{\partial y} = \alpha^2\left(\chi+\frac{4}{3}\right)\frac{\partial^2 u_y^{(2)}}{\partial y^2} + \alpha^2\left(\chi+\frac{1}{3}\right)\frac{\partial}{\partial y}\left(\frac{\partial u_x^{(2)}}{\partial x}\right)$$

By integrating with respect to y we find that

$$P^{(2)} = \frac{1}{3}\alpha^2\left(\chi+\frac{4}{3}\right)\frac{\partial u_y^{(2)}}{\partial y} + \frac{1}{3}\alpha^2\left(\chi+\frac{1}{3}\right)\frac{\partial u_x^{(2)}}{\partial x} + G(x)$$

or

$$P^{(2)} = \frac{1}{3}\alpha^2\frac{\partial u_y^{(2)}}{\partial y} - \frac{3}{2}\alpha^2\left(\chi+\frac{1}{3}\right)(1-x)(1-y^2)$$
$$+\frac{1}{280}\alpha^3 Re\left(\chi+\frac{1}{3}\right)(1-y^2)(67+28y^2-7y^4)+G(x), \quad \text{(A.36)}$$

where $G(x)$ is a function to be determined. Combining the $x-$momentum equation

$$\alpha\, Re\, \rho^{(2)}\left[u_x^{(0)}\,\frac{\partial u_x^{(0)}}{\partial x} + u_y^{(0)}\,\frac{\partial u_x^{(0)}}{\partial y}\right]$$
$$+\alpha\, Re\, \rho^{(1)}\left[u_x^{(0)}\,\frac{\partial u_x^{(1)}}{\partial x} + u_x^{(1)}\,\frac{\partial u_x^{(0)}}{\partial x} + u_y^{(0)}\,\frac{\partial u_x^{(1)}}{\partial y} + u_y^{(1)}\,\frac{\partial u_x^{(0)}}{\partial y}\right]$$

$$+\alpha\, Re\, \rho^{(0)} \left[u_x^{(0)} \frac{\partial u_x^{(2)}}{\partial x} + u_x^{(1)} \frac{\partial u_x^{(1)}}{\partial x} + u_x^{(2)} \frac{\partial u_x^{(0)}}{\partial x} + u_y^{(0)} \frac{\partial u_x^{(2)}}{\partial y} + u_y^{(1)} \frac{\partial u_x^{(1)}}{\partial y} + u_y^{(2)} \frac{\partial u_x^{(0)}}{\partial y} \right]$$
$$= -3\frac{\partial P^{(2)}}{\partial x} + \frac{\partial^2 u_x^{(2)}}{\partial y^2} + \alpha^2 \frac{\partial^2 u_x^{(2)}}{\partial x^2} + \alpha^2 \left(\chi + \frac{1}{3}\right) \left[\frac{\partial^2 u_y^{(2)}}{\partial x \partial y} + \frac{\partial^2 u_x^{(2)}}{\partial x^2} \right],$$

with

$$\rho^{(1)} u_x^{(0)} \frac{\partial u_x^{(1)}}{\partial x} = \frac{9}{4}(1-x)(1-y^2)^2$$
$$u_x^{(0)} \frac{\partial u_x^{(2)}}{\partial x} = -\frac{27}{4}(1-x)(1-y^2)^2 + \frac{9}{560}\alpha Re(1-y^2)^2(67+28y^2-7y^4) - \frac{3}{2}(1-y^2)\frac{\partial u_y^{(2)}}{\partial y}$$
$$u_x^{(1)} \frac{\partial u_x^{(1)}}{\partial x} = -\frac{9}{4}(1-x)(1-y^2)^2 + \frac{9}{560}\alpha Re(1-y^2)^2(-5+28y^2-7y^4)$$
$$u_y^{(2)} \frac{\partial u_x^{(0)}}{\partial y} = -3y u_y^{(2)}$$

leads to:

$$\alpha Re \left[-3y u_y^{(2)} - \frac{3}{2}(1-y^2)\frac{\partial u_y^{(2)}}{\partial y} - \frac{27}{4}(1-x)(1-y^2)^2 + \frac{9}{560}\alpha\, Re(1-y^2)^2(62+56y^2-14y^4) \right]$$
$$= -3G'(x) - \frac{9}{2}(1-x)^2 + \frac{\partial^3 u_y^{(2)}}{\partial y^3}(1-x) + F''(y) - \frac{3}{280}\alpha Re(1-x)(-78-420y^2+210y^4)$$
$$+\frac{9}{2}\alpha^2(1-y^2) + 3\alpha^2\left(\chi + \frac{1}{3}\right)(1-3y^2). \qquad \text{(A.37)}$$

Here, it is assumed that the terms involving both $(1-x)$ and y must be equal to a (scalar) multiple of $(1-x)$ in order to be able to seperate variables. Thus we can assume that

$$\frac{27}{4}\alpha\, Re(1-y^2)^2 + \frac{\partial^3 u_y^{(2)}}{\partial y^3} - \frac{3}{280}\alpha\, Re(-78-420y^2+210y^4) = \alpha\, Re\gamma. \qquad \text{(A.38)}$$

where γ is new constant to be determined. From Eq. (A.38) we have

$$\frac{\partial^3 u_y^{(2)}}{\partial y^3} = \alpha\, Re\gamma + \frac{3}{280}\alpha\, Re(-78-420y^2+210y^4) - \frac{27}{4}\alpha\, Re(1-y^2)^2$$

Integrating with respect to y gives

$$\frac{\partial^2 u_y^{(2)}}{\partial y^2} = \alpha\, Re\gamma y + \frac{3}{280}\alpha\, Re(-78y-140y^3+42y^5) - \frac{27}{4}\alpha\, Re\left(y - \frac{2}{3}y^3 + \frac{1}{5}y^5\right) + \gamma_1$$

where γ_1=0 when the boundary condition $\partial u_y^{(2)}/\partial y(0)$=0 is applied. By integrating once more and using $\partial^2 u_y^{(2)}/\partial y^2(1)$=0, we obtain

$$0 = \alpha Re \left(\frac{1}{2}\gamma - \frac{447}{140}\right) + \gamma_2 \tag{A.39}$$

and finally after another integration

$$u_y^{(2)} = \frac{1}{6}\alpha Re\gamma y^3 + \frac{3}{280}\alpha Re(-13y^3 - 7y^5 + y^7) - \frac{27}{4}\alpha Re\left(\frac{1}{6}y^3 - \frac{1}{30}y^5 + \frac{1}{210}y^7\right) + \gamma_2 y + \gamma_3$$

$$u_y^{(2)}(0) = 0 \quad \Longrightarrow \quad \gamma_3 = 0$$

Applying $u_y^{(2)}(1) = 0$ leads to

$$\alpha Re \left(\frac{1}{6}\gamma - \frac{159}{140}\right) + \gamma_2 = 0 \tag{A.40}$$

From Eqs. (A.39)-(A.40) we find that

$$\gamma = \frac{216}{35} \quad \text{and} \quad \gamma_2 = \frac{3}{28}\alpha Re$$

Thus, the transverse velocity reads

$$u_y^{(2)} = \frac{3}{140}\alpha\, Re\, y\, (1-y^2)^2(5-y^2). \tag{A.41}$$

Now, we substitute the transverse velocity in Eq. (A.35)

$$u_x^{(2)} = \frac{9}{4}(1-x)^2(1-y^2) - \frac{3}{4}\alpha^2\left(\chi + \frac{1}{3}\right)(1-y^2)^2$$

$$-\frac{3}{280}\alpha Re(1-y^2)(57 + 84y^2 - 21y^4)(1-x) + F(y). \tag{A.42}$$

Separating variables in Eq. (A.37) gives the following ODEs for $F(y)$ and $G(x)$:

$$\alpha Re\left[-3yu_y^{(2)} - \frac{3}{2}(1-y^2)\frac{\partial u_y^{(2)}}{\partial y} + \frac{9}{560}\alpha\, Re(1-y^2)^2(62 + 56y^2 - 14y^4)\right]$$

$$-F''(y) - \frac{9}{2}\alpha^2(1-y^2) - 3\alpha^2\left(\chi + \frac{1}{3}\right)(1-3y^2) = A \tag{A.43}$$

and

$$-3G'(x) - \frac{9}{2}(1-x)^2 + \alpha\, Re\, \gamma\, (1-x) \;=\; A. \tag{A.44}$$

where A is another constant to be determined. Integrating Eq. (A.43) once and applying the condition $F'(0)$=0, we obtain

$$F'(y) = -Ay - \frac{9}{2}\alpha^2\left(y - \frac{1}{3}y^3\right) - 3\alpha^2\left(\chi + \frac{1}{3}\right)(y - y^3) + \\ \frac{3}{140}\alpha^2 Re^2\left(39y - 3y^3 - \frac{117}{5}y^5 + 15y^7 - 2y^9\right)$$

We integrate once more to get

$$F(y) = -\frac{1}{2}Ay^2 - \frac{9}{2}\alpha^2\left(\frac{1}{2}y^2 - \frac{1}{12}y^4\right) - 3\alpha^2\left(\chi + \frac{1}{3}\right)(\frac{1}{2}y^2 - \frac{1}{4}y^4) + \\ \frac{3}{140}\alpha^2 Re^2\left(\frac{39}{2}y^2 - \frac{3}{4}y^4 - \frac{117}{30}y^6 + \frac{15}{8}y^8 - \frac{1}{5}y^{10}\right) + c_1 \tag{A.45}$$

where c_1 is a constant to be determined. By applying the condition $F(1)$=0, we get:

$$0 = -\frac{1}{2}A - \frac{15}{8}\alpha^2 - \frac{3}{4}\alpha^2\left(\chi + \frac{1}{3}\right) + \frac{1983}{5600}\alpha^2 Re^2 + c_1 \tag{A.46}$$

We apply the condition $\int_0^1 F(y)dy$=0 and find that

$$-\frac{1}{6}A - \frac{27}{40}\alpha^2 - \frac{7}{20}\alpha^2\left(\chi + \frac{1}{3}\right) + \frac{276415}{2156000}\alpha^2 Re^2 + c_1 = 0 \tag{A.47}$$

Solving the system of Eqs. (A.46) and (A.47) we find

$$A = -\frac{18}{5}\alpha^2 - \frac{6}{5}\alpha^2\left(\chi + \frac{1}{3}\right) + \frac{9132}{13475}\alpha^2 Re^2 \tag{A.48}$$

and

$$c_1 = \frac{3}{40}\alpha^2 + \frac{3}{20}\alpha^2\left(\chi + \frac{1}{3}\right) - \frac{6579}{431200}\alpha^2 Re^2 \tag{A.49}$$

By substituting Eqs. (A.48) and (A.49) in Eq. (A.45) we obtain

$$F(y) \;= \alpha^2\left(\chi + \frac{1}{3}\right)\left(\frac{3}{20} - \frac{9}{10}y^2 + \frac{3}{4}y^4\right) + \alpha^2\left(\frac{3}{40} - \frac{9}{20}y^2 + \frac{9}{24}y^4\right)$$

$$-\frac{3}{431200}\alpha^2 Re^2(2193-11356y^2+2310y^4+12012y^6-5775y^8+616y^{10}) \quad \text{(A.50)}$$

The horizontal velocity becomes

$$u_x^{(2)}=(1-y^2)\left[\frac{9}{4}(1-x)^2-\frac{3}{280}\alpha\, Re(57+84y^2-21y^4)(1-x)+\frac{3}{40}\alpha^2(1-5y^2)\right.$$
$$\left.-\frac{3}{5}\alpha^2\left(\chi+\frac{1}{3}\right)-\frac{3}{431200}\alpha^2\, Re^2(2193-9163y^2-6853y^4+5159y^6-616y^8)\right] \quad \text{(A.51)}$$

Integrating now Eq. (A.44) and substituting A under the condition $P^{(2)}(1,1)=0$ we obtain

$$G(x)=\frac{1}{2}(1-x)^3-\frac{6}{5}\alpha^2(1-x)-\frac{36}{35}\alpha\, Re(1-x)^2$$
$$+\frac{3044}{13475}\alpha^2Re^2(1-x)-\frac{2}{5}\alpha^2\left(\chi+\frac{1}{3}\right)(1-x) \quad \text{(A.52)}$$

Therefore, pressure is given by

$$P^{(2)}=\frac{1}{2}(1-x)^3-\frac{6}{5}\alpha^2(1-x)+\frac{3044}{13475}\alpha^2Re^2(1-x)-\frac{1}{10}\alpha^2\left(\chi+\frac{1}{3}\right)(19-15y^2)(1-x)$$
$$-\frac{36}{35}\alpha\, Re(1-x)^2+\frac{1}{280}\alpha^3Re(1-y^2)\left[2(5-28y^2+7y^4)+\left(\chi+\frac{1}{3}\right)(67+28y^2-7y^4)\right]. \quad \text{(A.53)}$$

Thus, the second order solution reads:

$$\rho^{(2)}=\frac{1}{2}\alpha^2\left(\chi+\frac{1}{3}\right)(1-y^2)-\frac{1}{2}(1-x)^2+\frac{18}{35}\alpha\, Re\,(1-x) \quad \text{(A.54)}$$

$$u_y^{(2)}=\frac{3}{140}\alpha\, Re\, y\,(1-y^2)^2(5-y^2) \quad \text{(A.55)}$$

$$u_x^{(2)}=(1-y^2)\left[\frac{9}{4}(1-x)^2-\frac{3}{280}\alpha\, Re(57+84y^2-21y^4)(1-x)+\frac{3}{40}\alpha^2(1-5y^2)\right.$$
$$\left.-\frac{3}{5}\alpha^2\left(\chi+\frac{1}{3}\right)-\frac{3}{431200}\alpha^2\, Re^2(2193-9163y^2-6853y^4+5159y^6-616y^8)\right] \quad \text{(A.56)}$$

$$P^{(2)}=\frac{1}{2}(1-x)^3-\frac{6}{5}\alpha^2(1-x)-\frac{36}{35}\alpha\, Re(1-x)^2+\frac{3044}{13475}\alpha^2Re^2(1-x)$$
$$-\frac{1}{10}\alpha^2\left(\chi+\frac{1}{3}\right)(19-15y^2)(1-x)$$
$$+\frac{1}{280}\alpha^3Re(1-y^2)\left[2(5-28y^2+7y^4)+\left(\chi+\frac{1}{3}\right)(67+28y^2-7y^4)\right]. \quad \text{(A.57)}$$

The assumptions we have used are:

$$F'(0) = F(1) = \int_0^1 F(y)dy = 0$$

$$u_y^{(2)}(x,y) = u_y^{(2)}(y) \quad \text{and} \quad u_y^{(2)}(0) = u_y^{(2)}(1) = 0$$

$$P^{(2)}(1,1) = 0$$

Summarizing the results, the solution of the flow problem up to the second order is as follows:

$$\rho = 1+\varepsilon(1-x)+\varepsilon^2\left[\frac{1}{2}\alpha^2\left(\chi+\frac{1}{3}\right)(1-y^2) - \frac{1}{2}(1-x)^2 + \frac{18}{35}\alpha\, Re\,(1-x)\right] + O(\varepsilon^3) \quad \text{(A.58)}$$

$$u_y = \frac{3}{140}\varepsilon^2\alpha\, Re\, y\,(1-y^2)^2(5-y^2) + O(\varepsilon^3) \quad \text{(A.59)}$$

$$\begin{aligned} u_x = \frac{3}{2}(1-y^2)\Bigg[1 - \varepsilon(1-x) + \frac{1}{140}\varepsilon\alpha\, Re(-5+28y^2-7y^4) + \frac{3}{2}\varepsilon^2(1-x)^2 \\ -\frac{1}{140}\varepsilon^2\alpha Re(57+84y^2-21y^4)(1-x) + \frac{1}{20}\varepsilon^2\alpha^2(1-5y^2) - \frac{2}{5}\varepsilon^2\alpha^2\left(\chi+\frac{1}{3}\right) \\ -\frac{1}{215600}\alpha^2\varepsilon^2\, Re^2(2193-9163y^2-6853y^4+5159y^6-616y^8)\Bigg] + O(\varepsilon^3) \end{aligned} \quad \text{(A.60)}$$

$$\begin{aligned} P = 1 - x + \frac{1}{2}\varepsilon\alpha^2\left(\chi+\frac{1}{3}\right)(1-y^2) - \frac{1}{2}\varepsilon(1-x)^2 + \frac{18}{35}\varepsilon\alpha\, Re\,(1-x) + \frac{1}{2}\varepsilon^2(1-x)^3 \\ -\frac{6}{5}\varepsilon^2\alpha^2(1-x) - \frac{36}{35}\varepsilon^2\alpha Re(1-x)^2 + \frac{3044}{13475}\varepsilon^2\alpha^2 Re^2(1-x) - \frac{1}{10}\varepsilon^2\alpha^2\left(\chi+\frac{1}{3}\right)(19-15y^2)(1-x) \\ +\frac{1}{280}\varepsilon^2\,\alpha^3 Re(1-y^2)\left[2(5-28y^2+7y^4) + \left(\chi+\frac{1}{3}\right)(67+28y^2-7y^4)\right] + O(\varepsilon^3). \end{aligned} \quad \text{(A.61)}$$

Appendix B

Compressible axisymmetric Poiseuille flow

In this Appendix, the two-dimensional perturbation solution of the compressible axisymmetric Poiseuille flow is derived. To nondimensionalize the equations, we scale z by L, r by R, the density by the reference density ρ_0, the axial velocity u_z by $U = \dot{M}/\rho_0 \pi R^2$, the radial velocity u_r by UR/L, and the pressure by $8\eta LU/R^2$. The dimensionless forms of the governing equations are:

$$\rho \;=\; 1 \;+\; \varepsilon\, P\,, \tag{B.1}$$

$$\frac{1}{r}\frac{\partial}{\partial r}\left(r\,\rho\,u_r\right) \;+\; \frac{\partial}{\partial z}\left(\rho\,u_z\right) \;=\; 0\,, \tag{B.2}$$

$$\begin{aligned}\alpha\, Re\,\rho\,\left(u_r\,\frac{\partial\,u_z}{\partial\,r} \;+\; u_z\,\frac{\partial\,u_z}{\partial\,z}\right) = -8\,\frac{\partial\,P}{\partial\,z} \;+\; \frac{1}{r}\,\frac{\partial}{\partial\,r}\left(r\,\frac{\partial\,u_z}{\partial\,r}\right) \;+\alpha^2\,\frac{\partial^2 u_z}{\partial\,z^2}\\ +\alpha^2\left(\chi \;+\; \frac{1}{3}\right)\left[\frac{\partial}{\partial\,z}\left(\frac{1}{r}\,\frac{\partial}{\partial\,r}\left(r\,u_r\right)\right) \;+\; \frac{\partial^2 u_z}{\partial\,z^2}\right]\,,\end{aligned} \tag{B.3}$$

$$\begin{aligned}\alpha^3\, Re\,\rho\,\left(u_r\,\frac{\partial\,u_r}{\partial\,r} \;+\; u_z\,\frac{\partial\,u_r}{\partial\,z}\right) = -8\,\frac{\partial\,P}{\partial\,r} \;+\; \alpha^2\,\frac{\partial}{\partial\,r}\left(\frac{1}{r}\,\frac{\partial}{\partial\,r}\left(r\,u_r\right)\right) \;+\alpha^4\,\frac{\partial^2 u_r}{\partial\,z^2}\\ +\alpha^2\left(\chi \;+\; \frac{1}{3}\right)\left[\frac{\partial}{\partial\,r}\left(\frac{1}{r}\,\frac{\partial}{\partial\,r}\left(r\,u_r\right)\right) \;+\; \frac{\partial^2 u_z}{\partial\,r\partial\,z}\right]\end{aligned} \tag{B.4}$$

where:

$$\chi \equiv \frac{\kappa}{\eta}, \quad \alpha \equiv \frac{R}{L}, \quad Re \equiv \frac{\rho_0 U R}{\eta}, \quad \text{and} \quad \varepsilon \equiv \frac{8\eta\beta L U}{R^2}.$$

The boundary conditions are similar to those used for the planar problem. Writing the primary fields as expansions in the perturbation parameter ε,

$$\left.\begin{aligned} \rho &= \rho^{(0)} + \varepsilon\rho^{(1)} + \varepsilon^2\rho^{(2)} + O(\varepsilon^3) \\ u_r &= u_r^{(0)} + \varepsilon\, u_r^{(1)} + \varepsilon^2\, u_r^{(2)} + O(\varepsilon^3) \\ u_z &= u_z^{(0)} + \varepsilon\, u_z^{(1)} + \varepsilon^2\, u_z^{(2)} + O(\varepsilon^3) \\ P &= P^{(0)} + \varepsilon\, P^{(1)} + \varepsilon^2\, P^{(2)} + O(\varepsilon^3) \end{aligned}\right\}, \tag{B.5}$$

substituting in the governing equations, and following similar steps as for the planar problem, we obtain the solution of the flow up to the second order.

Equation of state

$$\rho = 1 + \varepsilon P \quad \Longrightarrow$$

$$\rho^{(0)} + \varepsilon\rho^{(1)} + \varepsilon^2\rho^{(2)} = 1 + \varepsilon P^{(0)} + \varepsilon^2 P^{(1)} + \varepsilon^3 P^{(2)}$$

Therefore,

$$\rho^{(0)} = 1, \quad \rho^{(1)} = P^{(0)} \quad \text{and} \quad \rho^{(2)} = P^{(1)}$$

Continuity Equation

Substituting into

$$\frac{1}{r}\frac{\partial}{\partial r}(r\rho u_r) + \frac{\partial}{\partial z}(\rho u_z) = 0$$

we get

$$\frac{1}{r}\frac{\partial}{\partial r}\left[r(\rho^{(0)} + \varepsilon\rho^{(1)} + \varepsilon^2\rho^{(2)} + ...)(u_r^{(0)} + \varepsilon u_r^{(1)} + \varepsilon^2 u_r^{(2)} + ...)\right]$$
$$+\frac{\partial}{\partial z}\left[(\rho^{(0)} + \varepsilon\rho^{(1)} + \varepsilon^2\rho^{(2)} + ...)(u_z^{(0)} + \varepsilon u_z^{(1)} + \varepsilon^2 u_z^{(2)} + ...)\right] = 0$$

$\Longrightarrow$

$$\frac{1}{r}\frac{\partial}{\partial r}\left[r\left(\rho^{(0)}u_r^{(0)} + \varepsilon\rho^{(0)}u_r^{(1)} + \varepsilon^2\rho^{(0)}u_r^{(2)} + \varepsilon\rho^{(1)}u_r^{(0)} + \varepsilon^2\rho^{(1)}u_r^{(1)} + \varepsilon^2\rho^{(2)}u_r^{(0)}\right)\right]$$

$$+\frac{\partial}{\partial z}\left[\left(\rho^{(0)}u_z^{(0)}+\varepsilon\rho^{(0)}u_z^{(1)}+\varepsilon^2\rho^{(0)}u_z^{(2)}+\varepsilon\rho^{(1)}u_z^{(0)}+\varepsilon^2\rho^{(1)}u_z^{(1)}+\varepsilon^2\rho^{(2)}u_z^{(0)}\right)\right]+O(\varepsilon^3)=0$$

$\Longrightarrow$

$$\frac{1}{r}\frac{\partial}{\partial r}\left[r\rho^{(0)}u_r^{(0)}+\varepsilon r\left(\rho^{(0)}u_r^{(1)}+\rho^{(1)}u_r^{(1)}\right)+\varepsilon^2 r\left(\rho^{(0)}u_r^{(2)}+\rho^{(1)}u_r^{(1)}+\rho^{(2)}u_r^{(0)}\right)\right]$$

$$+\frac{\partial}{\partial z}\left[\rho^{(0)}u_z^{(0)}+\varepsilon\left(\rho^{(0)}u_z^{(1)}+\rho^{(1)}u_z^{(0)}\right)+\varepsilon^2\left(\rho^{(0)}u_z^{(2)}+\rho^{(1)}u_z^{(1)}+\rho^{(2)}u_z^{(0)}\right)\right]+O(\varepsilon^3)=0$$

Thus we get:

Zero - order

$$\frac{1}{r}\frac{\partial}{\partial r}\left(r\rho^{(0)}u_r^{(0)}\right)+\frac{\partial}{\partial z}\left(\rho^{(0)}u_z^{(0)}\right)=0$$

First - order

$$\frac{1}{r}\frac{\partial}{\partial r}\left[r\left(\rho^{(0)}u_r^{(1)}+\rho^{(1)}u_r^{(0)}\right)+\frac{\partial}{\partial z}\left(\rho^{(0)}u_z^{(1)}+\rho^{(1)}u_z^{(0)}\right)\right]=0$$

Second - order

$$\frac{1}{r}\frac{\partial}{\partial r}\left[r\left(\rho^{(0)}u_r^{(2)}+\rho^{(1)}u_r^{(1)}+\rho^{(2)}u_r^{(0)}\right)\right]+\frac{\partial}{\partial z}\left[\rho^{(0)}u_z^{(2)}+\rho^{(1)}u_z^{(1)}+\rho^{(2)}u_z^{(0)}\right]=0$$

z-component of the momentum equation

Substituting into

$$\alpha Re\rho\left(u_r\frac{\partial u_z}{\partial r}+u_z\frac{\partial u_z}{\partial z}\right)=-8\frac{\partial P}{\partial z}+\alpha^2\frac{\partial^2 u_z}{\partial z^2}+\frac{1}{r}\frac{\partial}{\partial r}\left(r\frac{\partial u_z}{\partial r}\right)$$
$$+\alpha^2\left(\chi+\frac{1}{3}\right)\left[\frac{\partial}{\partial z}\left(\frac{1}{r}\frac{\partial}{\partial r}\left(r\frac{\partial u_z}{\partial r}\right)\right)+\frac{\partial^2 u_z}{\partial z^2}\right]$$

we get

$$\alpha Re\left(\rho^{(0)}+\varepsilon\rho^{(1)}+\varepsilon^2\rho^{(2)}+...\right)\left[\left(u_r^{(0)}+\varepsilon u_r^{(1)}+\varepsilon^2 u_r^{(2)}+...\right)\frac{\partial}{\partial r}\left(u_z^{(0)}+\varepsilon u_z^{(1)}+\varepsilon^2 u_z^{(2)}+...\right)\right.$$
$$\left.+\left(u_z^{(0)}+\varepsilon u_z^{(1)}+\varepsilon^2 u_z^{(2)}+...\right)\frac{\partial}{\partial z}\left(u_z^{(0)}+\varepsilon u_z^{(1)}+\varepsilon^2 u_z^{(2)}+...\right)\right]$$
$$=-8\frac{\partial}{\partial z}\left(P^{(0)}+\varepsilon P^{(1)}+\varepsilon^2 P^{(2)}+...\right)+\frac{1}{r}\frac{\partial}{\partial r}\left(r\frac{\partial}{\partial r}\left(u_z^{(0)}+\varepsilon u_z^{(1)}+\varepsilon^2 u_z^{(2)}+...\right)\right)$$
$$+\alpha^2\frac{\partial^2}{\partial z^2}\left(u_z^{(0)}+\varepsilon u_z^{(1)}+\varepsilon^2 u_z^{(2)}+...\right)$$

$$+\alpha^2\left(\chi+\frac{1}{3}\right)\left\{\frac{\partial}{\partial z}\left[\frac{1}{r}\frac{\partial}{\partial r}\left(r\left(u_r^{(0)}+\varepsilon u_r^{(1)}+\varepsilon^2 u_r^{(2)}+...\right)\right)\right]+\frac{\partial^2}{\partial z^2}\left(u_z^{(0)}+\varepsilon u_z^{(1)}+\varepsilon^2 u_z^{(2)}+...\right)\right\}$$

$\Longrightarrow$

$$\begin{aligned}
&\alpha Re\left(\rho^{(0)}+\varepsilon\rho^{(1)}+\varepsilon^2\rho^{(2)}\right)\left[\left(u_r^{(0)}\frac{\partial u_z^{(0)}}{\partial r}+u_z^{(0)}\frac{\partial u_z^{(0)}}{\partial z}\right)\right.\\
&+\varepsilon\left(u_r^{(0)}\frac{\partial u_z^{(1)}}{\partial r}+u_r^{(1)}\frac{\partial u_z^{(0)}}{\partial r}+u_z^{(0)}\frac{\partial u_z^{(1)}}{\partial z}+u_z^{(1)}\frac{\partial u_z^{(0)}}{\partial z}\right)\\
&\left.+\varepsilon^2\left(u_r^{(0)}\frac{\partial u_z^{(2)}}{\partial r}+u_r^{(1)}\frac{\partial u_z^{(1)}}{\partial r}+u_r^{(2)}\frac{\partial u_z^{(0)}}{\partial r}+u_z^{(0)}\frac{\partial u_z^{(2)}}{\partial z}+u_z^{(1)}\frac{\partial u_z^{(1)}}{\partial z}+u_z^{(2)}\frac{\partial u_z^{(0)}}{\partial z}\right)\right]\\
&=-8\frac{\partial}{\partial z}\left(P^{(0)}+\varepsilon P^{(1)}+\varepsilon^2 P^{(2)}\right)+\alpha^2\frac{\partial^2}{\partial z^2}\left(u_z^{(0)}+\varepsilon u_z^{(1)}+\varepsilon^2 u_z^{(2)}\right)\\
&+\frac{1}{r}\frac{\partial}{\partial r}\left[r\frac{\partial}{\partial r}\left(u_z^{(0)}+\varepsilon u_z^{(1)}+\varepsilon^2 u_z^{(2)}\right)\right]\\
&+\alpha^2\left(\chi+\frac{1}{3}\right)\left\{\left[\frac{\partial}{\partial z}\left(\frac{1}{r}\frac{\partial}{\partial r}\left(ru_r^{(0)}\right)+\frac{\partial^2 u_z^{(0)}}{\partial z^2}\right)\right]+\varepsilon\left[\frac{\partial}{\partial z}\left(\frac{1}{r}\frac{\partial}{\partial r}\left(ru_r^{(1)}\right)+\frac{\partial^2 u_z^{(1)}}{\partial z^2}\right)\right]\right.\\
&\left.+\varepsilon^2\left[\frac{\partial}{\partial z}\left(\frac{1}{r}\frac{\partial}{\partial r}\left(ru_r^{(2)}\right)+\frac{\partial^2 u_z^{(2)}}{\partial z^2}\right)\right]\right\}+O(\varepsilon^3)
\end{aligned}$$

By collecting terms of equal order we get:

Zero - order

$$\begin{aligned}
\alpha Re\rho^{(0)}\left[u_r^{(0)}\frac{\partial u_z^{(0)}}{\partial r}+u_z^{(0)}\frac{\partial u_z^{(0)}}{\partial z}\right]&=-8\frac{\partial P^{(0)}}{\partial z}+\alpha^2\frac{\partial^2 u_z^{(0)}}{\partial z^2}+\frac{1}{r}\frac{\partial}{\partial r}\left(r\frac{\partial u_z^{(0)}}{\partial r}\right)\\
&+\alpha^2\left(\chi+\frac{1}{3}\right)\left[\frac{\partial}{\partial z}\left(\frac{1}{r}\frac{\partial}{\partial r}\left(ru_z^{(0)}\right)\right)+\frac{\partial^2 u_z^{(0)}}{\partial r}\right]
\end{aligned}$$

First - order

$$\begin{aligned}
&\alpha Re\rho^{(1)}\left[u_r^{(0)}\frac{\partial u_z^{(0)}}{\partial r}+u_z^{(0)}\frac{\partial u_z^{(0)}}{\partial z}\right]+\alpha Re\rho^{(0)}\left[u_r^{(0)}\frac{\partial u_z^{(1)}}{\partial r}+u_r^{(1)}\frac{\partial u_z^{(0)}}{\partial r}+u_z^{(0)}\frac{\partial u_z^{(1)}}{\partial z}+u_z^{(1)}\frac{\partial u_z^{(0)}}{\partial z}\right]\\
&=-8\frac{\partial P^{(1)}}{\partial z}+\alpha^2\frac{\partial^2 u_z^{(1)}}{\partial z^2}+\frac{1}{r}\frac{\partial}{\partial r}\left(r\frac{\partial u_z^{(1)}}{\partial r}\right)+\alpha^2\left(\chi+\frac{1}{3}\right)\left[\frac{\partial}{\partial z}\left(\frac{1}{r}\frac{\partial}{\partial r}\left(ru_z^{(1)}\right)\right)+\frac{\partial^2 u_z^{(1)}}{\partial z^2}\right]
\end{aligned}$$

Second - order

$$\begin{aligned}
&\alpha Re\rho^{(2)}\left[u_r^{(0)}\frac{\partial u_z^{(0)}}{\partial r}+u_r^{(0)}\frac{\partial u_z^{(0)}}{\partial z}\right]+\alpha Re\rho^{(1)}\left[u_r^{(0)}\frac{\partial u_z^{(1)}}{\partial r}+u_r^{(1)}\frac{\partial u_z^{(0)}}{\partial r}+u_z^{(0)}\frac{\partial u_z^{(1)}}{\partial z}+u_z^{(1)}\frac{\partial u_z^{(0)}}{\partial z}\right]\\
&+\alpha Re\rho^{(0)}\left[u_r^{(0)}\frac{\partial u_z^{(2)}}{\partial r}+u_r^{(1)}\frac{\partial u_z^{(1)}}{\partial r}+u_r^{(0)}\frac{\partial u_z^{(1)}}{\partial r}+u_z^{(0)}\frac{\partial u_z^{(2)}}{\partial z}+u_z^{(1)}\frac{\partial u_r^{(1)}}{\partial z}+u_z^{(2)}\frac{\partial u_z^{(0)}}{\partial z}\right]
\end{aligned}$$

$$= -8\frac{\partial P^{(2)}}{\partial z} + \alpha^2\frac{\partial^2 u_z^{(2)}}{\partial z^2} + \frac{1}{r}\frac{\partial}{\partial r}\left(r\frac{\partial u_z^{(2)}}{\partial r}\right) + \alpha^2\left(\chi+\frac{1}{3}\right)\left[\frac{\partial}{\partial z}\left(\frac{1}{r}\frac{\partial}{\partial r}\left(ru_z^{(2)}\right)\right) + \frac{\partial^2 u_z^{(2)}}{\partial z^2}\right]$$

r-component of the momentum equation

By substituting into

$$\alpha^3 Re\rho\left(u_r\frac{\partial u_r}{\partial r} + u_z\frac{\partial u_r}{\partial z}\right) = -8\frac{\partial P}{\partial r} + \alpha^4\frac{\partial^2 u_r}{\partial z^2} + \alpha^2\frac{\partial}{\partial r}\left(\frac{1}{r}\frac{\partial}{\partial r}(ru_r)\right)$$
$$+\alpha^2\left(\chi+\frac{1}{3}\right)\left[\frac{\partial}{\partial r}\left(\frac{1}{r}\frac{\partial}{\partial r}(ru_r)\right) + \frac{\partial^2 u_z}{\partial r\partial z}\right]$$

we get

$$\alpha^3 Re\left(\rho^{(0)}+\varepsilon\rho^{(1)}+\varepsilon^2\rho^{(2)}+...\right)\left[\left(u_r^{(0)}+\varepsilon u_r^{(1)}+\varepsilon^2 u_r^{(2)}+...\right)\frac{\partial}{\partial r}\left(u_r^{(0)}+\varepsilon u_r^{(1)}+\varepsilon^2 u_r^{(2)}+...\right)\right.$$
$$\left.+\left(u_z^{(0)}+\varepsilon u_z^{(1)}+\varepsilon^2 u_z^{(2)}+...\right)\frac{\partial}{\partial z}\left(u_r^{(0)}+\varepsilon u_r^{(1)}+\varepsilon^2 u_r^{(2)}+...\right)\right]$$
$$= -8\frac{\partial}{\partial r}\left(P^{(0)}+\varepsilon P^{(1)}+\varepsilon^2 P^{(2)}+...\right) + \alpha^4\frac{\partial^2}{\partial z^2}\left(u_r^{(0)}+\varepsilon u_r^{(1)}+\varepsilon^2 u_r^{(2)}+...\right)$$
$$+\alpha^2\frac{\partial}{\partial r}\left(\frac{1}{r}\frac{\partial}{\partial r}r\left(u_r^{(0)}+\varepsilon u_r^{(1)}+\varepsilon^2 u_r^{(2)}+...\right)\right)$$
$$+\alpha^2\left(\chi+\frac{1}{3}\right)\left[\frac{\partial}{\partial r}\left(\frac{1}{r}\frac{\partial}{\partial r}r\left(u_r^{(0)}+\varepsilon u_r^{(1)}+\varepsilon^2 u_r^{(2)}+...\right)\right) + \frac{\partial^2}{\partial r\partial z}\left(u_z^{(0)}+\varepsilon u_z^{(1)}+\varepsilon^2 u_z^{(2)}+...\right)\right]$$

$\Longrightarrow$

$$\alpha^3 Re\left(\rho^{(0)}+\varepsilon\rho^{(1)}+\varepsilon^2\rho^{(2)}\right)\left[\left(u_r^{(0)}\frac{\partial u_r^{(0)}}{\partial r} + u_z^{(0)}\frac{\partial u_r^{(0)}}{\partial z}\right)\right.$$
$$+\varepsilon\left(u_r^{(0)}\frac{\partial u_r^{(1)}}{\partial r} + u_r^{(1)}\frac{\partial u_r^{(0)}}{\partial r} + u_z^{(0)}\frac{\partial u_r^{(1)}}{\partial z} + u_z^{(1)}\frac{\partial u_r^{(0)}}{\partial z}\right)$$
$$\left.+\varepsilon^2\left(u_r^{(0)}\frac{\partial u_r^{(2)}}{\partial r} + u_r^{(1)}\frac{\partial u_r^{(1)}}{\partial r} + u_r^{(2)}\frac{\partial u_r^{(0)}}{\partial r} + u_z^{(0)}\frac{\partial u_r^{(2)}}{\partial z} + u_z^{(1)}\frac{\partial u_r^{(1)}}{\partial z} + u_z^{(2)}\frac{\partial u_r^{(0)}}{\partial z}\right)\right]$$
$$= -8\frac{\partial}{\partial r}\left(P^{(0)}+\varepsilon P^{(1)}+\varepsilon^2 P^{(2)}\right) + \alpha^4\frac{\partial^2}{\partial z^2}\left(u_r^{(0)}+\varepsilon u_r^{(1)}+\varepsilon^2 u_r^{(2)}\right)$$
$$+\alpha^2\frac{\partial}{\partial r}\left(\frac{1}{r}\frac{\partial}{\partial r}r\left(u_r^{(0)}+\varepsilon u_r^{(1)}+\varepsilon^2 u_r^{(2)}\right)\right)$$
$$+\alpha^2\left(\chi+\frac{1}{3}\right)\left\{\left[\frac{\partial}{\partial r}\left(\frac{1}{r}\frac{\partial}{\partial r}\left(ru_r^{(0)}\right)\right) + \frac{\partial^2 u_z^{(0)}}{\partial r\partial z}\right] + \varepsilon\left[\frac{\partial}{\partial r}\left(\frac{1}{r}\frac{\partial}{\partial r}\left(ru_r^{(1)}\right)\right) + \frac{\partial^2 u_z^{(1)}}{\partial r\partial z}\right]\right.$$
$$\left.+\varepsilon^2\left[\frac{\partial}{\partial r}\left(\frac{1}{r}\frac{\partial}{\partial r}\left(ru_r^{(2)}\right)\right) + \frac{\partial^2 u_z^{(2)}}{\partial r\partial z}\right]\right\} + O(\varepsilon^3)$$

Thus we have:

Zero - order

$$\alpha^3 Re\rho^{(0)}\left[u_r^{(0)}\frac{\partial u_r^{(0)}}{\partial r}+u_z^{(0)}\frac{\partial u_r^{(0)}}{\partial z}\right]=-8\frac{\partial P^{(0)}}{\partial r}+\alpha^4\frac{\partial^2 u_r^{(0)}}{\partial z^2}+\alpha^2\frac{\partial}{\partial r}\left(\frac{1}{r}\frac{\partial}{\partial r}(ru_r)\right)$$
$$+\alpha^2\left(\chi+\frac{1}{3}\right)\left[\alpha^2\frac{\partial}{\partial r}\left(\frac{1}{r}\frac{\partial}{\partial r}(ru_r^{(0)})\right)\frac{\partial^2 u_z^{(0)}}{\partial r\partial z}\right]$$

First - order

$$\alpha^3 Re\rho^{(1)}\left[u_r^{(0)}\frac{\partial u_r^{(0)}}{\partial r}+u_z^{(0)}\frac{\partial u_r^{(0)}}{\partial z}\right]+\alpha^3 Re\rho^{(0)}\left[u_r^{(0)}\frac{\partial u_r^{(1)}}{\partial r}+u_r^{(1)}\frac{\partial u_r^{(0)}}{\partial r}+u_z^{(0)}\frac{\partial u_r^{(1)}}{\partial z}+u_z^{(1)}\frac{\partial u_r^{(0)}}{\partial z}\right]$$
$$=-8\frac{\partial P^{(1)}}{\partial r}+\alpha^4\frac{\partial^2 u_r^{(1)}}{\partial z^2}+\alpha^2\frac{\partial}{\partial r}\left(\frac{1}{r}\frac{\partial}{\partial r}(ru_r^{(1)})\right)+\alpha^2\left(\chi+\frac{1}{3}\right)\left(\alpha^2\frac{\partial}{\partial r}\left(\frac{1}{r}\frac{\partial}{\partial r}(ru_r^{(1)})\right)+\frac{\partial^2 u_z^{(1)}}{\partial r\partial z}\right)$$

Second - order

$$\alpha^3 Re\rho^{(2)}\left[u_r^{(0)}\frac{\partial u_r^{(0)}}{\partial r}+u_z^{(0)}\frac{\partial u_r^{(0)}}{\partial z}\right]+\alpha^3 Re\rho^{(1)}\left[u_r^{(0)}\frac{\partial u_r^{(1)}}{\partial r}+u_r^{(1)}\frac{\partial u_r^{(0)}}{\partial r}+u_z^{(0)}\frac{\partial u_r^{(1)}}{\partial z}+u_z^{(1)}\frac{\partial u_r^{(0)}}{\partial z}\right]$$
$$+\alpha^3 Re\rho^{(0)}\left[u_r^{(0)}\frac{\partial u_r^{(2)}}{\partial r}+u_z^{(1)}\frac{\partial u_r^{(1)}}{\partial r}+u_r^{(0)}\frac{\partial u_r^{(1)}}{\partial r}+u_r^{(0)}\frac{\partial u_r^{(2)}}{\partial r}+u_z^{(0)}\frac{\partial u_r^{(2)}}{\partial z}+u_z^{(1)}\frac{\partial u_r^{(1)}}{\partial z}+u_z^{(2)}\frac{\partial u_r^{(0)}}{\partial z}\right]$$
$$=-8\frac{\partial P^{(2)}}{\partial r}+\alpha^4\frac{\partial^2 u_r^{(2)}}{\partial z^2}+\alpha^2\alpha^2\frac{\partial}{\partial r}\left(\frac{1}{r}\frac{\partial}{\partial r}(ru_r^{(2)})\right)+\alpha^2\left(\chi+\frac{1}{3}\right)\left[\alpha^2\frac{\partial}{\partial r}\left(\frac{1}{r}\frac{\partial}{\partial r}(ru_r^{(2)})\right)+\frac{\partial^2 u_z^{(2)}}{\partial r\partial z}\right]$$

Zero-order solution

Using the zero-order equation of state,

$$\rho^{(0)} \;=\; 1, \tag{B.6}$$

and the continuity equation,

$$\frac{1}{r}\frac{\partial}{\partial r}\left[r\rho^{(0)}u_r^{(0)}\right] \;+\; \frac{\partial}{\partial z}\left[\rho^{(0)}u_z^{(0)}\right] \;=\; 0, \tag{B.7}$$

and assuming that

$$u_r^{(0)}(z,r)=0 \tag{B.8}$$

we find that

$$u_z^{(0)} = u_z^{(0)}(r) \tag{B.9}$$

Now, from the r-component of the momentum equation

$$\alpha^3 Re\rho^{(0)}\left[u_r^{(0)}\frac{\partial u_r^{(0)}}{\partial r} + u_z^{(0)}\frac{\partial u_r^{(0)}}{\partial z}\right] = -8\frac{\partial P^{(0)}}{\partial r} + \alpha^4\frac{\partial^2 u_r^{(0)}}{\partial z^2} + \alpha^2\frac{\partial}{\partial r}\left(\frac{1}{r}\frac{\partial}{\partial r}(ru_r)\right)$$
$$+\alpha^2\left(\chi+\frac{1}{3}\right)\left[\alpha^2\frac{\partial}{\partial r}\left(\frac{1}{r}\frac{\partial}{\partial r}(ru_r^{(0)})\right)\frac{\partial^2 u_z^{(0)}}{\partial r\partial z}\right]$$

and Eqs. (B.6)-(B.9) we find that the pressure is a function of z only

$$P^{(0)} = P^{(0)}(z) \tag{B.10}$$

Substituting into the z-momentum equation

$$\alpha Re\rho^{(0)}\left[u_r^{(0)}\frac{\partial u_z^{(0)}}{\partial r} + u_z^{(0)}\frac{\partial u_z^{(0)}}{\partial z}\right] = -8\frac{\partial P^{(0)}}{\partial z} + \alpha^2\frac{\partial^2 u_z^{(0)}}{\partial z^2} + \frac{1}{r}\frac{\partial}{\partial r}\left(r\frac{\partial u_z^{(0)}}{\partial r}\right)$$
$$+\alpha^2\left(\chi+\frac{1}{3}\right)\left[\frac{\partial}{\partial z}\left(\frac{1}{r}\frac{\partial}{\partial r}\left(ru_z^{(0)}\right)\right) + \frac{\partial^2 u_z^{(0)}}{\partial r}\right]$$

we get

$$8\frac{\partial P^{(0)}}{\partial z} = \frac{1}{r}\frac{\partial}{\partial r}\left(r\frac{\partial u_z^{(0)}}{\partial r}\right) = c \tag{B.11}$$

where c is a constant to be determined. Integrating the resulting ODEs and applying the boundary conditions $P^{(0)}(0)$=1 and $P^{(0)}(1)$=0 for $P(z)$ we obtain the zero-order solution for the pressure, which reads:

$$P^{(0)} = 1 - z \tag{B.12}$$

From equations (B.11) and (B.12) we have

$$-8 = \frac{1}{r}\frac{\partial}{\partial r}\left(r\frac{\partial u_z^{(0)}}{\partial r}\right).$$

By integrating twice and applying the conditions $\partial u_z^{(0)}/\partial r(0)$=0 and $u_z^{(0)}(1)$=0 we obtain the zero-order solution for the velocity

$$u_z^{(0)} = 2(1 - r^2) \tag{B.13}$$

Summarizing, the zero-order solution is as follows:

$$\rho^{(0)} = 1 \tag{B.14}$$

$$u_r^{(0)} = 0 \tag{B.15}$$

$$u_z^{(0)} = 2(1 - r^2) \tag{B.16}$$

$$P^{(0)} = 1 - z \tag{B.17}$$

The assumptions we have used are:

$$\partial u_z^{(0)}/\partial r(0) = u_z^{(0)}(1) = 0$$

$$u_r^{(0)}(z, r) = 0$$

$$P^{(0)}(0) = 1, \quad P^{(0)}(1) = 0$$

First-order solution

From the equation of state we obtain,

$$\rho^{(1)} = P^{(0)}(z) \quad \Longrightarrow \quad \rho^{(1)} = 1 - z. \tag{B.18}$$

Now, from the continuity equation

$$\frac{1}{r}\frac{\partial}{\partial r}\left(r\rho^{(0)}u_r^{(0)}\right) + \frac{\partial}{\partial z}\left(\rho^{(0)}u_z^{(0)}\right) = 0$$

Substituting the zero-order variables, $\rho^{(0)}$=1, $u_r^{(0)}$=0, $u_z^{(0)}$=2(1 − r^2), assuming that $u_r^{(1)}$=0 and integrating we get

$$u_z^{(1)} = -2(1 - z)(1 - r^2) + f(r) \tag{B.19}$$

where the function $f(r)$ is unknown. From the r-momentum equation

$$\alpha^3 Re\rho^{(1)}\left[u_r^{(0)}\frac{\partial u_r^{(0)}}{\partial r} + u_z^{(0)}\frac{\partial u_r^{(0)}}{\partial z}\right]$$

$$+\alpha^3 Re\rho^{(0)}\left[u_r^{(0)}\frac{\partial u_r^{(1)}}{\partial r}+u_r^{(1)}\frac{\partial u_r^{(0)}}{\partial r}+u_z^{(0)}\frac{\partial u_r^{(1)}}{\partial z}+u_z^{(1)}\frac{\partial u_r^{(0)}}{\partial z}\right]$$

$$=-8\frac{\partial P^{(1)}}{\partial r}+\alpha^4\frac{\partial^2 u_r^{(1)}}{\partial z^2}+\alpha^2\frac{\partial}{\partial r}\left(\frac{1}{r}\frac{\partial}{\partial r}(ru_r^{(1)})\right)$$

$$+\alpha^2\left(\chi+\frac{1}{3}\right)\left(\alpha^2\frac{\partial}{\partial r}\left(\frac{1}{r}\frac{\partial}{\partial r}(ru_r^{(1)})\right)+\frac{\partial^2 u_z^{(1)}}{\partial r\partial z}\right) \tag{B.20}$$

using all the above results and integrating with respect to r, we get

$$P^{(1)}=\frac{1}{4}\alpha^2(\chi+\frac{1}{3})(1-r^2)+g(z) \tag{B.21}$$

where $g(z)$ is an unknown function. Substituting in the r-momentum equation

$$\alpha Re\rho^{(1)}\left[u_r^{(0)}\frac{\partial u_z^{(0)}}{\partial r}+u_z^{(0)}\frac{\partial u_z^{(0)}}{\partial z}\right]+\alpha Re\rho^{(0)}\left[u_r^{(0)}\frac{\partial u_z^{(1)}}{\partial r}+u_r^{(1)}\frac{\partial u_z^{(0)}}{\partial r}+u_z^{(0)}\frac{\partial u_z^{(1)}}{\partial z}+u_z^{(1)}\frac{\partial u_z^{(0)}}{\partial z}\right]$$

$$=-8\frac{\partial P^{(1)}}{\partial z}+\alpha^2\frac{\partial^2 u_z^{(1)}}{\partial z^2}+\frac{1}{r}\frac{\partial}{\partial r}\left(r\frac{\partial u_z^{(1)}}{\partial r}\right)+\alpha^2\left(\chi+\frac{1}{3}\right)\left[\frac{\partial}{\partial z}\left(\frac{1}{r}\frac{\partial}{\partial r}\left(ru_z^{(1)}\right)\right)+\frac{\partial^2 u_z^{(1)}}{\partial z^2}\right],$$

and separating variables we obtain the following two ODEs:

$$4\alpha\, Re\,(1-r^2)^2\;-\;\frac{1}{r}\frac{\partial}{\partial\, r}\left(r\, f'(r)\right)=-8\frac{\partial\, P^{(1)}}{\partial\, z}+\;\frac{1}{r}\frac{\partial}{\partial\, r}\left(4r^2(1-z)\right)=c$$

where c is a constant to be determined. Integrating the first ODE twice gives

$$f(r)=\alpha Re\left(r^2-\frac{1}{2}r^4+\frac{1}{9}r^6\right)-\frac{1}{4}c_1r^2+c_2 \tag{B.22}$$

Applying $f'(0)$=$f(1)$=0, we obtain

$$0=\frac{11}{18}\alpha Re-\frac{1}{4}c_1+c_2 \tag{B.23}$$

where c_1 and c_2 are contstants to be determined. By applying the condition $\int_0^1 rf(r)dr$=0 we also get

$$\frac{13}{72}\alpha Re-\frac{1}{16}c_1+\frac{1}{2}c_2=0 \tag{B.24}$$

The constants c_1 and c_2 are determined by solving the linear system (B.23) and (B.24)

$$c_1 = 2\alpha Re \quad \text{and} \quad c_2 = -\frac{1}{9}\alpha Re$$

Substituting now in Eq. (B.22) we find the function $f(r)$

$$f(r) = -\frac{1}{18}\alpha Re(1-r^2)(2-7r^2+2^4) \tag{B.25}$$

and from Eq. (B.19) we obtain the first-order velocity component

$$u_z^{(1)} \;=\; 2(1\;-\;r^2)\left[-(1-z) - \frac{1}{36}\,\alpha\,Re\,(2-7r^2+2r^4)\right]. \tag{B.26}$$

From the $z-$momentum equation we find that

$$g(z) = -\left(\frac{1}{4}\alpha Re + 1\right) z + \frac{1}{2}z^2 + \kappa$$

where κ is to be determined. By substituting in Eq. (B.21) and using $P^{(1)}(1,1)$=0, we get:

$$\kappa = \frac{1}{4}\alpha Re + \frac{1}{2}$$

Thus the solution for the pressure is

$$P^{(1)} \;= -\frac{1}{2}\,(1\;-\;z)^2 \;+\; \frac{1}{4}\alpha\,Re\,(1-z) \;+\; \frac{1}{4}\alpha^2\,\left(\chi + \frac{1}{3}\right)(1\;-\;r^2). \tag{B.27}$$

Summarizing, again the first-order solution, reads:

$$\rho^{(1)} \;=\; 1-z \tag{B.28}$$

$$u_r^{(1)} \;=\; 0 \tag{B.29}$$

$$u_z^{(1)} \;=\; 2(1\;-\;r^2)\left[-(1-z) - \frac{1}{36}\,\alpha\,Re\,(2-7r^2+2r^4)\right] \tag{B.30}$$

$$P^{(1)} \;=\; -\frac{1}{2}\,(1\;-\;z)^2 \;+\; \frac{1}{4}\alpha\,Re\,(1-z) \;+\; \frac{1}{4}\alpha^2\,\left(\chi + \frac{1}{3}\right)(1\;-\;r^2). \tag{B.31}$$

The assumptions we have used are:

$$f'(0) = f(1) = \int_0^1 r f(r) dr = 0$$

$$u_r^{(1)}(z,r) = 0$$

$$P^{(1)}(1,1) = 0$$

Second-order solution

For $\rho^{(2)}$ we simply have:

$$\rho^{(2)} \;=\; P^{(1)}(z,r) \Longrightarrow$$

$$\rho^{(2)} \;= -\frac{1}{2}\,(1-z)^2 \;+\frac{1}{4}\,\alpha\,Re(1-z) + \frac{1}{4}\,\alpha^2\left(\chi+\frac{1}{3}\right)(1-r^2). \tag{B.32}$$

Now, from the continuity equation

$$\frac{1}{r}\frac{\partial}{\partial r}\left[r\left(\rho^{(0)}u_r^{(2)}+\rho^{(1)}u_r^{(1)}+\rho^{(2)}u_r^{(0)}\right)\right]+\frac{\partial}{\partial z}\left[\rho^{(0)}u_z^{(2)}+\rho^{(1)}u_z^{(1)}+\rho^{(2)}u_z^{(0)}\right]=0,$$

we get:

$$\begin{aligned} u_z^{(2)} \;=\; & 3(1-r^2)(1-z)^2 - \frac{1}{2}\alpha^2\left(\chi+\frac{1}{3}\right)(1-r^2)^2 + \frac{1}{r}\frac{\partial}{\partial\, r}\left(ru_r^{(2)}\right)(1-z) \\ & + \frac{\alpha\, Re}{18}(1-r^2)(-7-7r^2+2r^4)(1-z) + F(r) \end{aligned} \tag{B.33}$$

where $F(r)$ is a function to be determined. At this point the assumption of zero transverse velocity is relaxed. Letting u_r to be a function of r, $u_r^{(2)}$=$u_r^{(2)}(r)$, from the r-momentum equation

$$\begin{aligned} & \alpha^3 Re\rho^{(2)}\left[u_r^{(0)}\frac{\partial u_r^{(0)}}{\partial r}+u_z^{(0)}\frac{\partial u_r^{(0)}}{\partial z}\right] \\ & +\alpha^3 Re\rho^{(1)}\left[u_r^{(0)}\frac{\partial u_r^{(1)}}{\partial r}+u_r^{(1)}\frac{\partial u_r^{(0)}}{\partial r}+u_z^{(0)}\frac{\partial u_r^{(1)}}{\partial z}+u_z^{(1)}\frac{\partial u_r^{(0)}}{\partial z}\right] \\ & +\alpha^3 Re\rho^{(0)}\left[u_r^{(0)}\frac{\partial u_r^{(2)}}{\partial r}+u_z^{(1)}\frac{\partial u_r^{(1)}}{\partial r}+u_r^{(0)}\frac{\partial u_r^{(1)}}{\partial r}+u_r^{(0)}\frac{\partial u_r^{(2)}}{\partial r}+u_z^{(0)}\frac{\partial u_r^{(2)}}{\partial z}+u_z^{(1)}\frac{\partial u_r^{(1)}}{\partial z}+u_z^{(2)}\frac{\partial u_r^{(0)}}{\partial z}\right] \\ & = -8\frac{\partial P^{(2)}}{\partial r}+\alpha^4\frac{\partial^2 u_r^{(2)}}{\partial z^2}+\alpha^2\alpha^2\frac{\partial}{\partial r}\left(\frac{1}{r}\frac{\partial}{\partial r}(ru_r^{(2)})\right)+\alpha^2\left(\chi+\frac{1}{3}\right)\left[\alpha^2\frac{\partial}{\partial r}\left(\frac{1}{r}\frac{\partial}{\partial r}(ru_r^{(2)})\right)+\frac{\partial^2 u_z^{(2)}}{\partial r\partial z}\right] \end{aligned}$$

we get

$$8\frac{\partial P^{(2)}}{\partial r} = \alpha^2\left(\chi+\frac{4}{3}\right)\frac{\partial}{\partial r}\left(\frac{1}{r}\frac{\partial}{\partial r}\left(ru_r^{(2)}\right)\right)+\alpha^2\left(\chi+\frac{1}{3}\right)\frac{\partial}{\partial r}\left(\frac{\partial u_z^{(2)}}{\partial r}\right)$$

Integrating with respect to r we get the following expression for the pressure

$$P^{(2)} = \frac{1}{8}\alpha^2\left(\frac{1}{r}\frac{\partial\left(ru_r^{(2)}\right)}{\partial\, r}\right) - \frac{3}{4}\alpha^2\left(\chi+\frac{1}{3}\right)(1-r^2)(1-z)$$
$$-\frac{1}{144}\alpha^3 Re\left(\chi+\frac{1}{3}\right)(1-r^2)(-7-7r^2+2r^4)+G(z) \quad \text{(B.34)}$$

where $G(z)$ is a function to be determined. Combining the $z-$momentum equation

$$\alpha Re\rho^{(2)}\left[u_r^{(0)}\frac{\partial u_z^{(0)}}{\partial r}+u_r^{(0)}\frac{\partial u_z^{(0)}}{\partial z}\right]+\alpha Re\rho^{(1)}\left[u_r^{(0)}\frac{\partial u_z^{(1)}}{\partial r}+u_r^{(1)}\frac{\partial u_z^{(0)}}{\partial r}+u_z^{(0)}\frac{\partial u_z^{(1)}}{\partial z}+u_z^{(1)}\frac{\partial u_z^{(0)}}{\partial z}\right]$$
$$+\alpha Re\rho^{(0)}\left[u_r^{(0)}\frac{\partial u_z^{(2)}}{\partial r}+u_r^{(1)}\frac{\partial u_z^{(1)}}{\partial r}+u_r^{(0)}\frac{\partial u_z^{(1)}}{\partial r}+u_z^{(0)}\frac{\partial u_z^{(2)}}{\partial z}+u_z^{(1)}\frac{\partial u_r^{(1)}}{\partial z}+u_z^{(2)}\frac{\partial u_z^{(0)}}{\partial z}\right]$$
$$=-8\frac{\partial P^{(2)}}{\partial z}+\alpha^2\frac{\partial^2 u_z^{(2)}}{\partial z^2}+\frac{1}{r}\frac{\partial}{\partial r}\left(r\frac{\partial u_z^{(2)}}{\partial r}\right)+\alpha^2\left(\chi+\frac{1}{3}\right)\left[\frac{\partial}{\partial z}\left(\frac{1}{r}\frac{\partial}{\partial r}\left(ru_z^{(2)}\right)\right)+\frac{\partial^2 u_z^{(2)}}{\partial z^2}\right],$$

with the following results

$$\rho^{(1)}u_z^{(0)}\frac{\partial u_z^{(1)}}{\partial z}=4(1-z)(1-r^2)^2$$
$$u_z^{(0)}\frac{\partial u_z^{(2)}}{\partial z}=-12(1-z)(1-r^2)^2-\frac{1}{9}\alpha Re(-7+7r^2+9r^4-11r^6+2r^8)-2(1-r^2)\frac{1}{r}\frac{\partial}{\partial r}\left(ru_r^{(2)}\right)$$
$$u_z^{(1)}\frac{\partial u_z^{(1)}}{\partial z}=-4(1-z)(1-r^2)^2-\frac{1}{9}\alpha Re(2-11r^2+18r^4-11r^6+2r^8)$$

leads to:

$$\alpha\, Re\left[-4ru_r^{(2)}-12(1-r^2)^2(1-z)-2(1-r^2)\left(\frac{1}{r}\frac{\partial\left(ru_r^{(2)}\right)}{\partial\, r}\right)\right.$$
$$\left.+\frac{1}{9}\alpha\, Re(1-r^2)^2(-4r^4+14r^2+5)\right]$$
$$=6\alpha^2(1-r^2)-\frac{1}{2}\alpha^2\left(\chi+\frac{1}{3}\right)(-8+16r^2)-8G'(z)-12(1-z)^2+\frac{1}{r}\frac{\partial}{\partial r}\left(r\frac{\partial}{\partial r}\left(ru_r^{(2)}\right)\right)(1-z)$$
$$+\frac{1}{r}\frac{\partial}{\partial\, r}(rF'(r))+4\alpha\, Re\, r^2(2-r^2)(1-z). \quad \text{(B.35)}$$

In order to have separable variables, it is assumed that the terms involving both z and r must be equal to a constant:

$$4\alpha Rer^2(2-r^2)+\frac{1}{r}\frac{\partial}{\partial r}\left(r\frac{\partial}{\partial r}\left(ru_r^{(2)}\right)\right)+12\alpha Re(1-r^2)^2=4\alpha\, Re\gamma. \quad \text{(B.36)}$$

where γ is new constant to be determined. Integrating the above expression with respect to r and assuming that $\partial\left(ru_r^{(2)}\right)/\partial r(0)=0$ lead to

$$\frac{1}{r}\frac{\partial}{\partial r}\left(ru_r^{(2)}\right)=\frac{1}{9}\alpha Re\left(9(\gamma-3)r^2+9r^4-2r^6+\gamma_1\right) \tag{B.37}$$

Integrating once more and using the boundary condition $u_r^{(2)}(0,z)=0$, we get

$$u_r^{(2)}=\frac{1}{36}\alpha Re\left(9(\gamma-3)r^3+6r^5-r^7+2\gamma_1 r\right) \tag{B.38}$$

Finally using the following boundary conditions $\partial u_r^{(2)}/\partial r(1)=u_r^{(2)}(1)=0$ we get the system

$$\left.\begin{aligned}27\gamma+2\gamma_1&=58\\9\gamma+2\gamma_1&=22\end{aligned}\right\} \tag{B.39}$$

which is easily solved yielding

$$\gamma=\gamma_1=2$$

Thus, the transverse velocity component reads

$$u_r^{(2)}=\frac{1}{36}\alpha\, Re\, r\,(1-r^2)^2(4-r^2). \tag{B.40}$$

and from Eq. (B.37) becomes:

$$\frac{1}{r}\frac{\partial}{\partial r}\left(ru_r^{(2)}\right)=\frac{1}{9}\alpha Re\left(-9r^2+9r^4-2r^6+2\right) \tag{B.41}$$

Now, from Eqs. (B.33) and (B.41) we get:

$$u_z^{(2)}=2(1-r^2)\left[\frac{3}{2}(1-z)^2-\frac{1}{12}\alpha Re(1+7r^2-2r^4)(1-z)\right]$$
$$-\frac{1}{2}\alpha\left(\chi+\frac{1}{3}\right)(1-r^2)^2+F(r) \tag{B.42}$$

Separating variables in Eq. (B.35) gives the following ODEs for $F(r)$ and $G(x)$:

$$\alpha Re\left[-4ru_r^{(2)}-2(1-r^2)\left(\frac{1}{r}\frac{\partial\,(ru_r^{(2)})}{\partial\, r}\right)-\frac{1}{9}\,\alpha\, Re(-5-4r^2+27r^4-22r^6+4r^8)\right]$$

$$-6\alpha^2(1-r^2)+\frac{\alpha^2}{2}\left(\chi+\frac{1}{3}\right)(-8+16r^2)-\frac{1}{r}\frac{\partial}{\partial r}(rF'(r))=A \qquad \text{(B.43)}$$

and

$$-8G'(z)-12(1-z)^2+4\alpha\, Re\,\gamma(1-z)\;=\;A. \qquad \text{(B.44)}$$

where A is another constant to be determined. Integrating Eq. (B.37) once and applying the condition $F'(0)$=0, we obtain

$$F'(r)=-\frac{1}{2}Ar-\frac{3}{2}\alpha^2 r(2-r^2)+2\alpha^2\left(\chi+\frac{1}{3}\right)(-1+r^2)$$
$$+\frac{1}{9}\alpha^2 Re^2\left(\frac{1}{2}r-\frac{11}{2}r^3-9r^5+\frac{19}{4}r^7-\frac{7}{10}r^9\right)$$

Integrating once more we get

$$F(r)=-\frac{1}{4}Ar^2-\frac{3}{8}\alpha^2 r^2\left(4-r^2\right)+\frac{1}{2}\alpha^2\left(\chi+\frac{1}{3}\right)(-2r^2+r^4)$$
$$+\frac{1}{9}\alpha^2 Re^2\left(\frac{1}{4}r^2+\frac{11}{8}r^4-\frac{3}{2}r^6+\frac{19}{32}r^8-\frac{7}{100}r^{10}\right)+c_1 \qquad \text{(B.45)}$$

where c_1 is a constant to be determined. By applying the condition $F(1)$=0 we have

$$0=-\frac{1}{4}A-\frac{9}{8}\alpha^2-\frac{1}{2}\alpha^2\left(\chi+\frac{1}{3}\right)+\frac{519}{7200}\alpha^2 Re^2+c_1 \qquad \text{(B.46)}$$

Apply the condition $\int_0^1 rF(r)dr$=0 gives

$$-\frac{1}{4}A-\frac{5}{4}\alpha^2-\frac{2}{3}\alpha^2\left(\chi+\frac{1}{3}\right)+\frac{757}{10800}\alpha^2 Re^2+2c_1=0 \qquad \text{(B.47)}$$

Solving the system of Eqs. (B.46) and (B.47) we find the constants

$$A=-4\alpha^2-\frac{4}{3}\alpha^2\left(\chi+\frac{1}{3}\right)+\frac{2}{27}\alpha^2 Re^2 \qquad \text{(B.48)}$$

and

$$c_1=\frac{1}{8}\alpha^2+\frac{1}{6}\alpha^2\left(\chi+\frac{1}{3}\right)-\frac{43}{21600}\alpha^2 Re^2 \qquad \text{(B.49)}$$

By substituting Eqs. (B.48) and (B.49) in Eq. (B.45) we obtain

$$F(r)\;=\frac{\alpha^2\,Re^2}{9}\left(\frac{43}{2400}-\frac{5}{12}r^2+\frac{11}{8}r^4-\frac{3}{2}r^6+\frac{19}{32}r^8-\frac{7}{100}r^{10}\right)$$

$$+\alpha^2\left(\frac{1}{8}-\frac{1}{2}r^2+\frac{3}{8}r^4\right)+\alpha^2\left(\chi+\frac{1}{3}\right)\left(-\frac{2}{3}r^2+\frac{1}{2}r^4+\frac{1}{6}\right) \quad \text{(B.50)}$$

Thus axial velocity component becomes

$$u_z^{(2)}=2(1-r^2)\left[\frac{3}{2}(1-z)^2-\frac{1}{6}\alpha^2\left(\chi+\frac{1}{3}\right)-\frac{1}{12}\alpha\, Re(1+7r^2-2r^4)(1-z)\right.$$
$$\left.+\frac{1}{16}\alpha^2(1-3r^2)+\frac{1}{43200}\alpha^2\, Re^2(43-957r^2+2343r^4-1257r^6+168r^8)\right] \quad \text{(B.51)}$$

Integrating now Eq. (B.44) and substituting A under the condition $P^{(2)}(1,1)$=0 we obtain

$$G(z)=\frac{1}{2}(1-z)^3-\frac{1}{2}\alpha^2(1-z)-\frac{1}{2}\alpha Re(1-z)^2-\frac{1}{27}\alpha^2Re^2(1-z)-\frac{1}{6}\alpha^2\left(\chi+\frac{1}{3}\right)(1-z) \quad \text{(B.52)}$$

Thus, the pressure is given by

$$P^{(2)}=\frac{1}{2}(1-z)^3-\frac{1}{12}\alpha^2\left(\chi+\frac{1}{3}\right)(11-9r^2)(1-z)-\frac{1}{2}\alpha Re(1-z)^2-\frac{1}{2}\alpha^2(1-z)$$
$$+\frac{1}{27}\alpha^2Re^2(1-z)+\frac{1}{144}\alpha^3\, Re(1-r^2)\left[(4-14r^2+4r^4)+\left(\chi+\frac{1}{3}\right)(7+7r^2-2r^4)\right]. \quad \text{(B.53)}$$

Thus, the second order solution reads:

$$\rho^{(2)} = -\frac{1}{2}(1-z)^2+\frac{1}{4}\alpha\, Re(1-z)+\frac{1}{4}\alpha^2\left(\chi+\frac{1}{3}\right)(1-r^2) \quad \text{(B.54)}$$

$$u_r^{(2)} = \frac{1}{36}\alpha\, Re\, r\,(1-r^2)^2(4-r^2) \quad \text{(B.55)}$$

$$u_z^{(2)} = 2(1-r^2)\left[\frac{3}{2}(1-z)^2-\frac{1}{6}\alpha^2\left(\chi+\frac{1}{3}\right)\right.$$
$$\left.-\frac{1}{12}\alpha\, Re(1+7r^2-2r^4)(1-z)+\frac{1}{16}\alpha^2(1-3r^2)\right.$$
$$\left.+\frac{1}{43200}\alpha^2\, Re^2(43-957r^2+2343r^4-1257r^6+168r^8)\right] \quad \text{(B.56)}$$

$$P^{(2)} = \frac{1}{2}(1-z)^3-\frac{1}{12}\alpha^2\left(\chi+\frac{1}{3}\right)(11-9r^2)(1-z)-\frac{1}{2}\alpha\, Re(1-z)^2$$
$$-\frac{1}{2}\alpha^2(1-z)+\frac{1}{27}\alpha^2Re^2(1-z)$$
$$+\frac{1}{144}\alpha^3\, Re(1-r^2)\left[(4-14r^2+4r^4)+\left(\chi+\frac{1}{3}\right)(7+7r^2-2r^4)\right]. \quad \text{(B.57)}$$

The assumptions we have used are:

$$F(1)=\int_0^1 rF(r)dr=0$$

$$u_r^{(2)} = u_r^{(2)}(r), \partial\left(r u_r^{(2)}\right)/\partial r(0) = u_r^{(2)}(0,z) = \partial u_r^{(2)}/\partial r(1) = u_r^{(2)}(1) = 0$$

$$P^{(2)}(1,1) = 0$$

The solution of the flow up to the second order is as follows:

$$\begin{aligned}
\rho &= 1 + \varepsilon(1-z) \\
&\quad + \varepsilon^2\left[-\frac{1}{2}(1-z)^2 + \frac{1}{4}\alpha\, Re(1-z) + \frac{1}{4}\alpha^2\left(\chi + \frac{1}{3}\right)(1-r^2)\right] + O(\varepsilon^3) \quad \text{(B.58)} \\
u_r &= \frac{1}{36}\varepsilon^2\alpha\, Re\, r\,(1-r^2)^2(4-r^2) + O(\varepsilon^3) \quad \text{(B.59)} \\
u_z &= 2(1-r^2)\left[1 - \varepsilon(1-z) - \frac{1}{36}\varepsilon\alpha\, Re(2-7r^2+2r^4) + \frac{3}{2}\varepsilon^2(1-z)^2\right. \\
&\quad - \frac{1}{12}\varepsilon^2\alpha\, Re(1+7r^2-2r^4)(1-z) + \frac{1}{16}\varepsilon^2\alpha^2(1-3r^2) - \frac{1}{6}\varepsilon^2\alpha^2\left(\chi + \frac{1}{3}\right) \\
&\quad \left. + \frac{1}{43200}\varepsilon^2\alpha^2\, Re^2(43 - 957r^2 + 2343r^4 - 1257r^6 + 168r^8)\right] + O(\varepsilon^3) \quad \text{(B.60)} \\
P &= (1-z) - \frac{1}{2}\varepsilon\,(1-z)^2 + \frac{1}{4}\varepsilon\,\alpha\, Re\,(1-z) \\
&\quad + \frac{1}{4}\varepsilon\,\alpha^2\left(\chi + \frac{1}{3}\right)(1-r^2) + \frac{1}{2}\varepsilon^2(1-z)^3 \\
&\quad - \frac{1}{12}\varepsilon^2\alpha^2\left(\chi + \frac{1}{3}\right)(11-9r^2)(1-z) \\
&\quad - \frac{1}{2}\varepsilon^2\alpha\, Re(1-z)^2 - \frac{1}{2}\alpha^2(1-z) + \frac{1}{27}\varepsilon^2\alpha^2 Re^2(1-z) \\
&\quad + \frac{1}{144}\varepsilon^2\alpha^3\, Re(1-r^2)\left[(4-14r^2+4r^4) + \left(\chi + \frac{1}{3}\right)(7+7r^2-2r^4)\right] \\
&\quad + O(\varepsilon^3). \quad \text{(B.61)}
\end{aligned}$$

Bibliography

[1] K.P. Adewale, A.I. Leonov, Modelling spurt and stress oscillations in flows of molten polymers, *Rheol. Acta.* **36** (1997) 110-127.

[2] S. Ansumali, I.V. Karlin, Consistent lattice Boltzmann method, *Phys. Rev. Let.* **95** (2005) 260605.

[3] E.B. Arkilic, M.A. Schmidt, K.S. Breuer, Gaseous slip flow in long microchannels, *J. MEMS.* **6** (1995) 167-178.

[4] A.H. Behravesh, C.B. Park, R.D. Venter, Challenge to the production of low-density, fine-cell HDPE foams using CO_2, *Cellular Polymers* **17** (1998) 309-326.

[5] K. Bekkour, Evaluation of slip effects in the capillary flow of foams, *Appl. Rheol.* **9** (1999) 10-16.

[6] F. Belblidia, I.J. Keshtiban, M.F. Webster, Stabilised computations for viscoelastic flows under compressible considerations, *J. Non-Newtonian Fluid Mech.* **134** (2006) 56-76.

[7] O. Belkessam, U. Fritsching, Modelling and simulation of continuous metal foaming process, *Modelling Simut. Mater. Sci. Eng.* **11** (2003) 823-837.

[8] H.R. van den Berg, C.A. ten Seldam, P. S. van der Gulik, Compressible laminar flow in a capillary, *J. Fluid Mech.* **246** (1993) 1-20.

[9] V. Bertola, F. Bertrand, H. Tabuteau, D. Bonn, P. Coussot, Wall slip and yielding in pasty materials, *J. Rheol.* **47** (2003) 1211-1226.

[10] C.R. Beverly, R.I. Tanner, Compressible extrudate swell, *Rheol Acta* **35** (1993) 526-531.

[11] R.B. Bird, W.E. Stewart, E.N. Lightfoot, *Transport Phenomena.*, John Wiley, 2002.

[12] C. Cai, Q. Sun, I.D. Boyd, Gas flows in microchannels and microtubes, *J. Fluid Mech.* **589** (2007) 305-314.

[13] F.N. Cogswell, Note: On the oscillating flow of HDPE in a capillary, *J. Rheol.* **37** (1993) 407-408.

[14] M.G. Cawkwell, M.E. Charles, Characterization of Canadian artic thixotropic gelled crude oils utilizing an eight-parameter model,*J. Pipelines* **7** (1989) 251264.

[15] M.R. Davidson, Q.D. Nguyen, H.P. Rønningsen, Restart model for a multi-plug gelled waxed oil pipeline, J. Petroleum Sci. Eng. **59** (2007) 1-16.

[16] C.F.J. Den Doelder, R.J. Koopmans, J. Molenaar, Quantitative modelling of HDPE spurt experiments using wall slip and generalised Newtonian flow, *J. Non-Newtonian Fluid Mech.* **79** (1998) 503-514.

[17] C.F.J. Den Doelder, R.J. Koopmans, J. Molenaar, A.A.F. Van de Ven, Comparing the wall slip and the constitutive approach for modelling spurt instabilities in polymer melt flows, *J. Non-Newtonian Fluid Mech.* **75** (1998) 25-41.

[18] M.M. Denn, Extrusion instabilities and wall slip, *Annu. Rev. Fluid Mech.* **33** (2001) 265-287.

[19] J.L.A. Dubbeldam, J. Molenaar, Dynamics of the spurt instability in polymer extrusion, *J. Non-Newtonian Fluid Mech.* **112** (2003) 217-235.

[20] V. Durand, B. Vergnes, J.F. Agassant, E. Benoit, R.J. Koopmans, Experimental study and modeling of oscillating flow of high density polyethylenes, *J. Rheology* **40** (1996) 383-394.

[21] N. El Kissi, J.M. Piau, Écoulement de fluides polymères enchevêtrés dans un capillaire. Modélisation du glissement macroscopique à la paroi, *C.R. Acad. Sci. Paris Série II* **309** (1989) 7-9.

[22] N. El Kissi, J.M. Piau, The different capillary flow regimes of entangled polydimethylsiloxane polymers: Macroscopic slip at the wall, hysteresis and cork flow, *J. Non-Newtonian Fluid Mech.* **37** (1990) 55-94.

[23] C. Enzendorfer, R.A. Harris, P. Valkó, M.J. Economides, P.A. Fokker, D.D. Davies, Pipe viscometry of foams, *J. Rheol.* **39** (1995) 345-358.

[24] J. Fan, J.R. Mitchell, J.M.V. Blanshard, A computer simulation of the dynamics of bubble growth and shrinkage during extrudate expansion, *J. Food Eng.* **23** (1994) 337-356.

[25] B.S. Gardiner, B.Z. Dlugogorski, G.J. Jameson, Yield stress measurements of aqueous foams in the dry limit, *J. Rheol.* **42** (1998a) 1437-1450.

[26] B.S. Gardiner, B.Z. Dlugogorski, G.J. Jameson, Rheology of fire-fighting foams, *Fire Safety J.* **31** (1998b) 61-75.

[27] B.S. Gardiner, B.Z. Dlugogorski, G.J. Jameson, Prediction of pressure losses in pipe flow of aqueous foams, *Ind. Eng. Chem. Res.* **38** (1999) 1099-1106.

[28] G.C. Georgiou, The compressible Newtonian extrudate swell problem, *Int. J. Numer. Methods Fluids* **20** (1995) 255-261.

[29] G. Georgiou, The time-dependent, Compressible Poiseuille and extrudate-swell flows of a Carreau fluid with slip at the wall, *J. Non-Newtonian Fluid Mech.* **109** (2003) 93-114.

[30] G. Georgiou, Stick-slip instability. Chapter 6 in Polymer Processing Instabilities: Control and Understanding, S.G. Hatzikiriakos, K. Migler (Eds.), Mercel Dekker, Inc. (2005) 161-206.

[31] G.C. Georgiou, A. Boudouvis, Converged solutions of the Newtonian extrudate swell problem, *Int. J. Numer. Methods Fluids* **29** (1999) 363-371.

[32] G.C. Georgiou, M.J.Crochet, Compressible viscous flow in slits with slip at the wall, *J. Rheol.* **38** (1994) 639-654.

[33] G.C. Georgiou, M.J. Crochet, Time-dependent compressible extrudate-swell problem with slip at the wall, *J. Rheol.* **38** (1994) 1745-1755.

[34] G.C. Georgiou, T.C. Papanastasiou, J.O. Wilkes, Laminar jets at high Reynolds and high surface tension, *AIChE J.* **34** (1988) 1559-1562.

[35] F. Golay, P. Helluy, Numerical simulation of a viscous compressible fluid based on a splitting method, Seminaire de mathematiques de lUniversite de Ferrare, Ferrare, 1998.

[36] J.M. Greenberg, Y. Demay, A simple model of the melt fracture instability, *Eur. J. Appl. Maths.* **5** (1994) 337-357.

[37] Z.Y. Guo, X.B. Wu, Compressibility effect on the gas flow and heat transfer in a microtube. *Int. J. Heat Mass Trans.* **40** (1997) 3251-3254.

[38] Z.Y. Guo, X.B. Wu, Further study on compressibility effects on the gas flow and heat transfer in a microtube, *Microscale Thermophys. Eng.* **2** (1998) 111-120.

[39] S.G. Hatzikiriakos, J.M. Dealy, Wall slip of molten high density polyethylenes. II. Capillary rheometer studies, *J. Rheol.* **36** (1992) 703-741.

[40] S.G. Hatzikiriakos, J.M. Dealy, Role of slip and fracture in the oscillating flow of HDPE in a capillary, *J. Rheol.* **36** (1992) 845-884.

[41] S.G. Hatzikiriakos, K. Migler (Eds.), Polymer processing instabilities: Control and Understanding, Mercel Dekker, Inc., New York (2004).

[42] B. Herzhaft, S. Kakadjian, M. Moan, Measurement and modeling of the flow behavior of aqueous foams using a recirculating pipe rheometer, *Colloids and Surfaces A: Physicochem Eng Aspects* **263** (2005) 153-164.

[43] R. Höhler, S. Cohen-Addad, Rheology of liquid foam, *J. Phys. Condens. Matter* **17** (2005) R1041-R1069.

[44] R.R. Huilgol, Z. You, On the importance of the pressure dependence of viscosity in steady non-isothermal shearing flows of compressible and incompressible fluids and in the isothermal fountain flow, *J. Non-Newton. Fluid Mech.* **136** (2006) 106-117.

[45] R.R. Huilgol, Z. You, Application of the augmented Lagrangian method to steady pipe flows of Bingham, Casson and Herschel-Bulkley fluids, *J. Non-Newton. Fluid Mech.* **128** (2005) 126-143.

[46] D.S. Kalika, M.M. Denn, Wall slip and extrudate distortion in linear low-density polyethylene, *J. Rheol.* **31** (1987) 815-834.

[47] I.J. Keshtiban, F. Belblidia, M.F. Webster, Computation of incompressible and weakly-compressible viscoelastic liquids flow: finite element/volume schemes, *J. Non-Newtonian Fluid Mech.* **126** (2005) 123-143.

[48] S.A. Khan, C. A. Schnepper, R. C. Armstrong, Foam rheology: III. Measurement of shear flow properties, *J. Rheol.* **32** (1988) 69-92.

[49] A.M. Kraynik, Foam flows, *Annu. Rev. Fluid Mech.* **20** (1988) 325-357.

[50] Y. Kwon, On Hadamard stability for compressible viscoelastic constitutive equations, *J. Non-Newtonian Fluid Mech.* **65** (1996) 151-163.

[51] P.C. Lee, J. Wang, C.B. Park, Extrusion of microcellular open-cell LDPE-based sheet foams, *J. Appl. Polym. Sci.* **102** (2006) 3376-3384.

[52] F.J. Lim, W.R. Schowalter, Wall slip of narrow molecular weight distribution polybutadienes, *J. Rheol.* **33** (1989) 1359-1382.

[53] J.M. Lupton, J.W. Regester, Melt flow of polyethylene at high rates, *Polym. Eng. Sci.* **5** (1965) 235.

[54] E. Mitsoulis, The numerical simulation of Boger fluids: A viscometric approximation approach, *Polymer Eng. Sci.* **26** (1986) 1552-1562.

[55] E. Mitsoulis, O.D. Velazquez, S.G. Hatzikiriakos, Transient capillary rheometry: Compressibility effects, *J. Non-Newtonian Fluid Mech.* **145** (2007) 102-108.

[56] C.I. Moraru, J.L. Kokini, Nucleation and expansion during extrusion and microwave heating of cereal foods, *Compr. Rev. Food Sci. Food Safety* **2** (2003) 147-165.

[57] H. Münstedt, M. Schmidt, E. Wassner, Stick and slip phenomena during extrusion of polyethylene melts as investigated by laser-Doppler velocimetry, *J. Rheol.* **44** (2000) 413-426.

[58] R.W. Myerholtz, Oscillating flow behavior of high-density polyethylene melts, *J. Appl. Polym. Sci.* **11** (1967) 687-698.

[59] H.E. Naguib, C.B. Park, N. Reichelt, Fundamental foaming mechanisms governing the volume expansion of extruded polypropylene foams, *J. Appl. Pol. Sci.* **91** (2004) 2661-2668.

[60] N.E. Naguib, C.B. Park, P.C. Lee, D. Xu, A study on the foaming behaviors of PP resins with talc as nucleating agent, *J. Polymer. Eng.* **26** (2006) 565-587.

[61] S. Okubo, Y. Hori, Model analysis of oscillating flow of high-density polyethylene melt, *J. Rheol.* **24** (1980) 253-257.

[62] C.B. Park, A.H. Behravesh, R.D. Venter, Low density microcellular foam processing in extrusion using CO_2, *Polymer. Eng. Sci.* **38** (1998) 1812-1823.

[63] C.B. Park, Y. Liu, H.E. Naguib, Challenge to forty-fold expansion of biodegradable polyester foams using carbon dioxide as a blowing agent, *Cellular Polymers* **18** (1999) 367-384.

[64] J. Pérez González, L. Pérez-Trejo, L. de Vargas, O. Manero, Inlet instabilities in the capillary flow of polyethylene melts, *Rheol. Acta* **36** (1997) 677-685.

[65] J.M. Piau, N. El Kissi, Measurement and modelling of friction in polymer melts during macroscopic slip at the wall, *J. Non-Newtonian Fluid Mech.* **54** (1994) 121-142.

[66] T.J. Poinsot, S.K. Lele, Boundary conditions for direct simulations of compressible viscous flows, *J. Comp. Phys.* **101** (1992) 104-129.

[67] R.K. Prud'homme, T.W. Chapman, J. R. Bowen, Laminar compressible flow in a tube, *Appl. Sci.Res.* **43** (1986) 67-74.

[68] F.H. Qin, D.J. Sun, X.Y. Yin, Perturbation analysis on gas flow in a straight microchannel, *Phys. Fluids* **19** (2007) 027103.

[69] A.V. Ramamurthy, Wall slip in viscous fluids and influence of materials of construction, *J. Rheol.* **30** (1986) 337-357.

[70] M. Ranganathan, M.R. Mackley, P.H.J. Spitteler, The application of the multipass rheometer to time-dependent capillary flow measurements of a polyethylene melt, *J. Rheol.* **43** (1999) 443-451.

[71] D.A. Reinelt, A.M. Kraynik, Simple shearing flow of dry soap foams with tetrahedrally close-packed structure, *J. Rheol.* **44** (2000) 453-471.

[72] L. Robert, B. Vergnes, Y. Demay, Flow birefringence study of the stick-slip instability during extrusion of high-density polyethylenes, *J. Non-Newtonian Fluid Mech.* **112** (2003) 27-42.

[73] L. Robert, B. Vergnes, Y. Demay, Complex transients in the capillary flow of linear polyethylene. *J. Rheol.* **44** (2001) 1183-1187.

[74] K. Sato, A. Toda, Physical mechanism of stick-slip behavior in polymer melt extrusion: Temperature dependence of flow curve, *J. Phys. Soc. Japan* **70** (2001) 3268-3273.

[75] L.W. Schwartz, A perturbation solution for compressible viscous channel flows, *J. Eng. Math.* **21** (1987) 69-86.

[76] L. Silva, T. Coupez, A unified model of the filling and post-filling stages in 3D injection moulding simulation, in: Proceedings of the PPS-18, Guimaraes, (2002).

[77] A.S. Sokhey, Y. Ali, M.A. Hanna, Effects of die dimensions on extruder performance, *J. Food Eng.* **31** (1997) 251-261.

[78] E. Taliadorou, G. Georgiou, A.N. Alexandrou, Two-dimensional numerical study of the effect of the reservoir region on polymer extrusion instabilities, *Proceedings of the 5th*

Hellenic Chemical Engineering Conference , Thessaloniki, Greece, May 26-28, Tziola Publications (2005) 121-124.

[79] E. Taliadorou, G. Georgiou, A.N. Alexandrou, Two-dimensional simulations of the effect of the reservoir region on the pressure oscillations observed in the stick-slip instability regime, *Proceedings of the 5th GRACM International Congress on Computational Mechanics* , Limassol, Cyprus, June 29-July 1, G Georgiou, P. Papanastasiou, M. Papadrakakis (Eds.) (2005) 629-636.

[80] E. Taliadorou, G. Georgiou, A. Alexandrou, Two-dimensional simulations of the effect of the reservoir region on the pressure oscillations observed in the stick-slip instability regime, *Int. J. Appl. Mech. Eng.* **11** (2006) 245-254.

[81] E. Taliadorou, G. Georgiou, E. Mitsoulis, Extrudate swell of strongly compressible foamed products, Proceedings of the 6^{th} *Hellenic Conference on Polymers*, Patras, 3-5 November (2006) 136-138.

[82] E. Taliadorou, G. Georgiou, A.N. Alexandrou, A two-dimensional numerical study of the stick-slip extrusion instability, *J. Non-Newtonian Fluid Mech.* **146** (2007) 30-44.

[83] E. Taliadorou, G. Georgiou, E. Mitsoulis, Numerical simulation of the extrusion of strongly compressible Newtonian liquids, *Rheol. Acta* **47** (2008) 49-62.

[84] E. Taliadorou, G. Georgiou, I. Moulitsas, Weakly compressible Poiseuille flows of a Herschel-Bulkley fluid, *J. Non-Newtonian Fluid Mech.*, accepted (2008).

[85] E. Taliadorou, M. Neophytou, G. Georgiou, Perturbation solutions of Poiseuille flows of weakly compressible Newtonian liquids, *J. Fluid Mech.*, submitted (2008).

[86] H.S. Tang, D.M. Kalyon, Unsteady circular tube flow of compressible polymeric liquids subject to pressure-dependent wall slip, *J. Rheol.* **52** (2008) 507-525.

[87] R.I. Tanner, Engineering Rheology, Oxford University Press, (2000) Oxford.

[88] D.C. Venerus, Laminar capillary flow of compressible viscous fluids, *J. Fluid Mech.* **555** (2006) 59-80.

[89] B. Vergnes, S. d'Halewyn, M.F. Boube, Wall slip and instabilities in the flow of EPDM compounds. In: P. Moldenaers, R. Keunings (eds), Theoretical and Applied Rheology, Amsterdam, Elsevier, Vol. 1, 399 (1992).

[90] G. Vinay, A. Wachs, I. Frigaard, Numerical simulation of weakly compressible Bingham flows: The restart of pipeline flows of waxy crude oils,*J. Non-Newtonian Fluid Mech.* **136** (2006) 93-105.

[91] G. Vinay, A. Wachs, I. Frigaard, Start-up transients and efficient computation of isothermal waxy crude oil flows,*J. Non-Newtonian Fluid Mech.* **143** (2007) 141-156.

[92] G.V. Vinogradov, A.Y. Malkin, Y.G. Yanovskii, E.K. Borisenkova, B.V. Yarlykov, G.V. Berezhnaya, Viscoelastic properties and flow of narrow distribution polybutadienes and polyisoprenes, *J. Polym. Sci. Part A2* **10** (1972) 1061-1084.

[93] L. Wang, G. M. Canjyal, D.D. Jones, C.L. Weller, M.A. Hanna, Modeling of bubble growth dynamics and nonisothermal expansion in starch-based foams during extrusion *Adv. Polymer. Techn.* **24** (2005) 29-45.

[94] S.Q. Wang, P.A. Drda, Superfluid-like stick-slip transition in capillary flow of linear Polyethylene. 1. General features, *Macromolecules* **29** (1996) 2627-2632.

[95] S.Q. Wang, P.A. Drda, Superfluid-like stick-slip transition in capillary flow of linear polyethylene. 2. Molecular weight and low-temperature anomaly, *Macromolecules* **29** (1996) 4115-4119.

[96] A. Weill, Capillary flow of linear polyethylene melt: Sudden increase of flow rate, *J. Non-Newtonian Fluid Mech.* **7** (1980) 303-314.

[97] J.L. Willett, R.L. Shogren, Processing and properties of extruded starch/polymer foams, *Polymer.* **43** (2002) 5935-5947.

[98] X. Xu, C.B. Park, D. Xu, R. Pop-Iliev, Effects of die geometry on cell nucleation of PS foams blown with CO_2, Polymer Eng. Sci. **43** (2003) 1378-1390.

[99] Y. Xu, M. A. Hanna, Preparation and properties of biodegradable foams from starch acetate and poly(tetramethylene adipate-co-terephthalate), *Carbohydrate Polymers* **59** (2005) 521-529.

[100] Z. Xu, P. Xue, F. Zhu, J. He, Effects of formulations and processing parameters on foam morphologies in the direct extrusion foaming of polypropylene using a single-screw extruder, *J. Cellular Plastics* **41** (2005) 169-185.

[101] Y. Zohar, S.Y.K. Lee, W.Y. Lee, L. Jiang, P. Tong, Subsonic gas flow in a straight and uniform microchannel. *J. Fluid Mech.* **472** (2002) 125-151.